Study on Piezoelectric Energy Generation under High Frequency Excitation

by

Yu Xiao

A Thesis submitted to the Faculty of Graduate Studies of
The University of Manitoba
in partial fulfilment of the requirements of the degree of

DOCTOR OF PHILOSOPHY

Department of Mechanical Engineering
University of Manitoba
Winnipeg, Manitoba, Canada

Declaration of Authorship

I, Yu Xiao, declare that this thesis titled, “Study on Piezoelectric Energy Generation under High Frequency Excitation” and the work presented in it are my own. I confirm that:

- This work was done wholly or mainly while in candidature for a research degree at this University.
- Where any part of this thesis has previously been submitted for a degree or any other qualification at this University or any other institution, this has been clearly stated.
- Where I have consulted the published work of others, this is always clearly attributed.
- Where I have quoted from the work of others, the source is always given. With the exception of such quotations, this thesis is entirely my own work.
- I have acknowledged all main sources of help.
- Where the thesis is based on work done by myself jointly with others, I have made clear exactly what was done by others and what I have contributed myself.

Abstract

The development of energy technology has stimulated the application of low-power wireless electronic devices. Batteries are commonly used to supply power for these devices, however, the limited lifespan and expensive replacement cost necessitate the development of generating electricity from waste energy. Energy generation, which collects wasted energy from external sources, has become a popular research topic. Over the past decades, the low cost and easy-to-apply characteristics of piezoelectric material have spurred various research endeavors aiming at developing piezoelectric energy generators based on different energy sources.

This thesis aims to develop piezoelectric energy generators (PEGs) under various working conditions using high frequency excitation, validate the accuracy of the corresponding models, investigate their dynamic behaviors, and evaluate their energy generation performance. A vehicle brake pad with embedded PEGs is developed by utilizing high-speed rotation of vehicle brake rotor. Charge dissipation from the measuring device is considered to accurately calculate the generated voltage from the piezoelectric patch during operation. Inspired by frictional contact during the braking process between the rotor and frictional layer, a shear mode PEG is proposed to explore its performance under self-excited friction-induced vibration (FIV). The dynamic voltage responses from experiment, closely matched with the analytical results, demonstrate the great performance from vibrations close to the resonant frequency of the system. A modified PEG employing bi-linear and impact techniques is then proposed, modeled, and tested through experiment to examine the improved performance and verify the continuous FIV under these conditions. To understand the mechanism and dynamic responses of nonlinear PEGs considering different connections between magnetic spring and piezoelectric element, mathematical models are proposed and solved through numerical iteration. The results from parameter studies demonstrate enhanced frequency bandwidth and operating velocity range using harmonic excitation and FIV, respectively. Furthermore, PEG using FIV has been extended to continuum

structures, and a piezoelectric coupled continuum beam using FIV is modeled, described, and studied for the first time to characterize its dynamic response and energy generation performance. Following that, a piezoelectric coupled stepped beam is modeled using a modified method, tested through experiment, and utilized as a case study of geometric optimization.

Acknowledgement

I would like to express my appreciation to my supervisor, Dr. Nan Wu, for providing countless guidance, feedback, and support throughout this research. His invaluable expertise in this research topic has helped me finish this work at a higher level, and it would not have been possible to complete this thesis without his contribution. Besides his technical support, I am also grateful to him for the financial support, reference letters, and valuable comments on different applications. Moreover, I am also grateful for his valuable advice in my life and future career development.

I would also like to express my appreciation to my esteemed internal members of the examination committee: Dr. Igor Telichev and Dr. Xihui Liang. I am thankful for the discussions we had in the past three years. I am also grateful for the insightful feedback on my thesis. I would also like to express my gratitude to the external member of the examination committee, Dr. Babak Safaei, for his thorough review and valuable comments, which have significantly contributed to the improvement of my thesis.

I would like to express my gratitude to Dr. Changguo Wang and Dr. Qingxiang Ji from the Harbin Institute of Technology for the collaboration in Chapter 3. I would also like to express my gratitude to Mr. Sviatoslaw Karnaoukh, a lab engineer at the University of Manitoba, who helped me set up the testing apparatus. I would like to express my gratitude to Mr. Sviatoslaw Karnaoukh, who helped me set up the testing apparatus for the experimental testing in Chapter 4. I would like to express my appreciation to Dr. Quan Wang from Shantou University for the valuable advices provided on mathematical modeling and technical writing in Chapter 5. I would like to express my gratitude to Dr. Ze-qi Lu and Mr. Wen-hang Liu from Shanghai University for the collaboration in Chapter 6.

I would also like to acknowledge every former and current member of the Sound and Vibration laboratory for their collaborative efforts on my research projects.

I am grateful for the financial support and scholarships I received in my Ph.D. program, including the Natural Sciences and Engineering Research Council of Canada (NSERC), the University of Manitoba Graduate Fellowship (UMGF), and the University of Manitoba Graduate Enhancement of Tri-Council Stipends (GETS).

Last but not least, I would like to take this opportunity to express my most profound appreciation to my beloved parents for their unconditional love, support, and encouragement throughout every step of my journey.

List of Publications

Journal Papers:

The chapters of this thesis are reproduced, with modifications, from the following publications:

Chapter 3:

Y. Xiao, Q. Ji, S. Karnaoukh, C. Wang, and N. Wu, “Design and analysis of a d33 mode piezoelectric energy generator for vehicle braking system,” Smart Mater. Struct., vol. 31, no. 6, p. 065027, 2022, doi: 10.1088/1361-665x/ac6d30.

Chapter 4:

Y. Xiao, S. Karnaoukh, and N. Wu, “Design and analysis of a d15 mode piezoelectric energy generator using friction-induced vibration,” Smart Mater. Struct., vol. 32, no. 3, p. 035040, 2023, doi: 10.1088/1361-665X/acbcb1.

Chapter 5:

Y. Xiao, N. Wu, and Q. Wang, “Analysis of a friction-induced vibration piezoelectric energy generator under linear, bi-linear, and impact conditions,” Int. J. Mech. Sci., vol. 272, no. December 2023, p. 109148, 2024, doi: 10.1016/j.ijmecsci.2024.109148.

Chapter 6:

Y. Xiao, W.-H. Liu, Z.-Q. Lu, and N. Wu, “Numerical investigation of nonlinear shear-mode piezoelectric energy generation under permanent magnetic conditions,” Nonlinear Dyn., vol. 111, pp. 18779–18817, 2023, doi: https://doi.org/10.1007/s11071-023-08805-z.

Y. Xiao, Z. Lu, and N. Wu, “Development and analysis of magnet-engaged piezoelectric energy generator under friction-induced vibration,” Int. J. Non. Linear. Mech., vol. 158, p. 104560, 2024, doi: 10.1016/j.ijnonlinmec.2023.104560.

Chapter 7:

Y. Xiao and N. Wu, “Energy generation from friction-induced vibration of a piezoelectric beam”, Int. J. Mech. Sci., Accepted, 2024.

Y. Xiao and N. Wu, “Modeling and optimization of a piezoelectric stepped beam under friction-induced vibration”, 2024. (Intended for submission)

The content of the following publications or research works intended for submission are not included in this thesis:

Y. Xiao, D. Song, and N. Wu, “Development of compact smart bearing and novel hybrid feature assessment for weak defect identification”, 2024. (Intended for submission)

P. Wang, Y. Xiao, and N. Wu, “Electrical power generation using dynamic piezoelectric shear deformation under friction,” Acta Mech. Solida Sin., vol. 34, pp. 977–988, 2021, doi: 10.1007/s10338-021-00291-3.

P. Wang, Y. Xiao, N. Wu, Z. Sun, and H. Luo, “Friction induced vibration and energy generation study of two-degree-of-freedom piezoelectric coupled system,” Eur. J. Mech. A/Solids, vol. 95, p. 104619, 2022, doi: 10.1016/j.euromechsol.2022.104619.

Conference Papers/Abstracts:

Y. Xiao and N. Wu, “Analysis of nonlinear piezoelectric energy generator under friction-induced vibration”, The 34th Canadian Materials Science Conference (CMSC 2023).

Y. Xiao and N. Wu, “Uncertainty analysis of nonlinear piezoelectric energy generator under friction”, The 5th International Conference on Vibration and Energy Harvesting Applications (VEH 2024).

MH. Shariar, Y. Xiao, N. Wu, and X. Liang, “Energy harvesting using piezoelectric transducer ring from rolling motion of ball bearing”, The 5th International Conference on Vibration and Energy Harvesting Applications (VEH 2024).

Contents

List of Tables

List of Figures

Nomenclature

A_{p}	Cross-section area of piezoelectric material	m^2
A_n	Iterative calculation coefficient	dimensionless
A	Cross-sectional area	m^2
a_{m}	Modal constant	dimensionless
B_n	Iterative calculation coefficient	dimensionless
b_{m}	Modal constant	dimensionless
b	Width of beam	m
b_{p}	Width of piezoelectric patch	m
C_i	Coefficients of mode shape function	dimensionless
C_{p}	Capacitance of the piezoelectric patch	Farad
C_{s}	Strain rate damping coefficient	$N/(m^2/s)$
c_1	Damping coefficient for equivalent mass 1	N/(m/s)
c_1	Damping coefficient for equivalent mass 2	N/(m/s)
c	Damping coefficient	N/(m/s)
c_{55}^{D}	Elastic constant at a constant electric displacement	N/m^2
c_{55}^{E}	Elastic constant at a constant electric field	N/m^2
D_1, D_2, D_3	Electric charge density displacement in direction 1, 2, and 3	$Coulomb/m^2$
D_{v}	Tolerance for zero velocity	dimensionless
d_{ij}	Piezoelectric coupling coefficient	Coulomb/N
E_1, E_2, E_3	Electric field in direction 1, 2, and 3	V/m
E	Elastic modulus	Pa
E_{p}	Elastic modulus of piezoelectric material	Pa
$(EI)'$	Equivalent distributed stiffness	Nm^2
F	Given function for the friction force outside the tolerance velocity	N

F_{p}	Piezoelectric coupling force	N
F_{f}	Friction force	N
F_{e}	Resultant of the external forces acting on the reference body	N
F_{static}	Static friction	N
F_{N}	Normal force	N
$F_{\mathrm{f-Stribeck}}$	Friction force using the Stribeck model	N
$F_{\mathrm{f-Karnopp}}$	Friction force using the Karnopp model	N
$F_{\mathrm{p},i}$	Equivalent point loads simulating the bending moment induced by the piezoelectric patch	N
f_1	Coefficient of mode shape function for the section without piezoelectric patch	dimensionless
f_2	Coefficient of mode shape function for the section with piezoelectric patch	dimensionless
h_{pa}	Distance from the top of piezoelectric patch to the neutral axis	m
h_{sa}	Distance from the bottom of the beam to the neutral axis	m
h_{pc}	Distance from the center of the piezoelectric layer to the neutral axis	m
H	Thickness of beam	m
h	Thickness of piezoelectric material	m
I	Second moment of area	m^4
I_{b}	Second moment of area of beam	m^4
I_{pzt}	Second moment of area of piezoelectric material	m^4
I_{p}	Current generated from piezoelectric material	A
I'	Equivalent second moment of area	m^4
k_{15}	Electromechanical coupling factor	dimensionless
k_1	Linear spring stiffness for equivalent mass 1	N/m
k_2	Linear spring stiffness for equivalent mass 2	N/m

k_{l}	Linear spring stiffness	N/m
k_{piezo}	Stiffness constant of the piezoelectric patch	N/m
k_{eq}	Equivalent stiffness	N/m
l_{p}	Length of the piezoelectric material	m
m'	Mass per length	kg/m
m_1	Equivalent mass 1	kg
m_2	Equivalent mass 2	kg
m_{eq}	Equivalent mass	kg
M_{e}	Bending moment induced by the piezoelectric patch	Nm
P_{e}	Electrical power during charging process	W
$P_{\mathrm{e}}^{\mathrm{RMS}}$	Root mean square (RMS) charging power	W
q_1	Time-dependent generalized coordinate for the first mode	dimensionless
q_2	Time-dependent generalized coordinate for the second mode	dimensionless
$\dot{q_1}$	Derivative of time-dependent generalized coordinate for the first mode	dimensionless
$\dot{q_1}$	Derivative of time-dependent generalized coordinate for the second mode	dimensionless
$\ddot{q_1}$	Second derivative of time-dependent generalized coordinate for the first mode	dimensionless
$\ddot{q_2}$	Second derivative of time-dependent generalized coordinate for the second mode	dimensionless
Q_1	Generalized forces associated with the first mode	N
Q_2	Generalized forces associated with the second mode	N
q_n	nth mode generalized coordinate	dimensionless
$\tilde{Q}$	Total charge generated on the piezoelectric material	Coulomb

Q_{p}	Charge on the piezoelectric material	Coulomb
Q'_{s}	Newly added charge to the storage capacitor	Coulomb
Q_{s}	Accumulated charge on the storage capacitor	Coulomb
R	Electric resistance	Ohm
r_{bp}	Ratio of elastic modulus	dimensionless
S_1, S_2, S_3	Mechanical normal strain in direction 1, 2, and 3	dimensionless
s	Elastic compliance coefficient matrix	m^2/N
T	Total calculation time	s
t	Time variable	s
t_i	Discrete time segments	s
T_1, T_2, T_3	Normal stress along direction 1, 2, and 3	N/m^2
t_{p}	Thickness of the piezoelectric material	m
V	Output voltage from piezoelectric material	V
V_{p}	Voltages across piezoelectric material along its poling direction	V
V_{R}	Output voltage from the piezoelectric material after considering charging dissipation in electric resistance	V
V_{s}	Voltages across storage capacitor	V
v_0	Sliding velocity	m/s
v_r	Relative velocity	m/s
w_{p}	Width of the piezoelectric material	m
w	Displacement	m
W_n	nth mode shape function	dimensionless
x	Position variable along the length of the beam	m
Y_1	Mode shape for first natural frequency	dimensionless
Y_2	Mode shape for second natural frequency	dimensionless
y_1	Displacement of the mass block 1	m
y_2	Displacement of the mass block 2	m
y	Displacement of the mass block	m

$\dot{y}_1$	Velocity of the mass block 1	m/s
$\dot{y}_2$	Velocity of the mass block 2	m/s
$\dot{y}$	Velocity of the mass block	m/s
y_{p}	Piezoelectric patch shear deformation	m
α	Force factor	Coulomb/m
β	Exponential decay factor	dimensionless
θ_{p}	Tuning factor	dimensionless
ε	Dielectric permittivity matrix	Farad/m
ε_{ij}	Dielectric permittivity coefficient	Farad/m
τ_{23}, τ_{13}, τ_{12}	Shear stress in plane 23, plane 13, and plane 12	N/m^2
μ_{s}	Friction coefficient related to relative velocity	dimensionless
μ_{k}	Dynamic friction coefficient	dimensionless
μ_{static}	Static friction coefficient	dimensionless
ζ	Damping ratio	dimensionless
ζ_i	Damping ratio of ith mode	dimensionless
ζ_n^{s}	Strain rate damping ratio of ith mode	dimensionless
ω	Natural frequency	rad/s
ω_1	First natural frequency	rad/s
ω_2	Second natural frequency	rad/s
ω_i	Natural frequency of ith mode	rad/s
ω_{d}	Damping frequency	rad/s
ω_{d1}	First damping frequency	rad/s
ω_{d2}	Second damping frequency	rad/s
$\omega_{\mathrm{d}i}$	Damping frequency of ith mode	rad/s
τ	Variable of Duhamel integration	dimensionless
ρ	Mass density	kg/m^3
ρ'	Mass density of piezoelectric material	kg/m^3
ψ	Empirical constant for calculating bending moment induced by the piezoelectric patch	dimensionless

φ	Empirical constant for calculating bending moment induced by the piezoelectric patch	dimensionless

Chapter 1 Introduction

1.1 Research background

For centuries, humans have relied on renewable energy sources such as windmills, watermills, and solar power. These natural energy sources have provided a sustainable and reliable means of power generation compared to traditional fossil fuel reserves. Energy generation technologies can be broadly categorized into macro and micro energy technologies. The former refers to systems capable of generating kilowatts (kW) or megawatts (MW) of power designed for high-power applications. In contrast, the latter focuses on milliwatt (mW) or microwatt (μW) level power generation, targeting low-power applications. Over the past two decades, the scientific community has been actively engaged in discussions about regenerative energy, focusing on portable devices and microelectromechanical systems (MEMS). The goal is to explore and develop innovative approaches to capture renewable/wasted energy for powering these devices and systems, thereby reducing reliance on traditional energy sources and promoting sustainability. Despite the achieved progress, there are still substantial remaining works, challenges, and opportunities for improvement and exploration in this area.

Energy generation is a prominent technology that involves harvesting energy from external sources and storing it for utilization. This field has attracted significant attention due to its cost-effectiveness, simplicity, and portability. The key advantage of energy generators is their capability to harness and utilize wasted or available energy from the ambient surroundings. For non-regenerative power supplies, such as batteries, which have served as the primary power source for operating low-power portable electronic devices. They are readily available in the market and demonstrate satisfactory reliability. However, their environmental effect for disposal and

replacement costs present limitations that hinder their suitability for powering wireless devices. Moreover, the device can be mounted in hard-to-reach locations in some applications. It is difficult to replace the battery. Alternative solutions are required to solve these issues. In such cases, energy harvesting from the environment is a promising approach. Compared to devices using conventional energy sources, self-powered devices demonstrate environmental friendliness.

Energy generation includes three common sources: mechanical energy, thermal energy, and light energy. Mechanical energy is derived from vibrations, mechanical stress, and strain occurring in the environment. Thermal energy is obtained from waste heat generated by furnaces and heaters. Light energy is captured through photo sensors, photodiodes, or solar panels, allowing for the conversion of sunlight or room light into usable electrical energy. These diverse energy sources provide opportunities for efficient energy generation in various applications.

Electromagnetic, piezoelectric, and electrostatic are the three main transduction mechanisms for mechanical energy, which have gained widespread adoption due to their effectiveness in converting mechanical energy into electrical energy. Among various methods, piezoelectric energy generator (PEG) has garnered significant attention from researchers due to its high-power density and relatively straightforward structural design [1], [2]. The abundant mechanical energy source is also presented in various settings, including industrial plants, machinery, aerial and ground vehicles, and construction structures, to offer opportunities for capturing mechanical energy for various applications under different conditions.

The piezoelectric energy generation process comprises three main elements: energy source, energy transducer, and regulatory circuit and storage apparatus. All three elements play a pivotal role in determining the overall performance of PEG. Therefore, it is imperative to carefully evaluate each of these elements, and ensure accurate analysis of the overall system. Their interplay and optimization are crucial for efficient energy conversion, system stability, and desired operational characteristics in the energy generation process. And there remain challenges in energy generation that require further exploration.

Energy generation is a dynamic process that can be described mathematically. Mathematical modeling of PEG provides a precise and quantitative representation of the system, allows a deeper understanding of the underlying dynamics, enables parameter optimization, and helps making predictions about the performance under different operating conditions. Overall, proper

mathematical modeling of PEG can enhance the energy generation capability through design optimization.

The operation frequency of PEG also plays a crucial role in the energy generation performance. A high-frequency operation PEG has the potential to enhance energy generation performance. High-frequency operation allows for faster energy conversion cycles, leading to a higher energy generation rate within a given time frame. It is essential to understand and consider the influence of the operational frequency of an energy generator to increase its performance. For vibration-based PEG, the performance is influenced by the alignment between the frequency of the energy source and the resonant frequency of the PEG. When these frequencies are closely matched, the PEG can operate at optimal efficiency, maximizing the energy harvested from the vibrations. If there's a significant mismatch, the energy conversion efficiency drops, resulting in lower power output. The operational bandwidth of PEG is another important aspect that needs to be analyzed and optimized to have better flexibility when facing different energy sources and varying environmental conditions, maximize overall energy generation performance, adapt to dynamic conditions, and possess better robustness towards interference.

This study primarily aims to design and analyze PEGs in different operating modes and conditions. The key focus lies in developing dynamic mathematical models that accurately predict the performance of PEGs. By establishing these models, the study seeks to provide valuable insights into the behavior of PEGs under various operating conditions and identify potential solutions to enhance their overall energy generation performance. Through a comprehensive examination of different operating modes and conditions, coupled with accurate mathematical modeling techniques, this study contributes to the development of energy generation technologies and the development of efficient and effective energy generators. A literature review will be presented in the next section to provide an overview of piezoelectric energy generation.

1.2 Literature review

The dynamic behaviors and energy generation performances of PEGs vary depending on operating mode, structural design, excitation source, and operating condition. The forthcoming review will concentrate on these aspects.

1.2.1 PEGs with longitudinal mode (d_{33})

There are three common modes for piezoelectric energy generation, transverse mode (d_{31}), longitudinal mode (d_{33}) and shear mode (d_{15}). The schematic of the different modes of operation is shown in Figure 1-1. In d_{33} mode, a compressive load is applied in direction 3 with the poling direction along direction 3. With d_{31} mode, the load is along direction 1 with the poling direction in direction 3. For d_{15} mode, a shear force is applied in direction 2, resulting in shear deformation in direction 5 and electrical potential along direction 1, while the poling direction remains in direction 3.

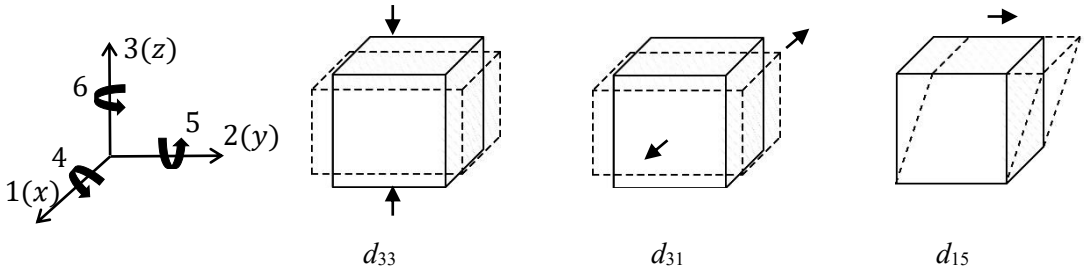

Figure 1-1 Deformation of PEGs under different operating modes.

Xie and Wang developed a d_{33} mode dual-mass piezoelectric bar harvester, which can collect vibration energy from vehicle suspension system subjected to different road conditions [3]. Bao et al. proposed a d_{33} mode hand-held piezoelectric energy-harvesting structure for human-motion energy harvesting [4]. Zhang et al. proposed a d_{33} mode energy harvester based on annular piezoelectric stacks [5]. Li et al. proposed a 2DOF d_{33} mode stacked piezoelectric energy harvester (SPEH) incorporated a frequency up-conversion mechanism through a mechanical limiter [6]. Min et al. proposed a piezoelectric stack energy harvester operating in d_{33} mode for railway system energy harvesting [7]. Wang et al. designed a d_{33} mode piezoelectric energy harvester to harness energy from traffic load, and field tests were conducted to assess its performance under various traffic conditions [8]. Xiao et al. developed a d_{33} mode piezoelectric energy generator embedded in vehicle brake pads and excited by magnetic repulsion [9]. Kim et al. integrated piezoelectric energy harvesters into a pen to capture energy during writing in both d_{33} and d_{31} modes [10]. Li et al. developed a piezoelectric energy harvester operating in the d_{33} mode based on a spring-mass-spring oscillator [11]. Sheng et al. proposed a d_{33} mode

piezoelectric energy harvester incorporating a dynamic amplifier as well as several composite piezoelectric transducer cells to capture vibration energy of railway bridges [12]. Narolia et al. developed a d_{33} mode rotary-type energy harvester to harvest the energy from rotary motion system [13].

1.2.2 PEGs with transverse mode (d_{31})

Wu et al. designed a d_{31} mode piezoelectric coupled buoy energy harvester by converting the transverse ocean wave energy to electrical energy [14]. Gibus et al. designed a tunable d_{31} mode piezoelectric energy harvesters utilizing electrical methods to extend the frequency bandwidth and the electromechanical coupling coefficient [15]. Bao et al. proposed a d_{31} mode piezoelectric cantilever–nonlinear magnetic pendulum structure to investigate the coupling effects between the internal resonance and nonlinear magnetic interaction [16]. Li et al. presented a d_{31} mode piezoelectric and electromagnetic hybrid energy harvester to harvest energy from low-frequency vibration [17]. Sadikbasha et al. presented a piezoelectric coupled auxetic hexachiral cantilever to collect vibration energy under transverse mode, and the piezo patch undertook the enhanced in-plane stress when the auxetic hexachiral structure was under uniaxial tension and compression [18]. Liu et al. proposed a d_{31} mode vibration energy harvester, in which the amplified inertial force of a mass acts on two clamped piezoelectric beams to induce large-amplitude vibrations and generate large outputs [19]. Xiao et al. proposed a piezoelectric beam to harvest energy from FIV [20]. Shi et al. developed a d_{31} mode piezoelectric energy harvester to capture vibration energy from multi-directional and ultra-low frequency waves [21]. Egbe et al. reported a hybrid rotational energy harvester comprising piezoelectric, triboelectric, and electromagnetic generators for energy harvesting from low-wind speeds, wherein PVDF strips operated under d_{31} mode are used for piezoelectric energy generation [22]. Haldkar et al. analyzed the energy generation performance of porous piezoelectric ceramics operated under d_{31} mode [23]. Xie et al. designed a special brick consisting of a double-storey piezoelectric coupled beam to harvest footstep energy [24].

1.2.3 PEGs with shear mode (d_{15})

Narolia et al. developed a d_{15} mode piezoelectric energy harvester based on rotary motion, which converted kinetic energy of rotation into electrical energy [25]. Wang and Liu put forward

a d_{15} mode energy harvester using piezoelectric film for collecting energy from water flow [26]. Zhao proposed a d_{15} mode piezoelectric energy harvester with two elements in series connection and compared the output voltage with the previous study using single element harvester [27]. Xiao et al. proposed a magnet-engaged shear-mode piezoelectric energy generator with two configurations and investigated the dynamic responses considering different connections between magnetic spring and piezoelectric element [28]. Berik compared the sensing capability of piezoelectric patches operated under d_{15} mode in both in parallel and in series connections [29]. Trindade and Benjeddou proposed a finite element homogenization method to characterize the properties of a d_{15} mode piezoelectric macro-fibre composite [30]. Xiao et al. proposed a shear mode piezoelectric energy generator, which utilizes the friction-induced vibration (FIV) and high shear mode piezoelectric coefficient to improve the energy output [31]. Li et al. proposed an asymmetric cruciform piezoelectric harvester operating in d_{15} mode and compared its performance with that of a d_{31} mode piezoelectric harvester having equal total mass [32]. Apart from the traditional piezoelectric materials, relaxor piezoelectric single crystals, such as $Pb(Mg_{1/3}Nb_{2/3})O_3$-$PbTiO_3$ (PMN-PT) and $Pb(In_{1/2}Nb_{1/2})O_3$-$Pb(Mg_{1/3}Nb_{2/3})O_3$-$PbTiO_3$ (PIN-PMN-PT), have also been studied and investigated for their energy generation ability [33]–[35].

1.2.4 PEGs with structural modification

Keshmiri and Wu proposed a broadband piezoelectric energy harvester using a group of nonlinearly tapered cantilevers arranged in an array [36]. Wang et al. proposed an electromechanical step-reduction method, considering both the structural continuity and parallel circuit factors, to depict the coupling behaviors of variable-section piezoelectric composite beams [37]. Sriramdas et al. proposed a multi-step piezoelectric cantilever design configuration with partial coverage of piezoelectric material in steps along the length of a cantilever beam to improve energy generation performance [38]. Zhang et al. developed a galloping-based piezoelectric energy harvester using a stepped cantilever beam and optimized its performance through sequential quadratic programming (SQP) and evolution strategy (ES) [39]. Usharani et al. proposed a piezoelectric cantilever with step design and compared its energy generation performance under tip-excitation, and an electromagnetic exciter was used in the experiment [40]. Rahimzadeh et al. designed an unimorph cantilever beam with different configurations and simulated its energy

generation performance under different parameters [41]. Usharani et al. proposed a multi-stepped piezoelectric cantilever with rectangular cavities and analyzed its performance in broadening the bandwidth during operation [42]. Shi et al. investigated the dynamic characteristics and vibration transmission behavior of single and coupled oscillators using bilinear stiffness and damping elements [43]. Hernández-Montes et al. investigated the energy response of single-degree-of-freedom systems with a range of hysteretic relationships that exhibit stiffness degrading inelastic and bilinear elastic behavior when subjected to earthquake ground motions in the presence or absence of P-delta effects [44]. Balasubramanian et al. studied the vibration responses of beams with nonlinear boundary conditions interpreted using a bi-linear spring model, and a piecewise linear stiffness function with additional switching points was introduced to describe the bi-linear behavior [45]. Shan and Zhu presented a piezo stack energy harvester with a frequency up-conversion method to achieve high-power generation using the impact between the inertial mass system and the piezo stack transducer system [46]. Fang et al. demonstrated a rotational impact energy harvester using the centrifugal softening effect of an inverted driving beam to improve the energy harvesting performance of two piezoelectric beams at low rotational frequencies [47]. Su et al. analytically studied a hybrid electromagnetic energy harvesting system considering mechanical impact, Coulomb friction, harmonic excitation, and Gaussian white noise [48]. Su proposed a novel impact-driven two-degree-of-freedom piezoelectric energy harvester to capture vibration energy harvesting in a wide frequency range that includes its two resonant frequencies [49]. Li et al. proposed a frequency up-converting generator using a piezoelectric stack that can scavenge vibration energy from human motion at ultra-low frequencies [50]. An equivalent spring-mass system, including a collision mechanism between the proof mass and spring limiter, was designed to describe the frequency up-converting process. Zhang and Qin introduced a piezoelectric vibration energy harvester with a hybrid mechanism of impact and rope-driving that enables tunable frequency up-conversion across a wideband [51].

1.2.5 PEGs under different excitations

Piezoelectric energy generation under rotating motion involves converting energy from rotational movement into electrical energy using piezoelectric materials. He et al. proposed a piezoelectric energy generation device with a wind turbine structure under rotating motion and investigated the effects of the number of wind turbine fan blades and blade shapes on energy

generation performance [52]. Micek and Grzybek presented an experimental analysis of the arrays of three Macro Fiber Composite (MFC) patches for energy harvesting from a rotating shaft [53]. Rizal et al. developed a magnetically impelled piezoelectric rotating energy generator integrated into a rotating spindle [54]. Gao et al. designed an auxetic structure piezoelectric energy harvester utilizing rotational motion [55]. Kan et al. developed a drum-like piezoelectric energy harvester using rotation, in which the external excitation is transmitted to the piezoelectric transducer through an air chamber [56]. He et al. proposed a hybrid energy harvester utilizing rotation, which combines piezoelectric and electromagnetic mechanisms [57]. Qin et al. developed a triboelectric-piezoelectric squirrel cage with self-sensing and self-powering capabilities, enabling energy harvesting from the relative motion of the rotor-stator structure and the vibration of elastic support [58]. Chand and Tyagi investigated the energy generation performance of an exponentially tapering width piezoelectric beam under rotation [59].

An energy harvester can perform well if the energy source frequency matches with the resonant frequency of the harvesters, and deviation between these two frequencies may affect the energy harvesting performance [60]. To solve this problem, FIV, a new approach utilizing friction as an excitation source independent of the ambient frequency, can achieve self-excited high-frequency vibration. Some research works have been conducted to study friction and FIV [61], [62]. Carlos Canudas et al. proposed a new dynamic model to depict friction, which included the Stribeck effect, hysteresis, spring-like characteristics for stiction, and varying break-away force [63]. Zong et al. proposed a new modeling method considering the surface fractal feature and normal load to better describe the tangential frictional stick-slip behaviors of contact interfaces, experimental studies were conducted to prove the accuracy of the model [64]. Leine et al. presented a simple and efficient alternate friction model to simulate stick-slip vibrations, which has the advantage of proper integration with an ODE-solver and is more efficient for computation [65]. Liu et al. studied and compared five friction models for micro stick-slip motion systems, including the Coulomb friction model, Stribeck friction model, Dahl model, LuGre model, and the elastoplastic friction model, with experimental testing [66]. Wei et al. established a dynamic model of a vehicle braking system and studied the stick-slip vibration characteristics of the system [67]. Al-Bender et al. proposed a novel multistate friction model based on the Maxwell-slip model by replacing the Coulomb law at the slip state with a rate-state law [68]. Wang et al. performed an experimental and theoretical study investigating friction-induced stick-slip vibration with a dual-pin-on-disc

model [69]. A non-smooth Coulomb's law of friction was adopted for the study, and the FIV was solved by the Switch Model method. Hu et al. conducted research on a pin-on-disc to study the effect of FIV on the corrugation of sliding surfaces [70]. Based on the FIV phenomenon, different studies have been conducted to analyze the source of friction and the method for eliminating friction. Körner and Mayer analyzed the friction at the contact surfaces of a vehicle body vibration damper [71]. The friction properties were characterized, and the effect of the internal pressure of the damper on its friction behavior was studied. Chen et al. proposed a new mechanism for FIV and noise, and the partial detachment and reattachment of the contact surfaces were studied to help control friction and noise in daily life [72]. Lin et al. presented a novel brake pad to reduce disc brake squeal with FEA and experiment testing [73]. Triches et al. used modal analysis techniques to minimize braking squeal by optimizing brake damper parameters [74]. Hammerström and Jacobson presented a spiral-shaped modification of the brake disc surface to reduce squeal noise during braking [75]. Zhao et al. investigated the origin of the FIV phenomenon, and piezoceramic actuators were designed to suppress stick-slip vibrations [76]. FIV has some negative effects in some cases; it will be helpful to either harvest the wasted vibration energy or use FIV. Wang et al. designed a novel piezoelectric actuator with stick-slip motion [77]. The dynamic model was established, and simulations were performed with experimental verification to evaluate the performance. Tadokoro et al. performed experiments and numerical analysis on d_{31} mode piezoelectric energy generation under friction [78]. Wang et al. studied d_{31} mode piezoelectric energy harvesting utilizing FIV through experiment and ABAQUS simulation [79]. Xiang et al. studied the energy harvesting performance by installing a piezoelectric cantilever beam on the braking system of a train, and they found that FIV can be reduced by the piezoelectric cantilever beam [80]. Helseth described the stick-slip motion using a hook and loop system which can generate force fluctuations, and compared the voltage generation characteristics of a piezoelectric macro fiber composite and a triboelectric generator excited by stick-slip motion [81].

1.2.6 PEGs under nonlinear operating conditions

To improve the operating range, researchers tried different methods. For linear generators, generator arrays [82] and combined eigenmodes [83] are the two popular approaches to increasing the operating range. For nonlinear generators, applying external magnetic force to create generators with more than one stable equilibrium position [84], setting vibration impact systems

that limit the vibration amplitude but widen the operating range [85], and using active resonant tuning by setting preload, stiffness and mass adaptions [86], are the three main techniques. Among these techniques, it is common to mount permanent magnets on piezoelectric structures to achieve magnetic coupling, which can increase the operating bandwidth and enhance energy generation performance. Abdelmoula et al. conducted research with an accurate electromechanical model of a piezoelectric energy harvester for low-frequency excitation purposes [84]. The result showed that the hardening behaviors occurred with dual attractive magnets compared to softening behaviors using a single magnet, while both configurations lead to broadband resonance regions. Upadrashta and Yang proposed an innovative method to model the magnetic interaction without including the magnetic module using the nonlinear spring element in ANSYS finite element analysis (FEA) package [87]. Their successful modeling of magnetic force simplified the simulation as an electromechanically coupled problem. A nonlinear monostable harvester with a cantilever configuration and a 2-DOF nonlinear energy harvester were used as case studies, and the simulation results were validated by using experimental methods. Alomari et al. experimentally compared the energy harvesting performance of a single piezoelectric cantilever beam with tip mass with the effect of applying an external magnetic force and thermal energy source [88]. The external magnetic force, which created a nonlinear coupling energy harvesting system, demonstrated the improvement of output voltage in different configurations. The thermal source further boosted the output voltage at different temperatures. Abdelkefi and Barsallo introduced an enhanced broadband low-frequency piezo-magneto-elastic energy harvester using a cantilever beam with a fixed tip magnet mass. The incorporation of attractive magnetic force resulted in a decrease in the natural frequency with a strong softening behavior, which benefits low-frequency broadband energy harvesting [89]. Their model was validated with previous experiment results, and parameter studies were conducted to seek the optimal configuration. Upadrashta and Yang designed an array of nonlinear monostable energy harvesters to scavenge energy from broadband vibrations with low amplitudes under harmonic and random excitations [90]. They combined two energy harvesters, one with an attractive configuration and the other with a repulsive configuration, to achieve broadband energy harvesting. Firoozy et al. investigated the behavior of a piezoelectric cantilever beam with a tip magnet and nonlinear boundary conditions under a harmonic base excitation for broadband energy harvesting [91]. The curvature and inertia terms were modeled to be nonlinear due to large amplitude vibrations. Rui et al. presented a magnetic coupled

piezoelectric energy harvester to increase the output and bandwidth, and they used a lumped parameter model for calculation with a parametric study [92]. Macro Fiber Composite (MFC) material was utilized for experiment, and the results revealed the positively correlated relationship between the optimal spacing and the different magnetic flux densities. Fan et al. introduced a monostable piezoelectric energy harvester with stoppers for low-level excitations [93]. Dhote et al. proposed a nonlinear multi-mode piezoelectric vibration-based energy harvester using geometric nonlinearity [94]. A lumped parameter model was derived and numerically solved. The experimental and simulation results showed the privilege of both wide bandwidth and high-voltage output in frequency sweeps. Yang et al. developed a broadband vibrational energy harvester with a strong softening effect using a soft magneto-sensitive elastomer [95]. The fabricated prototypes were tested to be capable of providing power over a wide frequency range. Alcala-Jimenez et al. presented a cantilever based piezoelectric magnetoelastic vibration energy harvester with enhanced mechanical robustness [96]. KOH etching was used to make the cantilever, and the proof mass was fabricated using micromachined Fe foils with a pair of miniature magnets attached. Yang and Towfighian proposed a parametric resonator for vibration energy harvesting, and a lumped parameter model coupled with the magnetic force was used to analyze the performance of the system [97]. Zhang et al. investigated the distance of magnet, noise spectrum density, and damping on the dynamic response of the proposed multi-field coupled piezoelectric energy harvester under random excitation [98]. The results indicated that reducing the system damping ratio, narrowing magnetic distance, or increasing excitation spectral density could enhance vibration amplitude and increase the average power of the system. The abovementioned literature focused on mono-stable energy generators, which can be achieved with a simple design and wider bandwidth. Bi-stable [99]–[101] and multi-stable [102]–[104] generators are also investigated by researchers. However, as mentioned in the literature, the performance of the bi-stable and the multi-stable energy generators depends on the excitation amplitude and the shape of the potential functions [105]. Mono-stable energy harvester, on the other hand, usually offers a simpler and less complex design, which can result in lower manufacturing costs and easier optimization for specific frequency or deformation amplitude conditions. Integrating multiple mono-stable energy generators into a single device can also further expand the working frequency range [106].

The selection of operating mode for a PEG depends on specific application requirements, available energy source, and vibration direction. Each mode has its own characteristics and scope

of applications. Though the shear mode piezoelectric charge coefficient d_{15} has a higher value compared to the compression mode d_{33} and d_{31} in common piezoelectric material, the actual performance still depends on various factors [107]–[109]. Certain energy sources may align better with transverse mode (d_{31}) and longitudinal mode (d_{33}) rather than shear mode (d_{15}), leading to higher energy conversion efficiency. The piezoelectric material properties, other than the piezoelectric charge coefficients, such as mechanical stiffness (Young's modulus) in different directions, may also affect the overall performance of a piezoelectric energy harvester. Therefore, it is important to investigate the PEG design under different modes and their proper applications.

The existing studies considering the structural modification and nonlinear operating conditions have contributed to the advancement of PEG design with special characteristics. The introduction of FIV can become a new possibility for piezoelectric energy generation in scenarios where friction is presented. However, the research work on PEG under high frequency excitation is limited. And there is almost no research work investigating FIV under nonlinear conditions. It is important to initiate the research with different structures to explore their dynamic characteristics under high frequency excitation and nonlinear conditions. Furthermore, it is worthy to identify proper parameters for enhancing energy generation performance.

1.3 Research objectives and thesis outline

1.3.1 Research objectives

The main objective of this research is to develop mathematical models for PEGs under various working conditions using high frequency excitation, validate the accuracy of the models through experiments, and conduct parameter studies to investigate the dynamic behaviors of PEGs and evaluate their energy generation performance. Developing mathematical models for different PEGs is beneficial to gain a comprehensive understanding of their dynamic behaviors under complex working conditions. Validating these models through experiments is essential to ensure their accuracy and reliability, which can also provide empirical evidence for further analysis. These models enable the simulation of PEG performance, reducing the need for prototyping different designs and thus saving time and resources. Conducting parameter studies can help to identify the important factors affecting PEG performance. By systematically investigating the dynamic behaviors of these PEGs, optimal values for parameters within certain ranges can be identified,

leading to more efficient and effective PEG designs. The research is carried out in the following perspectives.

1. Design and analysis of a PEG for vehicle braking system. A novel piezoelectric energy generator embedded in a vehicle brake pad and excited by magnetic repulsion is developed.
2. Design and analysis of a shear mode PEG using FIV. A shear mode piezoelectric energy generator that utilizes FIV and high shear mode piezoelectric coefficient is developed.
3. Analysis of a PEG under linear, bi-linear, and impact conditions using FIV. A novel PEG with linear, bi-linear, and impact design configurations is proposed.
4. Analysis of a magnet-engaged PEG using harmonic excitation. A magnet-engaged shear-mode piezoelectric energy generator with two nonlinear vibration system configurations is proposed. The dynamic responses of the PEGs, considering the different connections between magnetic spring and piezoelectric elements, are analyzed.
5. Analysis of a magnet-engaged PEG using FIV. This study investigated the characteristics of a magnet-engaged nonlinear piezoelectric energy generator under FIV.
6. Analysis of a PEG with continuum beam using FIV. A piezoelectric coupled continuum structure under FIV is modeled, described, and studied for the first time to characterize its dynamic response and energy generation performance.
7. Modeling and optimization of a PEG with stepped continuum beam using FIV. A piezoelectric coupled stepped beam is developed to capture vibrational energy induced by friction. A CNN-LSTM network is trained with simulation data and serves as the fitness function in GA optimization.

1.3.2 Thesis outline

The thesis online is described as follows, and the linkages of different chapters are summarized in Figure 1-2.

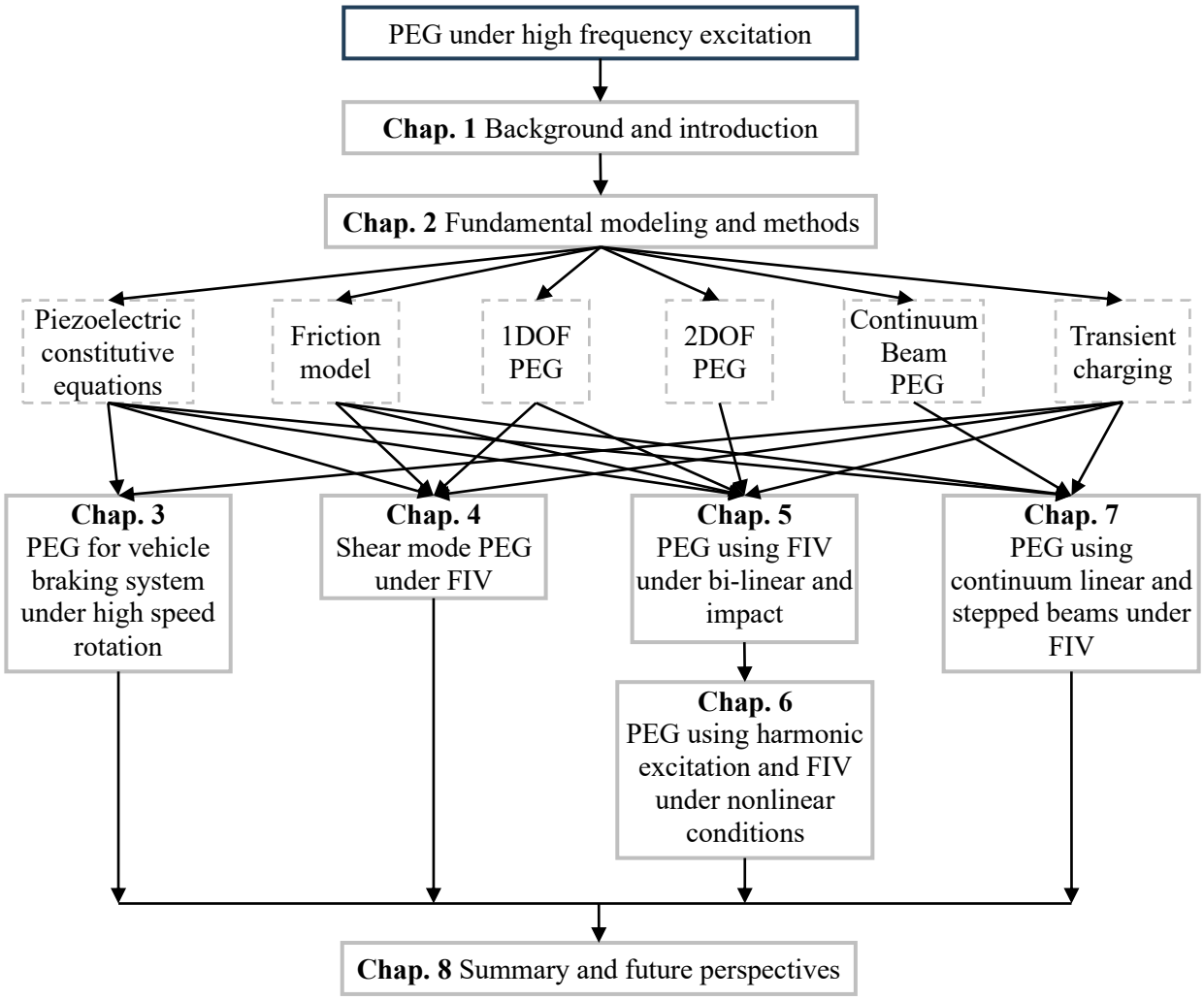

Figure 1-2 Linkages of different chapters.

Chapter 1

An overview of piezoelectric energy generation is introduced in this chapter. After reviewing the existing research, piezoelectric energy generation with high frequency rotation and FIV is proposed.

Chapter 2

The piezoelectric constitutive equations, friction model, and mathematical modeling of different piezoelectric coupled systems are described in this chapter.

Chapter 3

The design and analysis of an embedded PEG for vehicle braking system is illustrated in this chapter.

Chapter 4

The design and analysis of a linear shear mode PEG system under nonlinear FIV is depicted in this chapter.

Chapter 5 and *Chapter 6*

Different types of nonlinear PEG systems were modelled and studied in chapters 5 and 6. The modeling and analysis of a PEG considering bi-linear and impact conditions under nonlinear FIV is introduced in Chapter 5. The dynamic behavior of a magnet-engaged PEG under harmonic excitation is explored in the first section of Chapter 6. The dynamic behavior of a magnet-engaged PEG under FIV is investigated in the second section of Chapter 6.

Chapter 7

The modeling and analysis of a piezoelectric coupled continuum structure under FIV is depicted in the first section of Chapter 7. The modeling and geometric optimization of a piezoelectric coupled stepped continuum structure under FIV is introduced in the second section of Chapter 7.

Chapter 8

A summary of this thesis is given in this chapter, followed by an outline of future works.

Chapter 2 Fundamental modeling and methods for research tasks

In this chapter, the fundamental modeling and methods for research tasks are introduced. The piezoelectric constitutive equations, which are fundamental in the electromechanical behavior of piezoelectric materials, are first introduced in Section 2.1 to elucidate their role in piezoelectric energy generation. The friction model, which depicts the frictional behaviors, is then described in Section 2.2 to provide insights in understanding the variation of friction. The modeling of a single-degree-of-freedom (SDOF) piezoelectric-coupled energy generation system under friction is depicted in Section 2.3 to explain the interplay between mechanical motion, piezoelectric effect, and nonlinear friction. After introducing the SDOF system under friction, the modeling of a two-degree-of-freedom (2DOF) piezoelectric-coupled energy generation system under friction is demonstrated in Section 2.4 to describe the effect of friction on the system dynamics. Furthermore, the modeling of a piezoelectric-coupled continuum beam under friction is presented in Section 2.5. Finally, the transient charging method, utilized for energy generation evaluation, is described in Section 2.6.

2.1 Piezoelectric constitutive equations

The constitutive relations for piezoelectric materials are formulated as,

$$S = sT_{\mathrm{v}} + d^{T}E_{\mathrm{v}}, \tag{2.1}$$

$$D = dT_{\mathrm{v}} + \varepsilon E_{\mathrm{v}}, \tag{2.2}$$

where S is the strain vector (m/m); s is the elastic compliance coefficient matrix (m^2/N); T_v is the stress component vector (N/m^2); d and d^{T} are piezoelectric coupling coefficient and its transpose matrix (Coulomb/N); E_{v} is the electric field vector (N/Coulomb or V/m); D is the electric charge density displacement vector (Coulomb/m^2); and ε is the dielectric permittivity matrix (Farad/m) [110].

Eq. (2.2) is from the direct piezoelectric effect, which converts mechanical stress to electrical charge. Eq. (2.1) is based on the reverse piezoelectric effect that turns electrical input into mechanical deformation.

The elastic compliance coefficient matrix s can be expressed as,

$$s = \begin{bmatrix} s_{11} & s_{12} & s_{13} & 0 & 0 & 0 \\ s_{21} & s_{22} & s_{23} & 0 & 0 & 0 \\ s_{31} & s_{32} & s_{33} & 0 & 0 & 0 \\ 0 & 0 & 0 & s_{44} & 0 & 0 \\ 0 & 0 & 0 & 0 & s_{55} & 0 \\ 0 & 0 & 0 & 0 & 0 & s_{66} \end{bmatrix}, \tag{2.3}$$

The transpose of stress component vector T_v can be expressed as,

$$\mathrm{T}_v = [T_1 \quad T_2 \quad T_3 \quad T_4 \quad T_5 \quad T_6], \tag{2.4}$$

where T_1, T_2, and T_3 are the normal stress along direction 1, 2, and 3; and T_4, T_5, and T_6 are the shear stress in direction 4, 5, and 6, and they can also written as τ_{23}, τ_{13}, and τ_{12} which represent the shear stress in plane 23, plane 13, and plane 12, respectively.

The piezoelectric coupling coefficient matrix d can be presented as,

$$d = \begin{bmatrix} 0 & 0 & 0 & 0 & d_{15} & 0 \\ 0 & 0 & 0 & d_{24} & 0 & 0 \\ d_{31} & d_{32} & d_{33} & 0 & 0 & 0 \end{bmatrix}. \tag{2.5}$$

The dielectric permittivity matrix ε can be written as,

$$\varepsilon = \begin{bmatrix} \varepsilon_{11} & 0 & 0 \\ 0 & \varepsilon_{22} & 0 \\ 0 & 0 & \varepsilon_{33} \end{bmatrix}. \tag{2.6}$$

This research focuses on the direct piezoelectric effect utilizing Eq. (2.2), which transforms mechanical energy into electrical energy.

2.2 Friction model for dynamic analysis

Liu et al. conducted an experimental study of five friction models, including Coulomb friction model, Stribeck friction model, Dahl model, LuGre model, and the elastoplastic friction model [66]. The study concluded that the Stribeck model, Dahl model, and LuGre model all matched with experiment. The Coulomb friction model and elastoplastic model do not match very well.

The discrepancy between the Coulomb friction model and experimental results can be attributed to the stick-slip motion, wherein the sliding speed encompasses both stick and slip components. The Coulomb friction model describes the sliding friction force dependent solely on the sign of the sliding speed and the friction coefficient. However, in stick-slip scenarios, the required friction coefficient may vary between stick and slip motion. This disparity between the required coefficients can cause the Coulomb friction model to be inadequate.

The mismatch between the elastoplastic friction model and experimental results arises from the model's inadequate representation of the slip motion period. Although the friction force and sliding speed predicted by the elastoplastic model exhibit similarities to the LuGre model, the predicted displacement fails to capture the observed slip motion period accurately. This discrepancy can be attributed to a larger static friction force in the elastoplastic model, leading to the absence of relative motion during the slip motion period.

Several specific drawbacks can be identified when comparing the Dahl and LuGre friction models to the Stribeck friction model. Firstly, the Dahl and LuGre models exhibit a higher level of complexity by accounting for a wider range of frictional phenomena, including pre-sliding displacement and varying levels of stick-slip motion, compared to the Stribeck model. The detailed modeling involve more parameters and sophisticated equations, requiring more processing power and time to simulate accurately. However, it should be noted that these nuanced frictional phenomena are not universal, and they may occur in specific situations with particular friction materials. Secondly, the parameters in the Dahl and LuGre models lack direct physical interpretations, in contrast to the Stribeck model which provides a more intuitive understanding of friction behavior, particularly concerning the influence of velocity. Thirdly, the Dahl and LuGre models primarily focuses on dynamic friction behavior and may not adequately capture static

friction or stiction effects. Lastly, the applicability of the Dahl and LuGre models to various operating conditions may be limited. Consequently, the Stribeck friction model is used for our research. However, the selection of an appropriate friction model should be contingent upon the specific requirements and characteristics of the research.

The friction force using the Stribeck model can be expressed as,

$$F_{\mathrm{f-Stribeck}} = \mu_{\mathrm{s}}(v_r)F_{\mathrm{N}}, \tag{2.7}$$

$$\mu_{\mathrm{s}}(v_r) = \left(\mu_{\mathrm{k}} + (\mu_{\mathrm{static}} - \mu_{\mathrm{k}})e^{-\beta|v_{\mathrm{r}}|}\right)\mathrm{sgn}(v_r), \tag{2.8}$$

where $\mu_{\mathrm{s}}(v_r)$ is the friction coefficient, which is related to relative velocity v_r; F_{N} is the normal force applied to the structure. In the expression of $\mu_{\mathrm{s}}(v_r)$, μ_{k} stands for the dynamic friction coefficient, μ_{static} is the static friction coefficient, β is the exponential decay factor. The relationship among v_r, μ_{s}, and F_{f} are shown in Figure 2-1.

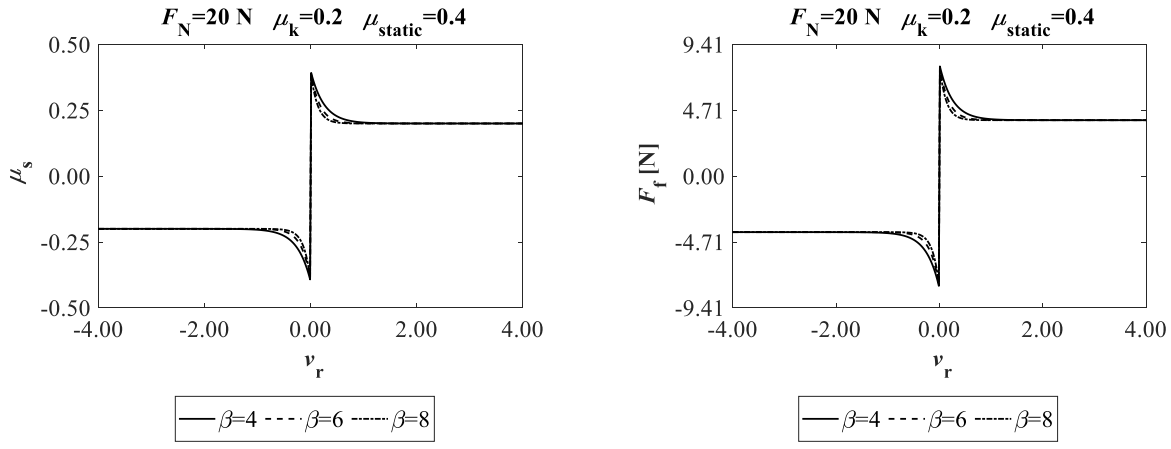

(a) (b)

Figure 2-1 Friction force as a function of relative velocity. (a) $\mu_{\mathrm{s}}(v_r)$. (b) F_{f}.

However, when considering the Dahl, LuGre, and Stribeck friction models, it should be noted that these models have limitations in accurately capturing the static behavior of friction. To overcome this difficulty, Karnopp proposed a model that the relative velocity v_r is considered zero for a specified range, and the static behavior can be depicted within this interval [111]. The Karnopp model can be expressed as,

$$F_{\mathrm{f-Karnopp}} = \begin{cases} F(v_r), & |v_r| > D_{\mathrm{v}} \\ \min(|F_{\mathrm{e}}|, F_{\mathrm{static}})\mathrm{sgn}(v_r), & |v_r| \le D_{\mathrm{v}}' \end{cases} \tag{2.9}$$

where D_{v} is the tolerance for zero velocity; $F(v_r)$ is a given function for the friction force outside the tolerance velocity; F_{e} represents the resultant of the external forces acting on the reference body; F_{static} is the magnitude of static friction.

In Figure 2-1(b), it is evident that the static behavior of friction manifests when the relative velocity v_r approaches zero. However, achieving an exact zero velocity during numerical computations is difficult. It is necessary to introduce a "zero" relative velocity region. Within this region, the friction force $F_{\mathrm{f-Karnopp}}$ is determined by considering other forces present in the system. The resultant force contributes to the static behavior of friction. By accounting for these forces, the model can accurately simulate the static behavior of friction, when the relative velocity remains within the "zero" region. Including the "zero" relative velocity region in the numerical computation ensures a more realistic representation of the friction dynamics. A combination of the Karnopp model and Stribeck model is hence introduced in my research and will be used for calculation, and it can be written as,

$$F_{\mathrm{f}} = \begin{cases} F_{\mathrm{N}}\left(\mu_{\mathrm{k}} + (\mu_{\mathrm{static}} - \mu_{\mathrm{k}})e^{-\beta|v_{\mathrm{r}}|}\right)\mathrm{sgn}(v_r), & |v_r| > D_{\mathrm{v}} \\ \min(|F_{\mathrm{e}}|, F_{\mathrm{static}})\mathrm{sgn}(v_r), & |v_r| \le D_{\mathrm{v}} \end{cases}. \tag{2.10}$$

The friction force can be shown as,

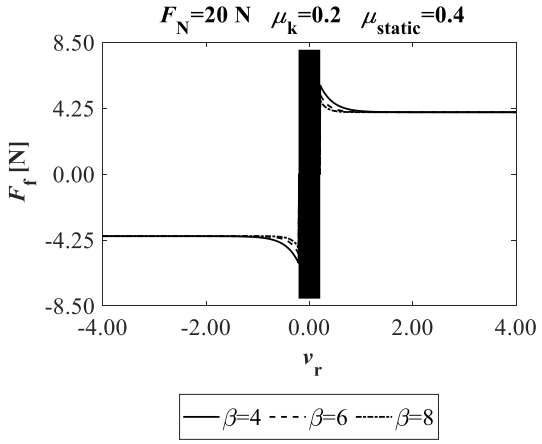

Figure 2-2 Friction force of the Karnopp and Stribeck models.

2.3 Single-degree-of-freedom (SDOF) piezoelectric-coupled energy generation system

The equation of motion for a single-degree-of-freedom (SDOF) system under friction is given by,

$$m_{\mathrm{eq}}\ddot{y}(t) + c\dot{y}(t) + k_{\mathrm{eq}}y(t) = F_{\mathrm{f}}(t), \tag{2.11}$$

where m_{eq} is the equivalent mass of the vibration system; $c = 2\zeta\sqrt{k_{\mathrm{eq}}m_{\mathrm{eq}}}$ is the damping coefficient, and ζ is the damping ratio; k_{eq} is the equivalent stiffness of the system; $F_{\mathrm{f}}(t)$ is the friction force applied to the mass block; $y(t)$ is the vibration response of the mass block under friction force.

The constitutive equation of the piezoelectric material for direct piezoelectric effect is given as,

$$\begin{bmatrix} D_1 \\ D_2 \\ D_3 \end{bmatrix} = \begin{bmatrix} 0 & 0 & 0 & 0 & d_{15} & 0 \\ 0 & 0 & 0 & d_{24} & 0 & 0 \\ d_{31} & d_{32} & d_{33} & 0 & 0 & 0 \end{bmatrix} \begin{bmatrix} T_1 \\ T_2 \\ T_3 \\ T_4 \\ T_5 \\ T_6 \end{bmatrix} + \begin{bmatrix} \varepsilon_{11} & 0 & 0 \\ 0 & \varepsilon_{22} & 0 \\ 0 & 0 & \varepsilon_{33} \end{bmatrix} \begin{bmatrix} E_1 \\ E_2 \\ E_3 \end{bmatrix}. \tag{2.12}$$

Taking the shear mode as an example, Eq. (2.12) can be written as,

$$D_1 = d_{15}T_5 + \varepsilon_{11}E_1. \tag{2.13}$$

The strength of the electric field on the piezoelectric patch is determined by the voltage difference across the piezoelectric layer, that is $E_1 = -V/h$, where V is the output voltage between the two ends of the piezoelectric layer, and h is the thickness of the piezoelectric shear patch. Eq. (2.13) can be written as,

$$D_1 = d_{15}T_5 - \varepsilon_{11}\frac{V}{h}. \tag{2.14}$$

where $T_5 = (k_{\mathrm{p}}y_{\mathrm{p}}(t))/(l_{\mathrm{p}}w_{\mathrm{p}})$; $k_{\mathrm{piezo}} = c_{55}^{\mathrm{D}}A_{\mathrm{p}}/t_{\mathrm{p}}$; $c_{55}^{\mathrm{D}} = c_{55}^{\mathrm{E}}/(1 - {k_{15}}^2)$; $A_{\mathrm{p}} = l_{\mathrm{p}}w_{\mathrm{p}}$.

k_{piezo} is the stiffness constant of the piezoelectric patch and can be calculated from the elastic constant at constant electric displacement c_{55}^{D} of the piezoelectric material in shear mode, the cross-section area A_{p} and the thickness t_{p} of the piezoelectric material; c_{55}^{E} is the elastic constant at a constant electric field; k_{15} is the electromechanical coupling factor; l_{p}, w_{p} are the length and width of the PZT patch, respectively; $\mathrm{y_p}(t)$ is the piezoelectric patch shear deformation at time t. Considering k_{l} and k_{piezo} in series connection, k_{eq} can be determined by $k_{\mathrm{eq}} = (k_{\mathrm{l}}k_{\mathrm{piezo}})/(k_{\mathrm{l}} + k_{\mathrm{piezo}})$.

The deformation of the piezoelectric shear patch y_{p} can be derived as,

$$y_{\mathrm{p}}(t) = y(t)\frac{k_{\mathrm{l}}}{k_{\mathrm{l}}+k_{\mathrm{piezo}}}. \tag{2.15}$$

Differentiating Eq. (2.14) with respect to time, yields,

$$V + RC_{\mathrm{p}}\dot{V} - Rk_{\mathrm{piezo}}d_{15}\dot{y}_{\mathrm{p}}(\mathrm{t}) = 0, \tag{2.16}$$

where R is electric resistance; C_{p} is the capacitance of the piezoelectric shear patch in farad and can be solved by $C_{\mathrm{p}} = \varepsilon_{11}\, A_{\mathrm{p}}/\, t_{\mathrm{p}}$.

α is defined as the force factor calculated from the piezoelectric coefficient d_{15}, the stiffness constant of piezoelectric material k_{piezo}, to evaluate the electromechanical coupling effect between the mechanical system and the piezoelectric material.

$$\alpha = \theta_{\mathrm{p}}d_{15}k_{\mathrm{piezo}}, \tag{2.17}$$

For the sake of representing the actual performance of piezoelectric material, a tuning factor, θ_{p}, is added to the force factor expression to reflect the influence of the non-perfect bonding and connection between mechanical structure and piezoelectric patch, and the possible imperfect fabrication of piezoelectric material.

The mechanical and piezoelectric coupling equation of the system can then be written as,

$$\begin{cases} m_{\mathrm{eq}}\ddot{y}(t) + c\dot{y}(t) + k_{\mathrm{eq}}y(t) + \alpha\frac{k_{\mathrm{l}}}{k_{\mathrm{l}}+k_{\mathrm{piezo}}}V_{\mathrm{R}}(t) = F_{\mathrm{f}}(t) \\ V_{\mathrm{R}}(t) + RC_{\mathrm{p}}\dot{V}_{\mathrm{R}}(t) - R\alpha\frac{k_{\mathrm{l}}}{k_{\mathrm{l}}+k_{\mathrm{piezo}}}\dot{y}(t) = 0 \end{cases}, \tag{2.18}$$

where V_{R} is the output voltage from the piezoelectric material after considering the charging dissipation in electric resistance. Considering the electromechanical coupling effect induced by the piezoelectric patch, an iterative process is applied to solve the response. The total calculation time T is divided into small discrete time segments t_i, where the subscript i indicates the iteration number and $\Delta t = t_{i+1} - t_i$ is the corresponding period of calculation. For the first iteration step ($t = 0$ s and $i = 1$), we assumed that the system is at rest and the initial condition is,

$$\begin{cases} y(t_1) = 0, \\ \dot{y}(t_1) = v_0, \\ V_{\mathrm{R}}(t_1) = 0, \end{cases} \tag{2.19}$$

where $y(t_1)$ is the initial displacement of the mass block at the equilibrium position; $V_{\mathrm{R}}(t_1)$ is the initial voltage across the electric resistance. Based on the relative sliding velocity v_{r}, which is equal to $v_0 - \dot{y}(t)$, the friction system has two states: slip states ($v_{\mathrm{r}} \neq 0$) and stick states ($v_{\mathrm{r}} = 0$). For the convenience of computation, the friction states changing conditions for $v_{\mathrm{r}} \neq 0$ and $v_{\mathrm{r}} = 0$

are $|v_r| > D_v$ and $|v_r| \leq D_v$, respectively, and D_v represents a close to zero threshold value for judging friction state change.

We assume that the mass block m initially moves with friction plate at a velocity v_0 in the period $t_1 - t_2$, the stick state friction force applied on the top of the mass should be considered. The displacement of the mass block in $t = t_1 - t_2$ is,

$$y(t) = v_0 t. \tag{2.20}$$

In the stick state, the friction force $F_f(t)$ is determined by the maximum static friction force $F_{static}(t)$ and the applied force $F_{applied}(t)$ on the mass block. $F_{static}(t)$ in $t = t_1 - t_2$ is represented as,

$$F_{static}(t) = \mu_{static} F_N \text{sgn}(v_r), \tag{2.21}$$

The applied force $F_{applied}(t)$ is expressed as,

$$F_{applied}(t) = k_{eq} y(t_1) + c\dot{y}(t_1) + \alpha \frac{k_l}{k_l + k_{piezo}} V_R(t_1). \tag{2.22}$$

$F_f(t)$ in $t = t_1 - t_2$ can be written as,

$$F_f(t) = \begin{cases} k_{eq} y(t_1) + c\dot{y}(t_1) \\ +\alpha \frac{k_l}{k_l + k_{piezo}} V_R(t_1), & |F_{applied}(t)| < \mu_s F_N \\ \mu_{static} F_N \text{sgn}(v_r), & |F_{applied}(t)| \geq \mu_s F_N \end{cases}. \tag{2.23}$$

In $t = t_2 - t_3$, if $|v_r| \leq D_v$, the system is still in stick state, $F_{applied}(t)$ is equal to,

$$F_{applied}(t) = k_{eq} y(t_2) + c\dot{y}(t_2) + \alpha \frac{k_{linear}}{k_{linear} + k_{piezo}} V_R(t_2). \tag{2.24}$$

$F_f(t)$ can be expressed as,

$$F_f(t) = \begin{cases} k_{eq} y(t_2) + c\dot{y}(t_2) \\ +\alpha \frac{k_l}{k_l + k_{piezo}} V_R(t_2), & |F_{applied}(t)| < \mu_s F_N \\ \mu_{static} F_N \text{sgn}(v_r), & |F_{applied}(t)| \geq \mu_s F_N \end{cases}. \tag{2.25}$$

However, if $|v_r| > D_v$, the system is in the sliding state, $F_f(t)$ in $t = t_2 - t_3$ is,

$$F_f(t) = \mu_s F_N \text{sgn}(\dot{y}(t_2) - v_0). \tag{2.26}$$

where μ_s is the friction coefficient in the sliding state, and it is described in Eq. (2.8). The vibration and voltage response from Eq. (2.18) in $t = t_2 - t_3$ is,

$$\begin{aligned} y(t) &= e^{-\zeta\omega t}[(A_2 \cos\omega_d t + B_2 \sin\omega_d t)] \\ &+ \frac{1}{m\omega_d} \int_0^{t-t_2} F_f(\tau + t_2) e^{-\zeta\omega(t-t_2-\tau)} \sin(\omega_d(t - t_2 - \tau)) \mathrm{d}\tau' \end{aligned} \tag{2.27}$$

$$V_{\mathrm{R}}(t) = V_{\mathrm{R}}(t_2)e^{-\frac{1}{C_{\mathrm{p}}R}(t-t_2)} + \int_0^{t-t_2} \frac{d_{33}}{C_{\mathrm{p}}} k_{\mathrm{eq}} \dot{y}(t) e^{-\zeta\omega(t-t_2-\tau)} \mathrm{d}\,\tau, \tag{2.28}$$

where ω is the natural frequency of the linear system and ω_{d} is the damping frequency solved by ${\omega_{\mathrm{d}}}^2 = \omega^2(1-\zeta^2)$; A_2 and B_2 are determined by $y(t_2)$ and $\dot{y}(t_2)$,

$$y(t_2) = e^{-\zeta\omega t_2}(A_2 \cos\omega_{\mathrm{d}} t_2 + B_2 \sin\omega_{\mathrm{d}} t_2), \tag{2.29}$$

$$\dot{y}(t_2) = e^{-\zeta\omega t_2}[\cos\omega_{\mathrm{d}} t_2 (B_2\omega_{\mathrm{d}} - A_2\zeta\omega) - \sin\omega_{\mathrm{d}} t_2 (B_2\zeta\omega\omega_{\mathrm{d}} + A_2\omega_{\mathrm{d}})], \tag{2.30}$$

reorganizing Eq. (2.29) and Eq. (2.30), yields,

$$B_2 = \frac{e^{\zeta\omega t_2}[\cos\omega_{\mathrm{d}} t_2 (\zeta\omega y(t_2) + \dot{y}(t_2)) + \omega_{\mathrm{d}} y(t_2) \sin\omega_{\mathrm{d}} t_2]}{\omega_{\mathrm{d}}}, \tag{2.31}$$

$$A_2 = \frac{1}{\cos\omega_{\mathrm{d}} t_2}\left[y(t_2)e^{\zeta\omega t_2} - B_2 \sin\omega_{\mathrm{d}} t_2\right]. \tag{2.32}$$

Following the similar idea, when the time is in the period $t = t_n - t_{n+1}$,

$$\begin{aligned} y(t) &= e^{-\zeta\omega t}[(A_n \cos\omega_{\mathrm{d}} t + B_n \sin\omega_{\mathrm{d}} t)] \\ &+ \frac{1}{m\omega_{\mathrm{d}}} \int_0^{t-t_n} F_{\mathrm{f}}(\tau + t_n) e^{-\zeta\omega(t-t_n-\tau)} \sin(\omega_{\mathrm{d}}(t - t_n - \tau)) \mathrm{d}\,\tau' \end{aligned} \tag{2.33}$$

$$V_{\mathrm{R}}(t) = V_{\mathrm{R}}(t_n)e^{-\frac{1}{C_{\mathrm{p}}R}(t-t_n)} + \int_0^{t-t_n} \frac{d_{33}}{C_{\mathrm{p}}} k_{\mathrm{eq}} \dot{y}(t) e^{-\zeta\omega(t-t_n-\tau)} \mathrm{d}\,\tau, \tag{2.34}$$

where A_n and B_n are determined by the initial conditions of $y(t_n)$ and $\dot{y}(t_n)$,

$$B_n = \frac{e^{\zeta\omega t_n}[\cos\omega_{\mathrm{d}} t_n (\zeta\omega y(t_n) + \dot{y}(t_n)) + \omega_{\mathrm{d}} y(t_n) \sin\omega_{\mathrm{d}} t_n]}{\omega_{\mathrm{d}}}, \tag{2.35}$$

$$A_n = \frac{1}{\cos\omega_{\mathrm{d}} t_n}\left[y(t_n)e^{\zeta\omega t_n} - B_n \sin\omega_{\mathrm{d}} t_n\right]. \tag{2.36}$$

2.4 Two-degree-of-freedom (2DOF) piezoelectric-coupled energy generation system

The equation of motion for a 2-degree-of-freedom (2DOF) system under friction is given by,

$$\begin{cases} m_1\ddot{y}_1(t) + (c_1 + c_2)\dot{y}_1(t) - c_2\dot{y}_2(t) + k_{\mathrm{eq}} y_1(t) - k_{\mathrm{eq}} y_2(t) = 0 \\ m_2\ddot{y}_2(t) + c_2(\dot{y}_2(t) - \dot{y}_1(t)) + k_{\mathrm{eq}}(y_2(t) - y_1(t)) = F_{\mathrm{f}}(t) \end{cases}. \tag{2.37}$$

Also, taking the shear mode as an example, the piezoelectric constitutive equation is the same as Eq. (2.13). Considering the electromechanical effect of the system, the mechanical and piezoelectric coupling equations of the systems under friction can be written as follows.

$$\begin{cases} m_1\ddot{y}_1(t) + (c_1 + c_2)\dot{y}_1(t) - c_2\dot{y}_2(t) + (k_1 + k_{\mathrm{eq}})y_1(t) - k_{\mathrm{eq}}y_2(t) = 0 \\ m_2\ddot{y}_2(t) + c_2(\dot{y}_2(t) - \dot{y}_1(t)) + k_{\mathrm{eq}}(y_2(t) - y_1(t)) + \alpha\frac{k_{\mathrm{l}}}{k_{\mathrm{l}}+k_{\mathrm{piezo}}}V_{\mathrm{R}}(t) = F_{\mathrm{f}}(t) \\ V_{\mathrm{R}}(t) + RC_{\mathrm{p}}\dot{V}_{\mathrm{R}}(t) - R\alpha\frac{k_{\mathrm{l}}}{k_{\mathrm{l}}+k_{\mathrm{piezo}}}(\dot{y}_2(t) - \dot{y}_1(t)) = 0 \end{cases}. \quad (2.38)$$

Eq. (2.38) demonstrates a two-degree-of-freedom piezoelectric-coupled systems, and the solution is found using a combination of the modal superposition method and Duhamel integral. Expressing Eq. (2.38) in a matrix form, it yields,

$$\begin{bmatrix} m_1 & 0 \\ 0 & m_2 \end{bmatrix}\begin{bmatrix} \ddot{y}_1(t) \\ \ddot{y}_2(t) \end{bmatrix} + \begin{bmatrix} c_1 + c_2 & -c_2 \\ -c_2 & c_2 \end{bmatrix}\begin{bmatrix} \dot{y}_1(t) \\ \dot{y}_2(t) \end{bmatrix} + \begin{bmatrix} k_{\mathrm{eq}} + k_1 & -k_{\mathrm{eq}} \\ -k_{\mathrm{eq}} & k_{\mathrm{eq}} \end{bmatrix}\begin{bmatrix} y_1(t) \\ y_2(t) \end{bmatrix} = \begin{bmatrix} 0 \\ F_{\mathrm{e}}(t) \end{bmatrix}. \quad (2.39)$$

where $F_{\mathrm{e}}(t)$ is the external force, which includes the friction force $F_{\mathrm{f}}(t)$ and the piezoelectric coupling term $F_{\mathrm{p}}(t) = -\alpha k_{\mathrm{l}}V_{\mathrm{R}}(t)/\left(k_{\mathrm{l}} + k_{\mathrm{piezo}}\right)$ in Eq. (2.38). After simplifying Eq. (2.39), it can be written in matrix form,

$$[m][\ddot{y}(t)] + [c][\dot{y}(t)] + [k][y(t)] = [F(t)]. \quad (2.40)$$

To solve Eq. (2.40) by modal analysis, it is necessary to solve the eigenvalue problem and find the natural frequency ω_1 and ω_2.

$$\omega^2[m][Y] = [k][Y]. \quad (2.41)$$

The determinant $\Delta = |[k] - \omega^2[m]|$ of the coefficient matrix must be zero. ω_1 and ω_2 can be solved as [112],

$$\omega_{1,2} = \left(\frac{1}{2}\left[\frac{k_1+k_{\mathrm{eq}}}{m_1} + \frac{k_{\mathrm{eq}}}{m_2} \mp \sqrt{\left(\frac{k_1+k_{\mathrm{eq}}}{m_1} + \frac{k_{\mathrm{eq}}}{m_2}\right)^2 - 4\frac{k_1k_{\mathrm{eq}}}{m_1m_2}}\right]\right)^{1/2}, \quad (2.42)$$

Pre-multiplying Eq. (2.41) by $[k]^{-1}$, it gives $[I][Y] = [k]^{-1}\omega^2[m][Y]$. Replacing the ω value with Eq. (2.42), the mode shapes of different mode $[Y]$ are obtained. The normalized mode shapes can be calculated by assuming ${Y_1}^{(1)} = a$ and ${Y_1}^{(2)} = a_{\mathrm{m}}$, and express ${Y_2}^{(i)}$ in terms of ${Y_1}^{(i)}$, and it can be expressed as,

$$[Y] = \begin{bmatrix} {Y_1}^{(1)} & {Y_1}^{(2)} \\ {Y_2}^{(1)} & {Y_2}^{(2)} \end{bmatrix} = \begin{bmatrix} a_{\mathrm{m}} & b_{\mathrm{m}} \\ a_{\mathrm{m}}\frac{k_1+k_{\mathrm{eq}}-m_1{\omega_1}^2}{k_{\mathrm{eq}}} & b_{\mathrm{m}}\frac{k_1+k_{\mathrm{eq}}-m_1{\omega_2}^2}{k_{\mathrm{eq}}} \end{bmatrix}. \quad (2.43)$$

Based on the orthonormalization, the constant a and b can be determined by normalizing $[Y]$ as,

$$[Y]^{\mathrm{T}}[m][Y] = [I], \quad (2.44)$$

and $[Y]$ can be solved as,

$$[Y]=\begin{bmatrix}\frac{k_{\mathrm{eq}}}{\sqrt{m_2(k_1+k_{\mathrm{eq}}-m_1{\omega_1}^2)^2+m_1{k_{\mathrm{eq}}}^2}} & \frac{k_{\mathrm{eq}}}{\sqrt{m_2(k_1+k_{\mathrm{eq}}-m_1{\omega_2}^2)^2+m_1{k_{\mathrm{eq}}}^2}}\\ \frac{k_1+k_{\mathrm{eq}}-m_1{\omega_1}^2}{\sqrt{m_2(k_1+k_{\mathrm{eq}}-m_1{\omega_1}^2)^2+m_1{k_{\mathrm{eq}}}^2}} & \frac{k_1+k_{\mathrm{eq}}-m_1{\omega_2}^2}{\sqrt{m_2(k_1+k_{\mathrm{eq}}-m_1{\omega_2}^2)^2+m_1{k_{\mathrm{eq}}}^2}}\end{bmatrix}. \tag{2.45}$$

According to the expansion theorem, the solution vector $[y]$ of Eq. (2.40) can be expressed by a linear combination of the normal modes,

$$[y]=[Y][q], \tag{2.46}$$

where $[q]$ is the time-dependent generalized coordinate vector, and can be expressed as,

$$[q]=\begin{bmatrix}q_1(t)\\ q_2(t)\end{bmatrix}. \tag{2.47}$$

Substituting Eq. (2.46) into Eq. (2.40), it gives,

$$[m][Y][\ddot{q}(t)]+[c][Y][\dot{q}(t)]+[k][Y][q(t)]=[F(t)]. \tag{2.48}$$

Multiplying Eq. (2.48) by $[Y]^{\mathrm{T}}$ leads to,

$$[Y]^{\mathrm{T}}[m][Y][\ddot{q}(t)]+[Y]^{\mathrm{T}}[c][Y][\dot{q}(t)]+[Y]^{\mathrm{T}}[k][Y][q(t)]=[Q(t)], \tag{2.49}$$

where $[Q(t)]$ is the vector of generalized forces associated with $[q]$,

$$[Q(t)]=\begin{bmatrix}Q_1(t)\\ Q_2(t)\end{bmatrix}=[Y]^{\mathrm{T}}[F(t)]. \tag{2.50}$$

According to the vibration mode's orthogonality, Eq. (2.49) can be simplified to the one describing the vibration corresponding to the individual vibration mode. For the ith vibration mode, we can have,

$$\ddot{q_i}(t)+2\zeta_i\omega_i\dot{q_i}(t)+{\omega_i}^2q_i(t)=Q_i(t),\ \ i=1,2, \tag{2.51}$$

Since the two equations represented by Eq. (2.51) are uncoupled. The response of the ith mode is similar to a single-degree-of-freedom system, and can be expressed as,

$$\begin{aligned}[q(t)]=\begin{bmatrix}q_1(t)\\ q_2(t)\end{bmatrix}=\begin{bmatrix}e^{-\zeta_1\omega_1t}(q_1\cos(\omega_{\mathrm{d}1}t)+\dot{q_1}\sin(\omega_{\mathrm{d}1}t))\\ e^{-\zeta_2\omega_2t}(q_2\cos(\omega_{\mathrm{d}2}t)+\dot{q_2}\sin(\omega_{\mathrm{d}2}t))\\ +\frac{1}{\omega_{\mathrm{d}1}}\int_0^{t-t_0}Q_1(\tau+t_0)e^{-\zeta_1\omega_1(t-t_0-\tau)}\sin(\omega_{\mathrm{d}1}(t-t_0-\tau))d\tau\\ +\frac{1}{\omega_{\mathrm{d}2}}\int_0^{t-t_0}Q_2(\tau+t_0)e^{-\zeta_2\omega_2(t-t_0-\tau)}\sin(\omega_{\mathrm{d}2}(t-t_0-\tau))d\tau\end{bmatrix},\end{aligned} \tag{2.52}$$

where ω_i is the natural frequency of ith mode; ζ_i is the damping ratio of ith mode; $\omega_{\mathrm{d}i}$ is the damping frequency of ith mode and the relationship between $\omega_{\mathrm{d}i}$ and ω_i can be expressed as ${\omega_{\mathrm{d}i}}^2=(1-{\zeta_i}^2){\omega_i}^2$; q_1, $\dot{q_1}$, q_2, $\dot{q_2}$ can be determined by the initial conditions of the time domain response, and at $t=t_0$, it yields,

$$\begin{cases} \dot{q_1} = \left[e^{\zeta_1\omega_1 t_0}\left(q_{0,1}(t_0)\zeta_1\omega_1 + \dot{q_{0,1}}(t_0)\right)\cos(\omega_{\mathrm{d}1}t_0) + \omega_{\mathrm{d}1}q_{0,1}(t_0)\sin(\omega_{\mathrm{d}1}t_0)\right]/\omega_{\mathrm{d}1} \\ q_1 = \left[q_{0,1}(t_0)e^{\zeta_1\omega_1 t_0} - \dot{q_1}\sin(\omega_{\mathrm{d}1}t_0)\right]/\cos(\omega_{\mathrm{d}1}t_0) \\ \dot{q_2} = \left[e^{\zeta_2\omega_2 t_0}\left(q_{0,2}(t_0)\zeta_2\omega_2 + \dot{q_{0,2}}(t_0)\right)\cos(\omega_{\mathrm{d}2}t_0) + \omega_{\mathrm{d}2}q_{0,2}(t_0)\sin(\omega_{\mathrm{d}2}t_0)\right]/\omega_{\mathrm{d}2} \\ q_2 = \left[q_{0,2}(t_0)e^{\zeta_2\omega_2 t_0} - \dot{q_2}\sin(\omega_{\mathrm{d}2}t_0)\right]/\cos(\omega_{\mathrm{d}2}t_0) \end{cases}, \quad (2.53)$$

where $[q_0(t_0)]$ and $[\dot{q_0}(t_0)]$ can be solved by,

$$\begin{cases} [q_0(t_0)] = \begin{bmatrix} q_{0,1}(t_0) \\ q_{0,2}(t_0) \end{bmatrix} = [Y]^{\mathrm{T}}[m][y_0(t_0)] \\ [\dot{q_0}(t_0)] = \begin{bmatrix} \dot{q_{0,1}}(t_0) \\ \dot{q_{0,2}}(t_0) \end{bmatrix} = [Y]^{\mathrm{T}}[m][\dot{y_0}(t_0)] \end{cases}. \quad (2.54)$$

The vibration response $[y(t)]$ and $[\dot{y}(t)]$ can be expressed as,

$$[y(t)] = \begin{bmatrix} y_1(t) \\ y_2(t) \end{bmatrix} = \begin{bmatrix} {Y_1}^{(1)}q_1(t) + {Y_2}^{(1)}q_2(t) \\ {Y_1}^{(2)}q_1(t) + {Y_2}^{(2)}q_2(t) \end{bmatrix}, \quad (2.55)$$

$$[\dot{y}(t)] = \begin{bmatrix} \dot{y_1}(t) \\ \dot{y_2}(t) \end{bmatrix} = \begin{bmatrix} {Y_1}^{(1)}\dot{q_1}(t) + {Y_2}^{(1)}\dot{q_2}(t) \\ {Y_1}^{(2)}\dot{q_1}(t) + {Y_2}^{(2)}\dot{q_2}(t) \end{bmatrix}. \quad (2.56)$$

From Eq. (2.38), it indicates that the voltage response is related to $[\dot{y}(t)]$ and it can be expressed as,

$$V_{\mathrm{R}}(t) = V_{\mathrm{R}}(t_0)e^{-\frac{1}{C_{\mathrm{p}}R}(t-t_0)} + \int_0^{t-t_0}\frac{d_{15}}{C_{\mathrm{p}}}k_{\mathrm{eq}}[\dot{y_2}(t) - \dot{y_1}(t)]e^{-\frac{1}{C_{\mathrm{p}}R}(t-t_0-\tau)}\,\mathrm{d}\,\tau, \quad (2.57)$$

where $V_{\mathrm{R}}(t_0)$ is the voltage from the previous time step and determined by the initial condition.

Following the similar iteration concept in Section 2.3, it is assumed that the initial condition at t = 0 s is known. The period of calculation, denoted as $\Delta t = t_{i+1} - t_i$, corresponds to the subscript i which indicates the iteration number. For the first iteration step (t = 0 s and i = 1), we make the assumption that there is no external force acting on the system. Additionally, we assume the initial velocity of m_2 equals to the sliding speed of the friction plate v_0, and the voltage on the piezoelectric patch is 0,

$$\begin{cases} y_1(t_1) = 0 \\ \dot{y_1}(t_1) = 0 \\ y_2(t_1) = 0 \\ \dot{y_2}(t_1) = v_0 \\ V_{\mathrm{R}}(t_1) = 0 \end{cases}. \quad (2.58)$$

The responses $y_1(t)$, $y_2(t)$ and $V_{\mathrm{R}}(t)$ during the time period $t = t_1 \sim t_2$ can be expressed as follows,

$$\begin{aligned} y_1(t) = {} & Y_1{}^{(1)}\Big[e^{-\zeta_1\omega_1 t}(q_1(t_1)\cos(\omega_{\mathrm{d}1}t) + \dot{q_1}(t_1)\sin(\omega_{\mathrm{d}1}t)) \\ & + \frac{1}{\omega_{\mathrm{d}1}}\int_0^{t-t_1} Q_1(\tau+t_1)e^{-\zeta_1\omega_1(t-t_1-\tau)}\sin(\omega_{\mathrm{d}1}(t-t_1-\tau))d\tau\Big] \\ & + Y_2{}^{(1)}\Big[e^{-\zeta_2\omega_2 t}(q_2(t_1)\cos(\omega_{\mathrm{d}2}t) + \dot{q_2}(t_1)\sin(\omega_{\mathrm{d}2}t)) \\ & + \frac{1}{\omega_{\mathrm{d}2}}\int_0^{t-t_1} Q_2(\tau+t_1)e^{-\zeta_2\omega_2(t-t_1-\tau)}\sin(\omega_{\mathrm{d}2}(t-t_1-\tau))d\tau\Big] \end{aligned}, \tag{2.59}$$

$$\begin{aligned} y_2(t) = {} & Y_1{}^{(2)}\Big[e^{-\zeta_1\omega_1 t}(q_1(t_1)\cos(\omega_{\mathrm{d}1}t) + \dot{q_1}(t_1)\sin(\omega_{\mathrm{d}1}t)) \\ & + \frac{1}{\omega_{\mathrm{d}1}}\int_0^{t-t_1} Q_1(\tau+t_1)e^{-\zeta_1\omega_1(t-t_1-\tau)}\sin(\omega_{\mathrm{d}1}(t-t_1-\tau))d\tau\Big] \\ & + Y_2{}^{(2)}\Big[e^{-\zeta_2\omega_2 t}(q_2(t_1)\cos(\omega_{\mathrm{d}2}t) + \dot{q_2}(t_1)\sin(\omega_{\mathrm{d}2}t)) \\ & + \frac{1}{\omega_{\mathrm{d}2}}\int_0^{t-t_1} Q_2(\tau+t_1)e^{-\zeta_2\omega_2(t-t_1-\tau)}\sin(\omega_{\mathrm{d}2}(t-t_1-\tau))d\tau\Big] \end{aligned}, \tag{2.60}$$

$$V_{\mathrm{R}}(t) = V_{\mathrm{R}}(t_1)e^{-\frac{1}{C_{\mathrm{p}}R}(t-t_1)} + \int_0^{t-t_1}\frac{d_{15}}{C_{\mathrm{p}}}k_{\mathrm{eq}}[\dot{y_2}(t)-\dot{y_1}(t)]e^{-\frac{1}{C_{\mathrm{p}}R}(t-t_1-\tau)}\,\mathrm{d}\,\tau, \tag{2.61}$$

where q_1, $\dot{q_1}$, q_2, $\dot{q_2}$ can be calculated as,

$$\begin{cases} \dot{q_1}(t_1) = \Big[e^{\zeta_1\omega_1 t_1}\Big(q_{0,1}(t_1)\zeta_1\omega_1 + \dot{q_{0,1}}(t_1)\Big)\cos(\omega_{\mathrm{d}1}t_1) \\ \qquad\qquad +\omega_{\mathrm{d}1}q_{0,1}(t_1)\sin(\omega_{\mathrm{d}1}t_1)\Big]/\omega_{\mathrm{d}1} \\ q_1(t_1) = \big[q_{0,1}(t_1)e^{\zeta_1\omega_1 t_1} - \dot{q_1}(t_1)\sin(\omega_{\mathrm{d}1}t_1)\big]/\cos(\omega_{\mathrm{d}1}t_1) \\ \dot{q_2}(t_1) = \Big[e^{\zeta_2\omega_2 t_1}\Big(q_{0,2}(t_1)\zeta_2\omega_2 + \dot{q_{0,2}}(t_1)\Big)\cos(\omega_{\mathrm{d}2}t_1) \\ \qquad\qquad +\omega_{\mathrm{d}2}q_{0,2}(t_1)\sin(\omega_{\mathrm{d}2}t_1)\Big]/\omega_{\mathrm{d}2} \\ q_2(t_1) = \big[q_{0,2}(t_1)e^{\zeta_2\omega_2 t_1} - \dot{q_2}(t_1)\sin(\omega_{\mathrm{d}2}t_1)\big]/\cos(\omega_{\mathrm{d}2}t_1) \end{cases}, \tag{2.62}$$

and $[q_0(t_1)]$ and $[\dot{q_0}(t_1)]$ can be solved from the vibration response of the last iteration step,

$$\begin{cases} [q_0(t_1)] = \begin{bmatrix} q_{0,1}(t_1) \\ q_{0,2}(t_1) \end{bmatrix} = [Y]^{\mathrm{T}}[m][y(t_1)] = [Y]^{\mathrm{T}}[m]\begin{bmatrix} y_1(t_1) \\ y_2(t_1) \end{bmatrix} \\ [\dot{q_0}(t_1)] = \begin{bmatrix} \dot{q_{0,1}}(t_1) \\ \dot{q_{0,2}}(t_1) \end{bmatrix} = [Y]^{\mathrm{T}}[m][\dot{y}(t_1)] = [Y]^{\mathrm{T}}[m]\begin{bmatrix} \dot{y_1}(t_1) \\ \dot{y_2}(t_1) \end{bmatrix} \end{cases}, \tag{2.63}$$

and $[Q(\tau+t_1)]$ can be expressed as,

$$[Q(\tau+t_1)] = \begin{bmatrix} Q_1(\tau+t_1) \\ Q_2(\tau+t_1) \end{bmatrix} = [Y]^{\mathrm{T}}\begin{bmatrix} 0 \\ F_{\mathrm{f}}(\tau+t_1) + F_{\mathrm{p}}(\tau+t_1) \end{bmatrix}, \tag{2.64}$$

Following the similar idea, when the time is in the period $t = t_i \sim t_{i+1}$, the vibration and voltage response can be expressed as,

$$
\begin{aligned}
y_1(t) = {} & Y_1{}^{(1)}\Big[e^{-\zeta_1\omega_1 t}(q_1(t_i)\cos(\omega_{\mathrm{d}1}t) + \dot{q_1}(t_i)\sin(\omega_{\mathrm{d}1}t)) \\
& + \tfrac{1}{\omega_{\mathrm{d}1}}\textstyle\int_0^{t-t_i} Q_1(\tau+t_i)e^{-\zeta_1\omega_1(t-t_i-\tau)}\sin(\omega_{\mathrm{d}1}(t-t_i-\tau))d\tau\Big] \\
& + Y_2{}^{(1)}\Big[e^{-\zeta_2\omega_2 t}(q_2(t_i)\cos(\omega_{\mathrm{d}2}t) + \dot{q_2}(t_i)\sin(\omega_{\mathrm{d}2}t)) \\
& + \tfrac{1}{\omega_{\mathrm{d}2}}\textstyle\int_0^{t-t_i} Q_2(\tau+t_i)e^{-\zeta_2\omega_2(t-t_i-\tau)}\sin(\omega_{\mathrm{d}2}(t-t_i-\tau))d\tau\Big]
\end{aligned}, \tag{2.65}
$$

$$
\begin{aligned}
y_2(t) = {} & Y_1{}^{(2)}\Big[e^{-\zeta_1\omega_1 t}(q_1(t_i)\cos(\omega_{\mathrm{d}1}t) + \dot{q_1}(t_i)\sin(\omega_{\mathrm{d}1}t)) \\
& + \tfrac{1}{\omega_{\mathrm{d}1}}\textstyle\int_0^{t-t_i} Q_1(\tau+t_i)e^{-\zeta_1\omega_1(t-t_i-\tau)}\sin(\omega_{\mathrm{d}1}(t-t_i-\tau))d\tau\Big] \\
& + Y_2{}^{(2)}\Big[e^{-\zeta_2\omega_2 t}(q_2(t_i)\cos(\omega_{\mathrm{d}2}t) + \dot{q_2}(t_i)\sin(\omega_{\mathrm{d}2}t)) \\
& + \tfrac{1}{\omega_{\mathrm{d}2}}\textstyle\int_0^{t-t_i} Q_2(\tau+t_i)e^{-\zeta_2\omega_2(t-t_i-\tau)}\sin(\omega_{\mathrm{d}2}(t-t_i-\tau))d\tau\Big]
\end{aligned}, \tag{2.66}
$$

$$
V_{\mathrm{R}}(t) = V_{\mathrm{R}}(t_i)e^{-\frac{1}{C_{\mathrm{p}}R}(t-t_{\mathrm{i}})} + \textstyle\int_0^{t-t_i}\frac{d_{15}}{C_{\mathrm{p}}}k_{\mathrm{eq}}[\dot{y_2}(t)-\dot{y_1}(t)]e^{-\frac{1}{C_{\mathrm{p}}R}(t-t_i-\tau)}\mathrm{d}\,\tau. \tag{2.67}
$$

2.5 Piezoelectric-coupled beam for energy generation

Based on the Euler–Bernoulli beam theory, the vibration governing equation of a uniform cantilever beam can be expressed as:

$$
\rho A(x)\frac{\partial^2 w(x,t)}{\partial t^2} + \frac{\partial^2}{\partial x^2}\left[EI(x)\frac{\partial^2 w(x,t)}{\partial t^2} + C_s I(x)\frac{\partial^3 w(x,t)}{\partial x^2 \partial t}\right] = F_{\mathrm{f}}(x,t), \tag{2.68}
$$

where x is the position variable along the length of the beam, t is the time variable, ρ is the equivalent mass density, $A(x)$ is cross-sectional area, $w(x,t)$is the displacement function, E is the equivalent elastic modulus, $I(x)$ is the second moment of area, C_s is the strain rate damping coefficient, $F_{\mathrm{f}}(x,t)$ is the friction.

It is noted that the piezoelectric cantilever is partially coated with piezoelectric patch. Therefore, the distributed stiffness, mass per length, and the second moment of area are different at the coating region and can be written as $(EI)'$, (m'), and (I'), leading to the following governing equation for the piezoelectric-coated section,

$$
(m')\frac{\partial^2 w(x,t)}{\partial t^2} + \frac{\partial^2}{\partial x^2}\left[(EI)'\frac{\partial^2 w(x,t)}{\partial x^2} + C_s(I')\frac{\partial^3 w(x,t)}{\partial x^2 \partial t}\right] = F_{\mathrm{f}}(x,t). \tag{2.69}
$$

Defining the elastic modulus of the aluminum and piezoelectric material (PZT) as $r_{\mathrm{bp}} = E/E_{\mathrm{p}}$; the distance from the top of PZT to the neutral axis as $h_{\mathrm{pa}} = \left(h^2 + 2r_{\mathrm{bp}}hH + r_{\mathrm{bp}}H^2\right)/\left(2h + 2r_{\mathrm{bp}}H\right)$; the distance from the bottom of the aluminum beam to the neutral axis as $h_{\mathrm{sa}} = \left(h^2 + 2hH + r_{\mathrm{bp}}H^2\right)/\left(2h + 2r_{\mathrm{bp}}H\right)$; the distance from the center of the

PZT layer to the neutral axis as $h_{\mathrm{pc}} = \left(r_{\mathrm{bp}} hH + r_{\mathrm{bp}} H^2\right)/\left(2h + 2r_{\mathrm{bp}} H\right)$; the equivalent stiffness as $(EI)' = EI_{\mathrm{b}} + E_{\mathrm{p}} I_{\mathrm{pzt}}$; the mass per length as $m' = \rho Hb + \rho' h b_{\mathrm{p}}$; the second moment of area $I' = I_{\mathrm{b}} + I_{\mathrm{pzt}}$; and the moment of inertia of the aluminum beam I_{b} and piezoelectric material I_{pzt} can be expressed as [113],

$$I_{\mathrm{b}} = \frac{b\left((h_{\mathrm{pa}} - h)^3 - (-h_{\mathrm{sa}})^3\right)}{3}, \tag{2.70}$$

$$I_{\mathrm{pzt}} = \frac{b_{\mathrm{p}}\left({h_{\mathrm{pa}}}^3 - (h_{\mathrm{pa}} - h)^3\right)}{3}, \tag{2.71}$$

where H and h are the thickness of aluminum beam and piezoelectric material; b and b_{p} are the width of the aluminum beam and piezoelectric material; ρ and ρ' are the density of aluminum and piezoelectric material, respectively.

$w(x,t)$ in Eq. (2.68) can be decomposed into two parts using the mode superposition method,

$$w(x,t) = \sum_{n=1}^{\infty} W_n(x) q_n(t), \tag{2.72}$$

and the subscript $n = 1, 2, 3, \ldots, \infty$ denotes the mode shape number. $W_n(x)$ is the nth mode shape function, and $q_n(t)$ is referred to as the generalized coordinate. As the system is proportionally damped, eigenfunction $W_n(x)$ are the normal mode eigenfunction of the corresponding undamped free vibration problem [113]. To properly solve the dynamic response of the piezoelectric-coupled cantilever, $w(x,t)$, the displacement function of the beam in Eq. (2.72) is divided into three sections: a piezoelectric-coated section in the middle ($L_1 \le x \le L_2$), and two non-coated sections ($0 \le x < L_1$ and $L_2 < x \le L$). The detailed mode shape functions of the separated beam sections and the boundary conditions are provided in Appendix A. This method can be expanded to model a continuum beam with multiple sections and piezoelectric patches.

It should be noted that the bending moment M_{e} induced by the piezoelectric patch, which is related to the voltage V_{p} across the piezoelectric material along its poling direction, can be obtained by the following equation [114],

$$M_{\mathrm{e}} = \left[\frac{EHb}{(\psi + \varphi)} \frac{d_{31} V_{\mathrm{p}}}{h}\right] \frac{H - h}{2}, \tag{2.73}$$

where $\psi = (EH)/(E_p h)$, and $\varphi = 6$. d_{31} is the piezoelectric coefficient.

To model the piezoelectric coupling effect on the mechanical vibration response of the beam, the bending moment M_{e} is simulated as two point loads with opposite directions at $x = L_1$ and $x = L_2$. The amplitudes of the loads are the same and can be calculated by $2M_{\mathrm{e}}/dx$. Substituting Eq. (2.72) into Eq. (2.68) and add the coupling terms, Eq. (2.68) can be written as,

$$\begin{gathered}\rho A(x)\sum_{n=1}^{\infty} W_n(x)\frac{\partial^2 q_n(t)}{\partial t^2} \\ +\frac{\partial^2}{\partial x^2}\left[EI(x)\sum_{n=1}^{\infty} q_n(t)\frac{\partial^2 W_n(x)}{\partial x^2}+C_s I(x)\sum_{n=1}^{\infty}\frac{\partial q_n(t)}{\partial t}\frac{\partial^2 W_n(x)}{\partial x^2}\right], \\ -\left[F_{\mathrm{p},1}(x,t)+F_{\mathrm{p},2}(x,t)+F_{\mathrm{p},3}(x,t)+F_{\mathrm{p},4}(x,t)\right]=F_{\mathrm{f}}(x,t)\end{gathered} \tag{2.74}$$

where $F_{\mathrm{p},1}(x,t)$, $F_{\mathrm{p},2}(x,t)$, $F_{\mathrm{p},3}(x,t)$, and $F_{\mathrm{p},4}(x,t)$ represent the equivalent point loads.

The constitutive relation for piezoelectric material can be expressed as follows:

$$D_3(x,t)=d_{31}T_1(x,t)+\varepsilon_{33}^{\mathrm{T}}E_3(t). \tag{2.75}$$

Rearranging Eq. (2.75) to express axial stress T_1 in terms of bending strain S_1 and Young's modulus of PZT ($E_p=1/s_{11}^{\mathrm{E}}$), the permittivity component must be replaced by permittivity at constant strain, which is given by $\varepsilon_{33}^{\mathrm{S}}=\varepsilon_{33}^{\mathrm{T}}-d_{31}^2E_p$. Replacing $E_3(t)$ with $-V_{\mathrm{p}}(t)/h$, Eq. (2.75) can be written as,

$$D_3(x,t)=d_{31}E_{\mathrm{p}}S_1(x,t)-\varepsilon_{33}^{\mathrm{S}}\frac{V_{\mathrm{p}}(t)}{h}. \tag{2.76}$$

The bending strain $S_1(x,t)$ at position x and time t in the PZT layer can be expressed as a function of the distance of the center of the PZT layer in the thickness direction to the neutral axis and curvature of the beam at position x and time t:

$$S_1(x,t)=-h_{\mathrm{pc}}\frac{\partial^2 w(x,t)}{\partial x^2}. \tag{2.77}$$

Eq. (2.76) can be written as,

$$D_3(x,t)=-d_{31}E_{\mathrm{p}}h_{\mathrm{pc}}\frac{\partial^2 w(x,t)}{\partial x^2}-\varepsilon_{33}^{\mathrm{S}}\frac{V_{\mathrm{p}}(t)}{h}. \tag{2.78}$$

The electric charge $Q_{\mathrm{p}}(t)$ developed in the PZT and collected by the electrode can be obtained by integrating the electric displacement over the electrode area as,

$$Q_{\mathrm{p}}(t)=-\int_{L_1}^{L_2}\left[d_{31}E_{\mathrm{p}}h_{\mathrm{pc}}b_{\mathrm{p}}\frac{\partial^2 w(x,t)}{\partial x^2}+\varepsilon_{33}^{\mathrm{S}}b_{\mathrm{p}}\frac{V_{\mathrm{p}}(t)}{h}\right]dx. \tag{2.79}$$

Then, the current generated by the PZT can be given by,

$$I_{\mathrm{p}}(t)=\frac{dQ_{\mathrm{p}}(t)}{dt}=-\int_{L_1}^{L_2}\left[d_{31}E_{\mathrm{p}}h_{\mathrm{pc}}b_{\mathrm{p}}\frac{\partial^3 w(x,t)}{\partial x^2\partial t}\right]dx-\frac{\varepsilon_{33}^{\mathrm{S}}b_{\mathrm{p}}(L_2-L_1)}{h}\frac{dV_{\mathrm{p}}(t)}{dt}. \tag{2.80}$$

The voltage is also related to the equivalent resistance R from the measuring device. Then, the voltage is expressed as,

$$V_{\mathrm{p}}(t)=I_{\mathrm{p}}(t)R=-R\int_{L_1}^{L_2}\left[d_{31}E_{\mathrm{p}}h_{\mathrm{pc}}b_{\mathrm{p}}\frac{\partial^3 w(x,t)}{\partial x^2\partial t}\right]dx-R\frac{\varepsilon_{33}^{\mathrm{S}}b_{\mathrm{p}}(L_2-L_1)}{h}\frac{dV_{\mathrm{p}}(t)}{dt}. \tag{2.81}$$

Eq. (2.75) can be written as,

$$\frac{\varepsilon_{33}^{S} b_{\mathrm{p}}(L_2-L_1)}{h}\frac{dV_{\mathrm{p}}(t)}{dt}+\frac{V_{\mathrm{p}}(t)}{R}+\int_{L_1}^{L_2}\left[d_{31}E_{\mathrm{p}}h_{\mathrm{pc}}b_{\mathrm{p}}\frac{\partial^3 w(x,t)}{\partial x^2\partial t}\right]dx=0, \tag{2.82}$$

Coupling Eqs. (2.74) and (2.82), the transient vibration response of the beam and the dynamic voltage output can be solved through modal analysis and an iteration calculation process, which is described in detail in Appendix B. Eqs. (B.14) and (B.15) show the solutions of mechanical and electrical dynamics responses.

2.6 Energy generation evaluation via transient charging

To evaluate the energy generation process, a transient charging simulation that has been experimentally validated is used [115]. The piezoelectric transient charging circuit depicted in Figure 2-3, consists of an equivalent resistor connected in parallel with the piezoelectric patch, four Schottky diodes, a toggle switch, and a storage capacitor C_{s}. An example of dynamic output during charging is shown in Figure 2-4.

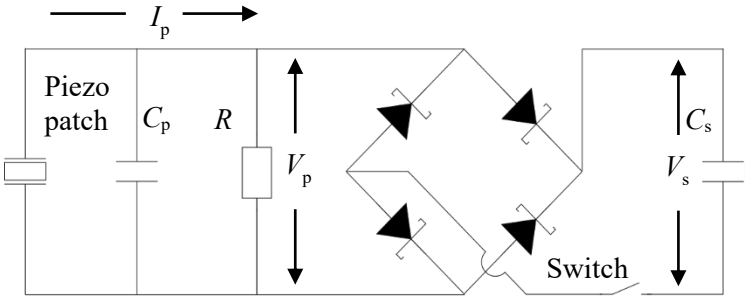

Figure 2-3 Charging circuit.

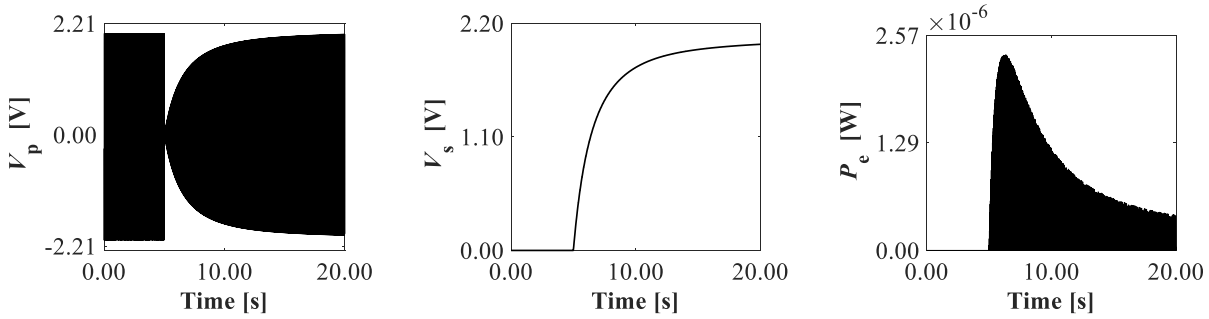

Figure 2-4 Dynamic output during charging. (a) V_{p}. (b) V_{s}. (c) P_{e}.

At the beginning of the process, the toggle switch is open, and the voltage across the storage capacitor V_s = 0. The voltage across the piezoelectric patch V_p is equal to the voltage across the equivalent resistor V_R. Once the toggle switch is closed, the Schottky diodes allow current to pass through only if $|V_p(t_i)| \geq V_s(t_{i-1})$. To prevent current from flowing back to the piezoelectric material, an ideal diode bridge circuit is used as a logic switch to allow current to flow in one direction only. If $|V_p(t_i)| < V_s(t_{i-1})$, the diodes do not conduct and the charge stored in the capacitor is maintained, resulting in $V_s(t_i)$ remaining equal to its previous value $V_s(t_{i-1})$. To simulate the charging process of the storage capacitor, an iterative calculation is used and solved by,

$$\tilde{Q}(t_i) = V_p C_p = V_p(t_i) C_p, \tag{2.83}$$

$$\tilde{Q}(t_i) = |Q_p(t_i)| + Q'_s(t_i), \tag{2.84}$$

$$Q_s(t_i) = Q_s(t_{i-1}) + Q'_s(t_i). \tag{2.85}$$

At $t = t_i$, the total charge generated on the piezoelectric material, taking into account charging dissipation in electric resistance, is denoted by $\tilde{Q}(t_i)$. $|Q_p(t_i)|$ and $Q'_s(t_i)$ represent the charge on the piezoelectric material and the newly added charge to the storage capacitor, respectively. The variable $Q_s(t_i)$ represents the accumulated charge on the storage capacitor until the $t = t_i$. The term $|Q_p(t_i)|$ indicates the rectification of the diode bridge circuit. The voltages across the storage capacitor $V_s(t_i)$ and the piezoelectric material $V_p(t_i)$ are calculated as follows.

First, the voltage on the piezoelectric material at the time t_i is assumed to be equal to $V_R(t_i)$, and can be expressed as,

$$V_p(t_i) = \frac{\tilde{Q}(t_i)}{C_p}. \tag{2.86}$$

Judging the charging state by comparing the value with $V_s(t_{i-1})$, then, the charges on the piezoelectric patch and the storage capacitor during the charging state can be obtained as:

$$Q_p(t_i) = \frac{C_p(Q_s(t_{i-1}) + \tilde{Q}(t_i))}{C_s + C_p}, \tag{2.87}$$

$$Q_s(t_i) = Q_s(t_{i-1}) + Q'_s(t_i) = Q_s(t_{i-1}) + \frac{\tilde{Q}(t_i)C_s - C_p Q_s(t_{i-1})}{C_s + C_p}. \tag{2.88}$$

For the non-charging state, the charges on the piezoelectric patch and the storage capacitor during the charging state can be obtained as:

$$Q_{\mathrm{p}}(t_i) = \begin{cases} \tilde{Q}(t_i), & t_{i-1}\text{: Non-charging} \\ Q_{\mathrm{p}}(t_{i-1}), & t_{i-1}\text{: Charging} \end{cases}. \tag{2.89}$$

The voltages $V_{\mathrm{p},i}$ and $V_{\mathrm{s},i}$ are as follows,

$$V_{\mathrm{p}}(t_i) = \frac{Q_{\mathrm{p}}(t_i)}{C_{\mathrm{p}}}, \tag{2.90}$$

$$V_{\mathrm{s}}(t_i) = \frac{Q_{\mathrm{s}}(t_i)}{C_{\mathrm{p}}}. \tag{2.91}$$

The circuit will not be charging if the voltage on the storage capacitor is higher than 95% of the peak steady-state voltage of the piezoelectric patch. Then, the electrical power output during the charging process, $P_{\mathrm{e}}(t_i)$, can be solved by,

$$P_{\mathrm{e}}(t_i) = \frac{1}{2}\frac{C_{\mathrm{s}}({V_{\mathrm{s}}}^2(t_i) - {V_{\mathrm{s}}}^2(t_{i-1}))}{\Delta t}. \tag{2.92}$$

The RMS (Root mean square value) of the charging power from time 0 to T is given as:

$$P_{\mathrm{e}}^{\mathrm{RMS}} = \sqrt{\frac{1}{T}\int_0^T [P_{\mathrm{e}}(t)]^2 dt}. \tag{2.93}$$

2.7 Summary of modeling methods

The fundamental modeling and methods studying piezoelectric energy generation are introduced in this chapter. The piezoelectric constitutive equations introduced in Section 2.1 are employed to illustrate the electromechanical behavior of piezoelectric materials under linear elastic deformation. The friction model described in Section 2.2 is utilized to depicts the dynamic frictional behaviors under FIV. Precise modeling of both stick state and slip state frictional behaviors is considered using the Karnopp and Stribeck friction models.

The modeling of a single-degree-of-freedom (SDOF) piezoelectric-coupled energy generation system under friction is depicted in Section 2.3, based on which an extended two-degree-of-freedom (2DOF) piezoelectric-coupled energy generation system under friction is then demonstrated in Section 2.4. These models are used to study the dynamics, mechanical responses, and piezoelectric charging of discrete systems under FIV. Furthermore, the dynamic model of a piezoelectric-coupled continuum beam under friction with continuously varying responses in space domain is presented in Section 2.5. The transient charging method described in Section 2.6, which is originated from previous literature, is utilized for piezoelectric energy generation evaluation.

However, the abovementioned modeling process is based on optimal environmental conditions and does not account for the effects of temperature and humidity. These environmental factors can possibly affect the performance of PEGs. Variations in temperature and humidity can alter the material properties of the PEG, which in turn can affect its performance. To simulate the effects of temperature and humidity on PEGs, varying material properties based on temperature-dependent equations and humidity effects need to be considered for analytical modeling. Finite Element Analysis (FEA) allow for thermal-mechanical and thermal-electric-structural coupling, enabling analysis of how environmental changes impact the PEG's performance. The effects of environment will be considered in my future study.

The inclusion of nonlinear friction introduces complexities that affect the energy generation capabilities and overall performance of different piezoelectric-coupled systems. Exploring the interplay among mechanical motion, piezoelectric effect, and nonlinear friction in different systems is crucial for gaining valuable insights into the design and operation of such systems. The experimental validations of these models and parameter studies based them will be presented in the following chapters.

Chapter 3 Piezoelectric energy generation of vehicle braking system

In this chapter, a novel piezoelectric energy generator embedded in vehicle brake pads and excited by magnetic repulsion is developed. Parameter study considering the dimensional and material properties of the piezoelectric stack and braking conditions of vehicle is performed to optimize the design. The modeling methods depicted in Sections 2.1 and 2.6 are utilized in this chapter.

3.1 System design

Figure 3-1 illustrates the schematic design of an integrated vehicle braking system incorporating piezoelectric energy generator. The assembly of the braking system, the slotted brake rotor, the brake pad assembly, and the piezoelectric energy generator are depicted in Figure 3-1(a)-(d), respectively. The slotted rotor, chosen for this study, is specifically designed to dissipate friction heat and gas, ensuring consistent braking performance. The brake pad comprises three layers: a backing plate, a bonding adhesive, and a friction block. The energy generators are embedded in the brake pad, as shown in Figure 3-1(c). The piezo stack ends are affixed to the backing plate, while magnets are attached to the piezo stack. The top holes in the friction block have the same diameter as the cylindrical magnet. Figure 3-1(d) provides an illustration of the piezoelectric energy generator, which consists of a piezo stack and a magnet. The previous literature studied the life time of piezoelectric stack by evaluating the degradation, and less than 5% of degradation was found within the first 10 billion cycles [116]. It proved the possibility of using piezoelectric stack for energy generation in practical operation. The purposed energy generator for vehicle braking system is still under conceptual and preliminary design stage. To ensure the actual application of the proposed system, a special protection layer, like a thin rubber between the piezoelectric material and the neighbor mechanical parts, needs to be designed during the prototype manufacturing stage. As the rotor rotates, a magnetic repulsion is generated between the embedded magnets in the brake rotor and the brake pads. During the braking process, the braking performance is mainly affected by the coefficient of friction of brake pads and the clamping force. The coefficient of friction of brake pads ranges from 0.3-0.5. The clamping force from a single caliper can easily reach 5000-10000 N, and performance braking system such as Brembo can achieve even higher clamping force using multiple pistons [117], [118]. The clamping force generated from the hydraulic braking system during the braking process is much higher than the magnetic repulsion in our designed energy generator. Therefore, it will not affect the braking performance of a vehicle.

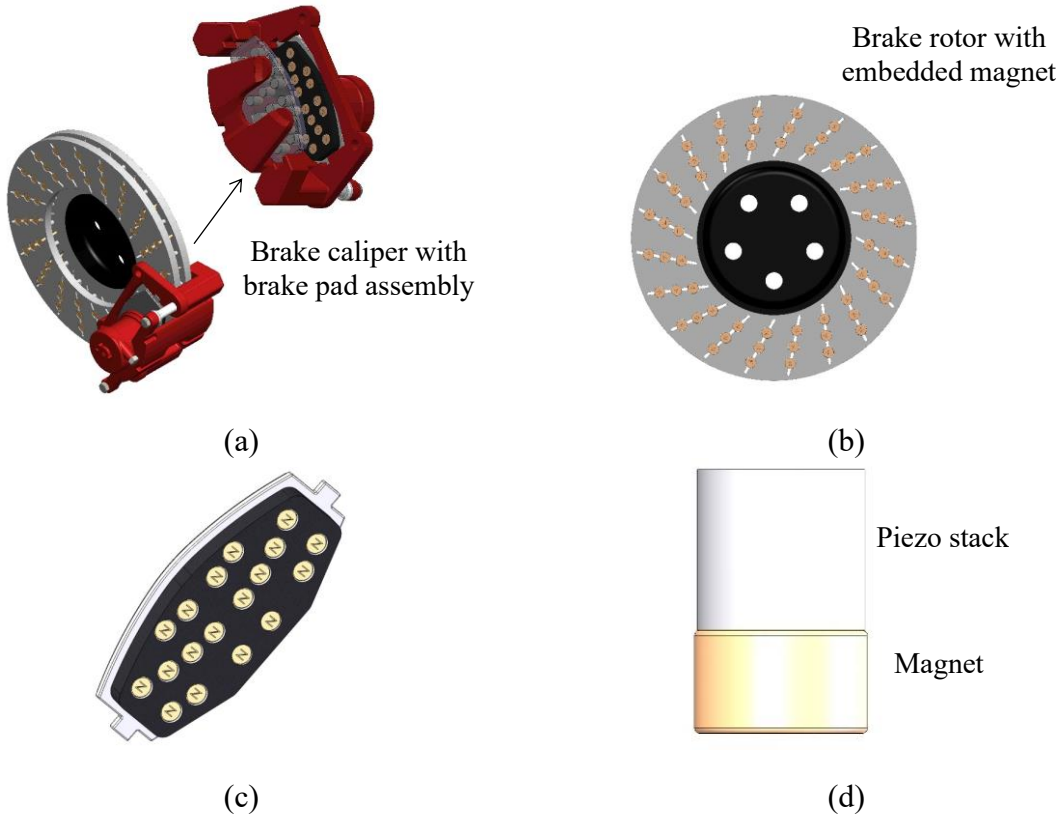

Figure 3-1 Schematic diagram and geometries of the novel braking system. (a) Disk brake assembly. (b) Brake rotor. (c) Brake pad assembly. (d) Piezoelectric energy generator.

3.2 Voltage generation

3.2.1 Energy generation using magnetic repulsion during vehicle braking process

A mathematical model is developed to explain the principle of the energy harvesting system using magnetic repulsion during the vehicle braking process. Figure 3-2(a) demonstrates how the magnets in the brake pad and brake rotor move close to each other during the braking process. The magnet embedded in the brake rotor acts as the actuator. The magnetic repulsion increases exponentially while the brake pad and the actuator move close to each other. With dynamic rotation of the brake rotor, the force changes periodically with the change of the magnets' overlapping area, which induces dynamic tension and compression deformation on the piezoelectric stack, leading to the generation of electric charge.

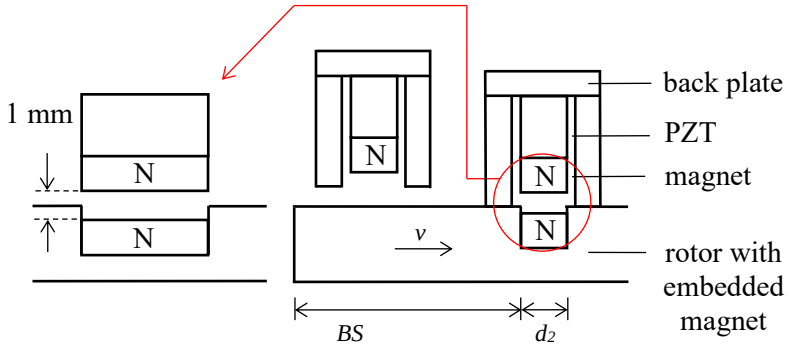

(a)

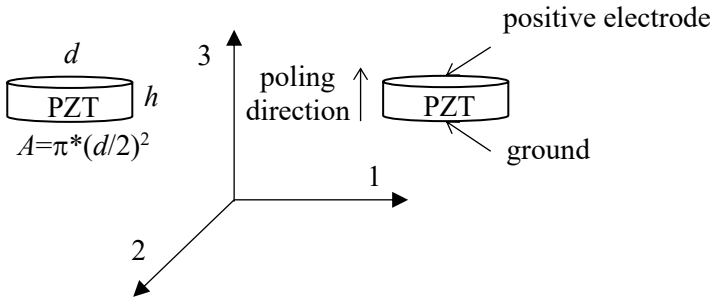

(b)

Figure 3-2 Principle of the energy harvesting system using magnetic repulsion during the vehicle braking process. (a) Vertical displacement of the cylindrical magnet. (b) Poling direction and terminals of PZT.

During the braking process, we assume that the brake pad makes contact with the smooth surface of the brake rotor, forming a separation gap of 1 mm between the rotor and brake pad magnets. We also assume the rotor moves at speed v. The horizontal relative displacement S of the cylindrical magnet in the brake rotor is,

$$S = vt. \tag{3.1}$$

Following the method in [119], the magnetic repulsion F_{rpl} between two cylindrical magnets as a function of their separation gap can be written as:

$$F_{\text{rpl}}(x) = \frac{\pi r^2 {B_0}^2}{2\mu_0}\left[\frac{2(x+t)}{\sqrt{(x+t)^2+r^2}} - \frac{x+2t}{\sqrt{(x+2t)^2+r^2}} - \frac{x}{\sqrt{x^2+r^2}}\right]. \tag{3.2}$$

However, for small values of x, the result from Eq. (3.2) becomes inaccurate and large [120]. Most of the theoretical magnetic repulsion calculation models are simplified with different assumptions and the results often fail to match with experimentally measured data. In this study, F_{rpl} is calculated using the magnetic repelling force calculator based on experiment data which

provide us with an accurate result [121]. The reaction force on the piezoelectric stack can be expressed in a piecewise function with respect to the overlapping area of the two magnets [122],

$$F(t)=\begin{cases}2\times((\frac{D}{2})^2 cos^{-1}\left(\frac{D-S}{D}\right)-\frac{(D-S)D}{4}\sqrt{1-(\frac{D-S}{D})^2})\times F_{rpl}, & 0<S\le\frac{D}{2}\\ 2\times((\frac{D}{2})^2 cos^{-1}\left(\frac{S-D}{D}\right)-\frac{(S-D)D}{4}\sqrt{1-(\frac{D-S}{D})^2})\times F_{rpl}, & \frac{D}{2}<S\le D\\ 0, & D<S\le BS\end{cases}, \tag{3.3}$$

where D is the diameter of the magnet; BS is the arc length between two slots in the rotor. The reaction force $F(t)$ is a piecewise periodic function. We expanded it in the Fourier series for our calculation to improve the calculation efficiency because the iteration calculation in Matlab using the analytical expression is faster than numerical integration. The Fourier series expansion is,

$$F_e(t)=\frac{a_0}{2}+\sum_{j=1}^{\infty}a_j\cos j\omega t+\sum_{j=1}^{\infty}b_j\sin j\omega t, \tag{3.4}$$

$$a_j=\frac{2}{\tau}\int_0^{\tau}F(t)\cos j\omega t\,dt\,,\ \ j=0,1,2,..., \tag{3.5}$$

$$b_j=\frac{2}{\tau}\int_0^{\tau}F(t)\sin j\omega t\,dt\,,\ \ j=1,2,..., \tag{3.6}$$

where τ is the period; a_j and b_j are the Fourier coefficients, respectively.

In this work, we consider a piezoelectric patch with a poling direction along its thickness (direction 3) Figure 3-2(b). The PZT is under tension or compression deformation subjected to normal stress along the poling direction. The electrodes are located along 3-axis on the top and bottom surfaces of each piezoelectric layer. The generated voltage on the piezoelectric material can be expressed as,

$$V(t)=e^{\frac{-t}{RC_p}}\frac{-d_{33}}{C_{\mathrm{p}}}\int_0^t e^{\frac{t}{RC_p}}\frac{dT_3}{dt}dt, \tag{3.7}$$

where T_3 is the normal stress along direction 3. It can be solved by $T_3=F_e(t)/A_{\mathrm{pzt}}$, and A_{pzt} is the cross-sectional area of the piezoelectric material. The transient generated charge Q_{g} can be calculated with Eq. (2.83).

3.2.2 Experimental verification of voltage output

In order to verify the output voltage from the numerical method, experimental tests of the voltage output from a piezoelectric patch are performed using an impact hammer. The excitation force from the impact hammer is to simulate the reaction force on the piezoelectric stack when the magnetic repulsion changes rapidly as a result of the changing overlapping area. The arc length

between the two slots is around 2.6 cm with 20 slots in the rotor and the distance from the rotor center to the actuator center ($RCAC$) of 82.5 mm. At 80 km/h (22.2 m/s) and a tire radius of 35 cm, the angular speed of the rotor is around 63.5 rad/s, and the speed at the $RCAC$ of 82.5 mm is 5.24 m/s. It takes around 0.00496 s to pass the arc length between two slots and 0.0015 s to pass the embedded magnet. While the impact period in the experiment is between 0.001 s to 0.003 s, the experiment result should be valid to verify the voltage output in our mathematical model under different conditions. The experimental test setup is shown in Figure 3-3. The data acquisition system is a four-channel Siemens LMS SCADAS mobile integrated with LMS TestLab [123]. An impact hammer with a force sensor (208C01) attached to its tip is used to apply the impact force on the piezoelectric patch [124]. The material properties and dimensions of the piezoelectric patch used in the experiment are: $d_{33} = 400 \times 10^{-12}$ C/N, $OD = 12.7$ mm and $h = 1$ mm [125]. The comparison of output voltage versus time from experiments and simulations under different excitations is shown in Figure 3-4, Figure 3-5, and Figure 3-6. In the simulation, a piecewise cubic hermite interpolating polynomial is applied for curve fitting the experimental discrete input force, and the corresponding output voltage is calculated using Eq. (3.7). The resistance R in Eq. (3.7) is used to simulate the charge dissipation of the piezoelectric system connecting the voltage meter. From the experimental results, it can be seen that the piezo-voltage output does not follow the mechanical inputs precisely due to the charge/potential dissipation in the piezoelectric material and the measuring device. Figure 3-4 illustrates different values and excitation periods of the reaction forces on the single piezoelectric patch. To further prove the model accuracy, two more voltage output validation experiments by connecting two and three patches in series are conducted to verify the output voltage from the numerical method. The theoretical voltage output model can hence be validated with experiments using different numbers of piezoelectric patches. The voltage variations obtained from simulations and experiments match well with each other with R = 1.8 MΩ, which is the equivalent resistance of the voltage measurement system. This proves the accuracy and effectiveness of the voltage output from Eq. (3.7).

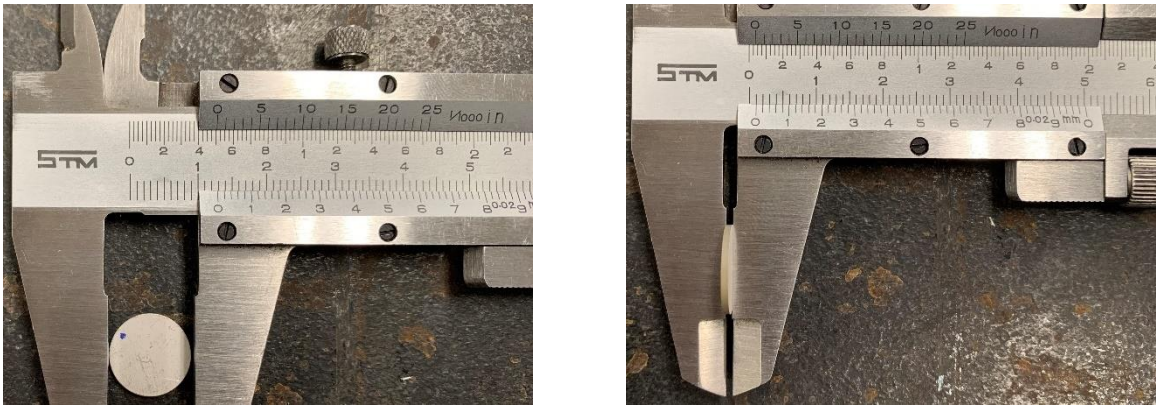

(a)

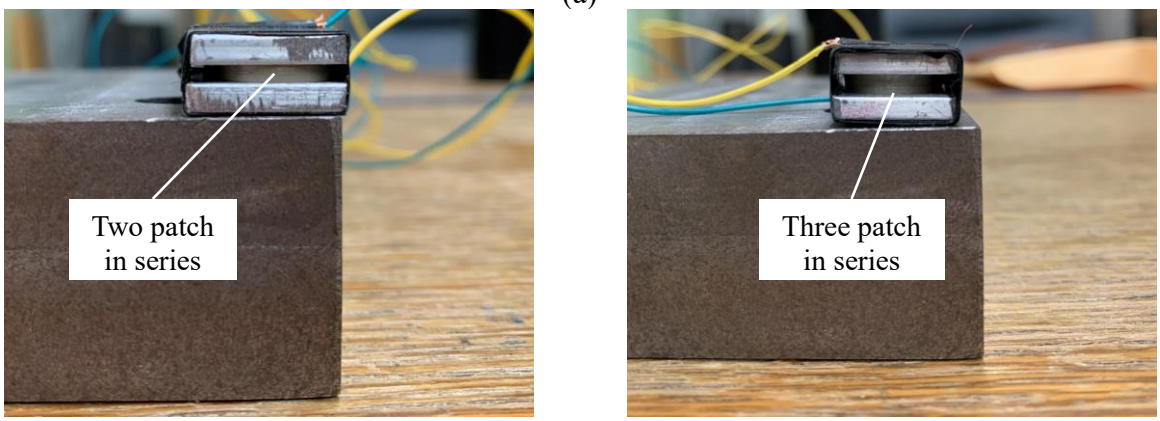

(b)

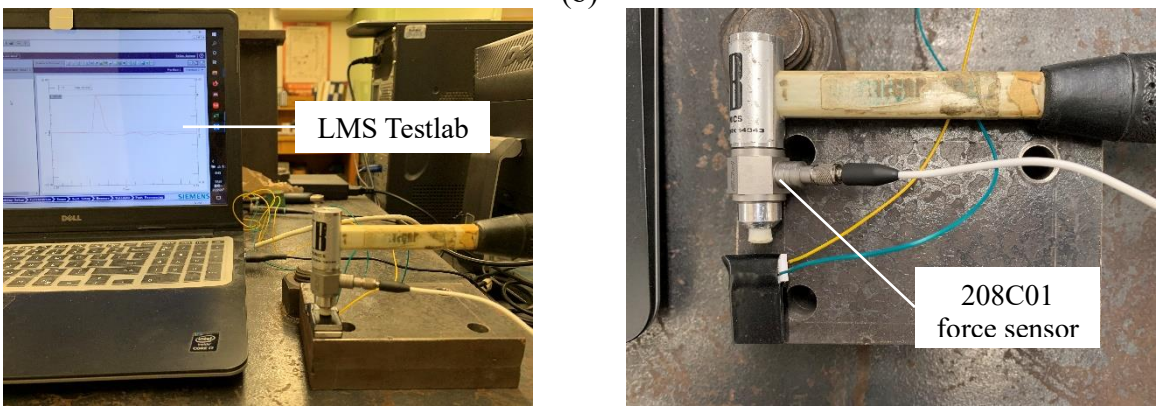

(c)

Figure 3-3 Experimental test setup. (a) Piezoelectric single patch dimension. (b) Piezoelectric patch connected in series. (c) Experimental setup.

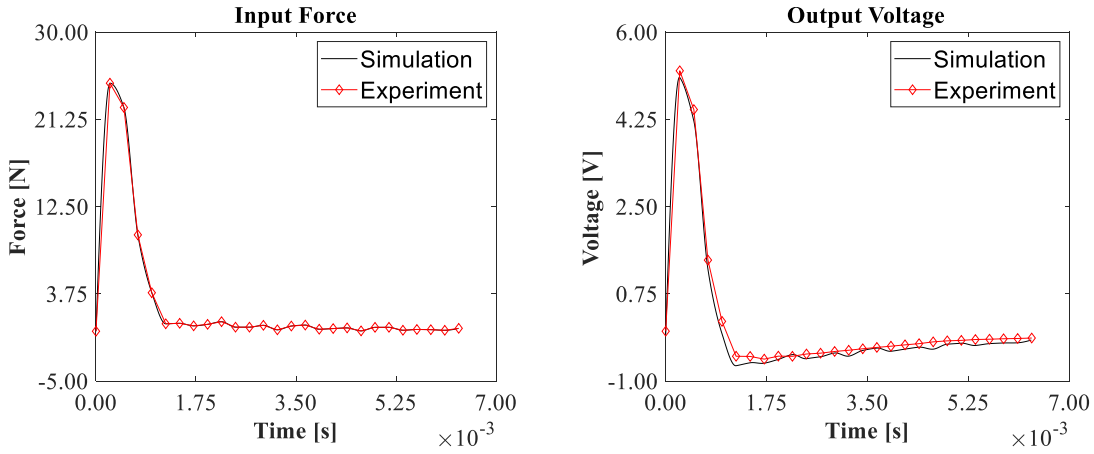

(a)

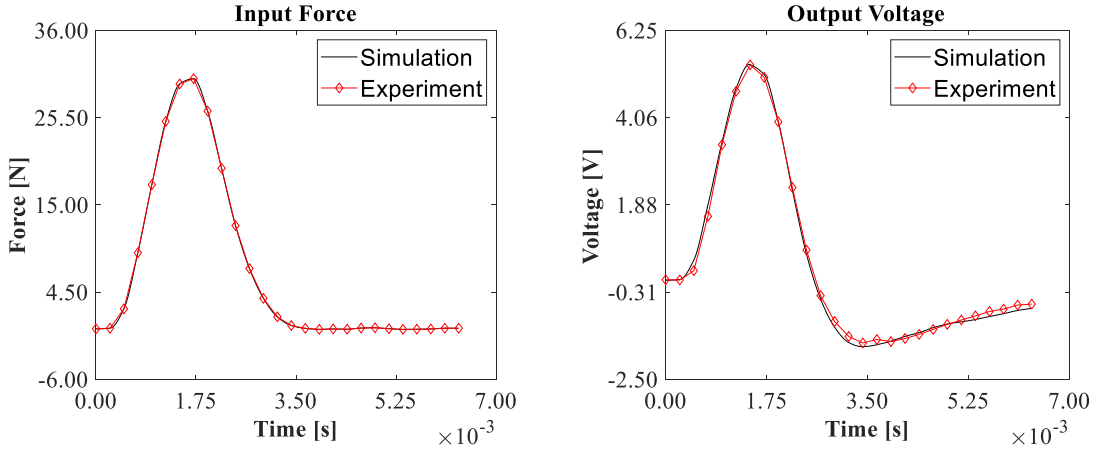

(b)

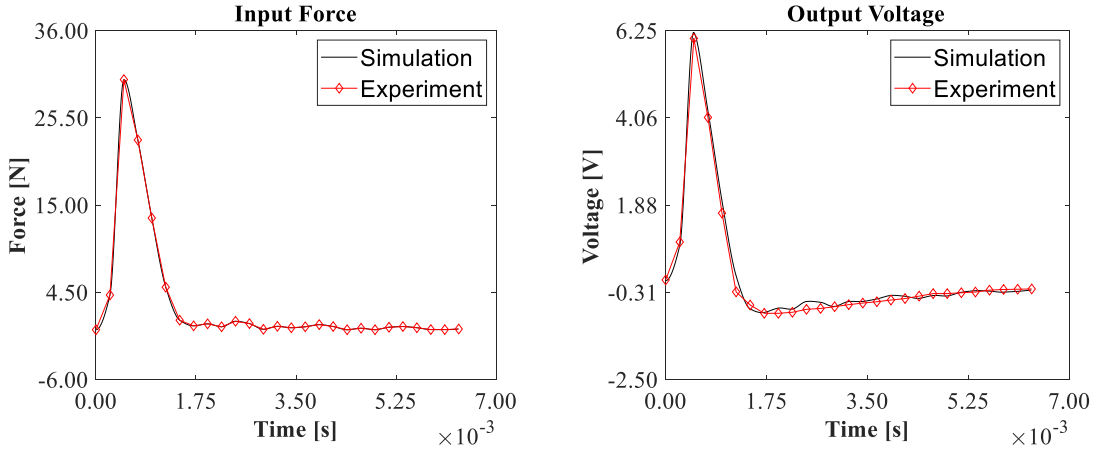

(c)

Figure 3-4 Comparison of curves of output voltage versus time from experiments and simulations under different impulse excitations with one patch. (a) 24.876 N input and voltage output with one patch. (b) 30.190 N input and voltage output with one patch. (c) 30.105 N input and voltage output with one patch.

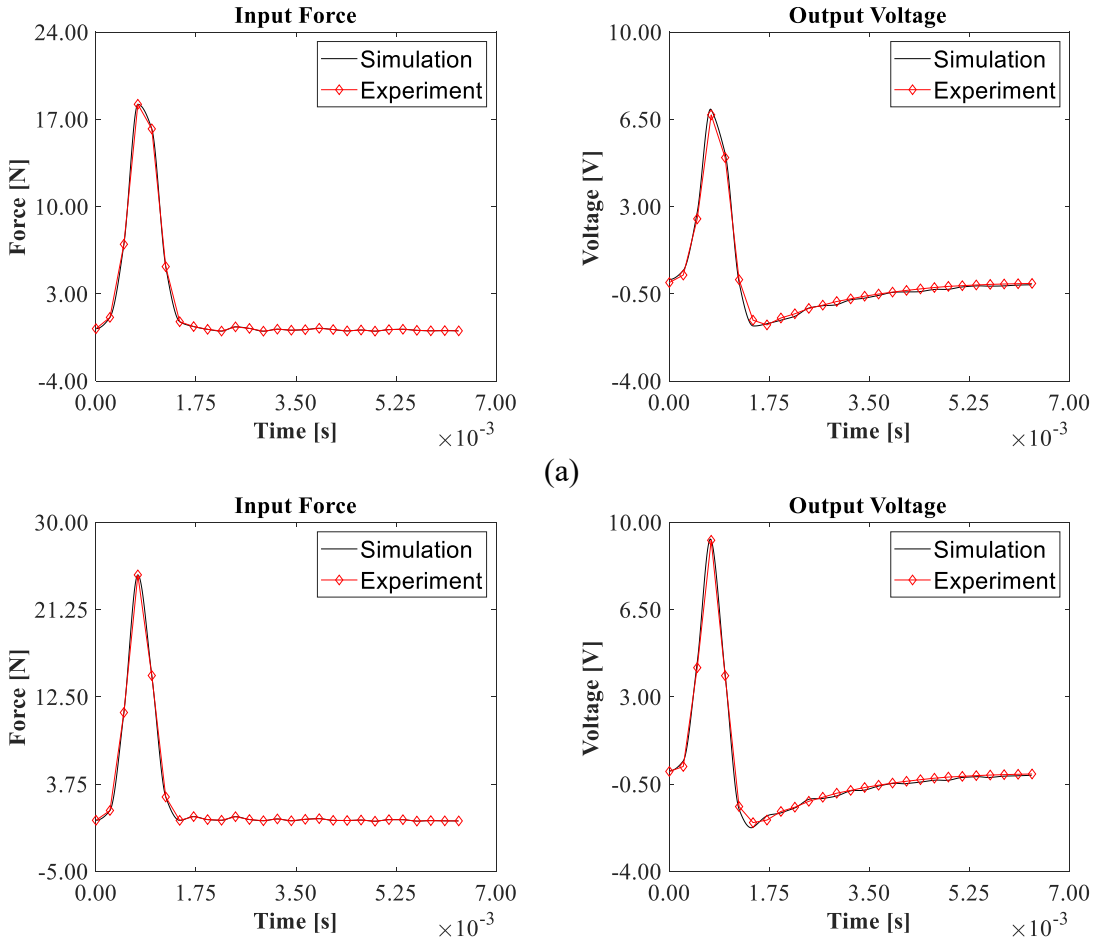

Figure 3-5 Comparison of curves of output voltage versus time from experiments and simulations under different impulse excitations with two patches connect in series. (a) 18.21 N input and voltage output with two patch stack in-series. (b) 24.73 N input and voltage output with two patch stack in-series.

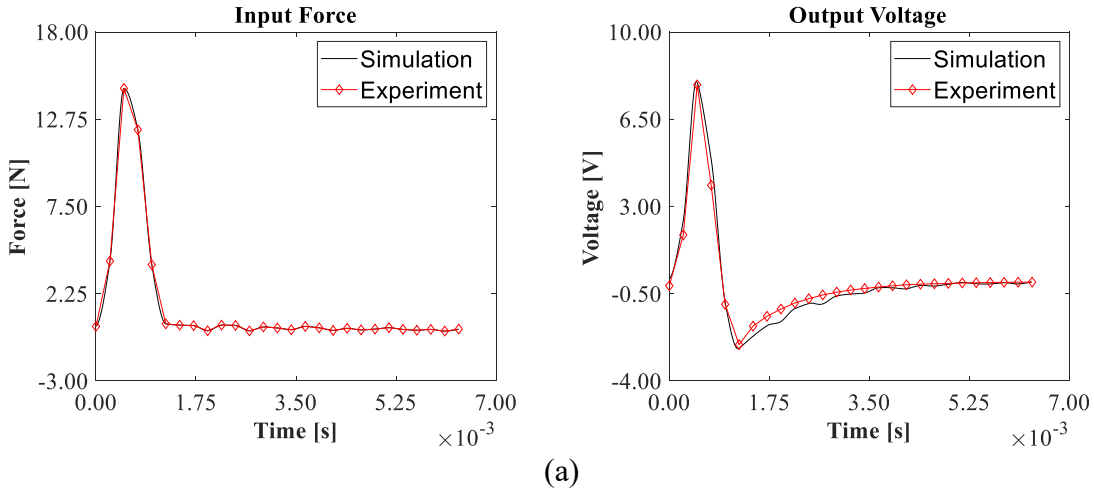

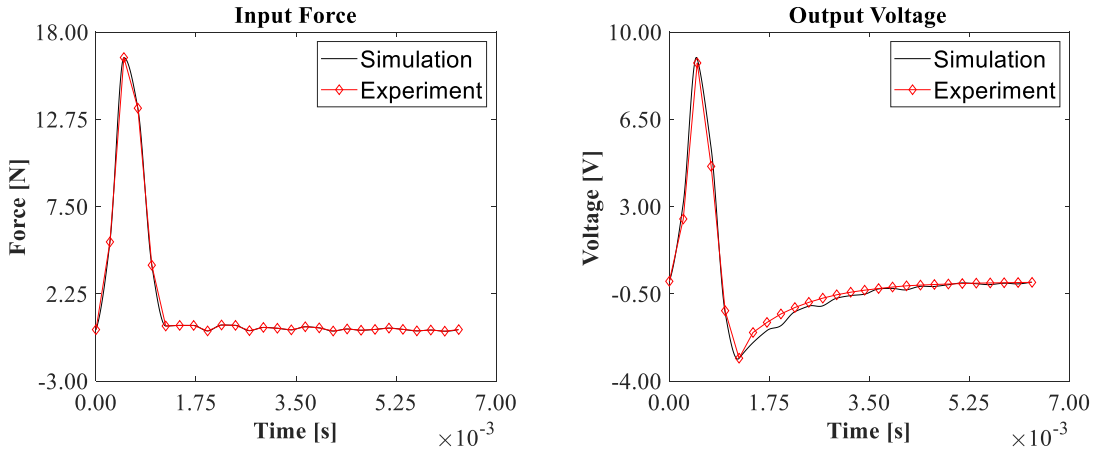

(b)

Figure 3-6 Comparison of curves of output voltage versus time from experiments and simulations under different impulse excitations with three patches connect in series. (a) 14.61 N input and voltage output with three patch stack in-series. (b) 16.47 N input and voltage output with three patch stack in-series.

3.3 Parameter studies and discussion

In this section, we investigate the influences of the dimensional and material properties of the piezoelectric patch, the vehicle speed, the magnetic force, the diameter of the cylindrical magnet, the capacitance of the storage capacitor, and the distance between the rotor center and the energy generator center on the charging power. The transient charging simulation described in Section 2.6 will be used to evaluate the energy generation process. The dimensions and material properties of the piezoelectric patch are provided in Table 3-1. For material PMN-PT-B, the following material property values will be used in calculations: K_{33}^{T} = 6000, d_{33} = 300.

A piezoelectric stack connected in parallel is considered in the study. Compared with a piezoelectric stack connected in series, which offers larger voltage output and less current, a piezoelectric stack connected in parallel provides much larger electrode area with higher electric current, which is beneficial for charging capacitor [126]. The piezoelectric stack connected in parallel system decreases the voltage but increases the current for charging the capacitor. The experiment study with different numbers of patches is for verifying the voltage output model. The piezoelectric stack connected in parallel will be used for parameter study and simulation to evaluate the performance of the purposed energy generator.

Table 3-1 Material properties and dimensions of the piezoelectric patch.

	APC 850 (PZT4)	PMN-PT-B (PT=0.3-0.33)
K_{33}^{T}	1900	5500-6500
d_{33} (10^{-12} C/N)	400	2000-3500
ε_0 (10^{-12} F/m)	8.85	8.85
POD (mm)	8-12	8-12
h (mm)	0.25-0.6	0.25-0.6
n (number of layers)	80	80

3.3.1 Parameter studies

Figure 3-7 displays the RMS charging power versus the vehicle speed under different magnetic repulsion conditions while charging a storage capacitor C_s = 100 μF. The abbreviations used in the parameter studies are defined as follows: VS for vehicle speed, MF for magnetic force, $Slot$ for slot number in rotor, PT for piezo layer thickness, AD for actuator diameter, $Layer$ for number of layers, POD for piezo layer diameter, and $RCAC$ for rotor center to actuator center. Considering practical vehicle operation condition, the parameters in this simulation are set to be: AD = 8 mm, h = 0.25 mm, n = 80, OD = 8 mm and $RCAC$ = 82.5 mm with VS changing from 80 km/h to 160 km/h under different magnetic repulsion conditions. It can be observed that the RMS charging power increases linearly with the increase in vehicle speed under the same magnetic force condition. The RMS values also increase with the increase of magnetic force under the same vehicle speed condition. It is easy to find from Eq. (3.1) and Eq. (3.3) that the higher vehicle speed leads to a higher excitation frequency of the magnetic force applied to the piezoelectric stack, resulting in an increase in the output charge. The higher magnetic force leads to a higher reaction force to the piezoelectric stack and the deformation of the piezoelectric material, which contributes to the higher power output. It is found that the RMS charging power from a single piezo-generator increases from 0.00028 W to 0.00050 W when the vehicle speed changes from 80 km/h to 160 km/h with the magnetic force of 15.48 N, while the RMS value from a single piezo-generator increases from 0.00028 W to 0.00032 W when the magnetic force changes from 15.48 N to 16.73 N at a vehicle speed of 80 km/h. The total RMS power of one brake caliper with thirty-six piezoelectric generators under 160 km/h and 40 N magnetic force conditions is 0.0908 W. Of the thirty-six generators, eight are located at $RCAC1$, sixteen at $RCAC3$ and twelve at $RCAC4$. The RMS charging power of generators at different $RCAC$ locations are shown in Table 3-2. As a result, increases in the vehicle speed and magnetic force lead to increased power output. However, it

should be noted that all outputs from our parameter studies are limited by physical dimensions and magnetic material constants. Higher output can be achieved by using more piezoelectric materials, stronger magnet, and an increase in the physical dimensions of the system.

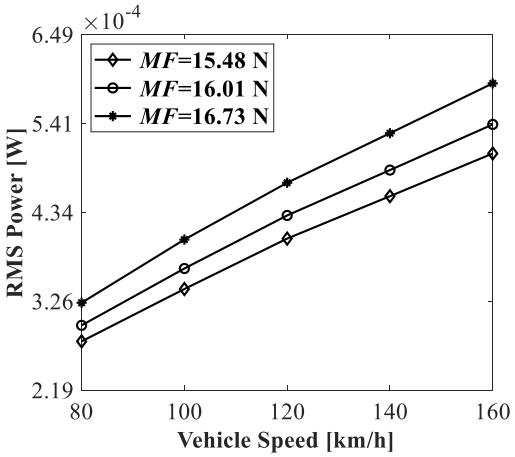

Figure 3-7 RMS charging power by a single piezoelectric energy harvester versus vehicle speed under different magnetic repulsion conditions. (AD = 0.008 m; PT = 0.00025 m; $Layer$ = 80; POD = 0.008 m; $RCAC$ = 0.0825 m; $Slot$ = 20.)

Table 3-2 RMS charging power comparison between APC850 and PMN-PT-B under 40 N magnetic repulsion at 120 km/h and 160 km/h.

	120 km/h		160 km/h	
	APC 850 (PZT4)	PMN-PT-B (PT=0.3-0.33)	APC 850 (PZT4)	PMN-PT-B (PT=0.3-0.33)
$RCAC1$ = 82.5 mm (W)	0.00193	0.03058	0.00245	0.03971
$RCAC2$ = 94.5 mm (W)	0.00195	0.03089	0.00248	0.03952
$RCAC3$ = 105 mm (W)	0.00197	0.03144	0.00253	0.03900
$RCAC4$ = 114.5 mm (W)	0.00200	0.03124	0.00256	0.04008
RMS Total	0.0710	1.1226	0.0908	1.26232

Figure 3-8 investigates the influences of the dimension of the piezoelectric material, the dimension of the actuator (cylindrical magnet embedded in the brake rotor), and the location of the energy generator on the charging power while charging a storage capacitor C_s = 100 μF.

Figure 3-8(a) shows the RMS charging power versus the diameter of AD. It can be found that the RMS charging power changes nonlinearly with the increase of AD. Under the same vehicle speed and magnetic repulsion condition, the increase of AD increases the overlapping area, and the stress changes slower on the piezoelectric material per unit time. At 80 km/h and a magnetic force of 15.48 N, it is found that the RMS charging power from a single piezo-generator decreases

from 0.00028 W to 0.00018 W when the diameter of the actuator changes from 8 mm to 12 mm. Hence, an increase in the actuator diameter causes a decrease in the power output.

Figure 3-8(b) shows the RMS charging power versus the piezoelectric layer thickness h. It can be seen that the RMS power increases with the increase in piezoelectric layer thickness. When the magnetic force is 15.48 N, the RMS charging power from a single piezo-generator increases from 0.00028 W to 0.00067 W when the piezoelectric layer thickness is increased from 0.25 mm to 0.6 mm. A thicker piezoelectric layer leads to a lower capacitance of the piezoelectric stack. Therefore, more charge can flow to the storage capacitor under the same charging condition.

Figure 3-8(c) describes the RMS charging power versus the piezoelectric layer diameter POD. It can be seen that the RMS power decreases with the increase of piezoelectric layer diameter. When the magnetic force is 15.48 N, the RMS charging power of a single piezo-generator decreases from 0.00028 W to 0.00012 W when the piezoelectric layer diameter is increased from 8 mm to 12 mm. The larger piezoelectric layer diameter leads to a bigger surface area of the piezoelectric layer, which results in a higher capacitance. This causes less charge flow to the storage capacitor, resulting in lower power output.

Figure 3-8(d) shows the RMS charging power versus the distance between the rotor center and the actuator center $RCAC$. The result indicates that the increase of $RCAC$ leads to slight variation of output power while the actuator size stays the same. At a vehicle speed of 80 km/h and a magnetic force of 15.48 N, the simulation shows that the RMS power from a single piezo-generator fluctuates between 0.00028 W and 0.00029 W when $RCAC$ changes from 70 mm to 150 mm. As there is no obvious correlation between them, the change of $RCAC$ does not have too much effect to charging power.

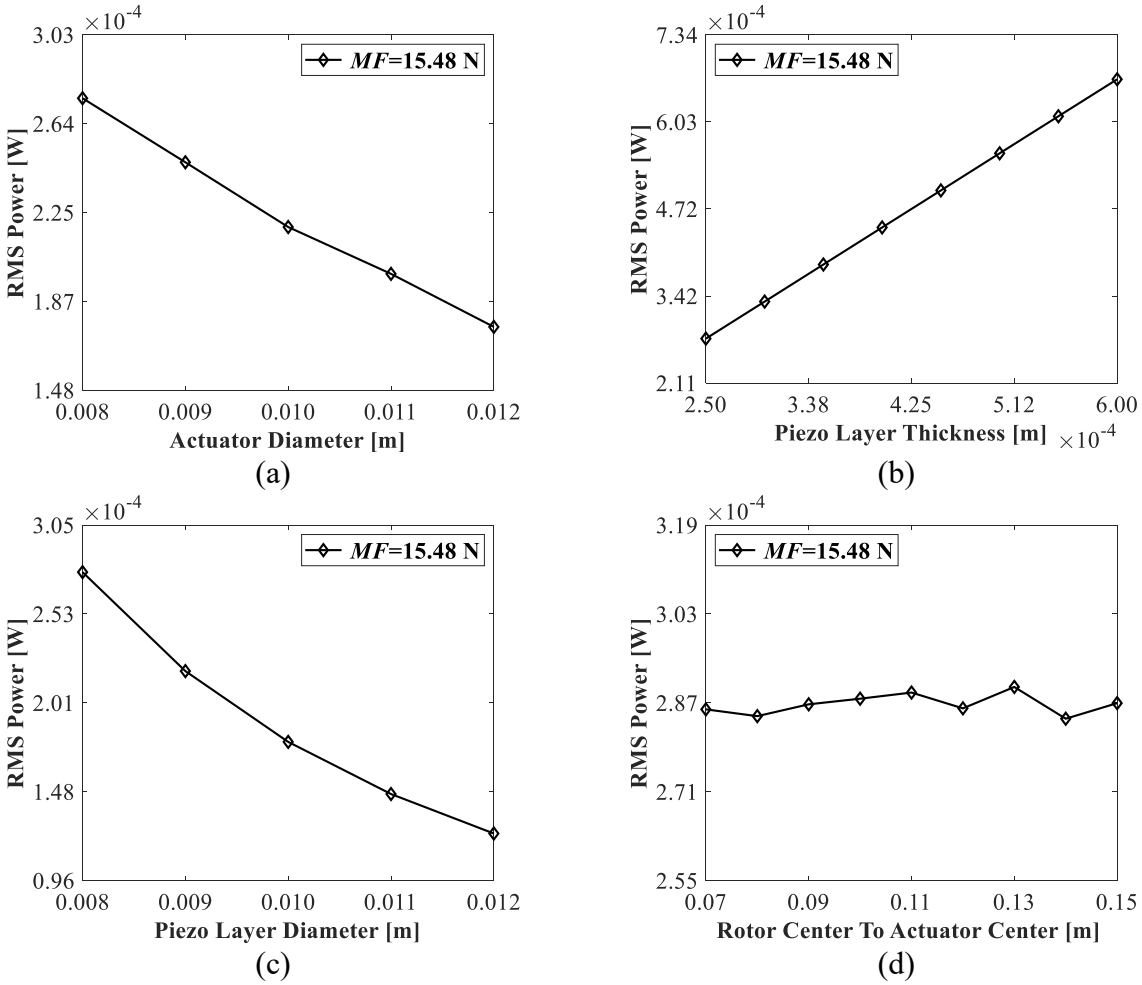

Figure 3-8 Effect of actuator diameter, piezoelectric patch layer thickness, piezoelectric layer diameter, and rotor center to actuator center on RMS charging power by a single piezoelectric energy harvester at constant vehicle velocity VS=80 km/h. (a) Actuator diameter (PT = 0.00025 m; $Layer$ = 80; POD = 0.008 m; $RCAC$ = 0.0825 m; $Slot$ = 20.). (b) Piezo layer thickness (AD = 0.008 m; $Layer$ = 80; POD = 0.008 m; $RCAC$ = 0.0825 m; $Slot$ = 20.). (c) Piezo layer diameter (AD = 0.008 m; PT = 0.00025 m; $Layer$ = 80; $RCAC$ = 0.0825 m; $Slot$ = 20.). (d) Rotor center to actuator center (AD = 0.008 m; PT = 0.00025 m; $Layer$ = 80; POD = 0.008 m; $Slot$ = 20.).

Figure 3-9 displays the RMS charging power for different storage capacitance values at VS = 80 km/h and VS = 160 km/h. The storage capacitor C_s capacitance is varied from 80 to 200 µF. The results indicate that the output power fluctuates slightly with the change in capacitance. The capacitance of the piezoelectric stack is much smaller than the capacitance of the storage capacitor. Therefore, most of the charge flows to the storage capacitor during the charging process. Figure 3-9 clearly shows that the capacitance of the storage capacitor does not have a significant impact on the RMS charging power.

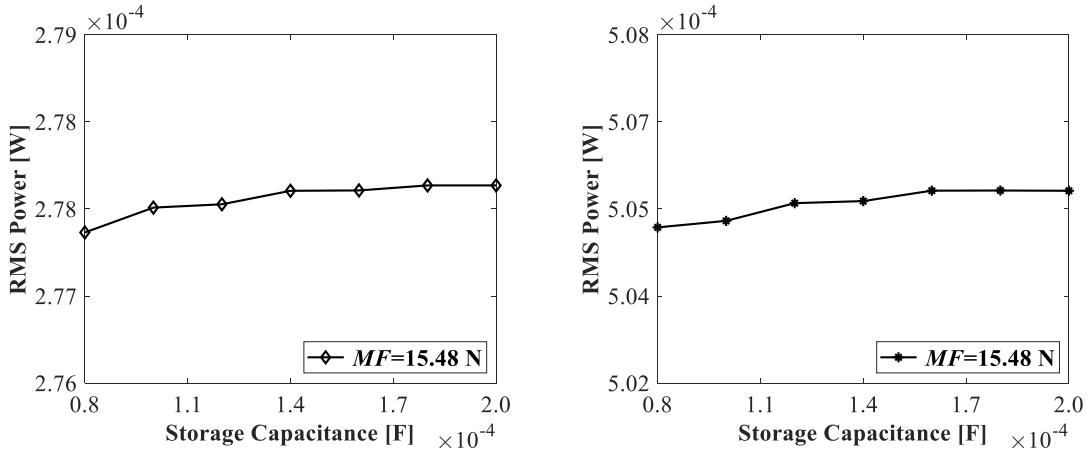

Figure 3-9 RMS charging power by a single piezoelectric energy harvester at constant vehicle velocities of VS=80 km/h and VS=160 km/h versus different storage capacitor capacitance. (a) 80 km/h (AD = 0.008 m; PT = 0.00025 m; $Layer$ = 80; POD = 0.008 m; $RCAC$ = 0.0825 m; $Slot$ = 20.). (b) 160 km/h (AD = 0.008 m; PT = 0.00025 m; $Layer$ = 80; POD = 0.008 m; $RCAC$ = 0.0825 m; $Slot$ = 20.)).

Figure 3-10, Figure 3-11, and Figure 3-12 display the RMS charging power versus the vehicle speed VS using different piezoelectric materials at different locations ($RCAC$). The RMS charging power increases with the increase of vehicle speed. It is found that the RMS charging power from a single piezo-generator using APC 850 reaches 0.00193 W when the vehicle speed is 120 km/h, MF = 40 N and the $RCAC$ is 82.5 mm; while the RMS charging power using PMN-PT-B, under the same conditions, is 0.03058 W. This is because the piezoelectric charge coefficient d_{33} of PMN-PT-B in direction 3 is much higher than that of APC 850, which results in a much higher output power. The RMS charging power comparison between APC 850 and PMN-PT-B is shown in Table 3-2. The total RMS charging power is calculated based on the current brake pad design shown in Figure 3-1(c). The assembly consists of two brake pads (inner and outer) in the brake caliper, and each of the brake pads contains 18 generators. Four generators are located at $RCAC1$, eight at $RCAC3$, and six at $RCAC4$. The peak transient charging power comparison between APC 850 and PMN-PT-B at 120 km/h is shown in Table 3-3. The corresponding voltage of the peak transient charging power is close to the saturation state voltage of the storage capacitance. The saturation state voltage is slightly different with different $RCAC$ values due to the reduction of the duration of the reaction force on the piezoelectric stack as $RCAC$ values increase. The peak voltage generated from the piezoelectric material changes a bit, and the saturation state voltage varies a little bit as well. This phenomenon can be observed from the experiment result of voltage output

in Figure 3-4. The peak voltage output in Figure 3-4(b), with a longer excitation period, is slightly lower than the output in Figure 3-4(c), where the excitation period is shorter.

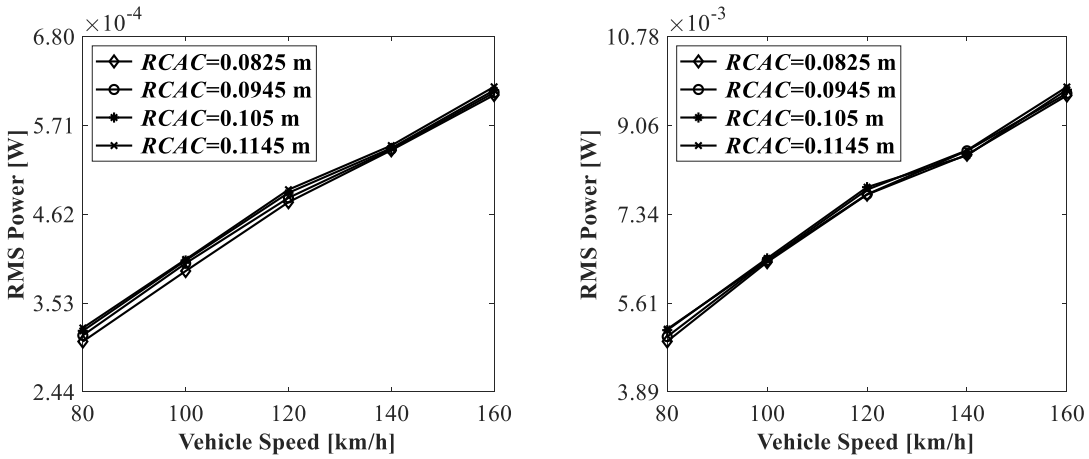

Figure 3-10 RMS charging power of different piezoelectric material by a single piezoelectric energy generator with MF=20 N at different locations versus vehicle speed. (a) APC 850 (AD = 0.012 m; PT = 0.00025 m; $Layer$ = 80; POD = 0.008 m; $Slot$ = 20.). (b) PMN-PT-B (AD = 0.012 m; PT = 0.00025 m; $Layer$ = 80; POD = 0.008 m; $Slot$ = 20.).

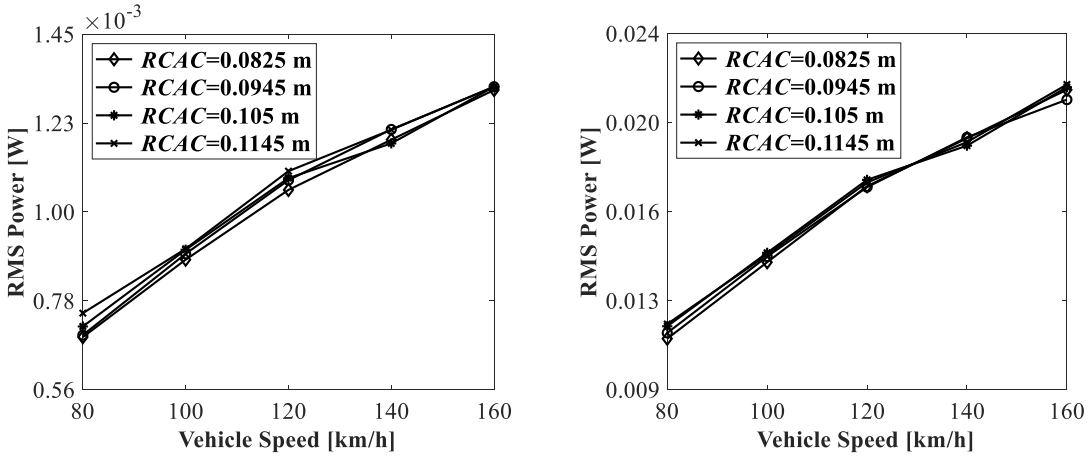

Figure 3-11 RMS charging power of different piezoelectric material by a single piezoelectric energy generator with MF=30 N at different locations versus vehicle speed. (a) APC 850 (AD = 0.012 m; PT = 0.00025 m; $Layer$ = 80; POD = 0.008 m; $Slot$ = 20.). (b) PMN-PT-B (AD = 0.012 m; PT = 0.00025 m; $Layer$ = 80; POD = 0.008 m; $Slot$ = 20.).

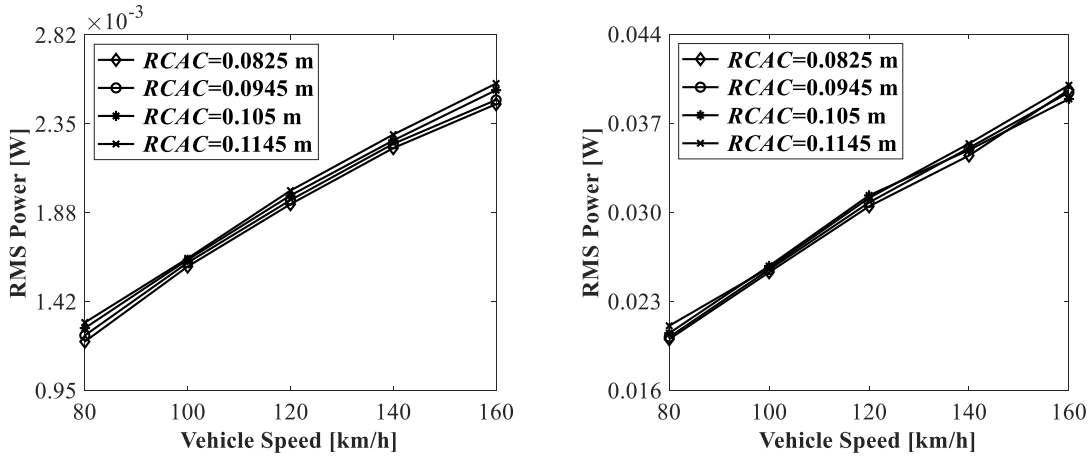

Figure 3-12 RMS charging power of different piezoelectric material by a single piezoelectric energy generator with MF=40 N at different locations versus vehicle speed. (a) APC 850 (AD = 0.012 m; PT = 0.00025 m; $Layer$ = 80; POD = 0.008 m; $Slot$ = 20.). (b) PMN-PT-B (AD = 0.012 m; PT = 0.00025 m; $Layer$ = 80; POD = 0.008 m; $Slot$ = 20.).

Table 3-3 Peak transient charging power from a single piezo-generator comparison between APC850 and PMN-PT-B under 40 N magnetic repulsion at 120 km/h.

		Peak power		Saturation
		Power (W)	Voltage (V)	voltage (V)
APC 850				
	$RCAC1$ = 82.5 mm	0.01399	3.1658	3.2827
	$RCAC2$ = 94.5 mm	0.01456	3.2267	3.3377
	$RCAC3$ = 105 mm	0.01533	3.3960	3.5037
	$RCAC4$ = 114.5 mm	0.01593	3.4595	3.5841
PMN-PT-B				
	$RCAC1$ = 82.5 mm	0.22354	6.5458	6.7788
	$RCAC2$ = 94.5 mm	0.23047	6.8471	7.0720
	$RCAC3$ = 105 mm	0.24148	7.1710	7.3922
	$RCAC4$ = 114.5 mm	0.25014	7.4337	7.6439

3.3.2 Summary and discussion

A novel vehicle brake pad-based piezoelectric energy generator has been developed, incorporating a magnetic repulsion mechanism. A mathematical model has been established to accurately calculate the output power generated by the piezoelectric stack. The unique design of the perforated brake pad, combined with the high excitation frequencies induced by the reaction forces at high vehicle speeds, enables efficient energy generation with a W level RMS charging power.

The study investigates the influences of various parameters on the RMS charging power, including the dimensions and material properties of the piezoelectric material, vehicle speed VS, magnetic force MF, actuator diameter AD, storage capacitance C_s, and the distance between the rotor center and the actuator center $RCAC$. The results indicate that increasing the thickness of the piezoelectric layer PT, vehicle speed VS, and magnetic force MF leads to higher RMS charging power. Conversely, an increase in the piezoelectric patch diameter POD and actuator diameter AD results in a decrease in the RMS value. The capacitance C_s and the distance between the rotor center and the actuator center $RCAC$ do not exert a significant influence on the RMS charging power. At a vehicle speed of 120 km/h, each caliper of the generator made of APC850 (PZT4) material produces a total RMS power of 0.0710 W, while generators made of PMN-PT-B (PT=0.3-0.33) material generate a total RMS power of 1.1226 W. Furthermore, at the same vehicle speed, a single piezo-generator using APC850 (PZT4) material generates a peak transient charging power of 0.01593 W, while using PMN-PT-B (PT=0.3-0.33) material results in a peak transient charging power of 0.25014 W.

Compared to some existing research that integrates cantilever-based PEGs in vehicle wheel and utilizes centrifugal force during rotation to harness vibration energy, the unique design of the perforated brake pad enables installation of PEGs inside the brake pad in a limited space. The findings from parameter study suggest that this novel generator design holds potential for energy generation during vehicle braking processes. To further enhance the energy harvesting performance and meet the demands of charging vehicle batteries and powering wireless electrical devices, improvements can be made in modifying the brake caliper and brake pad design. Additionally, integrating the energy generator into the brake rotor, employing magnets with higher magnetic flux density, and implementing a boosted parallel-SSHI (Synchronized Switch Harvesting on Inductor) circuit can also enhance the performance.

Chapter 4 Shear mode piezoelectric energy generation under FIV

In this chapter, a shear mode piezoelectric energy generator, which utilizes the FIV and high shear mode piezoelectric coefficient to improve the energy output, is introduced. Parameter studies have been conducted to investigate the influences of the piezoelectric patch dimensional parameters, vibration system parameters, friction model parameters, methods of electrical connections, and different piezoelectric materials on the energy generation performance to guide better design. The modeling methods depicted in Sections 2.1, 2.2, 2.3, and 2.6 are utilized in this chapter.

4.1 Testing system design

In this work, a single-degree-of-freedom piezoelectric shear mode energy generation device is mounted on a self-designed test setup. The schematic of the system is shown in Figure 4-1. In the test setup, the DC motor provides power to the rotating shaft, and the coupling connects the motor and the shaft. The motor controller is used to control the speed of the motor. The energy generator is installed on a mounting structure which is fixed on the base plate, and the mounting structure is made from 3D printing using poly lactic acid (PLA) material. The detail of the energy generation system is depicted on the bottom left in Figure 4-1. It contains a load cell installed in the channel of the mounting structure, a compression spring to provide a normal load, and a single-degree-of-freedom piezoelectric shear mode energy generator. The bolt on the back of the mounting structure can move forward or backward to press the compression spring to provide a normal load. A signal acquisition system is used to measure the generated voltage from the piezoelectric patch. A tachometer is mounted on the right side of the test setup to measure the rotating speed of the friction plate.

The design in Figure 4-1 can be regarded as a composite patch, which is designed for shear mode energy generation. The diagram of the equivalent 1-DOF friction system is displayed at the bottom right corner in Figure 4-1. It contains three parts: the piezoelectric material, the elastic shear deformation layer, and the friction layer. The sliding plate is contacting with the friction layer and moving at a constant velocity. Due to the high stiffness of the elastic shear deformation layer and the relatively small equivalent mass of the friction layer, the composite patch deforms and vibrates along the horizontal direction with small deformation, and the piezoelectric material is under dynamic shear deformation simultaneously. The elastic shear deformation layer and the piezoelectric material can be considered as two springs connected in series, making the mechanism a single-degree-of-freedom spring-mass system. It is easy to realize energy harvesting with this simple mechanism, and using the shear piezoelectric mode is relatively simple without introducing other mechanical parts. It is noteworthy that surface conditions of the PZT affect the interface bonding and, consequently, the electromechanical coupling effect, and it should be considered for practical application.

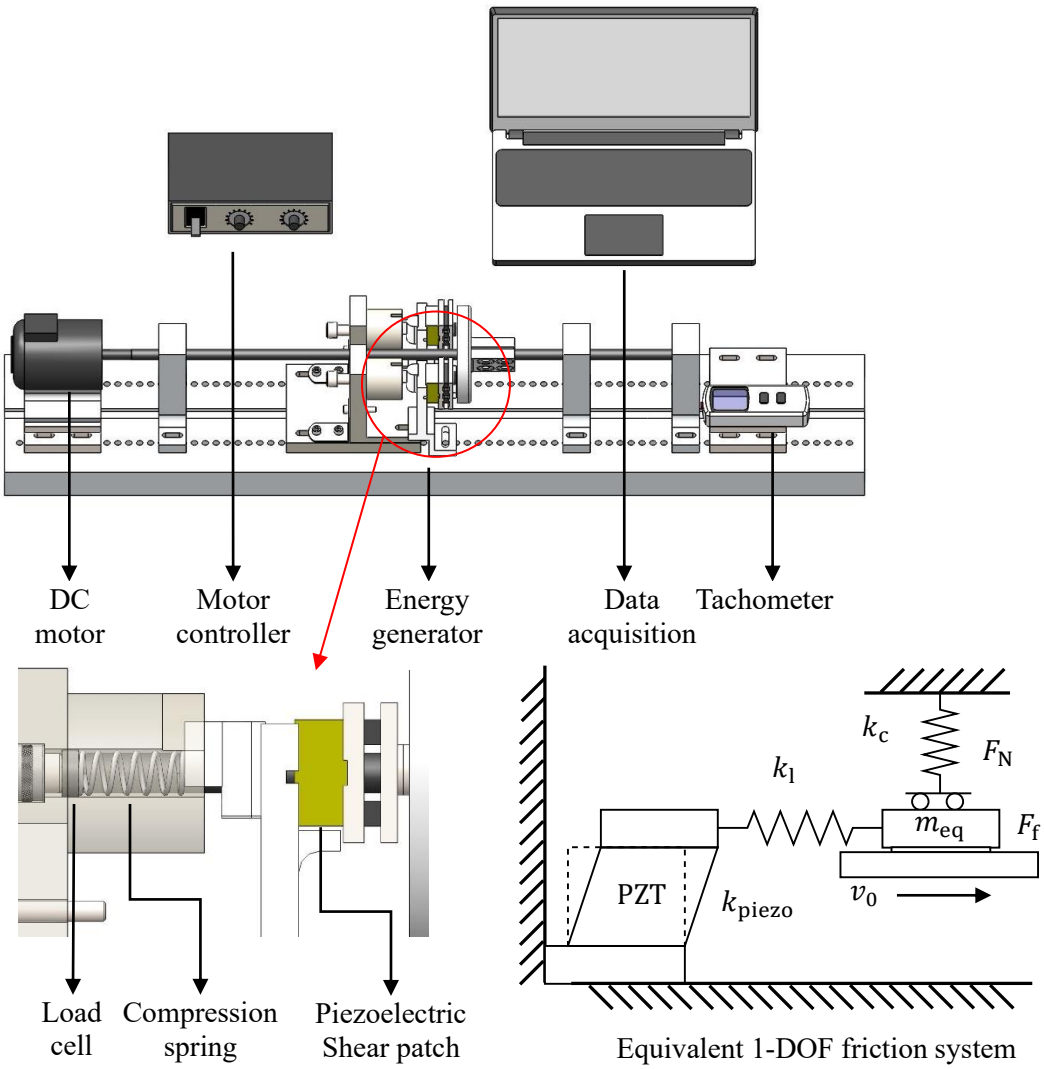

Figure 4-1 Schematic of the testing system design.

4.2 Energy generation

4.2.1 Mechanical and piezoelectric-coupling of SDOF vibration system

The mechanical and piezoelectric coupling equation of the system can then be written as,

$$\begin{cases} m_{eq}\ddot{y}(t) + c\dot{y}(t) + k_{eq}y(t) + \alpha\dfrac{k_l}{k_l + k_{piezo}}V_R(t) = F_f(t), \\ V_R(t) + RC_p\dot{V}_R(t) - R\alpha\dfrac{k_l}{k_l + k_{piezo}}\dot{y}(t) = 0, \end{cases} \tag{4.1}$$

where m_{eq} is the equivalent mass of the vibration system; $c = 2\zeta\sqrt{k_{eq}m_{eq}}$ is the damping coefficient, and ζ is the damping ratio; k_{eq} is the equivalent stiffness of the system; k_{piezo} is the

stiffness constant of the piezoelectric patch; k_l is the linear spring stiffness; $F_f(t)$ is the friction force applied to the mass block; $y(t)$ is the vibration response of the mass block under friction force; $V_R(t)$ is the actual output voltage from the piezoelectric material after considering the charging dissipation in electric resistance; R is electric resistance; C_p is the capacitance of the piezoelectric patch; and α is the force factor. The detail iterative solving process is depicted in Section 2.3.

4.2.2 Experimental verification of voltage output

Our initial design of the energy generator and the corresponding experiment test are shown in Figure 4-2. The initial idea is to introduce a simple piezoelectric energy harvester that is easy to operate in practical applications and has no complex mechanical structure. The possible application scenarios are shown in Figure 4-3. The dynamic deformation of the structure is shown at the top right corner of Figure 4-2. While the sliding surface moves horizontally, the composite patch deforms and vibrates along the horizontal direction, and the piezoelectric material is under dynamic shear deformation. The shear piezoelectric coefficient is usually higher than the normal ones, leading to more efficient piezoelectricity generation. With the advantage of the simple and compact design, piezoelectric energy harvesting can be easily realized by pushing the piezoelectric shear patch against any moving surfaces, which can be rotating disks, cylinders, or running belts. For example, the technique can be incorporated into the vehicle braking system and utilize the wasted energy. It can also be combined with the rotating structure of the wind turbine to harvest the wind energy. Some rotating fitness equipment can also be adopted to collect released energy during the workout. In summary, energy from any kinematic motions with ultra-low operation frequency can generate piezoelectric power due to the high frequency FIV.

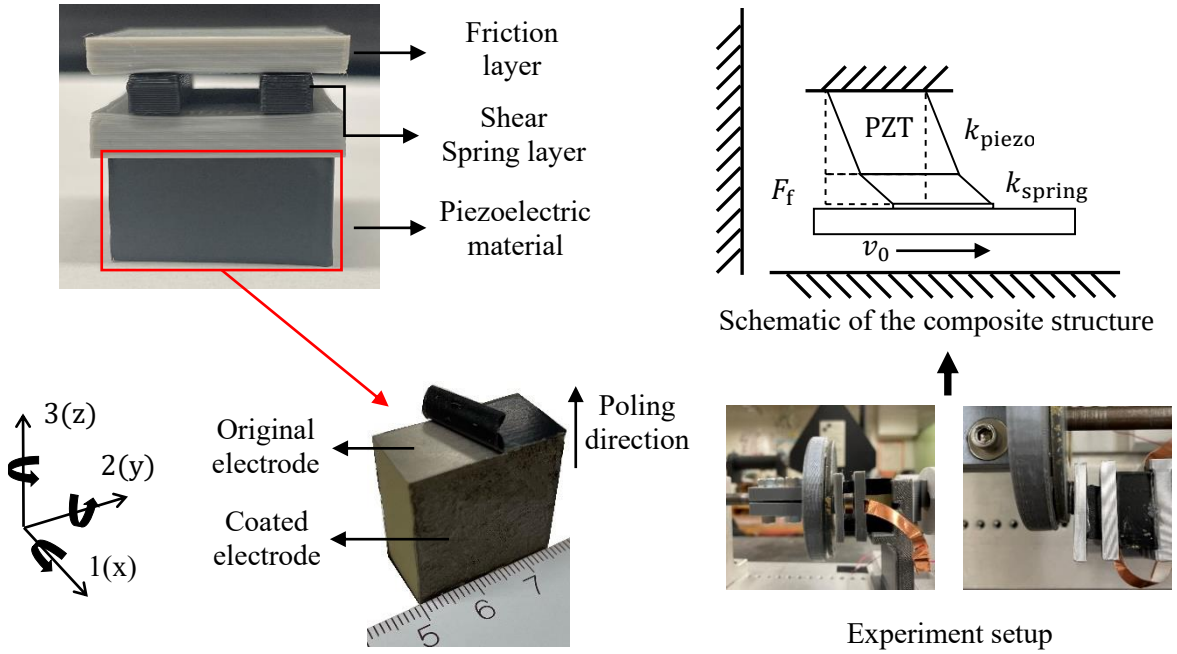

Figure 4-2 Illustration of the shear mode piezoelectric composite energy generator.

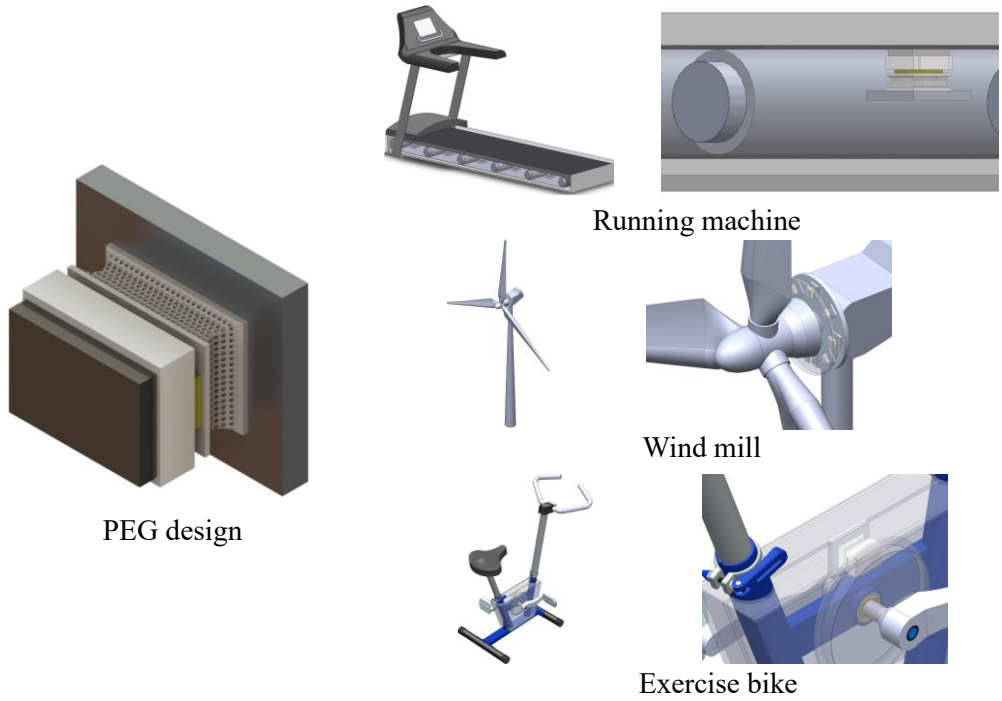

Figure 4-3 Application scenarios of the shear mode piezoelectric composite energy generator.

Figure 4-4(a)-(d) shows the dynamic voltage responses of the initial design under different conditions. The high frequency dynamic response can be observed due to the stiffness of the shear rubber. However, the shear modulus of the rubber we used in the experiment is unknown and close

to linear under a certain small strain range, which is difficult to control by regular test setup. In addition, the piezoelectric material we used in the experiment is a general d33 mode piezoelectric patch with original electrodes arranged perpendicularly to its polling direction. The electrodes along direction 1 are made by coating a thin layer of conductive paste, while the original electrodes are covered by electrical tape to isolate it from the electrode along direction 1. The accurate shear piezoelectric constant is also unknown. As a result, it is difficult to perform an accurate simulation study of this initial design at the current stage. To describe and study the influence of different parameters on shear patch energy generation with a linear elastic part, a representative spring mass setup shown in Figure 4-5(a) is applied in the study, and the experimental verification is demonstrated in the next section. A theoretical study of the compact composite patch considering the possible material nonlinearity will be conducted in our future work.

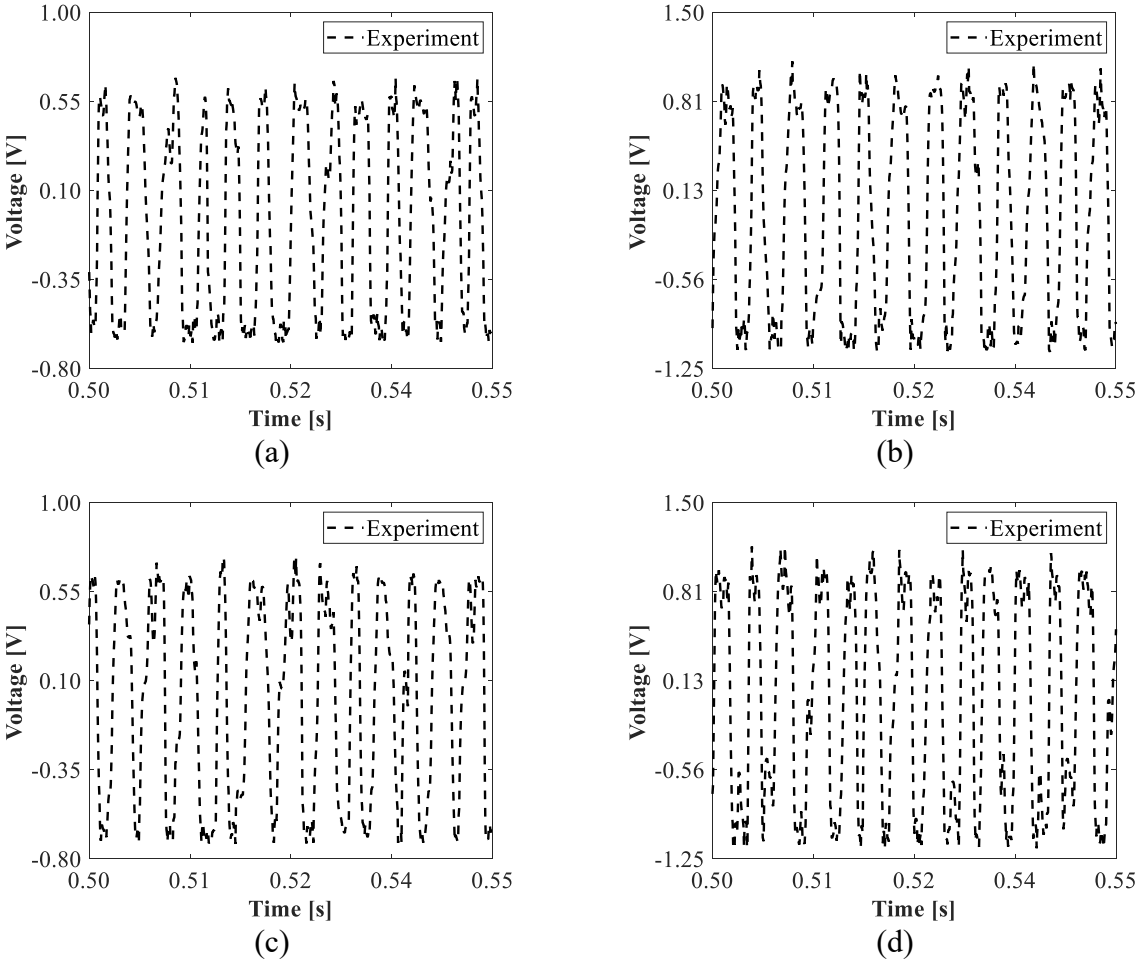

Figure 4-4 Experimental result from shear mode piezoelectric composite energy generator. (a) F_{N} = 0.5 N and v_0 = 1.9792 m/s. (b) F_{N} = 0.5 N and v_0 = 5.9376 m/s. (c) F_{N} = 2.5 N and v_0 = 1.9792 m/s. (d) F_{N} = 2.5 N and v_0 = 5.9376 m/s.

It can be seen from Figure 4-5(a) that the piezoelectric patch is mounted on a small rigid block. On the left side of the piezoelectric patch, another rigid block is attached and used to connect with the linear tension spring. A mass block with a friction layer on one end is connected with the tension spring. The sliding plate is contacting with the friction layer of the mass block and moving at a constant velocity. In order to verify the output voltage from the mechanical and piezoelectric coupled model with the designed test setup, experimental tests of the voltage output from the piezoelectric shear patch under different normal forces and the rotating speeds of the friction plate are performed. The piezoelectric shear patch is shown in Figure 4-5(b), and the left and right sides show the overall width and thickness, respectively. A piezoelectric shear patch (PL5FBP3) with flat end plates and electrodes on both ends, which has an overall dimension of 5×5×1.8 mm, is used for the experiment. The actual dimension of the piezoelectric material is 5×5×0.5 mm. The material properties of the piezoelectric patch are: d_{15} = 590e^{-12} C/N, c_{55}^{E} = 21.8e^{9} Pa, and k_{15} = 0.68 [30].

To integrate the piezoelectric shear patch into the test setup, two small rigid blocks are used, as seen in Figure 4-5(c). The two small rigid blocks, which are 3D printed using Polyactic Acid (PLA) with 100% infill, clamp the flat end plates of the piezoelectric shear patch. The other two ends of the small rigid blocks are connected to the linear spring and the fixed end, correspondingly. Resin adhesive is used to ensure each of these parts is securely attached. A linear spring C14-047-032 with k_{l} = 4553.3 N/m is used to connect the left side rigid block on the piezoelectric patch and the mass block [127].

The data acquisition system is a four-channel Siemens LMS SCA- DAS mobile integrated with LMS TestLab. A rotor kit with a 0.1 horsepower DC motor and a motor speed controller manufactured by Bently Nevada corp. is used to supply power and control the input rpm of the rotating shaft. A DT-2234C+ digital tachometer is used to measure the actual output rpm of the friction plate.

In the test, the distance between the center of the friction layer of the mass block and the shaft is 31.5 mm. The velocity v_0 during the FIV process is calculated to be $\mathrm{v_0 = 0.1047 v_s d_{m-s}}$, where v_{s} is the rotating speed of the shaft in revolutions per minute (rpm), $d_{\mathrm{m-s}}$ is the distance between

the center of the friction layer of the mass block and the shaft, and 0.1047 is calculated from 0.1047 = 2π/60, which converts rpm to rad/s. The contact interfaces of the rotating friction plate and the friction layer of the mass block are cleaned before each test.

The influence of the bonding between these parts and the bonding during the 3D printing process is difficult to reflect in the theoretical modeling. In the theoretical modeling process, these parts are assumed to be rigid for simplification, and the effect of structural vibration is also ignored. In order to match the experiment result with theoretical modeling, a tuning factor θ_p is used in Eq. (2.17) and selected to be 0.05 for the current test setup based on the experiment results. The comparison of output voltage versus time from experiments and simulations under different normal forces and rotating speeds is displayed in Figure 4-6. And the following parameters are used: m_{eq} = 0.0062 kg, ζ = 1e^{-6}, k_l = 4553.2977 N/m, μ_k = 0.42, μ_{static} = 0.62, C = 4.2, A_p = 2.5e^{-5} m^2, t_p = 0.0005 m, α = 0.059812 V/N, C_p = 8.4075e^{-10} F, and R = 1.8 MΩ. In the experiment, three different normal forces F_N under two different velocities v_0 are performed. In simulation, the corresponding output voltage is calculated using Eq. (2.34). The resistance R in Eq. (2.34) is used to simulate the charge dissipation of the piezoelectric system while connecting to the data acquisition system, and R = 1.8 MΩ which is based on previous experiment result [9]. The time domain voltage variations obtained from simulations and experiments match each other, proving the accuracy and effectiveness of the voltage output from Eq. (2.34). The experimental results show around 7 vibration peaks within 0.05 s. It indicates the actual vibration frequency of 140-150 Hz and proves the possibility of exciting continuous high-frequency vibration through friction. It will be helpful for vibration-based piezoelectric energy generation.

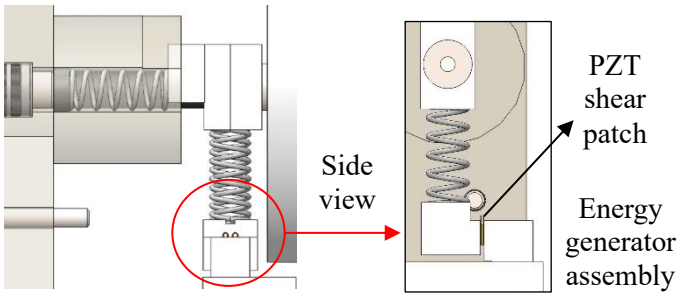

(a)

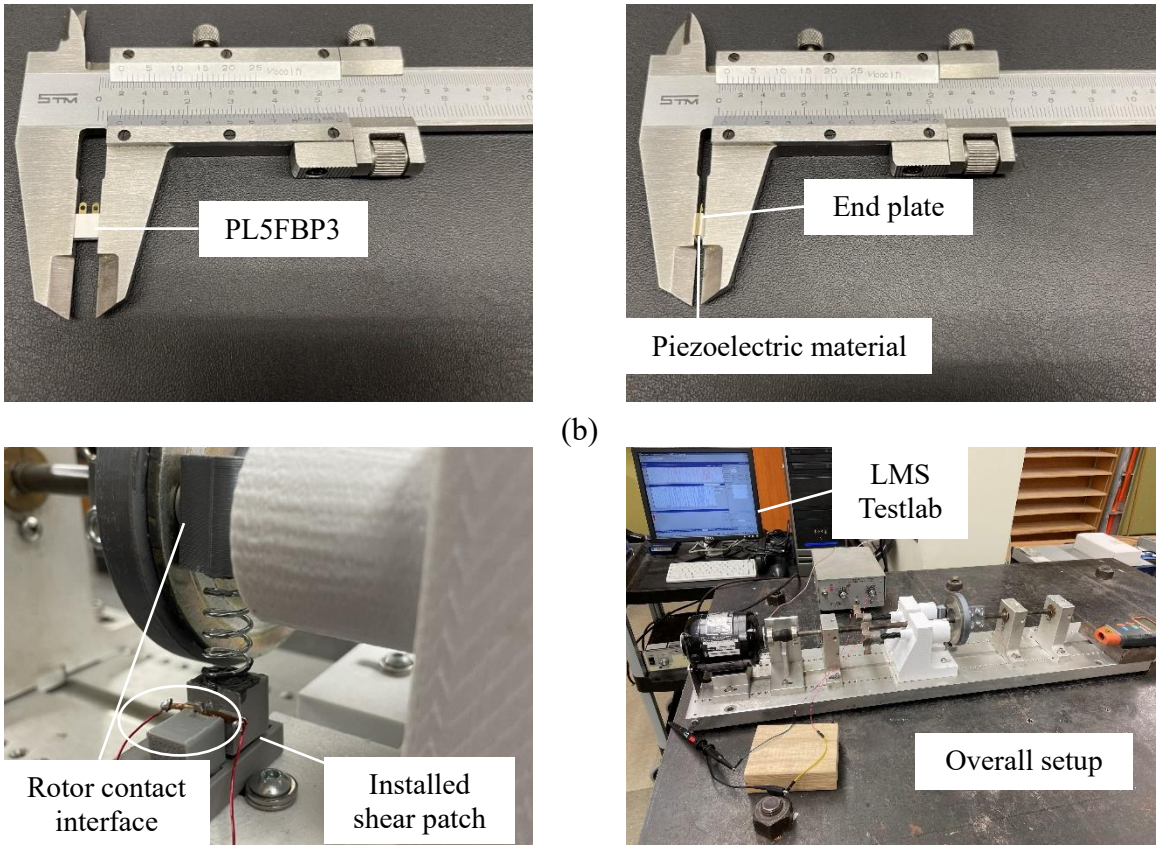

Figure 4-5 Experimental test setup. (a) Shear mode piezoelectric energy generator with linear spring. (b) Piezoelectric shear patch. (c) Piezoelectric shear patch connection.

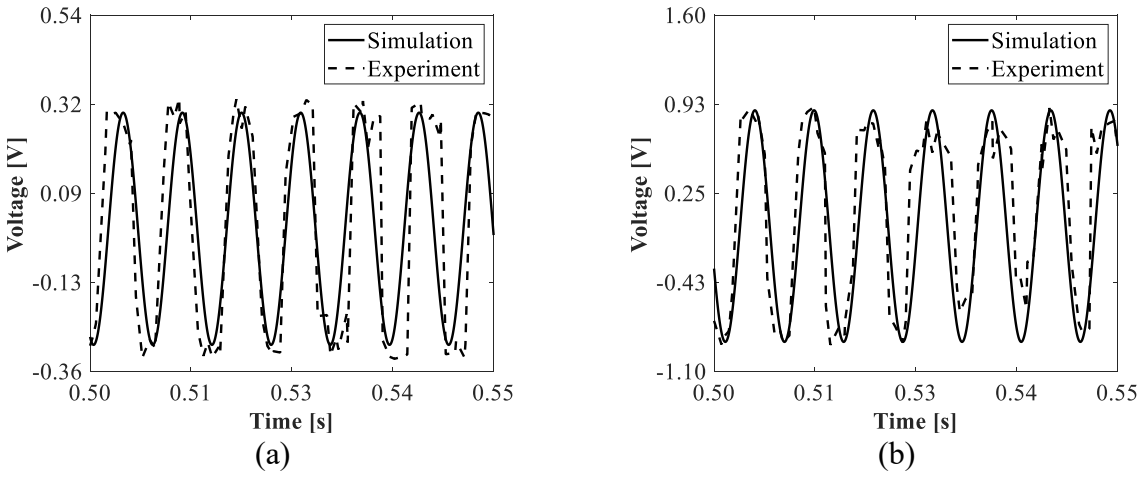

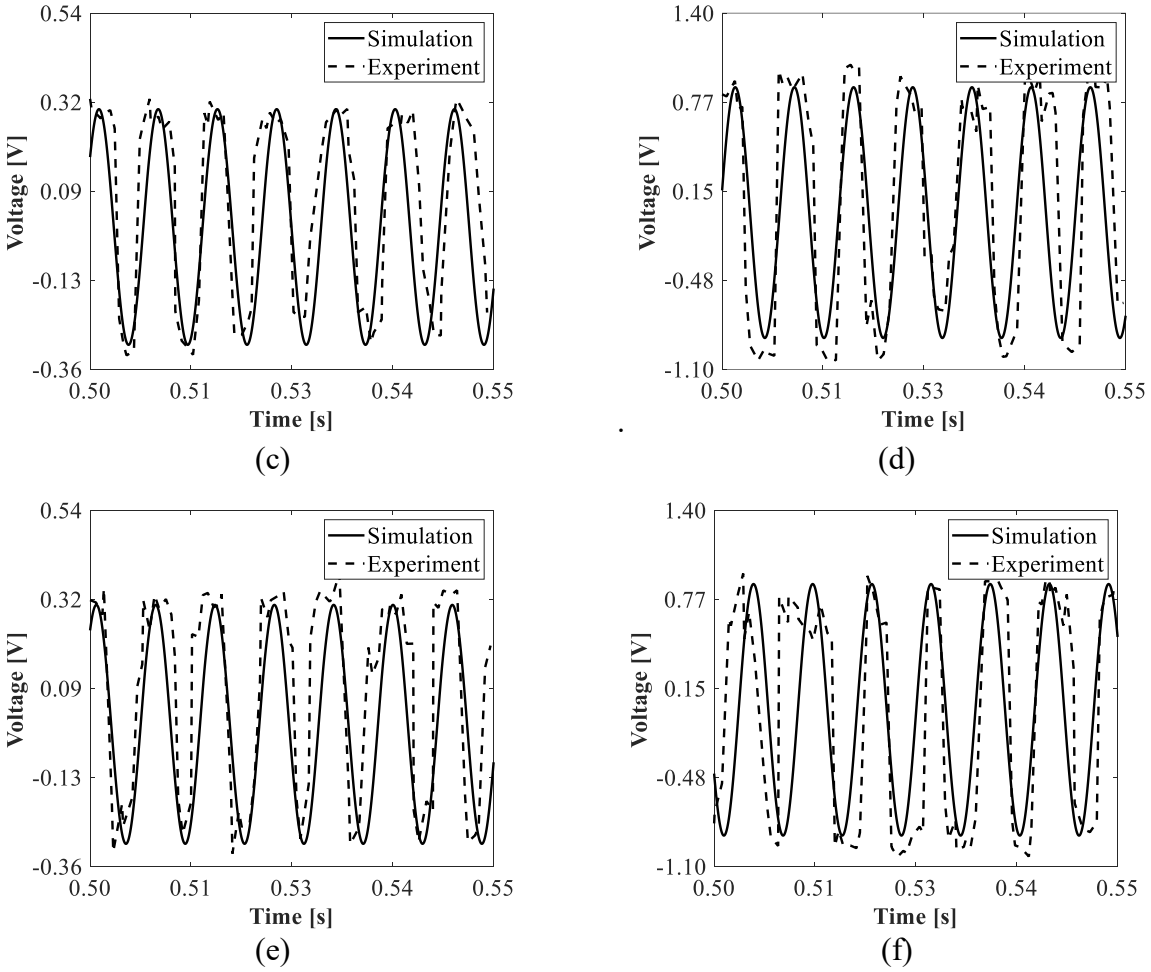

Figure 4-6 Comparison of output voltage versus time from experiments and simulations under different normal forces and sliding velocities during FIV. (a) F_N = 0.5 N and v_0 = 1.9792 m/s. (b) F_N = 0.5 N and v_0 = 5.9376 m/s. (c) F_N = 2.5 N and v_0 = 1.9792 m/s. (d) F_N = 2.5 N and v_0 = 5.9376 m/s. (e) F_N = 4.5 N and v_0 = 1.9792 m/s. (f) F_N = 4.5 N and v_0 = 5.9376 m/s.

4.3 Parameter studies and discussion

In this section, the verified model is used for transient charging simulation, which is experimentally verified in previous research [115], to evaluate the actual energy generation performance by charging storage capacitance. The effects of the different design parameters are analyzed and discussed. In order to obtain a higher energy output, piezoelectric material with higher piezoelectric constants can be adopted for the application. The possible output of replacing the PZT with the single crystal of PMN-PT is calculated for comparison. The parameters used in the simulation are shown in the figure caption.

4.3.1 Parameter studies

Figure 4-7 displays the RMS charging power, peak instant charging power and saturated voltage versus different cross-section area A_{p}, which are achieved by changing the width of the piezoelectric patch, w_{p}, without changing the thickness, t_{p}. Two different electric resistance R conditions are studied while charging a storage capacitor C_{s} = 300 nF. And the following parameters are used: m_{eq} = 0.0062 kg, ζ = 1e^{-6}; k_{l} = 4553.2977 N/m, v_0 = 5.9376 m/s, μ_{k} = 0.42, μ_{static} = 0.62, C = 4.2, and t_{p} = 0.0005 m. Considering a similar operation condition to the experiment setup, θ_{p} is set to be 0.05 leading to a smaller value of α because of the bonding interface, and other parameter values are shown in the figure titles. It can be observed that the RMS charging power, although more piezoelectric material is used, the peak instant charging power and saturated voltage decrease with the increase of the cross-section area A_{p} under both R = 1.8 MΩ and R = 36 MΩ conditions. It is easy to find from the capacitance calculation formula in Section 2.3 that the larger cross-section area leads to a higher effective capacitance of piezoelectric material, and k_{piezo} also increase which results in smaller deformation. Larger effective capacitance results in smaller output voltage, when the piezoelectric charge coefficient d_{15} and the generated shear force stay unchanged. With A_{p} increases from 1e^{-5} to 4.1e^{-4} m^2, R = 1.8 MΩ, and F_{N} = 0.5, 2.5, 4.5 N, the RMS charging power decreases from 99.12 nW to 9.78 nW, 99.43 nW to 9.82 nW, and 99.82 nW to 9.86 nW, respectively. When R = 36 MΩ and F_{N} = 0.5, 2.5, 4.5 N, the RMS charging power decreases from 393.64 nW to 10.08 nW, 395.78 nW to 10.12 nW, and 398.15 nW to 10.15 nW, correspondingly. The reason for the higher RMS charging power with R = 36 MΩ is that 36 MΩ is much larger than 1.8 MΩ, leading to less charge consumed by the electric resistance, which is beneficial for collecting generated energy.

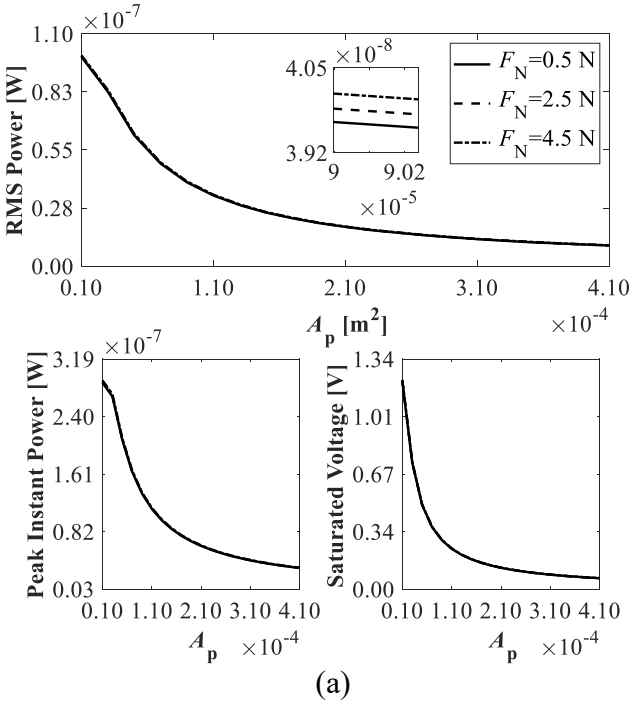

(a)

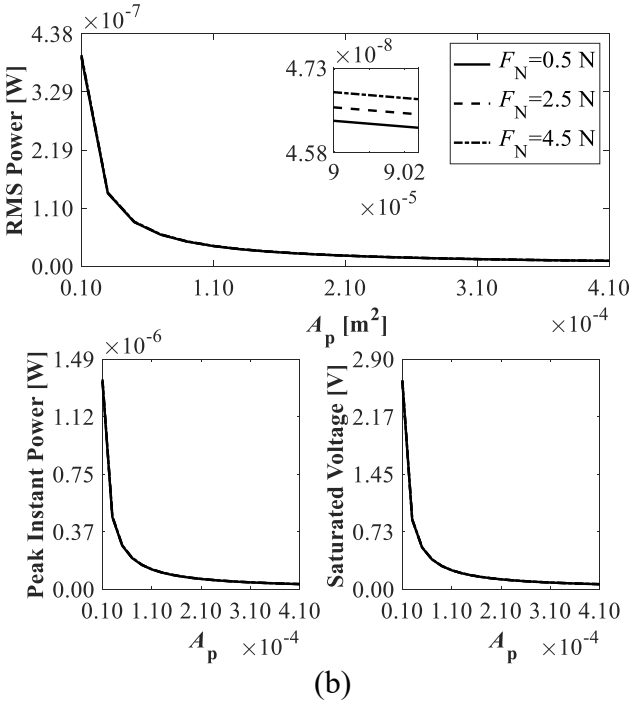

(b)

Figure 4-7 RMS charging power with different A_p under conditions. (a) R = 1.8 MΩ. (b) R = 36 MΩ.

Figure 4-8 demonstrates the RMS charging power, peak instant charging power and saturated voltage versus different piezoelectric patch thicknesses t_p under two different electric resistance R conditions while charging a storage capacitor C_s = 300 nF. And the following parameters are

used: m_{eq} = 0.0062 kg, ζ = 1e^{-6}; k_{l} = 4553.2977 N/m, v_0 = 5.9376 m/s, μ_{k} = 0.42, μ_{static} = 0.62, C = 4.2, t_{p} = 0.0005 m, and R = 36 MΩ. It can be seen that the RMS charging power, peak instant charging power, and saturated voltage increase with the increase of t_{p} under R = 36 MΩ condition. It can be found that the increase of t_{p} results in smaller effective capacitance C_{p} and smaller stiffness constant k_{piezo} of piezoelectric patch, correspondingly. And Eq. (2.15) indicates that the smaller stiffness constant k_{piezo} causes larger shear deformation of the piezoelectric shear patch. The smaller C_{p} and larger shear deformation contributes to larger output voltage with the same piezoelectric coefficient and external excitation. With t_{p} increases from 5e^{-4} to 1.55e^{-2} m, A_{p} = 2.5e^{-5} m^2, and F_{N} = 0.5, 2.5, 4.5 N, the RMS charging power increases from 164.10 nW to 1963.51 nW, 165.00 nW to 1972.21 nW, and 166.01 nW to 1981.77 nW, respectively. When A_{p} = 2.5e^{-4} m^2 and F_{N} = 0.5, 2.5, 4.5 N, effective capacitance C_{p} and stiffness constant k_{piezo} are larger, the RMS charging power increases from 16.63 nW to 479.63 nW, 16.71 nW to 482.24 nW, and 16.78 nW to 485.17 nW, correspondingly. The RMS charging power, peak instant charging power and saturated voltage are smaller than the values with A_{p} = 2.5e^{-5} m^2 because of the higher stiffness constant k_{piezo} and smaller shear deformation.

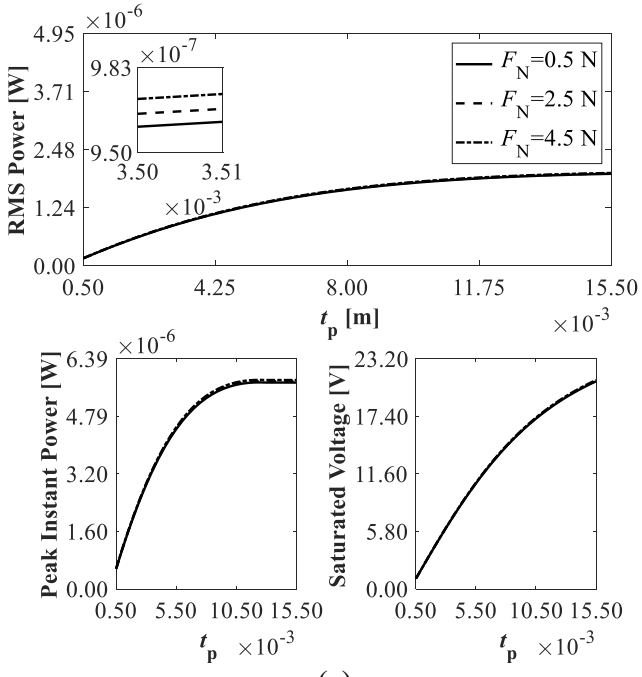

(a)

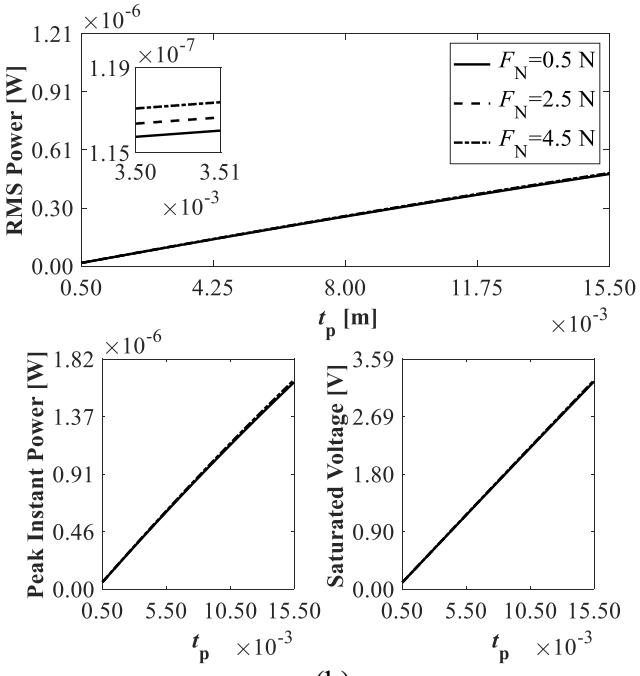

(b)

Figure 4-8 RMS charging power with different t_p under different conditions. (a) Cross-section area A_p = 0.000025 m^2. (b) Cross-section area A_p = 0.00025 m^2.

Figure 4-9 demonstrates the effect of the equivalent mass of the vibration system m_{eq} on energy generation performance under two different electric resistance R conditions while charging a storage capacitor C_s = 300 nF. And the following parameters are used: ζ = 1e^{-6}; k_l = 4553.2977 N/m, v_0 = 5.9376 m/s, μ_k = 0.42, μ_{static} = 0.62, C = 4.2, A_p = 2.5e^{-5} m^2, t_p = 0.0005 m, and α = 0.059812 V/N. The RMS charging power, peak instant charging power, and saturated voltage increase with the increase of m_{eq} under both R = 1.8 MΩ and R = 36 MΩ conditions. With m_{eq} increases from 0.0025 to 0.0075 kg, R = 1.8 MΩ, and F_N = 0.5 N, the RMS charging power increases from 72.02 nW to 91.41 nW, representing a 26.9% increase. With m_{eq} increases from 0.0125 to 0.0175 kg under the same condition, the RMS charging power increases from 96.80 nW to 98.66 nW, representing a 1.9% increase. With m_{eq} increases from 0.0025 to 0.0075 kg, R = 36 MΩ, and F_N = 0.5 N, the RMS charging power increases from 105.39 nW to 179.94 nW, representing a 70.7% increase. With m_{eq} increases from 0.0125 to 0.0175 kg under the same condition, the RMS charging power increases from 230.15 nW to 270.41 nW, representing a 17.9% increase. The increase rate of the RMS charging power under both R = 1.8 MΩ and R = 3.6 MΩ

conditions become more gradual, which indicates that m_{eq} does not have a significant influence on energy generation when it reaches a certain value with other parameters unchanged.

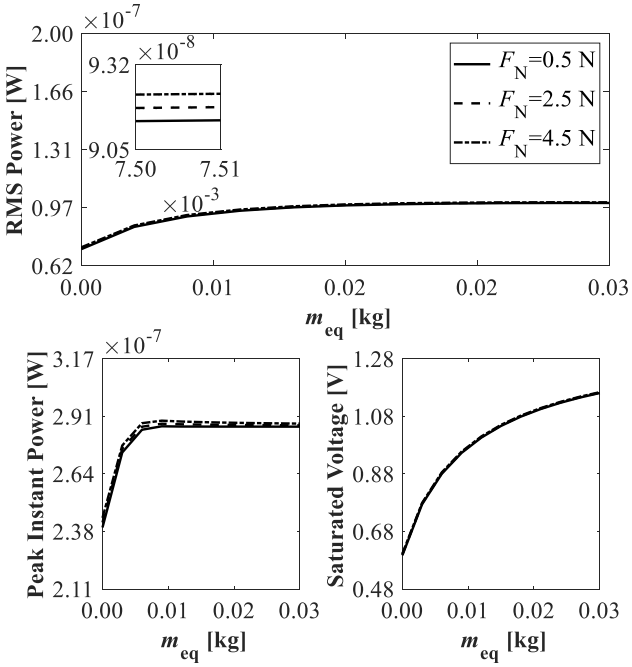

(a)

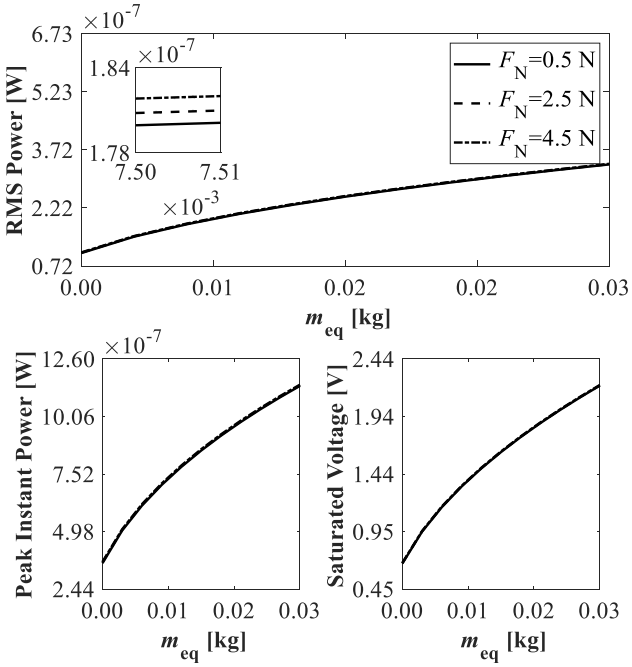

(b)

Figure 4-9 RMS charging power with different m_{eq} under different R. (a) R = 1.8 MΩ. (b) R = 36 MΩ.

Figure 4-10 illustrates the effect of the linear tension spring stiffness k_{l} on energy generation performance under two different electric resistance R conditions while charging a storage capacitor C_{s} = 300 nF. And the following parameters are used: m_{eq} = 0.0062 kg, ζ = 1e^{-6}, v_0 = 5.9376 m/s, μ_{k} = 0.42, μ_{static} = 0.62, C = 4.2, A_{p} = 2.5e^{-5} m^2, t_{p} = 0.0005 m, and α = 0.059812 V/N. The RMS charging power, peak instant charging power, and saturated voltage increase almost linearly with the increase of k_{l} under both R = 1.8 MΩ and R = 36 MΩ conditions. It can be found from Eq. (2.15) that the equivalent stiffness of the system k_{eq} is calculated from k_{l} and k_{piezo}. k_{piezo} is several orders of magnitude larger than k_{l}, thus, k_{eq} is mainly determined by k_{l}. The increase of k_{l} leads to a higher vibration frequency. Though the vibration amplitude may decrease a bit, the resulting $y_{\mathrm{p}}(t)$ with higher rate of deformation overcomes the decreased vibration amplitude and shows advantages in energy generation.

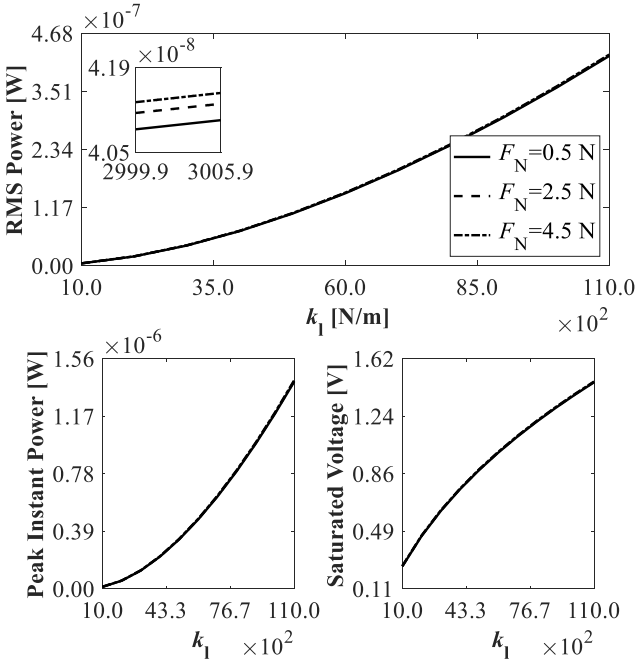

(a)

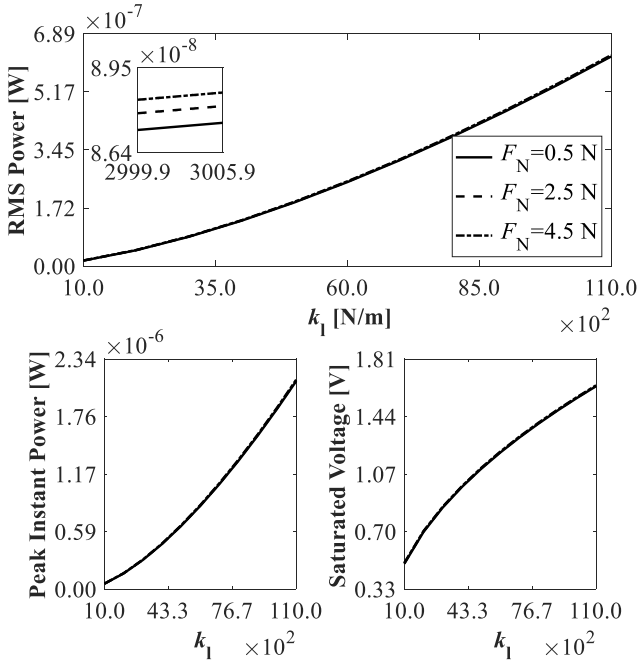

(b)

Figure 4-10 RMS charging power with different k_l under different R. (a) R = 1.8 MΩ. (b) R = 36 MΩ.

Figure 4-11 compares energy generation performance while charging different values of the storage capacitor C_s and charging the same capacitor C_s = 300 nF with different R. And the following parameters are used: m_{eq} = 0.0062 kg, ζ = 1e^{-6}, k_l = 4553.2977 N/m, v_0 = 5.9376 m/s, μ_k = 0.42, μ_{static} = 0.62, C = 4.2, A_p = 2.5e^{-5} m^2, t_p = 0.0005 m, and α = 0.059812 V/N. Figure 4-11(a) shows that the RMS charging power, peak instant charging power, and saturated voltage stay almost unchanged with the increase of C_s. It proves that increasing C_s does not have a significant effect on the energy generation performance. Figure 4-11(b) indicates that the RMS charging power, peak instant charging power, and saturated voltage increase with the increase of electric resistance R, and the increase rate turns gradual with the increase of R. The reason is that the larger R brings the circuit close to an open-circuit condition, and there is less charge dissipation happened on R and most of the generated energy by piezoelectric patch is stored in C_s.

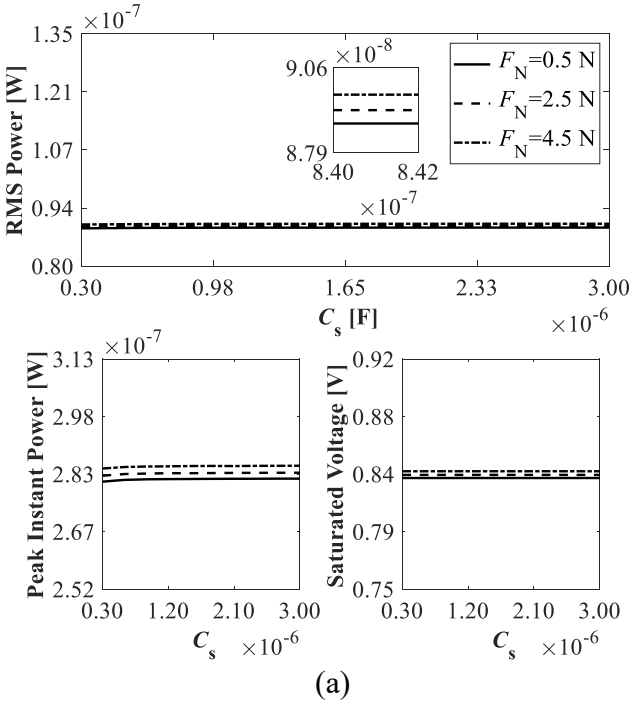

(a)

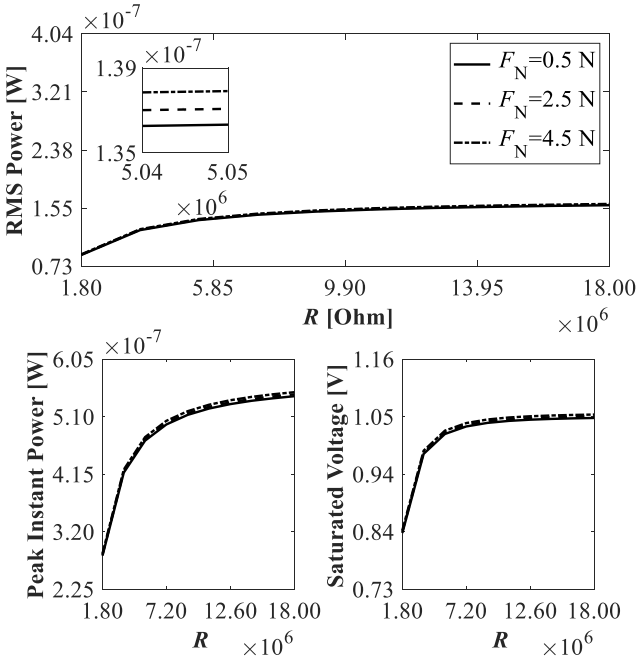

(b)

Figure 4-11 RMS charging power with different C_s and different R. (a) R = 1.8 MΩ. (b) C_s = 3e^{-7} F.

Figure 4-12(a) depicts energy generation performance with the increase in sliding velocity v_0 under R = 36 MΩ conditions while charging a storage capacitor C_s = 300 nF. And the following parameters are used: m_{eq} = 0.0062 kg, ζ = 1e^{-6}, k_l = 4553.2977 N/m, μ_k = 0.42, μ_{static} = 0.62, C

= 4.2, A_p = 2.5e^{-5} m^2, t_p = 0.0005 m, and α = 0.059812 V/N. The RMS charging power, peak instant charging power, and saturated voltage increase with the increase of v_0. The reason could be that the larger v_0 increase the amplitude of vibration system and, consequently, the shear deformation of the piezoelectric patch and voltage output. Considering the better fabrication of the experimental test setup, there is less influence on the bonding interface between parts, and the small blocks are solid. Figure 4-12(b) demonstrates energy generation performance with the increase of the tuning factor θ_p under R = 36 MΩ conditions while charging a storage capacitor C_s = 300 nF. The poor connection between different parts and the imperfect fabrication of piezoelectric material will affect voltage response from piezoelectric material, and these factors are complicated to include in theoretical modeling. For a better representation of the actual performance of the prototype, a tuning factor θ_p, which is used to adjust the force factor α, is defined. From Eq. (2.17), it can be seen that θ_p is related to the force factor α which is related to electromechanical coupling phenomenon of the system. With the increase of θ_p, α will be increased with improved electromechanical coupling effect, which will boost the energy output from piezoelectric material. If θ_p increases from 0.05 to 0.75 and F_N = 0.5 N, the RMS charging power increases from 164.10 nW to 36922.20 nW which represents a huge improve. When θ_p = 1, it represents a perfect experiment system with perfect rigid foundation and connection between the spring and piezo-patch.

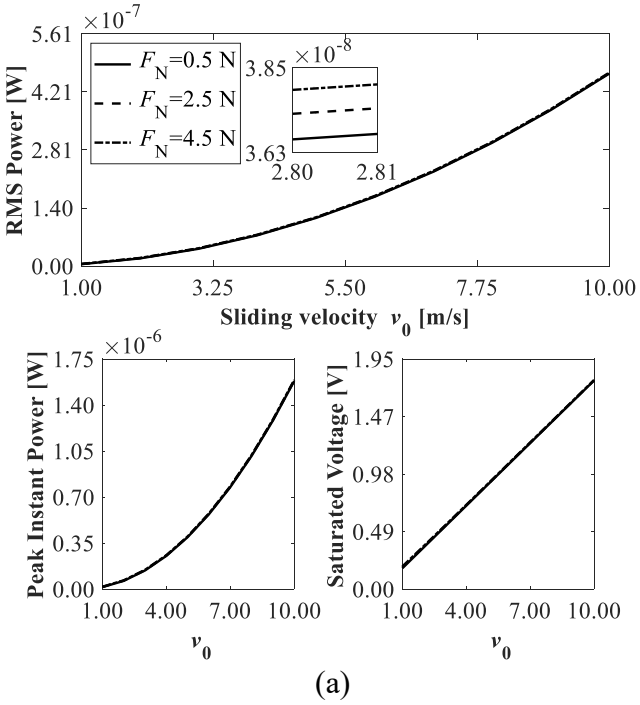

(a)

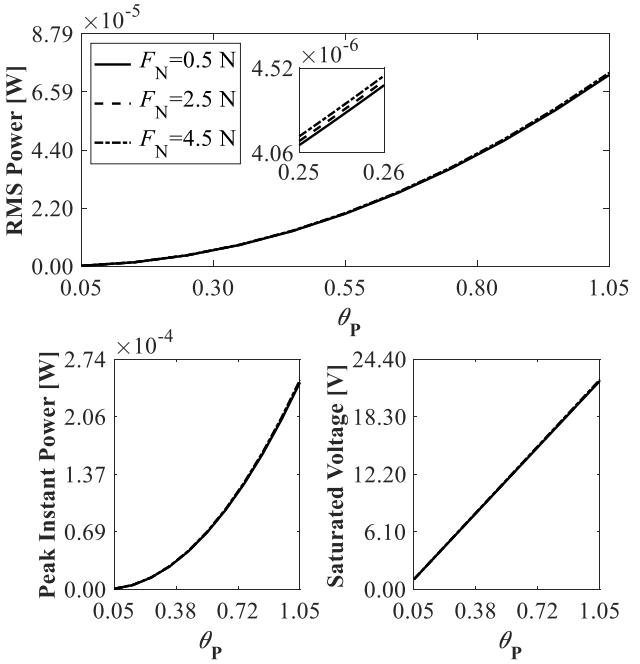

(b)

Figure 4-12 RMS charging power with different v_0 and θ_p. (a) α = 0.059812 V/N. (b) v_0 = 5.9376 m/s.

Figure 4-13(a) studies energy generation performance with the increase of the normal force F_{N} under R = 1.8, 9, 18 MΩ conditions while charging a storage capacitor C_{s} = 300 nF. And the following parameters are used: m_{eq} = 0.0062 kg, ζ = 1e^{-6}, k_{l} = 4553.2977 N/m, A_{p} = 2.5e^{-5} m^2,

t_p = 0.0005 m, and α = 0.059812 V/N. The RMS charging power, peak instant charging power, and saturated voltage increase with the increase of F_N. The reason could be that the larger F_N increase the amplitude of excitation and, consequently, the voltage output seen from the variation of saturated voltage. Based on equations demonstrating the stick-slip transition described in Section 2.3, the stick-slip frequency may be reduced with the increase of the normal force F_N. However, the simulation result of RMS charging power indicates that the increased voltage output outperforms the reduced stick-slip frequency, which suggests that larger F_N can be beneficial for energy generation. An obvious phenomenon regarding charge dissipation happened on R can be found from the simulation result of RMS charging power that the difference in RMS charging power under the same F_N but different R is noticeable. While F_N = 10 N and R = 1.8, 9, 18 MΩ, the RMS charging powers are 90.80 nW, 154.49 nW, and 163.95 nW, respectively. The value is getting closer with the increase of R which brings the circuit close to an open-circuit condition, but the effect of charge dissipation with small R is worth noticing and designing a better charging circuit for storing generated energy is necessary.

Figure 4-13(b) discusses energy generation performance with the increase of exponential decay factor C which represents decaying effect of $\mu_{slide}(v_r)$, under different F_N conditions while charging a storage capacitor C_s = 300 nF. And the following parameters are used: m_{eq} = 0.0062 kg, ζ = 1e^{-6}, k_l = 4553.2977 N/m, A_p = 2.5e^{-5} m^2, t_p = 0.0005 m, and α = 0.059812 V/N. The larger the value of C, the faster conversion from μ_{static} to $\mu_{slide}(v_r)$, and based on Eq. (2.8), $\mu_{slide}(v_r)$ fluctuate around μ_k in the sliding state. It can be seen from Figure 4-13(b) that the RMS charging power, peak instant charging power, and saturated voltage grow gradually with the increase of C. The reason for the difference before C reaches 5 can be the slow conversion from μ_{static} to $\mu_{slide}(v_r)$ which means that there is a longer time period of stick-slip transition and the friction amplitude in this period is higher than the sliding state. Generally, C does not have significant effect on system energy generation performance.

Figure 4-13(c) and (d) illustrate energy generation performance with the increase of dynamic friction coefficient μ_k and static friction coefficient μ_{static}, separately. And the following parameters are used: m_{eq} = 0.0062 kg, ζ = 1e^{-6}, k_l = 4553.2977 N/m, A_p = 2.5e^{-5} m^2, t_p = 0.0005 m, and α = 0.059812 V/N. It is shown in Figure 4-13(c) that the RMS charging power, peak instant charging power, and saturated voltage grow gradually with the increase of μ_k, and the

difference in the early stage can also be the slow conversion from μ_{static} to $\mu_{\mathrm{slide}}(v_{\mathrm{r}})$ at the beginning. With the increase of μ_{k} and $\mu_{\mathrm{slide}}(v_{\mathrm{r}})$, the transition period is shortened and the energy generation process tends to be stable. Figure 4-13(d) displays the energy generation performance with the increase of μ_{static}, and it shows a slow linear increase in RMS charging power, peak instant charging power and saturated voltage. Larger F_{N} shows faster variation in the same increase range of μ_{static}. The larger μ_{static} and F_{N} contribute to higher friction force which leads to higher vibrational amplitude and consequently the shear deformation and voltage output.

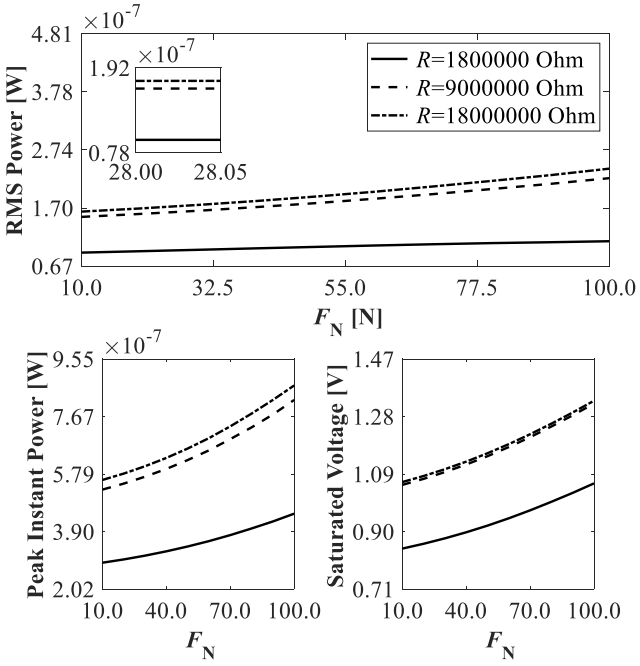

(a)

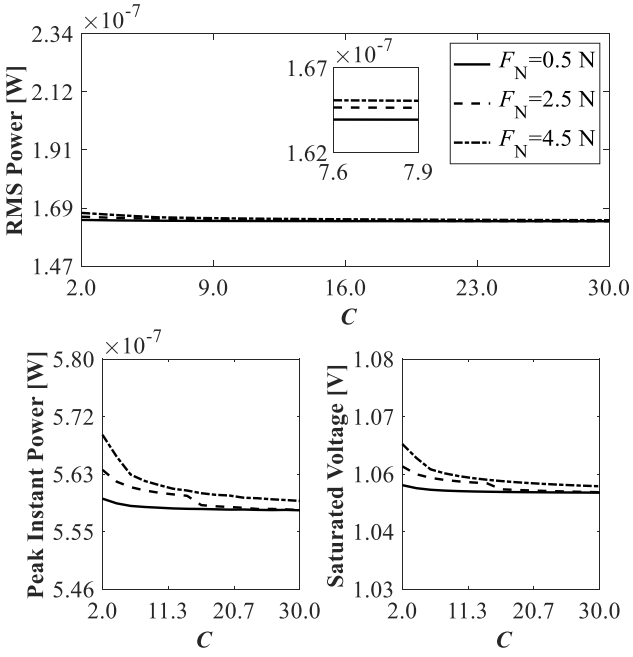
×10^-7
2.34
2.12
1.91
1.69
1.47
RMS Power [W]
1.67
1.62
7.6
7.9
F_N=0.5 N
F_N=2.5 N
F_N=4.5 N
2.0
9.0
16.0
23.0
30.0
C
×10^-7
5.80
5.72
5.63
5.55
5.46
Peak Instant Power [W]
2.0
11.3
20.7
30.0
C
1.08
1.07
1.06
1.04
1.03
Saturated Voltage [V]
2.0
11.3
20.7
30.0
C

(b)

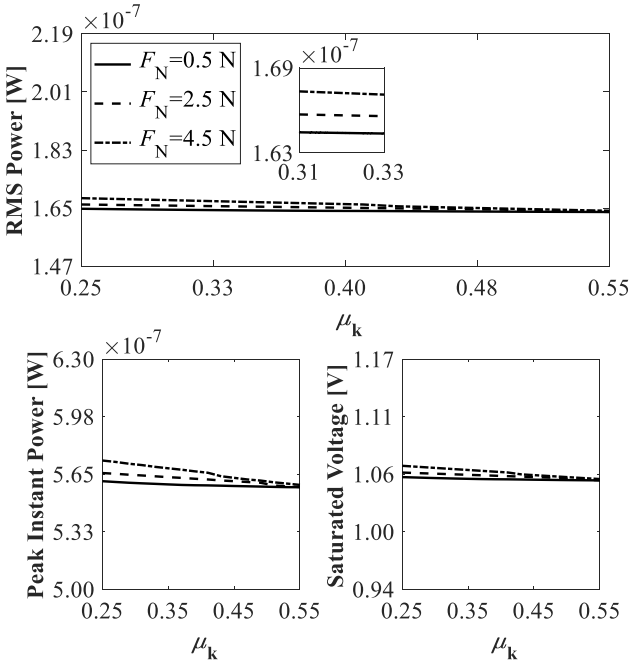
×10^-7
2.19
2.01
1.83
1.65
1.47
RMS Power [W]
F_N=0.5 N
F_N=2.5 N
F_N=4.5 N
1.69
1.63
0.31
0.33
0.25
0.33
0.40
0.48
0.55
μ_k
×10^-7
6.30
5.98
5.65
5.33
5.00
Peak Instant Power [W]
0.25
0.35
0.45
0.55
μ_k
1.17
1.11
1.06
1.00
0.94
Saturated Voltage [V]
0.25
0.35
0.45
0.55
μ_k

(c)

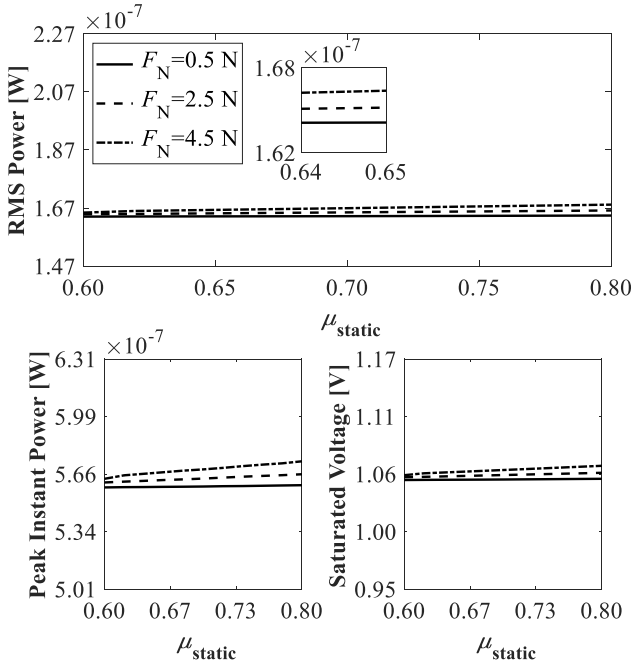

(d)

Figure 4-13 RMS charging power with different F_N, C, μ_k, and μ_{static}. (a) μ_k = 0.42, μ_{static} = 0.62, C = 4.2. (b) μ_k = 0.42, μ_{static} = 0.62, R = 36 MΩ. (c) μ_{static} = 0.62, C = 4.2, R = 36 MΩ. (d) μ_k = 0.42, C = 4.2, R = 36 MΩ.

The simulation result in Figure 4-8 demonstrates that the system can generate more energy with the increase of t_p. Two setups of connections for thick piezoelectric material can be expected for the current system design: mechanically in parallel and electrically in parallel, and mechanically in parallel but electrically in series. For d_{15} mode, shown in Figure 4-14(a), shear force is applied in direction 2, resulting in shear deformation in direction 5, while the poling direction of the piezoelectric material remains along direction 3, and the direction of electrode setup is orthogonal to the induced electrical potential along direction 1. As both setups are mechanically in parallel, the corresponding stiffness constants of piezoelectric material are the same. The electrically in parallel setup offers a larger electrode area with higher effective capacitance, and the electrically in series setup offers a smaller electrode area with lower effective capacitance because of the increased t_p and unchanged electrode area. And the following common parameters are used: m_{eq} = 0.0062 kg, ζ = 1e^{-6}, k_1 = 4553.2977 N/m, v_0 = 5.9376 m/s, μ_k = 0.42, μ_{static} = 0.62, C = 4.2, A_p = 2.5e^{-5} m^2, and C_s = 6e^{-7} F. With t_p = 0.0005 m and n_p = 5, which represent 5 pieces of 0.0005 m thick piezoelectric shear patch in parallel electrical connection, the RMS charging power in perfect experiment system with R = 1.8 MΩ and R = 36 MΩ are 0.335

mW and 0.336 mW, correspondingly. With t_p = 0.0025 m and n_p = 1, which represent 1 piece of 0.0025 m thick piezoelectric shear patch electrically in series connected, the RMS charging power with R = 1.8 MΩ and R = 36 MΩ are 0.250 mW and 0.294 mW, respectively. Assuming the saturated voltage on a storage capacitor C_s is less than the standard working voltage of capacitor, energy generation performance of the electrically in-parallel setup is better than that of the electrically in series setup. Moreover, in practical applications, an electrically in parallel setup is desired because it can decrease the output voltage to a convenient level. Also, the higher effective capacitance is essential for energy transfer.

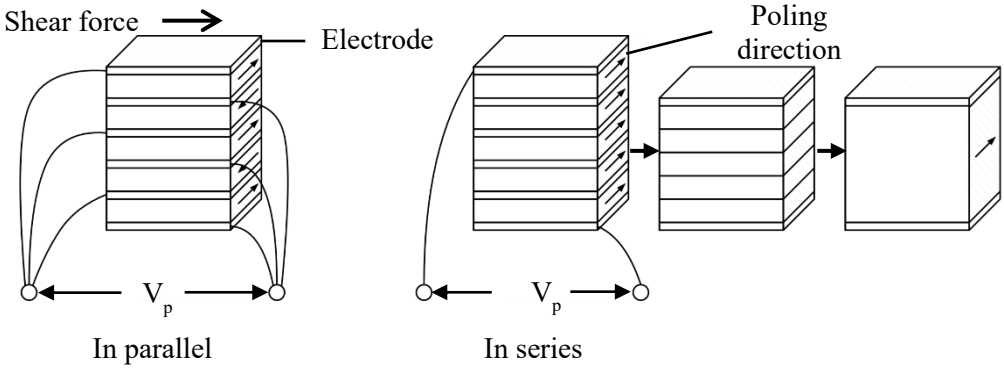

(a)

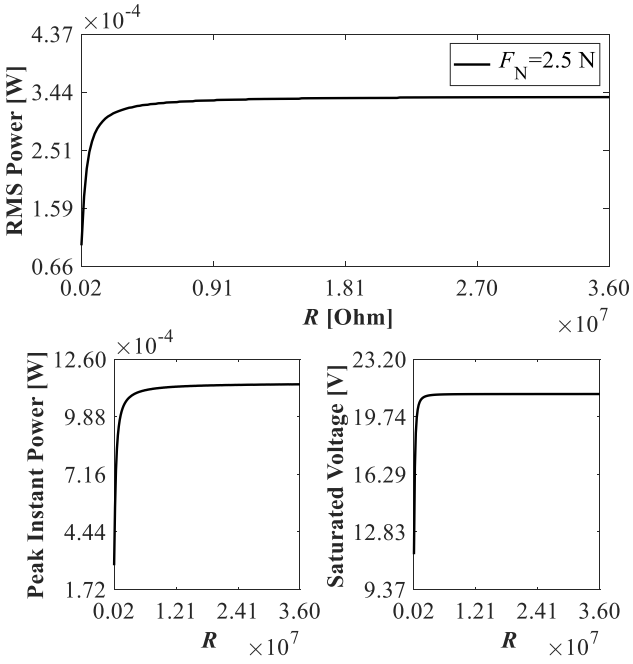

(b)

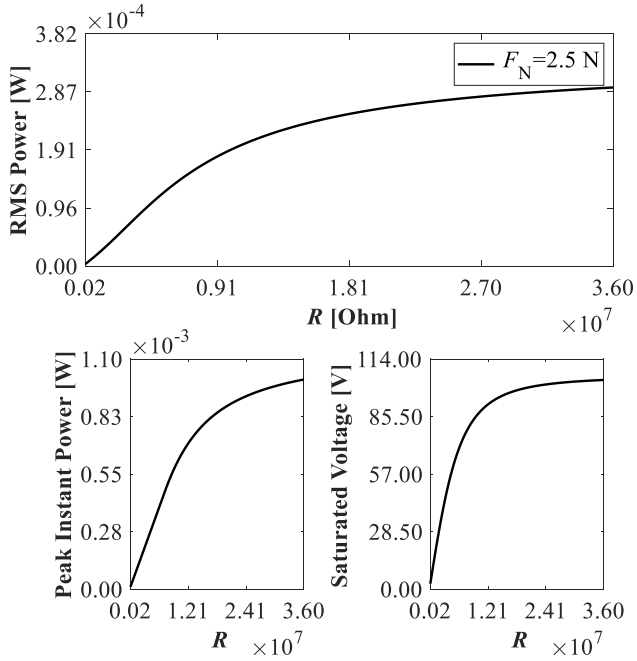

(c)

Figure 4-14 RMS charging power with electrically in parallel and in series connections. (a) Electrical connection. (b) In parallel (t_p = 0.0005 m, n_p = 5, α = 1.1962 V/N, and C_p = 4.2038e^{-9} F). (c) In series (t_p = 0.0025 m, n_p = 1, α = 0.23925 V/N, and C_p = 1.6815e^{-10} F).

Figure 4-15 compares the transient charging performance of the electrically in parallel and the electrically in series setups of PZT4 and PMN-PT under R = 36 MΩ conditions. And the following common parameters are used: m_eq = 0.0062 kg, ζ = 1e^{-6}, k_l = 4553.2977 N/m, v_0 = 5.9376 m/s, μ_k = 0.42, μ_static = 0.62, C = 4.2, A_p = 2.5 e^{-5} m^2, and C_s = 3 e^{-6} F. With the electrically in parallel setups, both of the saturated voltages are around 20 V, PMN-PT shows RMS charging power of 1.70 mW and peak instant charging power of 5.61 mW, PZT4 shows RMS charging power of 0.336 mW and peak instant charging power of 1.14 mW. With the electrically in series setups, both saturated voltages are around 100 V, PMN-PT shows RMS charging power of 1.61 mW and peak instant charging power of 5.54 mW, PZT4 shows RMS charging power of 0.29 mW and peak instant charging power of 1.00 mW. With the same amount of material and electrical connections, PMN-PT exhibits five times larger RMS charging power and peak instant charging power than PZT4 due to the high d_{15} and ε_{11} values.

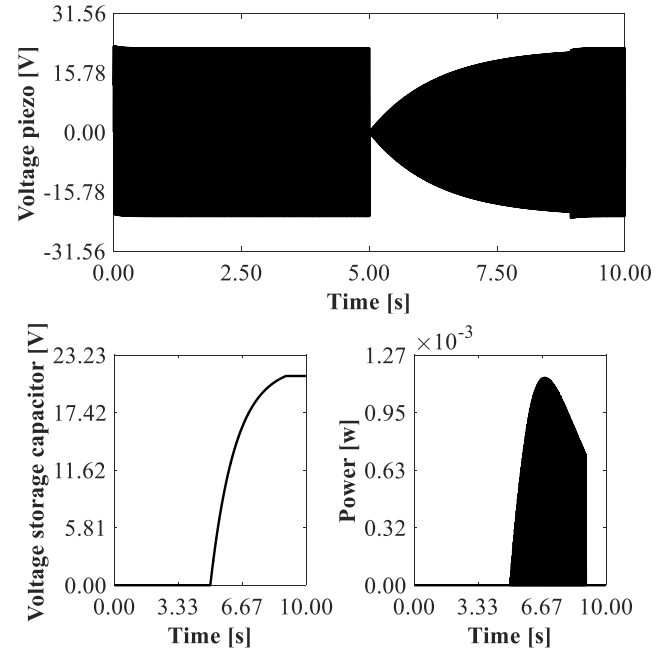
31.56
15.78
0.00
-15.78
-31.56
Voltage piezo [V]
0.00
2.50
5.00
7.50
10.00
Time [s]
23.23
17.42
11.62
5.81
0.00
Voltage storage capacitor [V]
0.00
3.33
6.67
10.00
Time [s]
×10-3
1.27
0.95
0.63
0.32
0.00
Power [w]
0.00
3.33
6.67
10.00
Time [s]

(a)

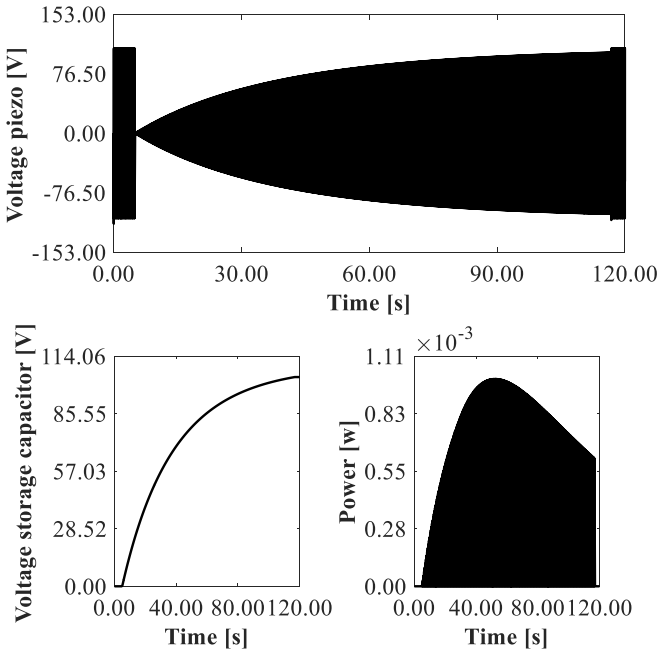
153.00
76.50
0.00
-76.50
-153.00
Voltage piezo [V]
0.00
30.00
60.00
90.00
120.00
Time [s]
114.06
85.55
57.03
28.52
0.00
Voltage storage capacitor [V]
0.00
40.00
80.00
120.00
Time [s]
×10-3
1.11
0.83
0.55
0.28
0.00
Power [w]
0.00
40.00
80.00
120.00
Time [s]

(b)

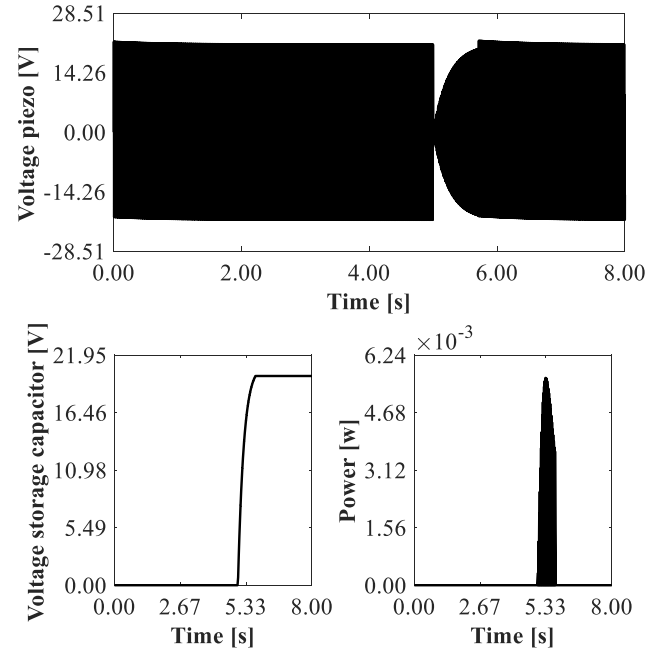

(c)

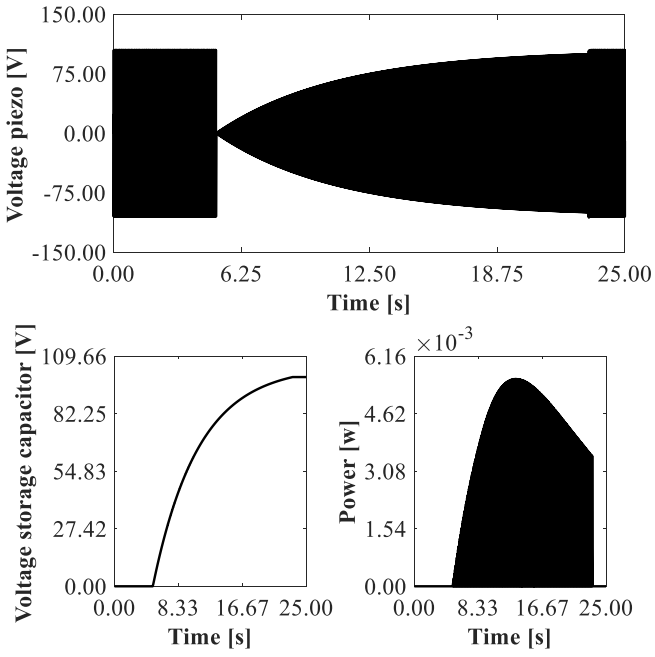

(d)

Figure 4-15 RMS charging power with different piezoelectric materials. (a) In parallel (APC 850). (b) In series (APC 850). (c) In parallel (PMN-PT). (d) In series (PMN-PT).

4.3.2 Summary and discussion

This study proposed a novel shear mode piezoelectric energy generation system employing friction. A mathematical model incorporating piezoelectric coupling is developed to accurately predict the dynamic vibration response and voltage output. The energy generation performance is evaluated through transient charging simulations of a storage capacitor. Various factors influencing the energy generation performance, such as dimensional parameters of the piezoelectric patch, vibration system parameters, friction model parameters, methods of electrical connections, and different piezoelectric materials, are discussed.

The results indicate that the energy generation performance can be enhanced by increasing the thickness of the piezoelectric patch t_{p}, the stiffness of the linear tension spring k_{l}, the electric resistance R, the velocity of the friction plate v_0, the force factor α, the normal force F_{N}, the static friction coefficient μ_{static}, as well as improving the piezoelectric coefficient d_{15} and permittivity ε_{11}. Conversely, the equivalent mass of the system m_{eq}, the storage capacitor C_{s}, the exponential decay factor C, and the dynamic friction coefficient μ_{k} have negligible effects on the energy generation performance. Under ideal experimental conditions, utilizing a PZT4 piezoelectric material with a volume of $0.005 \times 0.005 \times 0.0025 = 6.25\mathrm{e}^{-8}$ m^3, RMS charging power of 0.336 mW and 0.294 mW can be achieved through electrically in-parallel and in-series setups, respectively. This corresponds to power densities of $5.38\mathrm{e}^{3}$ Wm^{-3} and $4.70\mathrm{e}^{3}$ Wm^{-3}. By replacing PZT4 with single crystal PMN-PT, which has a higher piezoelectric coefficient, RMS charging power of 1.70 mW in the electrically in-parallel setup and 1.61 mW in the electrically in-series setup can be obtained, resulting in power densities of $2.72\mathrm{e}^{4}$ Wm^{-3} and $2.58\mathrm{e}^{4}$ Wm^{-3}, respectively.

Further improvements in energy generation performance, such as increasing the amount of piezoelectric material and incorporating multiple generators for simultaneous charging, may potentially realize RMS charging power outputs close to the watt-level. Additionally, the integration of a similar generator into vehicle braking systems can harness wasted energy and provide a power supply for low-power wireless electrical devices.

Chapter 5 Piezoelectric energy generation using FIV under bi-linear and impact conditions

In this chapter, a novel piezoelectric energy generator with linear, bi-linear, and impact design configurations is proposed. The reliability of the model and the stable high-frequency FIV phenomenon with linear, bi-linear, and impact design configurations are validated by experiment. Furthermore, parameter studies are conducted to investigate their effects on the efficiency and effectiveness of energy generation. The modeling methods depicted in Sections 2.1, 2.2, 2.3, and 2.6 are utilized in this chapter.

5.1 Schematic diagram of testing rig and energy generators

In this work, a longitudinal mode (d_{33}) piezoelectric energy generator with different configurations is mounted on a self-designed testing rig. The schematic of the testing rig is shown in Figure 5-1(a). In the test setup, the three-phase motor provides power to the built-in shaft, and a variable frequency drive (VFD) module is connected to the motor to control the rotating rpm. A friction plate, which is used to provide friction excitation to the energy generator, is mounted on the shaft. The energy generator is installed on a mounting structure made from aluminum angle iron. A load cell is installed on the other end of the mounting structure to measure the normal load. The detail of the energy generator with different configurations is depicted in Figure 5-1(b), (c), and (d). Apart from the special designed bi-linear and impact structures, the common components of the three configurations are a compression spring, a mass block with a friction plate mounted on the top, and a piezoelectric material with a protection layer fixed at the left end. Figure 5-1(c), and (d) showed the bi-linear and impact configurations, respectively. The bi-linear design includes a nested spring, and the impact design has a solid column whose stiffness is assumed to be much bigger than the compression spring. An oscilloscope is used to measure the generated voltage from the piezoelectric material during FIV. The corresponding equivalent lumped parameter models are shown in the bottom of Figure 5-1(b), (c), and (d).

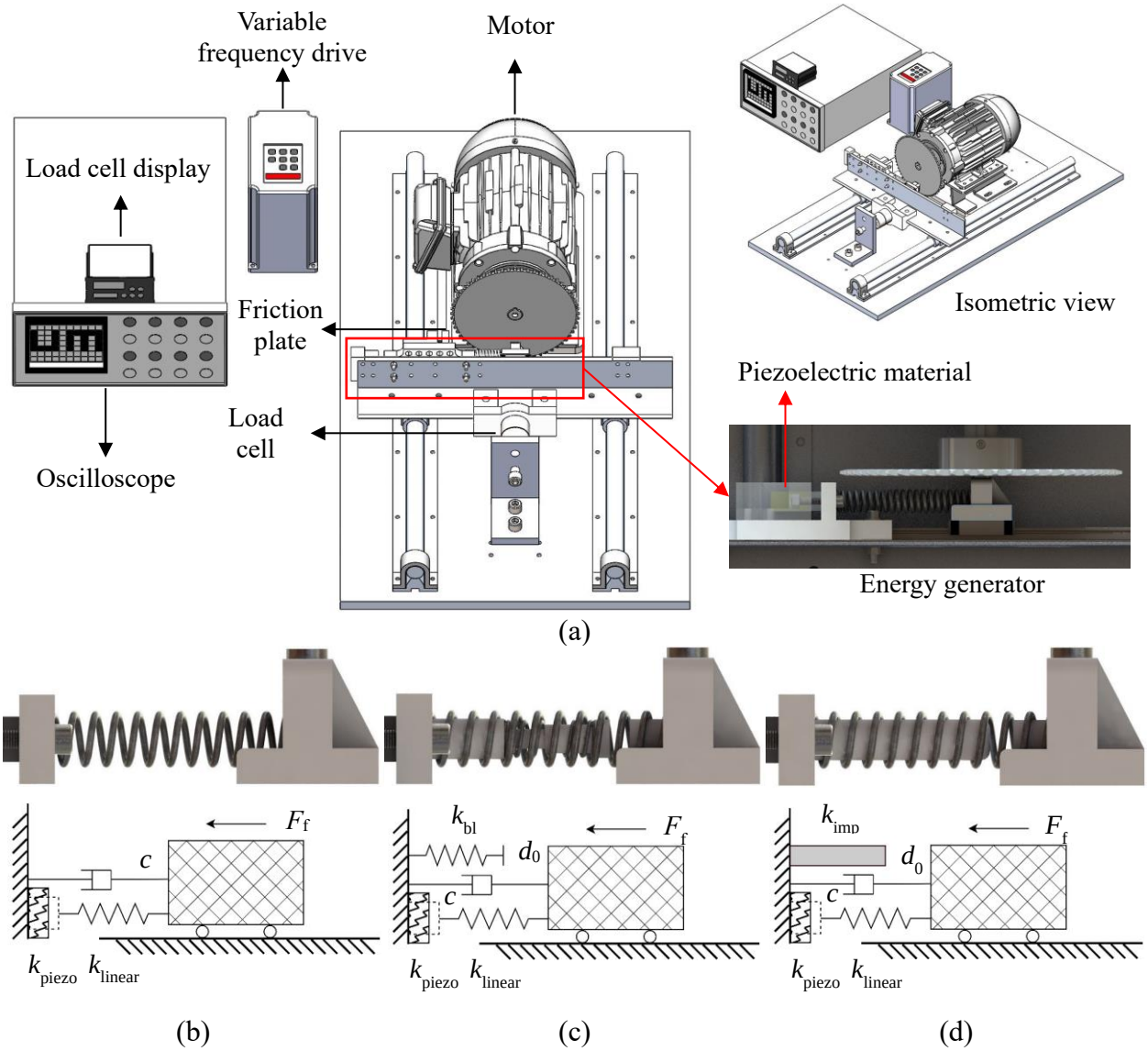

Figure 5-1 Schematic diagram of the testing rig and energy generators. (a) Schematic of the testing rig. (b) Linear generator. (c) Bi-linear generator. (d) Impact generator.

5.2 Energy generation

5.2.1 Governing equations of systems under linear, bi-linear, and impact conditions

The mechanical and piezoelectric coupling equation of the system under linear spring can then be written as,

$$\begin{cases} m_{\mathrm{eq}}\ddot{y}(t) + c\dot{y}(t) + k_{\mathrm{eq}}y(t) + \alpha\dfrac{k_{\mathrm{linear}}}{k_{\mathrm{linear}} + k_{\mathrm{piezo}}}V_{\mathrm{R}}(t) = F_{\mathrm{f}}(t) \\ V_{\mathrm{R}}(t) + RC_{\mathrm{p}}\dot{V}_{\mathrm{R}}(t) - R\alpha\dfrac{k_{\mathrm{linear}}}{k_{\mathrm{linear}} + k_{\mathrm{piezo}}}\dot{y}(t) = 0 \end{cases}, \tag{5.1}$$

where m_{eq} is the equivalent mass of the vibration system; $c = 2\zeta\sqrt{k_{\mathrm{eq}}m_{\mathrm{eq}}}$ is the damping coefficient and ζ is the damping ratio; k_{eq} is the equivalent stiffness of the system; k_{piezo} is the stiffness constant of the piezoelectric patch; k_{linear} is the linear spring stiffness; $F_{\mathrm{f}}(t)$ is the friction force applied to the mass block; $y(t)$ is the vibration response of the mass block under friction force; $V_{\mathrm{R}}(t)$ is the actual output voltage from the piezoelectric material after considering the charging dissipation in electric resistance; R is electric resistance; C_{p} is the capacitance of the piezoelectric patch; and α is the force factor.

For the bi-linear design configurations, the induced nonlinear force is described by a piecewise linear function as,

$$F_{\mathrm{bl}}(t) = \begin{cases} k_{\mathrm{bl}}(y(t) - d_0), & y(t) \le d_0 \\ 0, & y(t) > d_0 \end{cases}, \tag{5.2}$$

The induced nonlinear force of the impact design configuration is expressed as,

$$F_{\mathrm{imp}}(t) = \begin{cases} k_{\mathrm{imp}}(y(t) - d_0), & y(t) \le d_0 \\ 0, & y(t) > d_0 \end{cases}, \tag{5.3}$$

where d_0 is the initial separation distance, and it is shown in Figure 5-1(c) and (d); k_{bl} and k_{imp} are the corresponding piecewise linear stiffness, and they are equal to zero if $y(t) > d_0$. And the mechanical and piezoelectric coupling equation of the system under bi-linear and impact configurations can be written as,

$$\begin{cases} m_{\mathrm{eq}}\ddot{y}(t) + c\dot{y}(t) + k_{\mathrm{eq}}y(t) + F_{\mathrm{bl}}(t) + \alpha\dfrac{k_{\mathrm{linear}} + k_{\mathrm{bl}}}{k_{\mathrm{linear}} + k_{\mathrm{bl}} + k_{\mathrm{piezo}}}V_{\mathrm{R}}(t) = F_{\mathrm{f}}(t) \\ V_{\mathrm{R}}(t) + RC_{\mathrm{p}}\dot{V}_{\mathrm{R}}(t) - R\alpha\dfrac{k_{\mathrm{linear}} + k_{\mathrm{bl}}}{k_{\mathrm{linear}} + k_{\mathrm{bl}} + k_{\mathrm{piezo}}}\dot{y}(t) = 0 \end{cases}, \tag{5.4}$$

$$\begin{cases} m_{\mathrm{eq}}\ddot{y}(t) + c\dot{y}(t) + k_{\mathrm{eq}}y(t) + F_{\mathrm{imp}}(t) + \alpha\dfrac{k_{\mathrm{linear}} + k_{\mathrm{imp}}}{k_{\mathrm{linear}} + k_{\mathrm{imp}} + k_{\mathrm{piezo}}}V_{\mathrm{R}}(t) = F_{\mathrm{f}}(t) \\ V_{\mathrm{R}}(t) + RC_{\mathrm{p}}\dot{V}_{\mathrm{R}}(t) - R\alpha\dfrac{k_{\mathrm{linear}} + k_{\mathrm{imp}}}{k_{\mathrm{linear}} + k_{\mathrm{imp}} + k_{\mathrm{piezo}}}\dot{y}(t) = 0 \end{cases}. \tag{5.5}$$

The detail iterative solving process is depicted in Section 2.3.

5.2.2 Experimental verification of voltage output and charging process

The experimental setup incorporates an oscilloscope (DSO6014A) with an internal resistance of R = 1 MΩ, which is used for data acquisition. To provide power and regulate the input revolutions per minute (rpm) of the rotating shaft, a three-phase motor (WEG CT002404NPW22) and a VFD module (CFW500B07P3B2DBN1H00) are employed. Throughout the testing procedure, the separation distance between the center of the friction layer of the mass block and the shaft, referred to as $d_{\text{m-s}}$, is measured to be 57.5 mm. The velocity v_0 during the FIV process is determined using the relationship $v_0 = 0.1047 N d_{\text{m-s}}$, where N denotes the rotating speed of the shaft in rpm. The conversion factor 0.1047 is derived from $0.1047 = 2\pi/60$, enabling the conversion of rpm to rad/s. To ensure consistent test conditions, the contact interfaces between the rotating friction plate and the friction layer of the mass block will be cleaned before each test. For the charging experiment, a conventional charging circuit shown in Figure 5-3(b) will be employed. It should be noted that the current study investigates the mechanism of FIV in a 1DOF PEG with bi-linear and impact design configurations and explored its energy generation performance. A motor is employed to generate and maintain a stable sliding motion. Therefore, a motor is used for representation in the structural diagram and experimental setup. The motor is not the energy source for the PEG to harvest energy for practical applications. Additionally, in practical applications, using proper materials with enhanced properties is essential to reduce wear and ensure a longer lifespan.

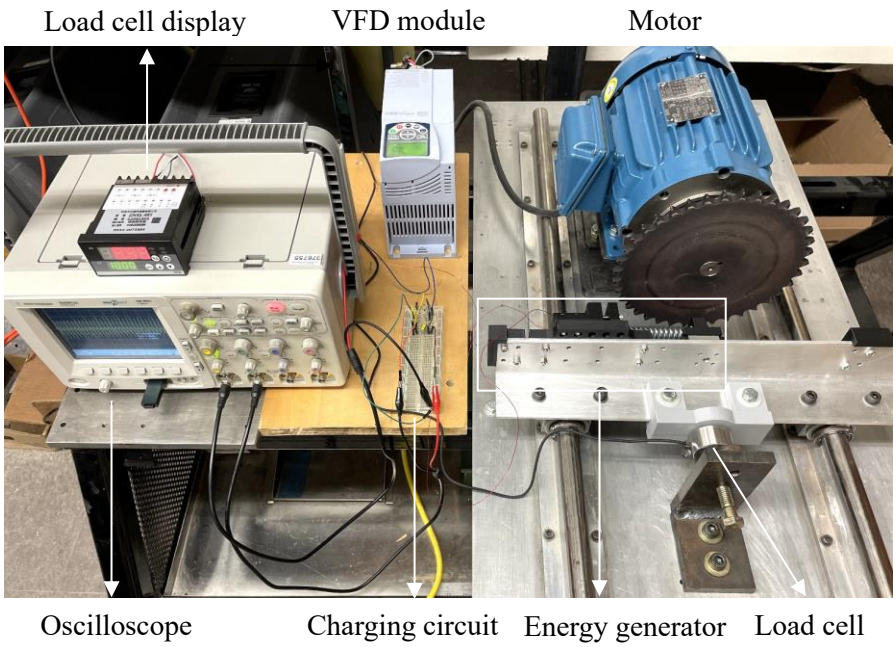

Figure 5-2 Overall setup of the system.

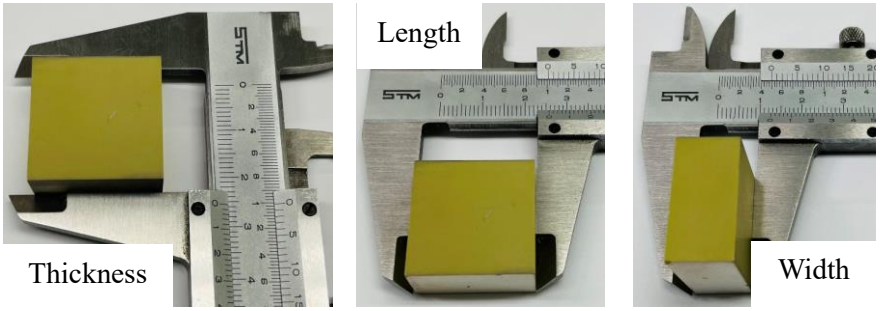

(a)

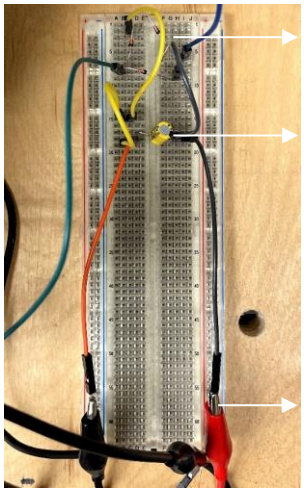

(b)

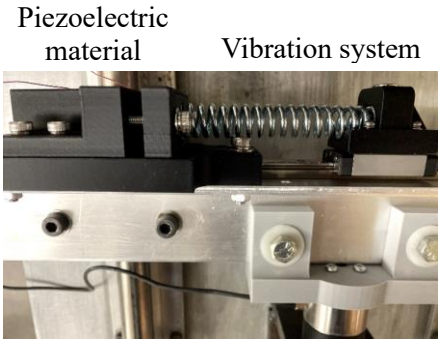

(c)

Figure 5-3 Piezoelectric material, charging circuit, and energy generator. (a) Piezoelectric material. (b) Charging circuit. (c) Energy generator.

The influence of bonding between parts in theoretical modeling considers challenging, and in this study, it is assumed to be rigid connections and disregarding structural vibration effects. Figure 5-4 compares output voltage in the time domain between experimental and simulated results at varying rotating speeds. Figure 5-4(a) and (d), (b) and (e), and (c) and (f) depict the linear, bi-linear, and impact design configurations, respectively. And the following common parameters are used: m_{eq} = 0.125 kg, ζ = 1e^{-4}, k_{l} = 5428 N/m, μ_{k} = 0.2, μ_{static} = 0.5, C = 4.3, A_{p} = 3.226e^{-4} m^2, t_{p} = 0.0254 m, and α = 0.564 V/N. The simulated output voltage is calculated after considering the charge dissipation in the energy generation system when connected to the oscilloscope, and a resistance value of R = 1 MΩ is employed. Notably, the impact stiffness k_{imp} from the rod is tuned to simulate the equivalent stiffness after impact due to the possible imperfect rigid setup and structural vibration. In this study, the solid rod for simulating impact is 3D printed with polylactic acid (PLA) at 100% infill. The temporal voltage outputs from simulations match with the experimental results, indicating the accuracy and efficacy of the voltage output calculation.

The experimental findings for the linear design configuration reveal the occurrence of approximately six vibration peaks within a time span of 0.2 s. This observation indicates the system vibrates at a frequency of around 30 Hz which is close to its natural frequency (~30 Hz). It also substantiates the feasibility of inducing continuous high-frequency vibrations through friction. In the case of the bi-linear and impact design configurations, a discernible peak emerges during the vibration cycle, which can be attributed to the effects of bi-linear and impact contacts. This phenomenon can possibly enhance piezoelectric energy generation compared to the linear configuration.

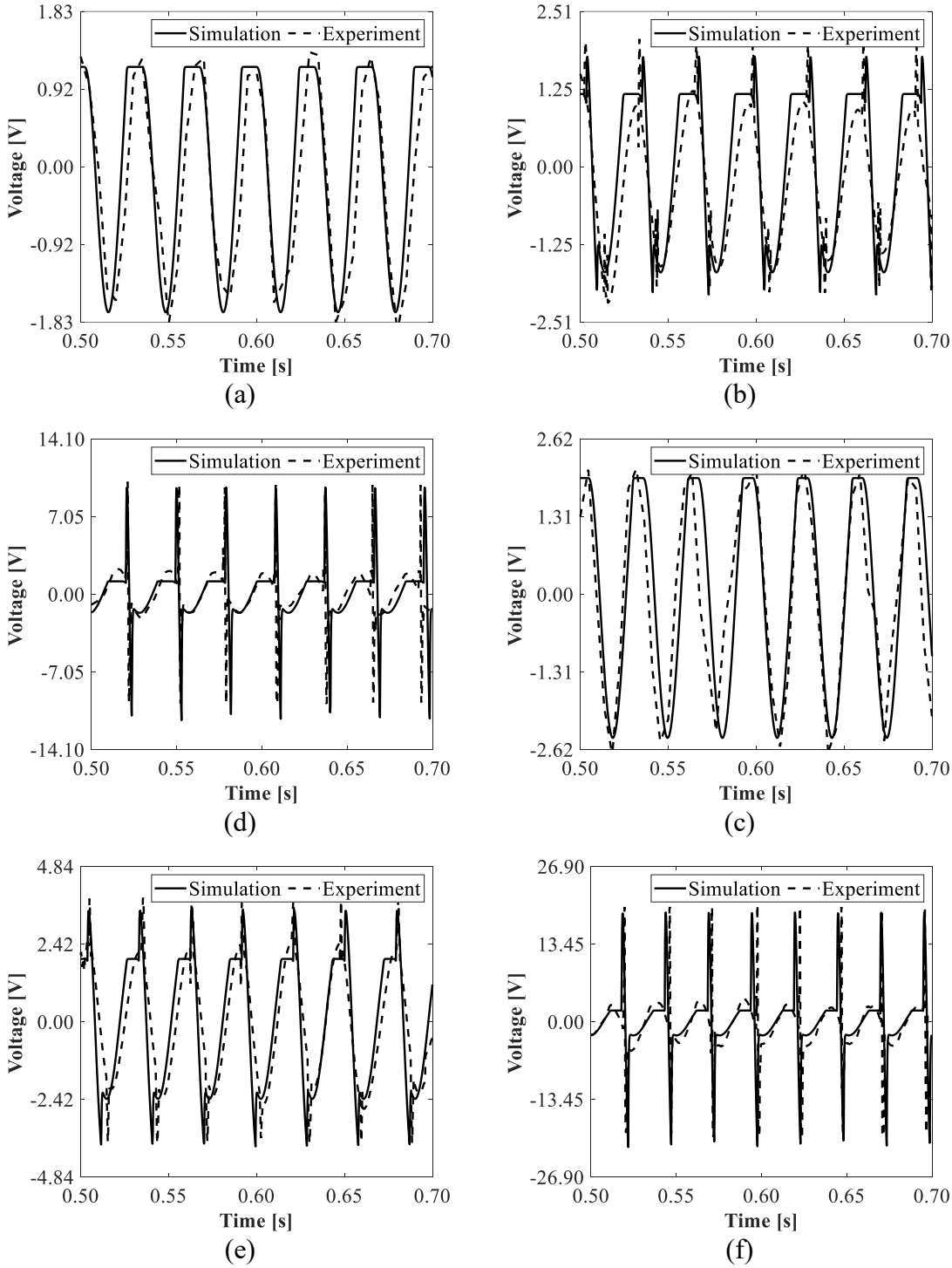

Figure 5-4 Comparison of output voltage from experiments and simulations under different sliding velocities v_0 during friction. (a) Linear (F_N = 30 N and v_0 = 0.542 m/s). (b) Bi-linear (F_N = 30 N, v_0 = 0.542 m/s, and k_{bl} = 4553 N/m). (c) Impact (F_N = 30 N, v_0 = 0.542 m/s, and k_{imp} = 58351 N/m). (d) Linear (F_N = 30 N and v_0 = 0.903 m/s). (e) Bi-linear (F_N = 30 N, v_0 = 0.903 m/s, and k_{bl} = 4553 N/m). (f) Impact (F_N = 30 N, v_0 = 0.903 m/s, and k_{imp} = 58351 N/m).

Figure 5-5 compares the voltage on the storage capacitor C_s during the charging process under varying rotating speeds. Charging curves corresponding to the linear, bi-linear, and impact configurations are presented in Figure 5-5(a) and (d), (b) and (e), and (c) and (f), respectively. And the following common parameters are used: m_{eq} = 0.125 kg, ζ = 1e^{-4}, k_l = 5428 N/m, μ_k = 0.2, μ_{static} = 0.5, C = 4.3, A_p = 3.226e^{-4} m^2, t_p = 0.0254 m, α = 0.564 V/N, and C_s = 10e^{-6} F. The switch shown in Figure 5-3(b) closes at T = 5 seconds to ensure the system reaching a steady state. The results depicted in Figure 5-5(a), (b), and (c) indicate that, with F_N = 30 N and v_0 = 0.542 m/s, the minimum voltages among the three design configurations reach approximately 1 V. Notably, both the linear and bi-linear design configurations display a tendency to reach a saturation voltage level, whereas the impact design configuration exhibits an upward trend. The outcomes in Figure 5-5(d), (e), and (f) reveal that, under the conditions of F_N = 30 N and v_0 = 0.903 m/s, the minimum voltages among the three design configurations reach approximately 1.75 V. The experimental charging curves exhibit some discernible fluctuations, likely attributed to loose connections within the charging circuit and the influence of structural vibrations. Overall, the simulation results align well with the experiments.

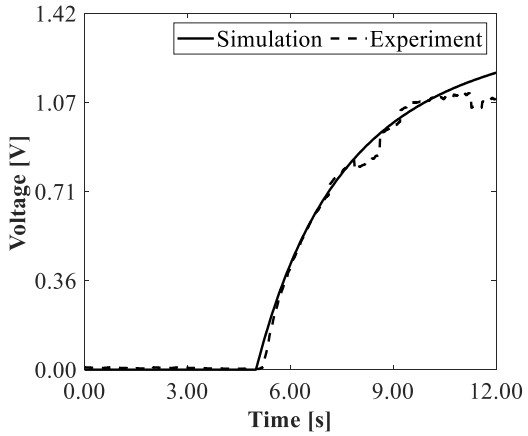

(a)

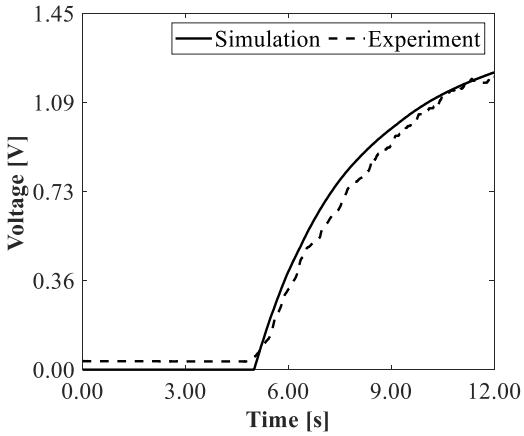

(b)

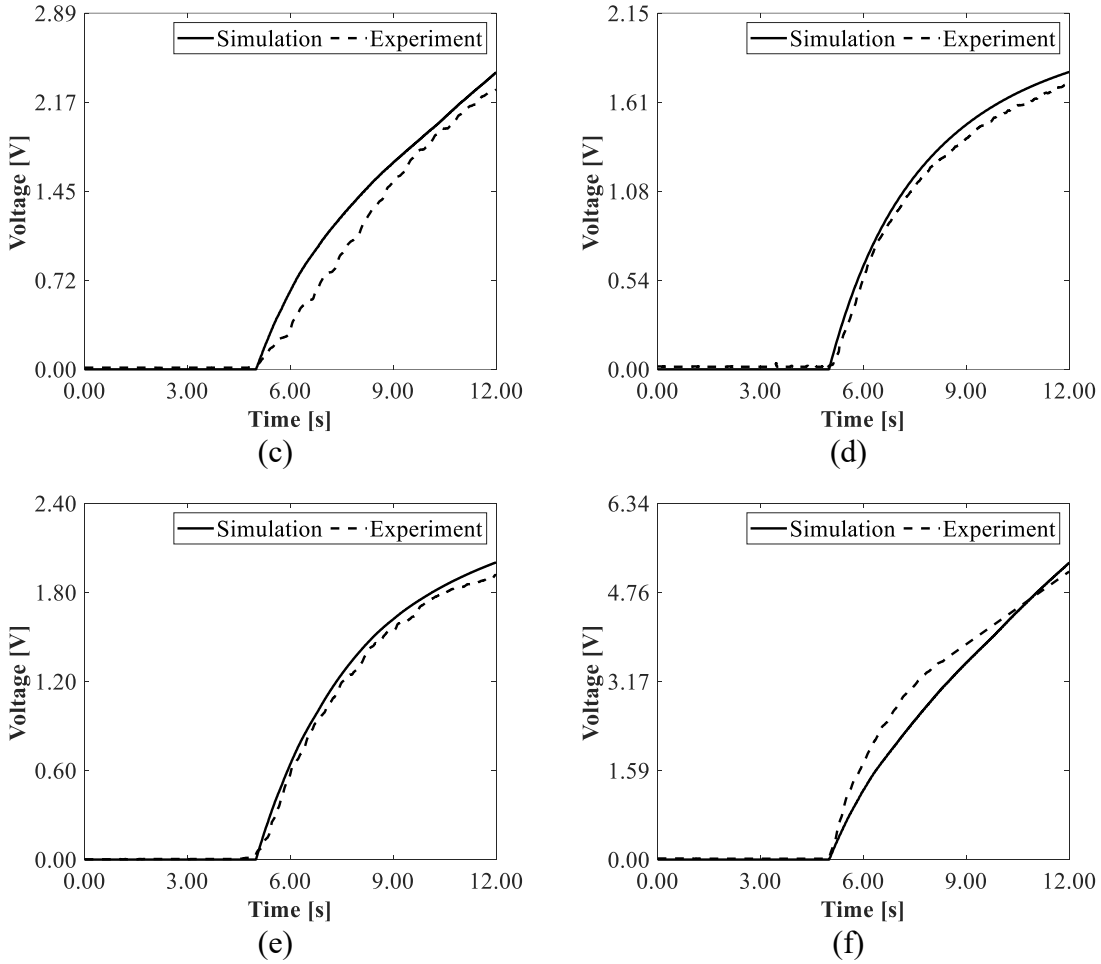

Figure 5-5 Comparison of charging output from experiments and simulations under different sliding velocities v_0 during FIV. (a) Linear (F_N = 30 N and v_0 = 0.542 m/s). (b) Bi-linear (F_N = 30 N, v_0 = 0.542 m/s, and k_{bl} = 4553 N/m). (c) Impact (F_N = 30 N, v_0 = 0.542 m/s, and k_{imp} = 58351 N/m). (d) Linear (F_N = 30 N and v_0 = 0.903 m/s). (e) Bi-linear (F_N = 30 N, v_0 = 0.903 m/s, and k_{bl} = 4553 N/m). (f) Impact (F_N = 30 N, v_0 = 0.903 m/s, and k_{imp} = 58351 N/m).

5.3 Parameter studies and discussion

In this section, we investigate the influences of the equivalent mass, spring stiffness, and initial separation distance of the corresponding systems on energy generation performance. The effect of the dimensional properties of piezoelectric material has been studied in previous literature. The investigation aims to provide insights into the underlying mechanisms governing the behavior of the corresponding energy generation systems, thereby aiding in improving the performance. The parameters listed in Table 5-1 will be used as the control parameters for studies.

Table 5-1 System parameters.

	Linear	Bi-linear	Impact
Equivalent mass m_{eq} (kg)	0.125	0.125	0.125
Damping ratio ζ	1e^{-4}	1e^{-4}	1e^{-4}
Linear spring stiffness k_{l} (N/m)	5428	5428	5428
Bi-linear spring stiffness k_{bl} (N/m)	-	4553	-
Impact stiffness k_{imp} (N/m)	-	-	58351
Initial separation distance d_0 (m)	-	0.004	0.004
Kinetic friction coefficient μ_{k}	0.2	0.2	0.2
Static friction coefficient μ_{static}	0.5	0.5	0.5
Exponential decay factor C	4.3	4.3	4.3
Sliding velocity v_0 (m/s)	0.723	0.723	0.723
Normal force F_{N} (N)	20, 30, 40	20, 30, 40	20, 30, 40
Equivalent resistance R (Ohm)	1000000	1000000	1000000
Cross-sectional area of PZT A_{p} (m^2)	3.226e^{-4}	3.226e^{-4}	3.226e^{-4}
Thickness of PZT t_{p} (m)	0.0254	0.0254	0.0254
Force factor α (V/N)	0.564	0.564	0.564
Capacitance of PZT C_{p} (F)	2.136e^{-10}	2.136e^{-10}	2.136e^{-10}
Storage capacitor capacitance C_{s} (F)	10e^{-6}	10e^{-6}	10e^{-6}

5.3.1 Parameter studies

Figure 5-6 shows the effect of the equivalent mass m_{eq} on the RMS charging power and the peak instant charging power under different normal load F_{N} conditions. The other parameters of the systems remain the same. Figure 5-6(a) demonstrates that, with fully charging the storage capacitor C_{s}, the RMS charging power and peak instant charging power decrease as m_{eq} increases. Figure 5-6(d) reveals that, during a 10-second charging period, the RMS charging power and voltage on the storage capacitor V_{s} similarly decrease with increasing m_{eq}. These results indicate that, in the linear design configuration, an increase in m_{eq} negatively affects energy generation. In Figure 5-6(b), it shows that the RMS charging power and peak instant charging power initially decrease and then increase as m_{eq} increases. This trend is also observed in Figure 5-6(e). This can be due to the fact that the bi-linear effect does not contribute to energy generation under small equivalent mass and normal load conditions, resulting in the system closely resembling the linear design configuration. However, the transiting point indicates the more obvious bi-linear effect, which can be advantageous for energy generation. The transition point moves towards smaller m_{eq}

values with increasing normal load. It is shown in Figure 5-6(c) that the RMS charging power and the peak instant charging power exhibit an initial flat followed by an increase with the increase of m_{eq}. Similar behavior is observed in Figure 5-6(f). This can be attributed to the fact that under small equivalent mass and normal load conditions, the impact effect has limited effect on energy generation. Consequently, the system behavior aligns closely with the linear design configuration. For the impact design configuration, a transition point also exists, shifting towards a smaller m_{eq} values with increasing normal load. Beyond this point, an increase in m_{eq} becomes advantageous for energy generation.

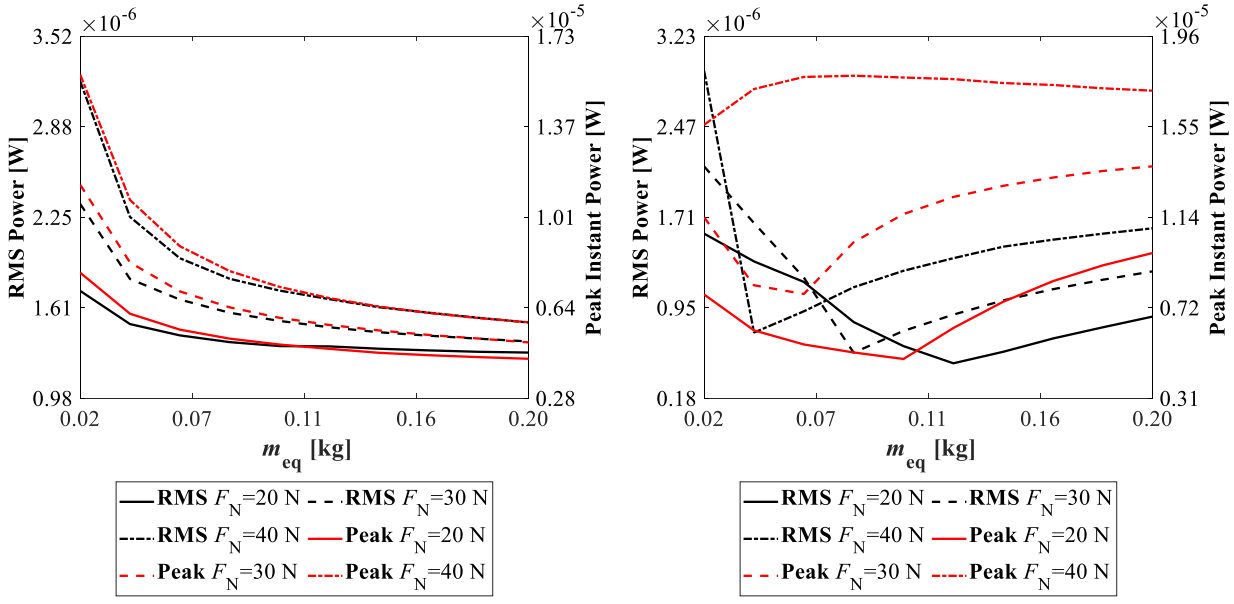

(a) (b)

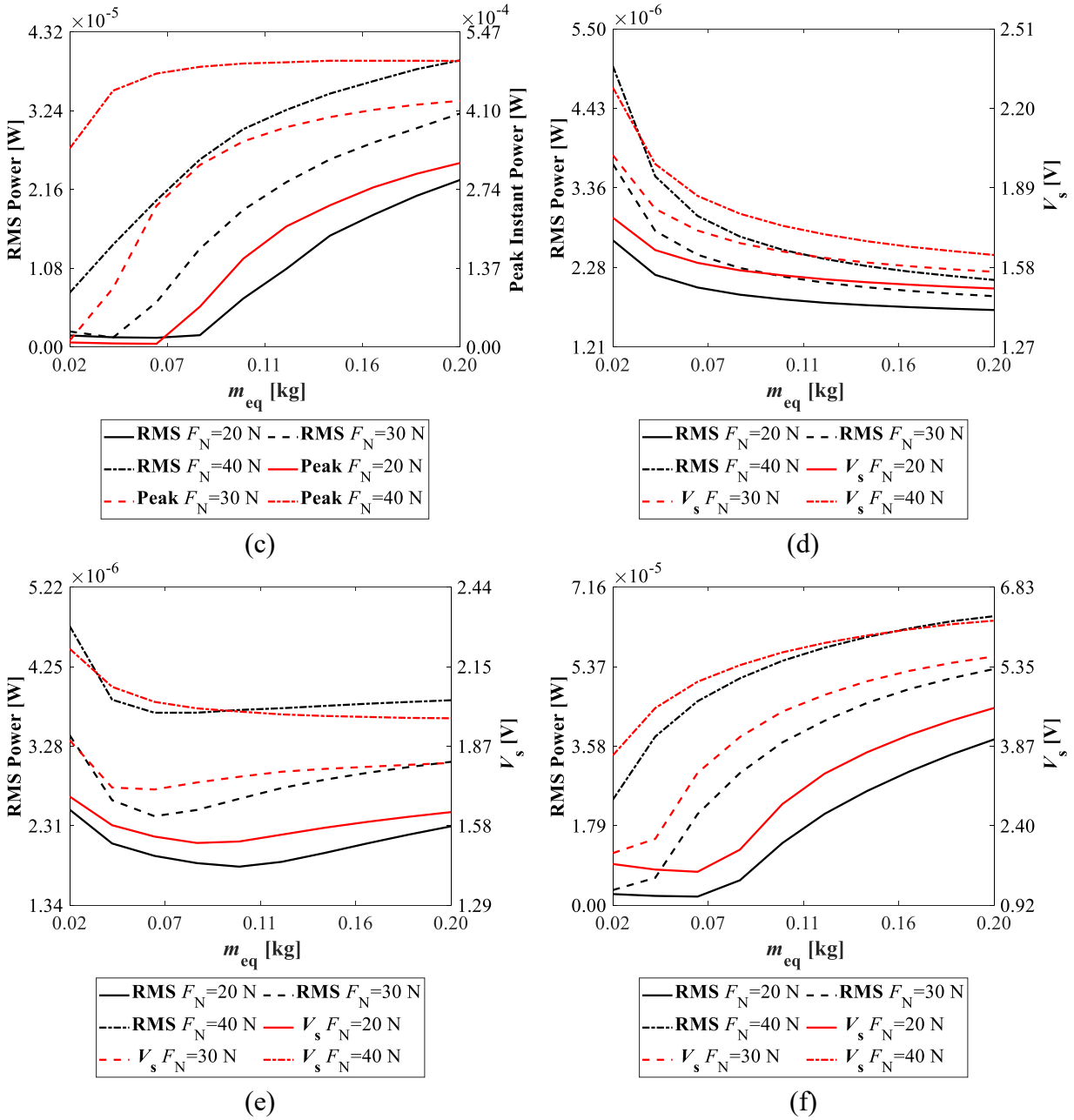

Figure 5-6 Charging power with different m_{eq}. (a) Linear generator (Full charge). (b) Bi-linear generator (Full charge). (c) Impact generator (Full charge). (d) Linear generator (10 s charge). (e) Bi-linear generator (10 s charge). (f) Impact generator (10 s charge).

Figure 5-7 displays the effect of the linear spring stiffness k_1 on the RMS charging power and the peak instant charging power. Figure 5-7(a) illustrates the correlation between the linear spring stiffness k_1 and the charging power. The results demonstrate an incremental trend in both the RMS charging power and peak instant charging power as the value of k_1 increases. This observation is reinforced by the data presented in Figure 5-7(d), which exhibits a similar growth pattern in the

RMS charging power and voltage on the storage capacitor V_s over a 10-second charging period. These findings provide evidence that larger k_l, within the linear design configuration, exerts a favorable influence on energy generation. In Figure 5-7(b), it is observed that the RMS charging power decreases as the linear spring stiffness k_l increases. Additionally, the peak instant charging powers initially increase and then decrease. A sudden increase in RMS charging power is observed when k_l changes from 5500 N/m to 6500 N/m under the F_N = 20 N condition. The saturated voltages corresponding to different k_l values and design configurations are presented in Table 5-2. It is noteworthy that the saturated voltages for k_l = 6500 N/m and F_N = 20 N are very similar between the linear and bi-linear design configurations. This similarity is also evident in the RMS and peak instant charging power. Hence, it can be inferred that the sudden jump in RMS charging power occurs due to the fact that the bi-linear effect barely occurs under that specific condition. Furthermore, an interesting observation is that, under certain conditions, the RMS charging power in the bi-linear design configuration is smaller than that in the linear design configuration as k_l increases. Figure 2-4 shows that the sample instant charging power P_e starts to decrease after the peak instant charging power, indicating that the RMS charging power diminishes after this peak. This may explain the reason for the smaller RMS charging power in the bi-linear design configuration compared to the linear design configuration under specific conditions. During the 10-second charging period, Figure 5-7(e) and Figure 5-7(d) demonstrate that the RMS charging power in the bi-linear design configuration is larger than that in the linear design configuration. These findings provide evidence that, while maintaining other system parameters constant, an increased k_l has a positive influence on the system's saturated voltage. However, beyond a certain threshold, the occurrence of the bi-linear effect may be affected, subsequently affecting energy generation. Figure 5-7(c) depicts the variations in the RMS charging power and peak instant charging power for the impact design configuration as the linear spring stiffness k_l increases. Both the RMS charging power and peak instant charging power exhibit a decrease with the increase of k_l. This consistent behavior is also observed in Figure 5-7(f). The observed trend can be attributed to the fact that while the normal load F_N remains constant, an increased k_l negatively affects the occurrence of the impact effect, consequently influencing energy generation. Furthermore, as the value of k_l surpasses a certain threshold, the system behavior aligns more closely with the linear design configuration, where the impact effect is absent.

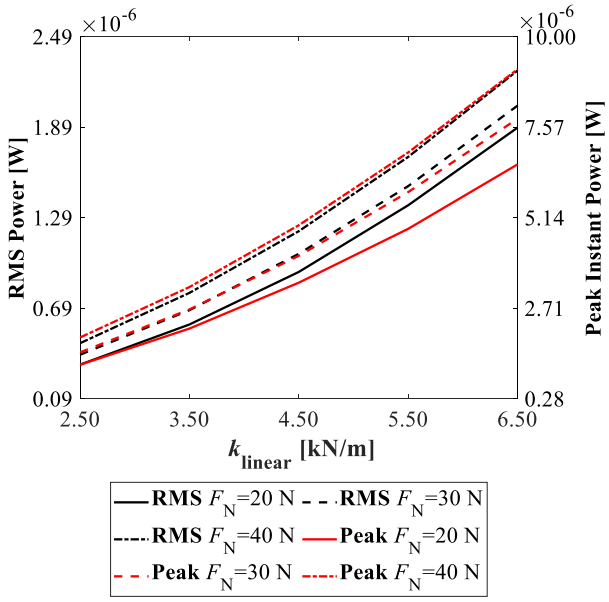
×10^-6
×10^-6
2.49
1.89
1.29
0.69
0.09
10.00
7.57
5.14
2.71
0.28
2.50
3.50
4.50
5.50
6.50
RMS Power [W]
Peak Instant Power [W]
k_linear [kN/m]
RMS F_N=20 N
RMS F_N=30 N
RMS F_N=40 N
Peak F_N=20 N
Peak F_N=30 N
Peak F_N=40 N

(a)

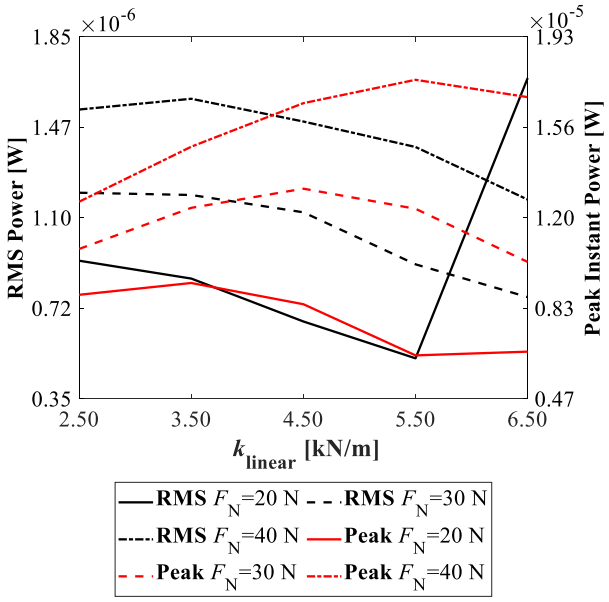
×10^-6
×10^-5
1.85
1.47
1.10
0.72
0.35
1.93
1.56
1.20
0.83
0.47
2.50
3.50
4.50
5.50
6.50
RMS Power [W]
Peak Instant Power [W]
k_linear [kN/m]
RMS F_N=20 N
RMS F_N=30 N
RMS F_N=40 N
Peak F_N=20 N
Peak F_N=30 N
Peak F_N=40 N

(b)

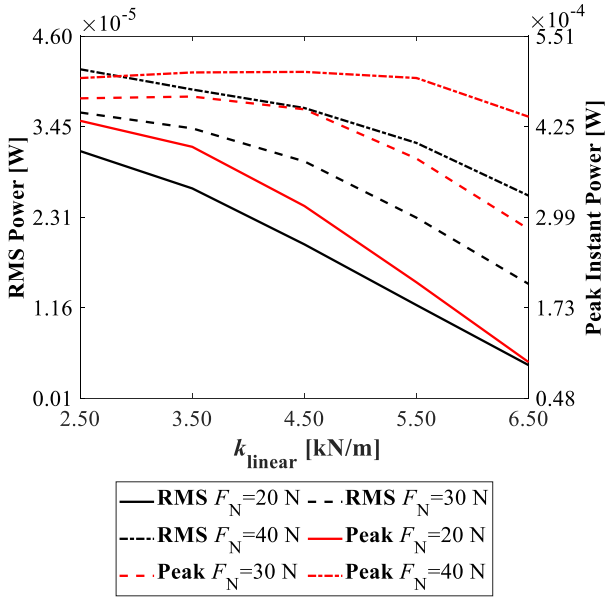
×10^-5
×10^-4
4.60
3.45
2.31
1.16
0.01
5.51
4.25
2.99
1.73
0.48
2.50
3.50
4.50
5.50
6.50
RMS Power [W]
Peak Instant Power [W]
k_linear [kN/m]
RMS F_N=20 N
RMS F_N=30 N
RMS F_N=40 N
Peak F_N=20 N
Peak F_N=30 N
Peak F_N=40 N

(c)

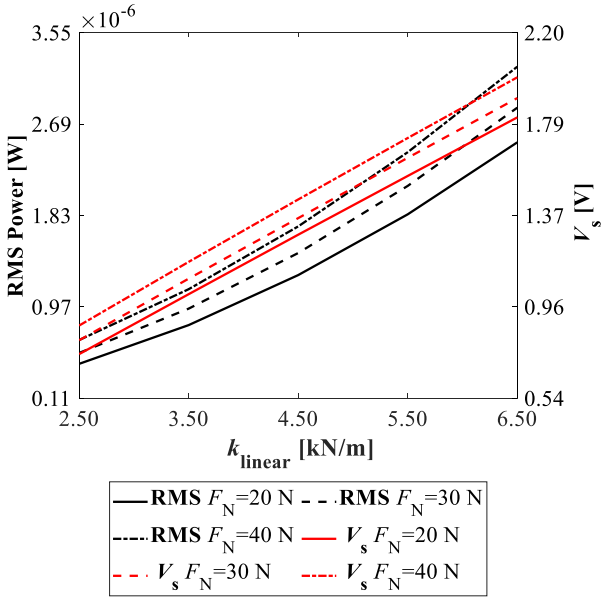
×10^-6
3.55
2.69
1.83
0.97
0.11
2.20
1.79
1.37
0.96
0.54
2.50
3.50
4.50
5.50
6.50
RMS Power [W]
V_s [V]
k_linear [kN/m]
RMS F_N=20 N
RMS F_N=30 N
RMS F_N=40 N
V_s F_N=20 N
V_s F_N=30 N
V_s F_N=40 N

(d)

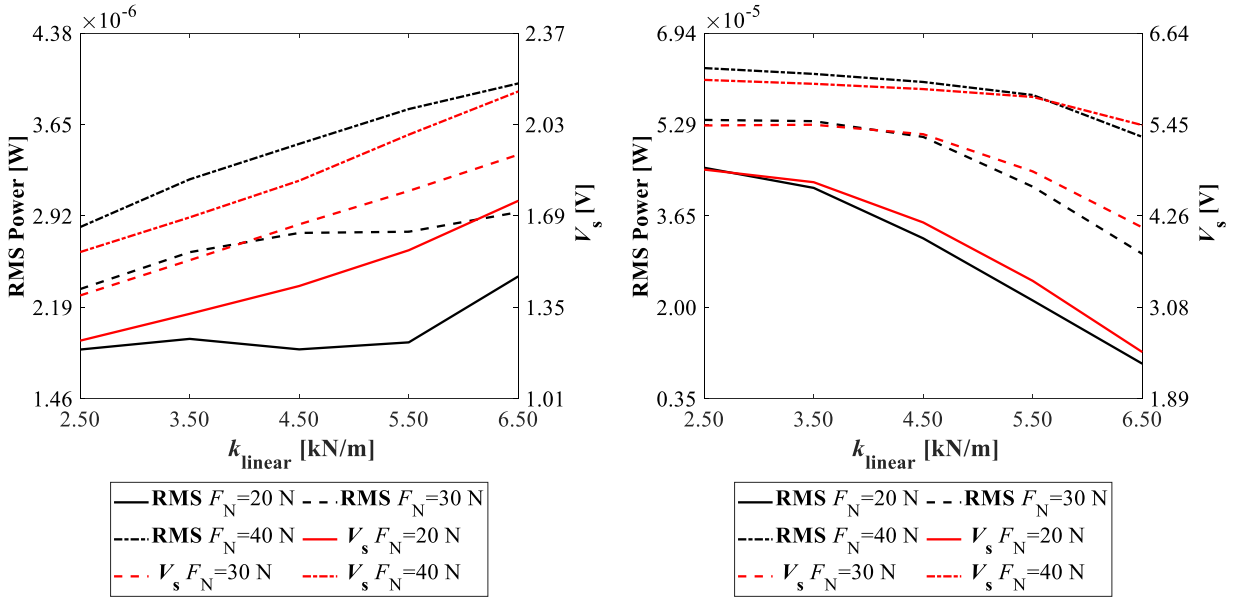

(e) (f)

Figure 5-7 Charging power with different k_{linear}. (a) Linear generator (Full charge). (b) Bi-linear generator (Full charge). (c) Impact generator (Full charge). (d) Linear generator (10 s charge). (e) Bi-linear generator (10 s charge). (f) Impact generator (10 s charge).

Table 5-2 Full charge Saturated voltage with different k_{linear}.

		F_N = 20 N Saturated voltage (V)	F_N = 30 N Saturated voltage (V)	F_N = 40 N Saturated voltage (V)
Linear				
	k_1 = 2500 N/m	0.853	0.965	1.083
	k_1 = 3500 N/m	1.147	1.277	1.413
	k_1 = 4500 N/m	1.436	1.581	1.733
	k_1 = 5500 N/m	1.715	1.881	2.046
	k_1 = 6500 N/m	1.998	2.177	2.354
Bi-linear				
	k_1 = 2500 N/m	2.319	2.551	2.771
	k_1 = 3500 N/m	2.382	2.740	3.003
	k_1 = 4500 N/m	2.265	2.823	3.174
	k_1 = 5500 N/m	1.975	2.738	3.267
	k_1 = 6500 N/m	1.997	2.489	3.196
Impact				
	k_1 = 2500 N/m	16.213	16.786	17.288
	k_1 = 3500 N/m	15.536	16.838	17.426
	k_1 = 4500 N/m	13.819	16.507	17.396
	k_1 = 5500 N/m	11.251	15.190	17.293
	k_1 = 6500 N/m	7.693	13.077	16.290

Figure 5-8 displays the effect of the bi-linear spring stiffness k_{bl} and impact stiffness k_{imp} on the charging power of the bi-linear and impact design configurations. In Figure 5-8(a), it is evident

that both the RMS charging power and the peak instantaneous charging power exhibit an upward trend with increasing bi-linear spring stiffness k_{bl}. Similar trends are observed in Figure 5-8(c) for the RMS charging power and the voltage on the storage capacitor V_{s} during a 10-second charging period. Figure 5-8(b) illustrates the variations in the RMS charging power and peak instantaneous charging power as the impact stiffness k_{imp} increases. Both the RMS charging power and the peak instantaneous charging power show a consistent increase with increasing k_{imp}. This consistent behavior is also observed in Figure 5-8(d). As the linear spring and PZT are connected in series, and the bi-linear spring and impact spring are connected in parallel with the linear spring, it implies that the effective linear spring stiffness increases when the vibration response $y(t)$ exceeds the initial separation distance d_0. In accordance with Eq. (2.15), a larger k_{linear} results in greater deformation in the piezoelectric material, leading to increased energy generation.

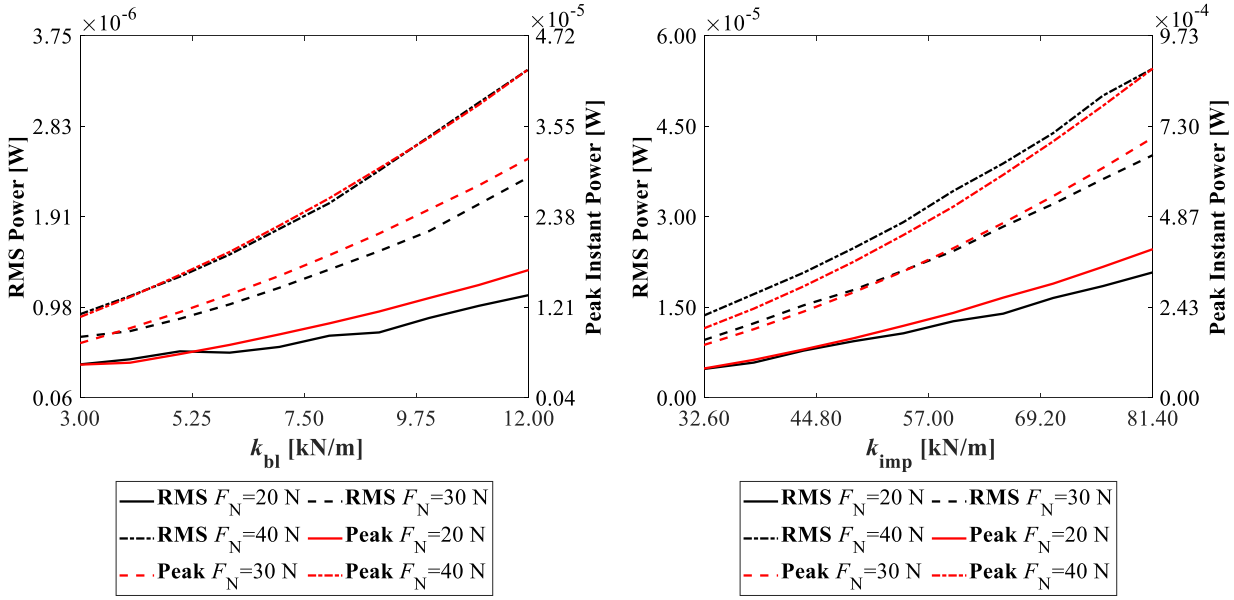

(a) (b)

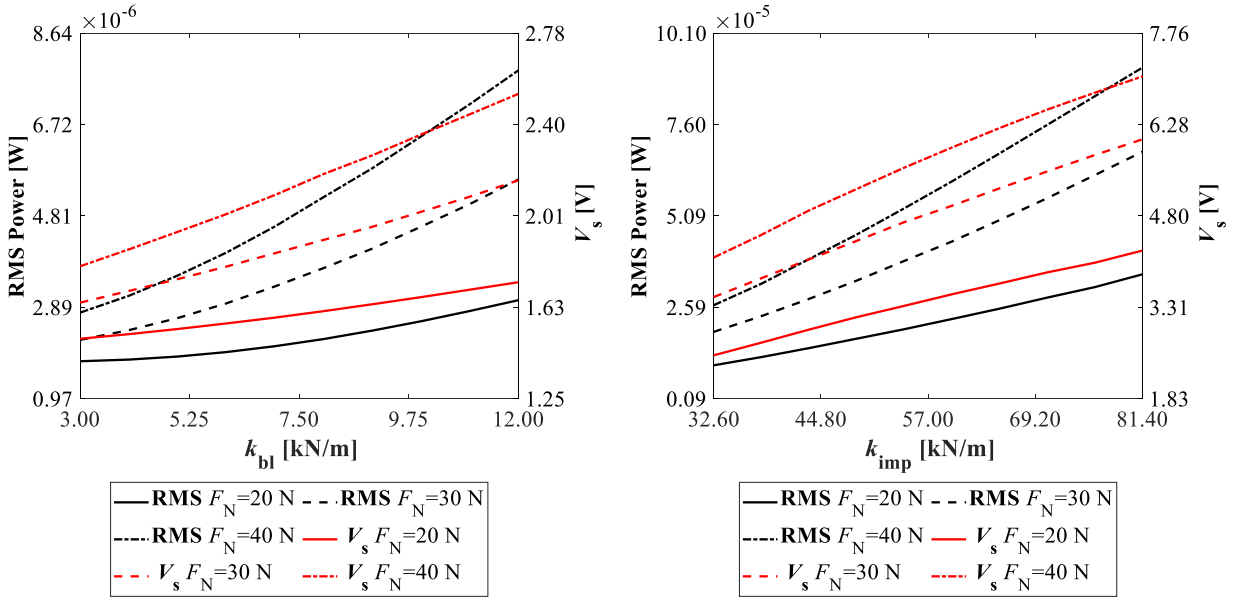

Figure 5-8 Charging power with different k_{bl} and k_{imp}. (a) Bi-linear generator (Full charge). (b) Impact generator (Full charge). (c) Bi-linear generator (10 s charge). (d) Impact generator (10 s charge).

Figure 5-9 demonstrates the influence of the initial separation distance d_0 on energy generation performance of the bi-linear and impact design configurations. In Figure 5-9(a), it can be observed that in the bi-linear design configuration, an increase in d_0 initially leads to a decrease in both RMS charging power and peak instantaneous charging power. However, beyond a certain threshold, a sudden jump occurs, followed by a plateau where the values remain constant. This phenomenon can be explained by referring to the explanation for the jump observed in Figure 5-7(b). The occurrence of the bi-linear effect may be affected once d_0 exceeds a specific threshold. For the 10-second charging period depicted in Figure 5-9(c), the RMS charging power and voltage on the storage capacitor V_{s} exhibit a decrease first, and eventually reaching a steady-state value. The effect of d_0 on the energy generation performance for the impact design configuration follow a similar decreasing trend, but without the sudden jump observed during fully charging.

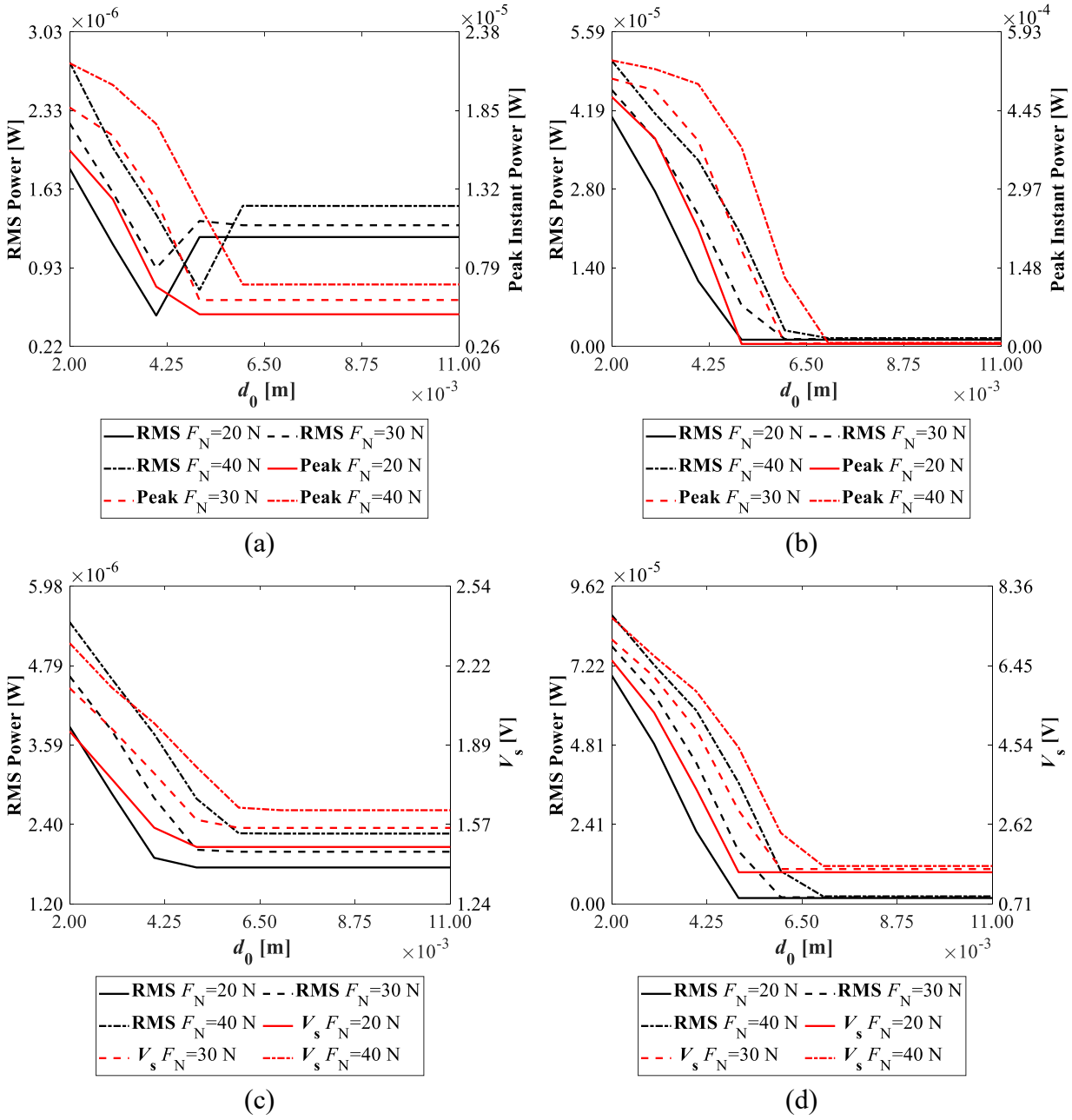

Figure 5-9 Charging power with different d_0. (a) Bi-linear generator (Full charge). (b) Impact generator (Full charge). (c) Bi-linear generator (10 s charge). (d) Impact generator (10 s charge).

In the next section, we examine the normal load, sliding velocity, and friction coefficients on the energy generation performance. The findings from this section will contribute to the development and optimization of proper friction working conditions of the piezoelectric energy generation system.

Figure 5-10 presents the influence of the normal load F_N and sliding velocity v_0 on the energy generation performance. It is shown in Figure 5-10(a), Figure 5-10(b), and Figure 5-10(c) that all

three design configurations exhibit an increasing trend in both RMS charging power and peak instantaneous charging power as v_0 increases. However, the trend lines for the bi-linear design configuration display some fluctuations at low values of v_0. The saturated voltages corresponding to different v_0 values are provided in Table 5-3. The saturated voltages for the bi-linear design configuration increase with the rise in v_0, and it indicates a positive effect induced by higher sliding velocities. Consequently, the fluctuations observed in the RMS charging power for the bi-linear design configuration may be attributed to the diminishing effect of the instantaneous charging power P_e after reaching its peak value. Furthermore, it is worth mentioning that the trend lines for larger values of F_N consistently lie above those for smaller values in all three design configurations. This observation supports the notion that increasing F_N within the selected parameter range has a positive impact on energy generation efficiency.

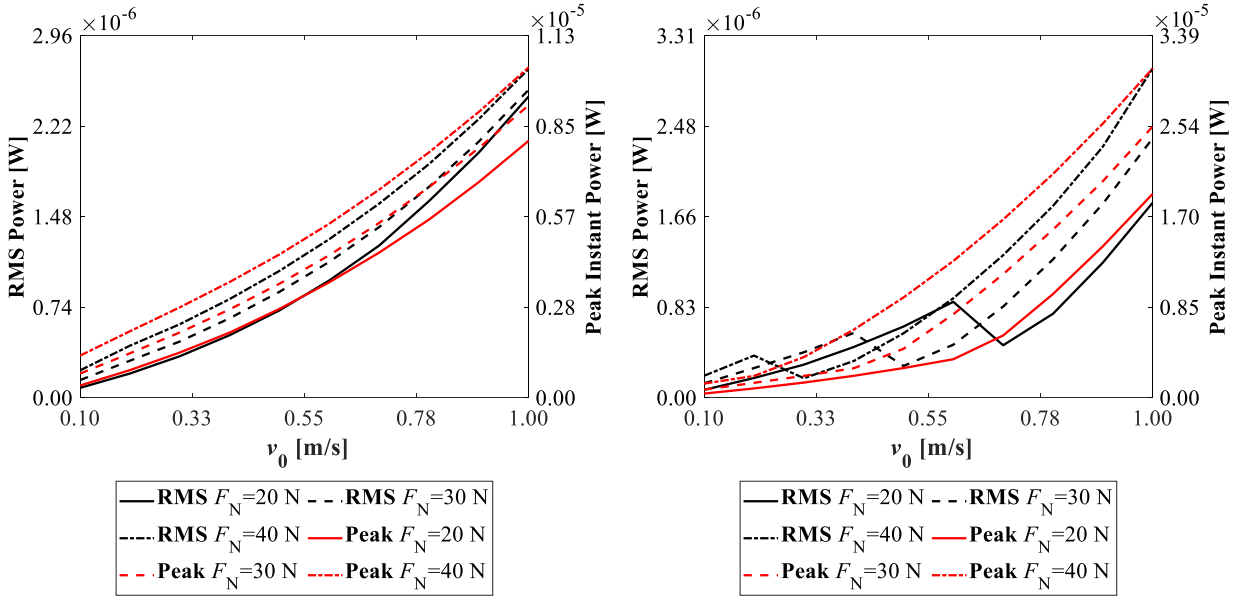

(a) (b)

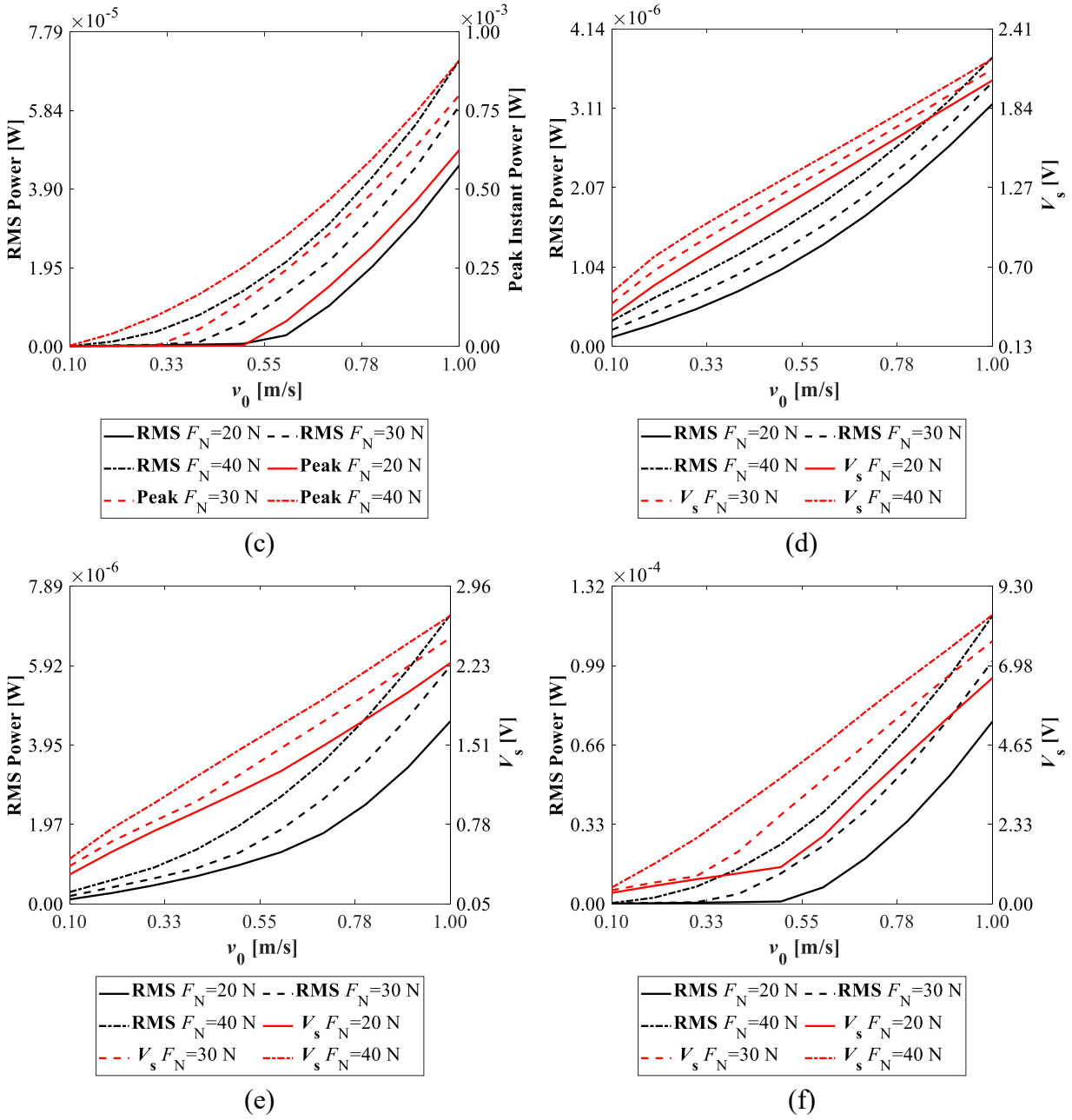

Figure 5-10 Charging power with different F_N and v_0. (a) Linear generator (Full charge). (b) Bi-linear generator (Full charge). (c) Impact generator (Full charge). (d) Linear generator (10 s charge). (e) Bi-linear generator (10 s charge). (f) Impact generator (10 s charge).

Table 5-3 Full charge Saturated voltage with different v_0.

		F_N = 20 N Saturated voltage (V)	F_N = 30 N Saturated voltage (V)	F_N = 40 N Saturated voltage (V)
Linear				
	v_0 = 0.1 m/s	0.478	0.675	0.893
	v_0 = 0.3 m/s	0.925	1.112	1.308
	v_0 = 0.5 m/s	1.230	1.469	1.649
	v_0 = 0.7 m/s	1.661	1.820	1.985
	v_0 = 0.9 m/s	2.021	2.175	2.328
Bi-linear				
	v_0 = 0.1 m/s	0.479	0.675	0.897
	v_0 = 0.3 m/s	0.925	1.112	1.964
	v_0 = 0.5 m/s	1.296	1.661	2.385
	v_0 = 0.7 m/s	1.879	2.648	3.180
	v_0 = 0.9 m/s	2.934	3.511	3.950
Impact				
	v_0 = 0.1 m/s	0.479	0.675	1.174
	v_0 = 0.3 m/s	0.924	1.112	7.643
	v_0 = 0.5 m/s	1.296	9.311	12.321
	v_0 = 0.7 m/s	10.795	14.764	16.836
	v_0 = 0.9 m/s	16.755	19.666	21.282

Figure 5-11 depicts the influence of the static friction coefficient μ_{static} on the energy generation performance. All three design configurations exhibit an increasing trend in both the RMS charging power and peak instantaneous charging power as μ_{static} increases, which are observed in Figure 5-11(a), Figure 5-11(b), and Figure 5-11(c). The rationale behind this increasing trend can be attributed to the rise in the maximum static friction force. The amplitude of the maximum static friction force is directly related to the static friction coefficient μ_{static} and the normal force F_N. While the normal force F_N remains constant, an increase in the static friction coefficient μ_{static} leads to a corresponding increase in the static friction force $F_{\text{static}}(t)$. The vibration amplitude is influenced by the maximum static friction force, which, in turn, affects the deformation of the PZT. As the maximum static friction force represents the threshold force required to initiate sliding motion, a higher maximum static friction force implies more stored elastic energy during the transition from stick to slip.

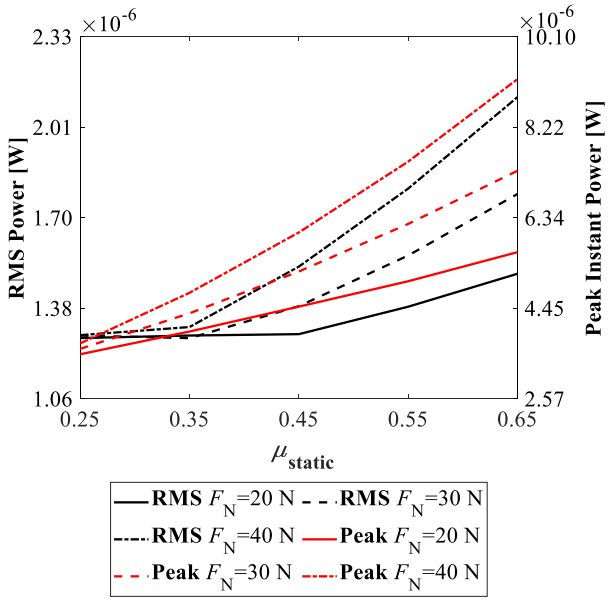
×10^-6
×10^-6
RMS Power [W]
Peak Instant Power [W]
2.33
2.01
1.70
1.38
1.06
10.10
8.22
6.34
4.45
2.57
0.25
0.35
0.45
0.55
0.65
μstatic
RMS FN=20 N
RMS FN=30 N
RMS FN=40 N
Peak FN=20 N
Peak FN=30 N
Peak FN=40 N

(a)

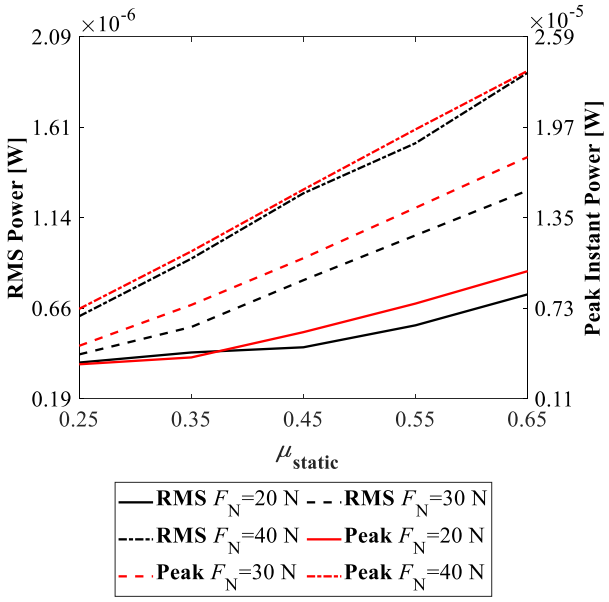
×10^-6
×10^-5
RMS Power [W]
Peak Instant Power [W]
2.09
1.61
1.14
0.66
0.19
2.59
1.97
1.35
0.73
0.11
0.25
0.35
0.45
0.55
0.65
μstatic
RMS FN=20 N
RMS FN=30 N
RMS FN=40 N
Peak FN=20 N
Peak FN=30 N
Peak FN=40 N

(b)

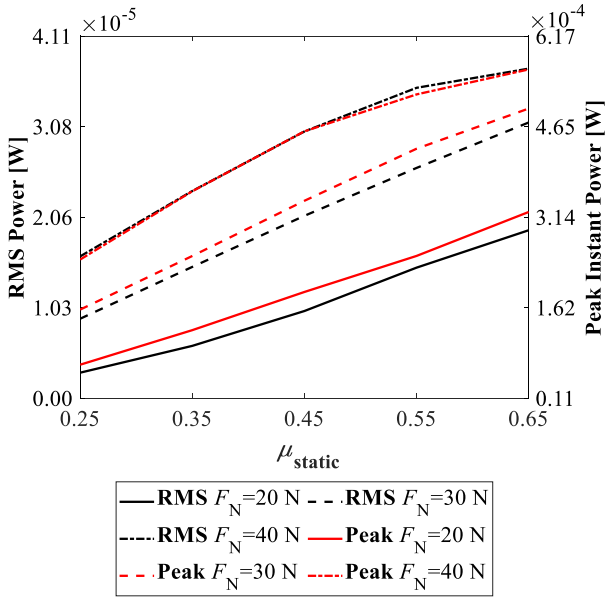
×10^-5
×10^-4
RMS Power [W]
Peak Instant Power [W]
4.11
3.08
2.06
1.03
0.00
6.17
4.65
3.14
1.62
0.11
0.25
0.35
0.45
0.55
0.65
μstatic
RMS FN=20 N
RMS FN=30 N
RMS FN=40 N
Peak FN=20 N
Peak FN=30 N
Peak FN=40 N

(c)

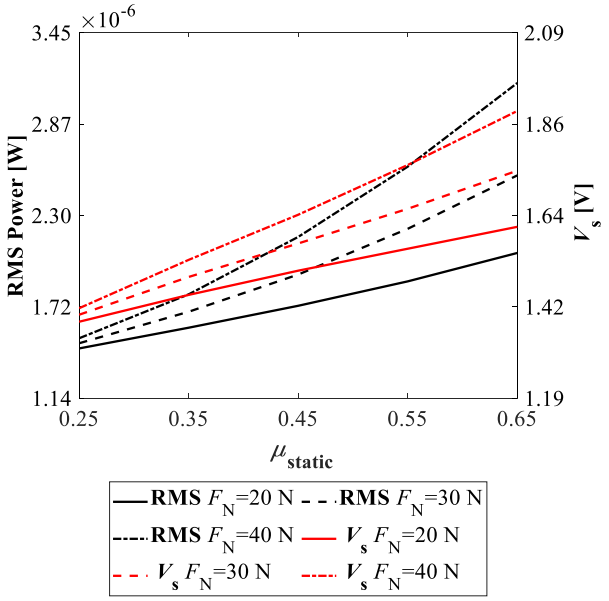
×10^-6
RMS Power [W]
Vs [V]
3.45
2.87
2.30
1.72
1.14
2.09
1.86
1.64
1.42
1.19
0.25
0.35
0.45
0.55
0.65
μstatic
RMS FN=20 N
RMS FN=30 N
RMS FN=40 N
Vs FN=20 N
Vs FN=30 N
Vs FN=40 N

(d)

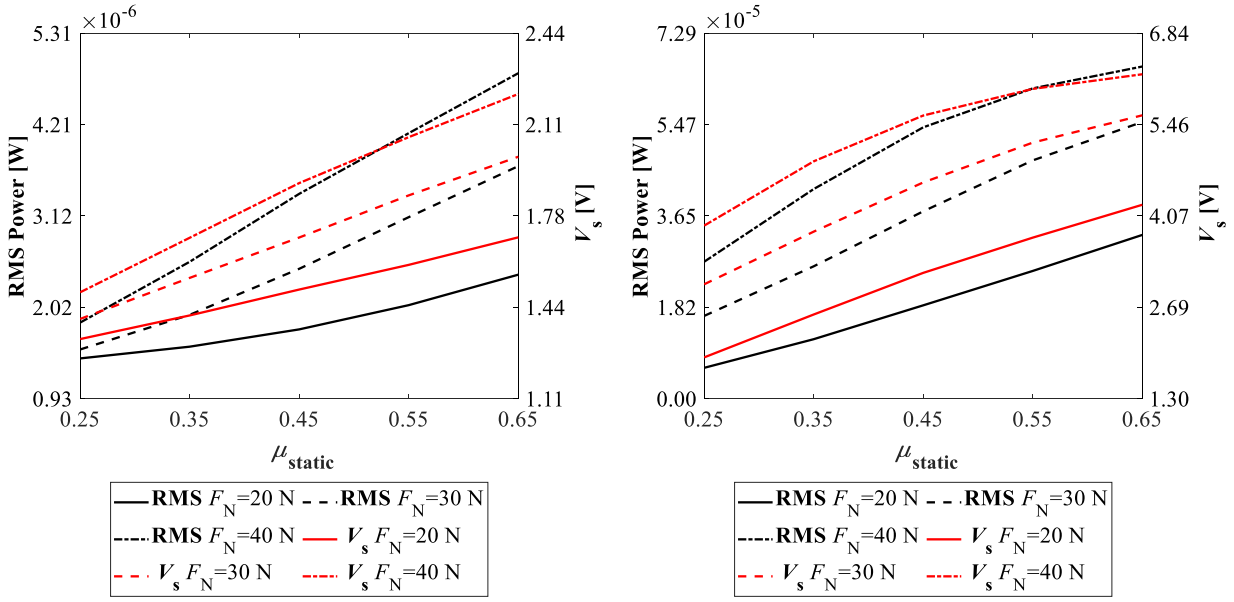

Figure 5-11 Charging power with different μ_{static}. (a) Linear generator (Full charge). (b) Bi-linear generator (Full charge). (c) Impact generator (Full charge). (d) Linear generator (10 s charge). (e) Bi-linear generator (10 s charge). (f) Impact generator (10 s charge).

Figure 5-12 demonstrates the influence of the kinetic friction coefficient μ_k on the energy generation performance. In Figure 5-12(a), the linear design configuration exhibits a decreasing trend in both the RMS charging power and peak instantaneous charging power as μ_k increases. This can be attributed to the fact that, while keeping the static friction coefficient μ_{static} unchanged, a higher μ_k facilitates sustained sliding motion and increases energy dissipation, resulting in smaller slip amplitudes. On the other hand, the bi-linear and impact design configurations display a slightly increasing trend in both the RMS charging power and peak instantaneous charging power as μ_k increases, which are shown in Figure 5-12(b) and Figure 5-12(c). This trend may be explained by the fact that a higher μ_k enhances a longer slip phases during stick-slip motion. This, in turn, increases the likelihood of bi-linear and impact effects occurring. However, the amplitude of stick-slip motion is not directly affected by the kinetic friction coefficient. The characteristics of the slip event, as well as the occurring frequency of bi-linear and impact effects, may contribute to the inconsistency in energy generation trends with increasing μ_k.

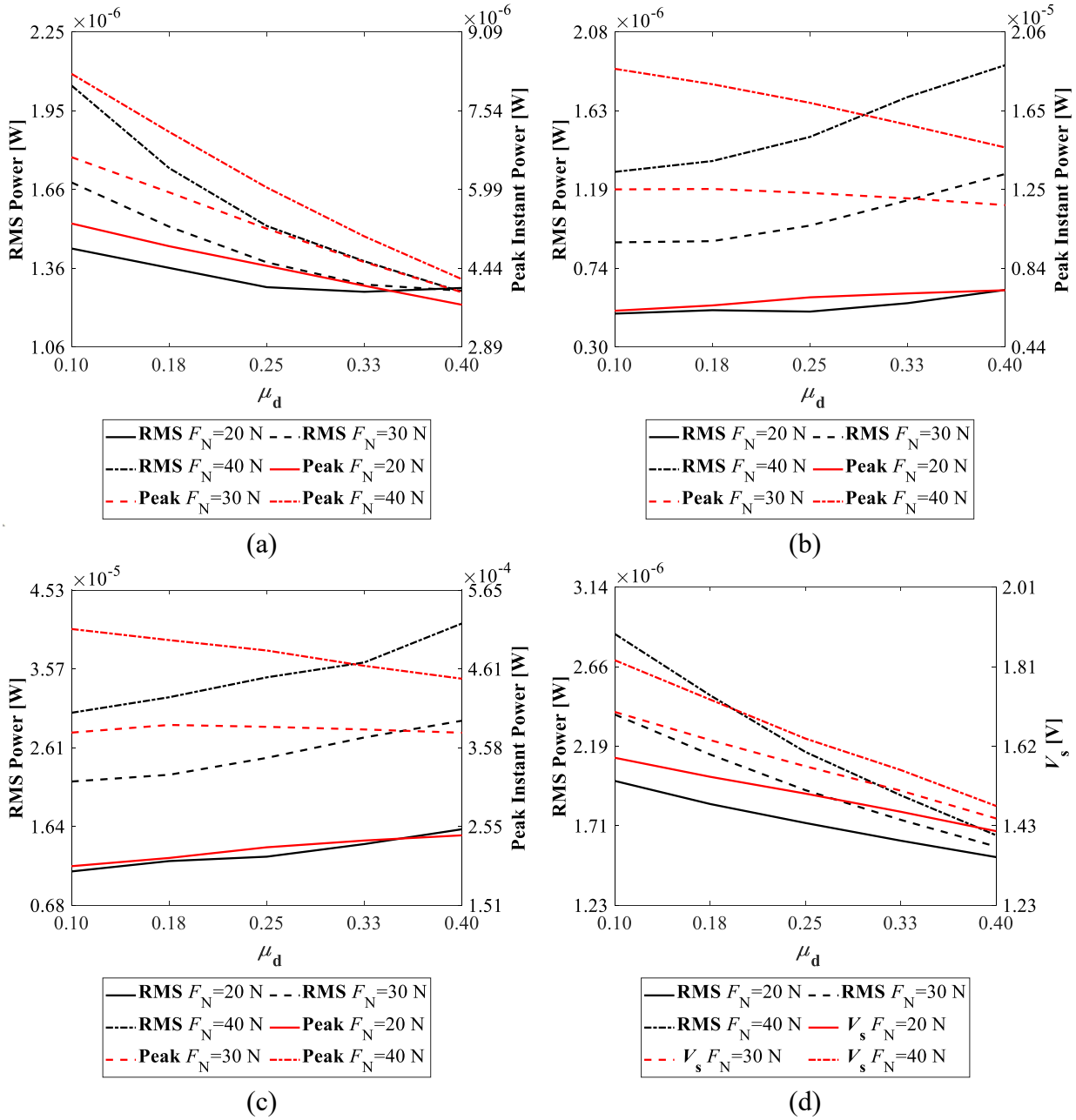
×10^-6
2.25
1.95
1.66
1.36
1.06
×10^-6
9.09
7.54
5.99
4.44
2.89
RMS Power [W]
Peak Instant Power [W]
0.10
0.18
0.25
0.33
0.40
μd
RMS FN=20 N
RMS FN=30 N
RMS FN=40 N
Peak FN=20 N
Peak FN=30 N
Peak FN=40 N
(a)
×10^-6
2.08
1.63
1.19
0.74
0.30
×10^-5
2.06
1.65
1.25
0.84
0.44
RMS Power [W]
Peak Instant Power [W]
0.10
0.18
0.25
0.33
0.40
μd
RMS FN=20 N
RMS FN=30 N
RMS FN=40 N
Peak FN=20 N
Peak FN=30 N
Peak FN=40 N
(b)
×10^-5
4.53
3.57
2.61
1.64
0.68
×10^-4
5.65
4.61
3.58
2.55
1.51
RMS Power [W]
Peak Instant Power [W]
0.10
0.18
0.25
0.33
0.40
μd
RMS FN=20 N
RMS FN=30 N
RMS FN=40 N
Peak FN=20 N
Peak FN=30 N
Peak FN=40 N
(c)
×10^-6
3.14
2.66
2.19
1.71
1.23
2.01
1.81
1.62
1.43
1.23
RMS Power [W]
Vs [V]
0.10
0.18
0.25
0.33
0.40
μd
RMS FN=20 N
RMS FN=30 N
RMS FN=40 N
Vs FN=20 N
Vs FN=30 N
Vs FN=40 N
(d)

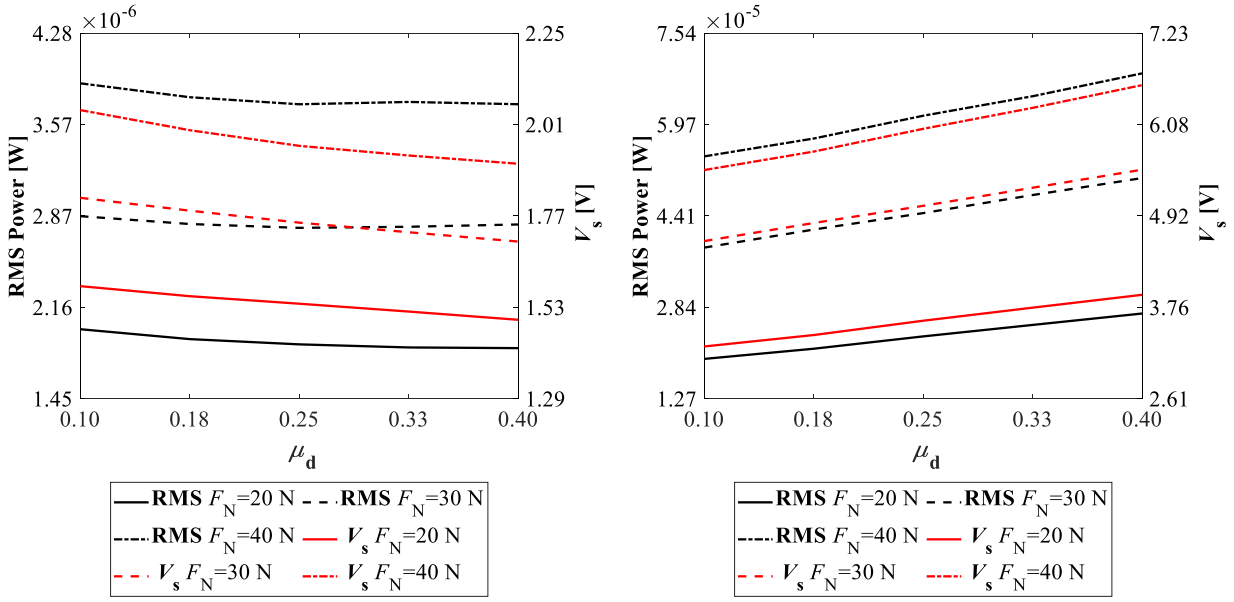

(e) (f)

Figure 5-12 Charging power with different μ_k. (a) Linear generator (Full charge). (b) Bi-linear generator (Full charge). (c) Impact generator (Full charge). (d) Linear generator (10 s charge). (e) Bi-linear generator (10 s charge). (f) Impact generator (10 s charge).

5.3.2 Summary and discussion

The work introduces a piezoelectric energy generator that harnesses energy from FIV at low sliding velocities. Three design configurations are proposed and analyzed: linear, bi-linear, and impact. Experimental and numerical results demonstrate the potential for high-frequency dynamic voltage generation, with peak-to-peak voltages of approximately 2.9 V, 3.8 V, and 20.6 V for the respective configurations. Enhanced voltage outputs are realized under higher normal load and sliding velocity operating conditions. A comparison among the linear, bi-linear, and impact design configurations reveals that the introduced bi-linear and impact effects through structural modifications enhance energy generation. Strong bi-linear and impact effects can enhance energy output by setting an appropriate initial separation distance under proper operating conditions. The designed generators exhibit the capability to operate at close to the systems' resonant frequencies under low sliding velocities excitation, and further improvement in energy generation performance can be achieved through modifications such as increasing the linear spring stiffness, applying larger normal load, replacing the piezoelectric chunk with piezoelectric stack, and applying materials with better properties.

Moving forward, several areas of research can be explored to further enhance the piezoelectric energy generator's performance. Optimization efforts can focus on increasing the amount of piezoelectric material used in the generator to maximize energy conversion. Additionally, incorporating multiple generators in parallel can enable simultaneous charging and enhance the overall power output. Exploring the integration of the generator into rotating or sliding equipment with suitable friction layers can lead to practical applications in harvesting energy from existing machinery. Lastly, engineering realizations for self-powering wireless devices using this generator present an interesting avenue for future exploration, where the focus can be on designing efficient energy storage and management systems to support continuous operation.

Chapter 6 Piezoelectric energy generation with permanent magnetic springs

In this chapter, a numerical investigation is conducted on PEGs that utilize permanent magnets as nonlinear springs. The study involves comparing different configurations of nonlinear magnetic and linear piezo-element connections to analyze the dynamic responses of single and multiple degrees of freedom PEG systems. The modeling methods depicted in Sections 2.1, 2.2, 2.3, 2.4, and 2.6 are utilized in this chapter.

Two specific configurations of nonlinear vibration systems are considered: one with harmonic excitation and the other with friction excitation. For harmonic excitation, the analysis primarily focuses on the essential characteristics of the nonlinear systems, including the frequency responses of the PEGs, operating bandwidth, and the sum of the Root Mean Square (RMS) charging powers (SRCP) considering the nonlinear magnetic spring. This analysis aims to understand how the PEGs respond to harmonic vibrations and their ability to convert these vibrations into electrical power. It will be introduced in Section 6.1.

For friction excitation, the analysis focuses on examining the PEGs' performance under different friction parameters and working conditions. The PEGs' operating velocity range and SRCP are investigated. Moreover, this study also provides insights into the behavior and efficiency of the PEG system subjected to varying normal load and sliding velocity, which is similar to practical friction operating conditions. It will be described in Section 6.2.

6.1 Magnet-engaged piezoelectric energy generation under harmonic excitation

The schematics of the proposed piezoelectric energy generators are shown in Figure 6-1(a)-(e), which represent shear mode linear in parallel system, compression mode linear in parallel system, shear mode nonlinear in parallel system, shear mode linear in series system and shear mode nonlinear in series system, respectively. The difference between shear mode linear in parallel system and compression mode linear in parallel system is the layout of the piezoelectric patch and its deformation. The piezoelectric patch in both systems is considered as connected in series with the linear tension spring k_{l}, but the stiffness constant k_{piezo} of the piezoelectric patch in shear mode is calculated from the elastic constant c_{55}^{E}, and k_{piezo} in compression mode is obtained from elastic constant c_{33}^{E} due to the different deformation. And there is an equivalent mass block located at the free end. Figure 6-1(c) demonstrates the shear mode nonlinear in parallel system with the addition of the magnetic force. While the magnet is attached to the mass block, the magnet is equivalent to a nonlinear spring and connected in parallel with the system described in Figure 6-1(a) to form a nonlinear system. Figure 6-1(d) displays the shear mode linear in series system by adding an equivalent linear spring with the same stiffness of the linear term of the nonlinear spring to the left side of m_1, which is the equivalent mass of the magnet and other components shown in Figure 6-1(e). Figure 6-1(e) indicates the shear mode nonlinear in series system by adding the magnet to left side of the linear tension spring k_{l}, the nonlinear spring is connected in series with the system described in Figure 6-1(a) to form a new nonlinear system. The calculation of the equivalent magnetic force and its representation is described in the following section, and the detail of the system parameter is then explained.

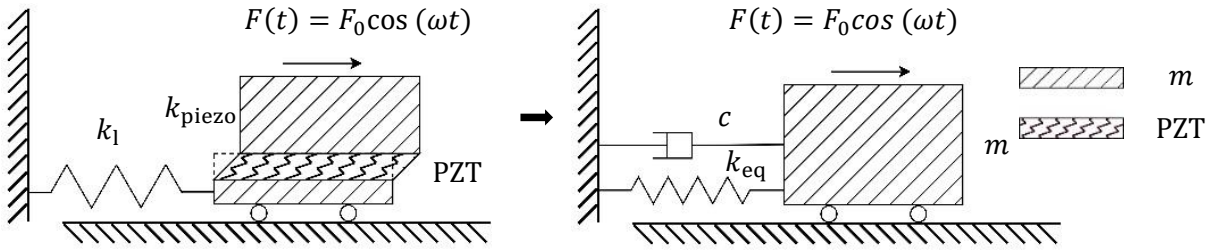

(a)

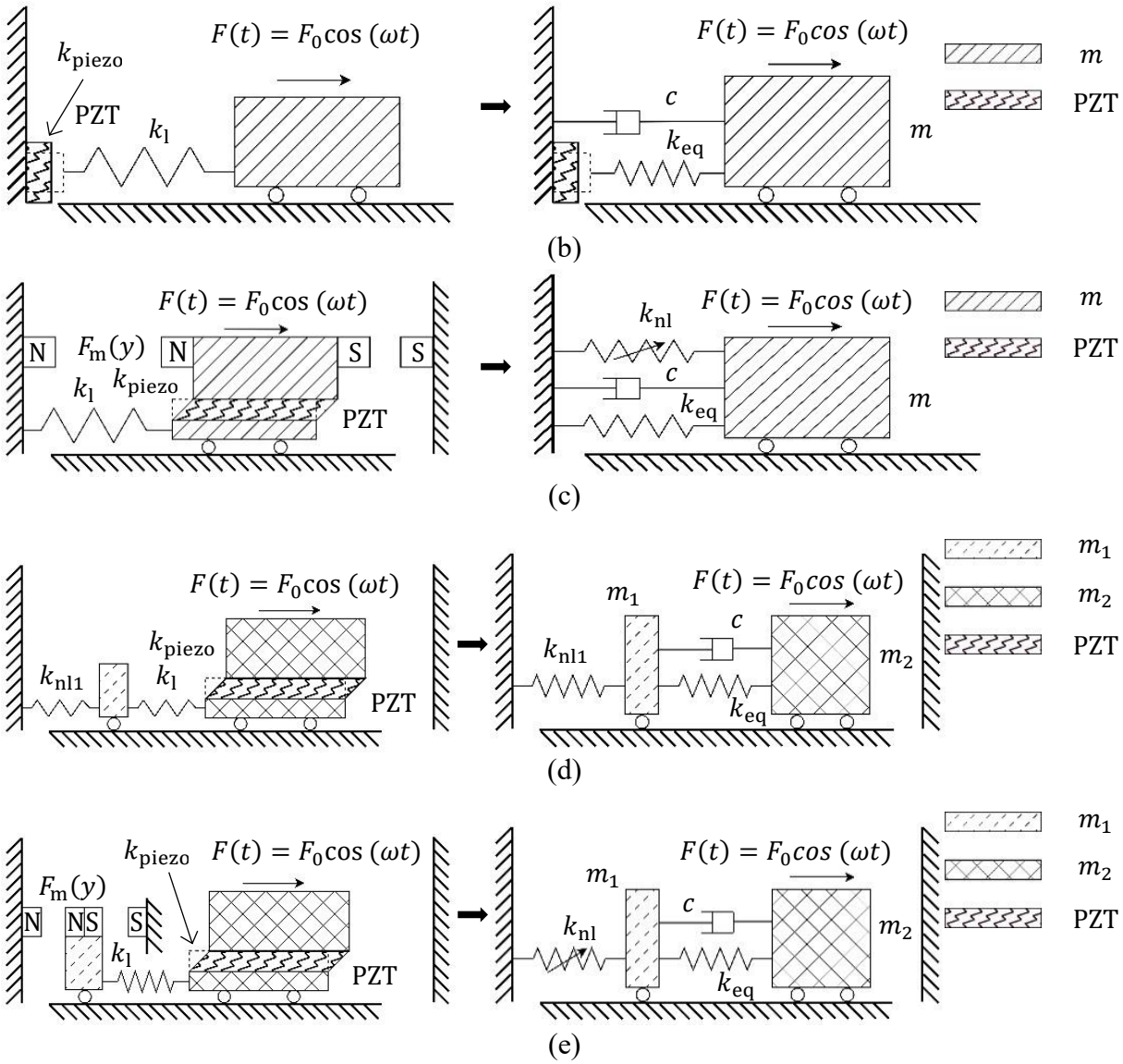

Figure 6-1 Schematic diagrams of the proposed piezoelectric energy generators. (a) Shear-mode system under harmonic excitation. (b) Compression-mode system under harmonic excitation. (c) Shear-mode system with nonlinear spring in parallel under harmonic excitation. (d) Shear-mode system with linear spring in series under harmonic excitation. (e) Shear-mode system with nonlinear spring in series under harmonic excitation.

According to experimental measurement data from [121], an empirical equation for magnetic force F_{m} between two magnets is determined [128], F_{m} can be written as,

$$F_{\text{m}} = l_{\text{m}} w_{\text{m}} t_{\text{m}}^{\frac{1}{3}} B_r |B(d)| f(d), \tag{6.1}$$

where l_{m}, w_{m} and t_{m} are the length, width, and thickness of the magnet, respectively; B_r is the residual flux density of the magnet in tesla (T), B_r is between 1 to 1.5 for Neodymium, and B_r is 1.45 for calculation; $B(d)$ is the magnitude of the magnetic flux density field; $f(d)$ is the function

describing the decay of the magnetic force between the two magnets. Following the method in [13], [128], for rectangular magnet, $B(d)$ and $f(d)$ can be rewritten as,

$$B(d) = \frac{B_r}{\pi}\left[tan^{-1}\left\{\frac{l_{\mathrm{m}}w_{\mathrm{m}}}{2d\sqrt{4d^2+{l_{\mathrm{m}}}^2+{w_{\mathrm{m}}}^2}}\right\} - tan^{-1}\left\{\frac{l_{\mathrm{m}}w_{\mathrm{m}}}{2(t_{\mathrm{m}}+d)\sqrt{4(t_{\mathrm{m}}+d)^2+{l_{\mathrm{m}}}^2+{w_{\mathrm{m}}}^2}}\right\}\right], \tag{6.2}$$

$$f(d) = \left[1.749 + 1.145e^{\left(-\frac{d}{d_0}\right)}\right] \times 10^6\left(NT^{-2}m^{-7/3}\right), \tag{6.3}$$

where d is the facing distance between the two magnets; d_0 is 1 mm based on the derived formula [128]. For the system shown in Figure 6-1(c), the nonlinear spring is in parallel connection with the mass block. The horizontal distance y is equal to the vibration response of the system, and the equivalent mass of the system is the summation of the mass block, the mass of the magnet, and the mass of the rest of the system components. For the system shown in Figure 6-1(e), the nonlinear spring is in series connection with the mass block, and the horizontal distance y is equal to the vibration response of m_1 which is the mass of the magnet. The schematic of the system under magnetic force is shown in Figure 6-2.

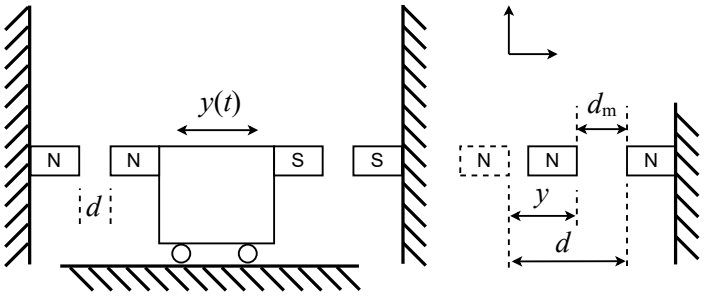

Figure 6-2 System under magnetic force.

In order to study the effect of magnet dimension (l_{m}, w_{m} and t_{m}) to magnetic force, the volume of the magnet is fixed to V_{m} = 4.125e^{-6} m^3. While B_r = 1.45 T, l_{m} = 0.015 m, w_{m} = 0.007-0.019 m, $t_{\mathrm{m}} = V_{\mathrm{m}}/(l_{\mathrm{m}}w_{\mathrm{m}})$ m, the magnetic force versus displacement diagram indicating the effect of magnet dimensions on magnetic force is shown in Figure 6-3.

Accordingly, a polynomial can be employed to simulate the magnetic force while the system is in an equilibrium position with a separation gap d between the two magnets, given by,

$$F_{\mathrm{m}}(y(t)) = \sum_{j=1}^{\infty} k_{\mathrm{n}lj}y(t)^j, j = 1, 3, 5, \cdots. \tag{6.4}$$

The linear, cubic, quintic, and septic polynomial curve fittings for approximating the magnetic force versus different distances are compared using the Matlab Curve Fitting tool, and the result is shown in Figure 6-3(a). The cubic, quintic, and septic curve fitting results almost overlap with the values calculated from the experimental validated force equation. The representations of cubic, quintic, and septic curve fitting are: $F_{\mathrm{m}}(y(t)) = 750.2\,y(t) + 11078024.8\,y^3(t)$, $F_{\mathrm{m}}(y(t)) = 750.2\,y(t) + 11078024.8\,y^3(t) + 1656452154.6\,y^5(t)$, and $F_{\mathrm{m}}(y(t)) = 750.2\,y(t) + 11078024.8\,y^3(t) + 1656452154.6\,y^5(t) + 2484678231.8\,y^7(t)$, respectively. It proves the feasibility of using the empirical form ($F_{\mathrm{m}}(y(t)) = k_{\mathrm{nl1}}y(t) + k_{\mathrm{nl3}}y^3(t)$) to approximate the magnetic force. Figure 6-3(b) shows the linear and nonlinear coefficients of magnetic force corresponding to different w_{m}.

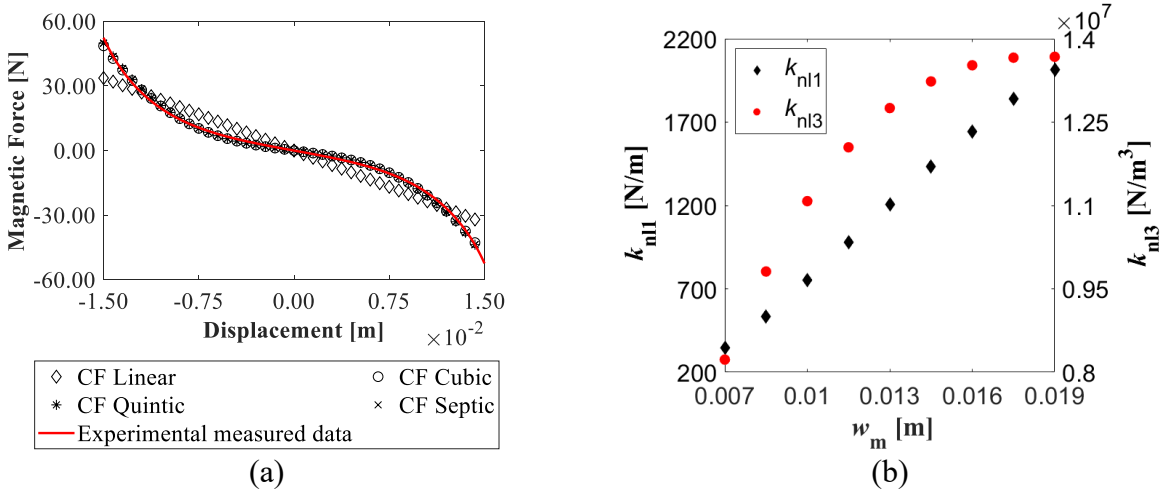

(a) (b)

Figure 6-3 Magnetic force versus displacement of different w_{m}. (a) Curve fitting comparison (B_r = 1.45 T, l_{m} = 0.015 m, w_{m} = 0.01 m, and t_{m} = 0.0275 m). (b) Cubic curve fitting coefficients (B_r = 1.45 T, V_{m} = 4.125e^{-6} m^3, and l_{m} = 0.015 m).

6.1.1 Equation of motion under magnetic and harmonic force

The mechanical and piezoelectric coupling equation of a 1-DOF system with harmonic force and magnetic force in parallel as excitation can be written as:

$$\begin{cases} m\ddot{y}(t) + c\dot{y}(t) + k_{\mathrm{eq}}y(t) + k_{\mathrm{nl1}}y(t) + k_{\mathrm{nl3}}y^3(t) \\ \qquad -\alpha\frac{k_{\mathrm{l}}}{k_{\mathrm{l}}+k_{\mathrm{piezo}}}V_{\mathrm{R}}(t) = F_0 cos(\omega t) \\ V_{\mathrm{R}}(t) + RC_{\mathrm{p}}\dot{V}_{\mathrm{R}}(t) + R\alpha\frac{k_{\mathrm{l}}}{k_{\mathrm{l}}+k_{\mathrm{piezo}}}\dot{y}(t) = 0 \end{cases} . \tag{6.5}$$

The mechanical and piezoelectric coupling equation of the 2-DOF system with harmonic force and magnetic force in series as excitation is given by,

$$\begin{cases} m_1\ddot{y}_1(t) - c\left(\dot{y}_2(t) - \dot{y}_1(t)\right) + (k_{\mathrm{nl1}} + k_{\mathrm{eq}})y_1(t) \\ \quad +k_{\mathrm{nl3}}{y_1}^3(t) - k_{\mathrm{eq}}y_2(t) = 0 \\ m_2\ddot{y}_2(t) + c\left(\dot{y}_2(t) - \dot{y}_1(t)\right) + k_{\mathrm{eq}}\left(y_2(t) - y_1(t)\right) \\ \quad -\alpha\frac{k_1}{k_1+k_{\mathrm{piezo}}}V_{\mathrm{R}}(t) = F_0 cos(\omega t) \\ V_{\mathrm{R}}(t) + RC_{\mathrm{p}}\dot{V}_{\mathrm{R}}(t) + R\alpha\frac{k_1}{k_1+k_{\mathrm{piezo}}}\left(\dot{y}_2(t) - \dot{y}_1(t)\right) = 0 \end{cases} . \tag{6.6}$$

The detail iterative solving process is depicted in Section 2.3 and Section 2.4.

6.1.2 Model validation

Figure 6-5 compares the experimental result with the frequency response curve in previous literature [129]. It can be seen from Figure 6-5 that the simulation results using the numerical model are close to the experimental results in the literature, which proves the correctness of applying the numerical model for simulation. And the following common parameters are used: m = 0.022 kg, c = 0.034 N/(m/s), F_0 = 0.06 N, α = 7.095e^{-5} V/N, C_{p} = 1.1e^{-7} F, and R = 115000 Ω. The corresponding k_{nl1} for case 1, 2, and 3 is 50.3, 77.5, and 109 N/m. The corresponding k_{nl3} for case 1, 2, and 3 are 54400, 114000, and 195000 N/m^3.

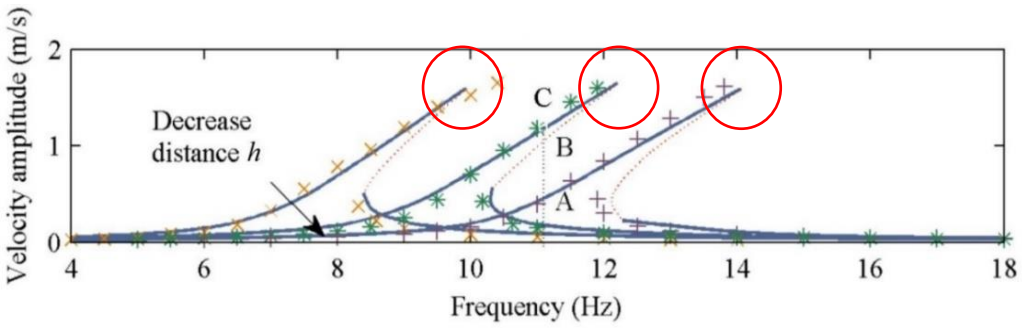

Figure 6-4 Experimental result from previous literature [129].

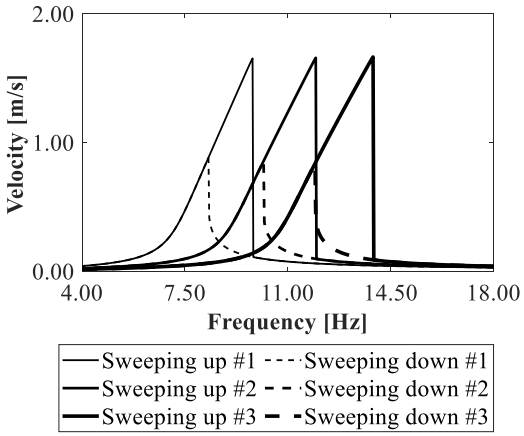

Figure 6-5 Simulation results with the numerical model.

The ordinary differential equations describing the three systems can be solved by numerical method, and the result of the numerical method is compared with the approximate analytical method to prove its accuracy for simulation. Several approximate analytical methods have been developed, such as perturbation method and harmonic balance method. The harmonic balance method is used for comparison in this study. Figure 6-6(a)-(b) compare the nonlinear in parallel system with different excitation amplitude F_0. And the following common parameters are used: m = 0.18563 kg, ζ = 0.005, k_{l} = 1050 N/m, k_{nl1} = 381.26 N/m, k_{nl3} = 8261267.7 N/m^3, α = 0.23152 V/N, C_{p} = 3.0267e^{-10} F, and R = 5400000 Ohm.

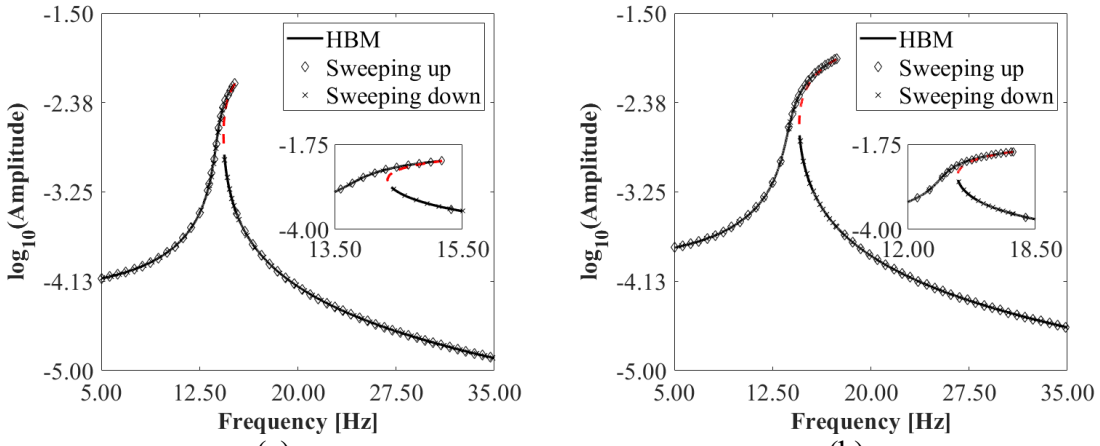

Figure 6-6 Comparison of frequency response using harmonic balance method and numerical method for nonlinear in parallel system. (a) In parallel (F_0 = 0.1 N). (b) In parallel (F_0 = 0.2 N).

Figure 6-7(a)-(b) show the nonlinear in series system with different linear spring stiffness k_1. The simulation results using the numerical model match well with the harmonic balance method (HB), which proves the correctness of the applied numerical method for simulation. And the following common parameters are used: m_1 = 0.02925 kg, m_2 = 0.15637 kg, ζ = 0.005, k_{nl1} = 381.26 N/m, k_{nl3} = 8261267.7 N/m^3, α = 0.23152 V/N, C_{p} = 3.0267e^{-10} F, and R = 5400000 Ohm.

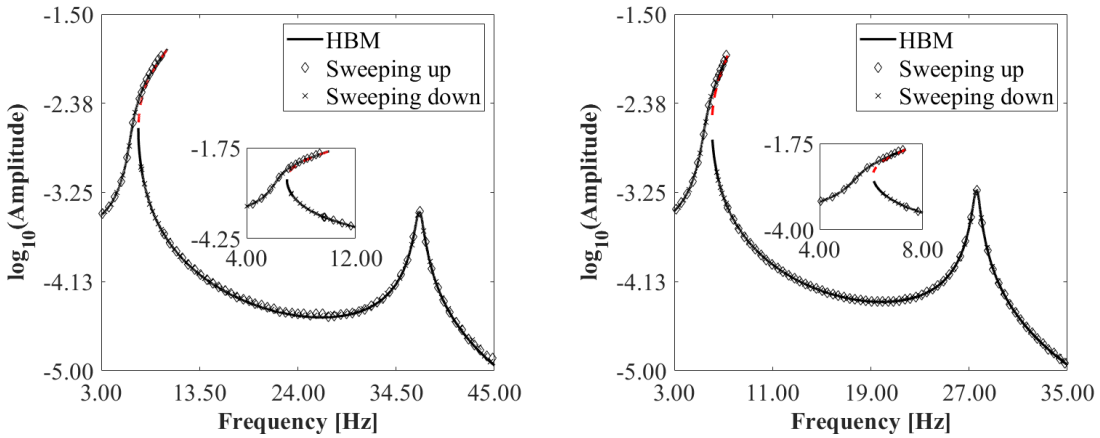

Figure 6-7 Comparison of frequency response using harmonic balance method and numerical method for nonlinear in series system. (a) In series (F_0 = 0.1 N and k_1 = 1050 N/m). (b) In series (F_0 = 0.1 N and k_1 = 450 N/m).

In order to prove the validity of the approach, experiment tests are conducted, and a compression mode PZT patch is used instead of shear one just showing the setup of magnetic spring connection. Figure 6-8(a) provides a schematic representation of the overall testing setup, comprising two modules: the data acquisition system and the energy generator test setup. The data acquisition system is an integrated four-channel Siemens LMS SCA-DAS mobile system connected with LMS TestLab software. Figure 6-8(b) presents a detailed illustration of the energy generator test setup. A K2007E01 shaker is mounted on the left side to provide harmonic excitation. Three N52 grade permanent magnets from McMaster-CARR, each with an outer diameter of 0.5 inch and a thickness of 1 inch, and priced at $7.73 each, are strategically employed to induce nonlinear magnetic repulsion. One magnet is affixed to the equivalent mass, while the remaining two magnets are fixed onto the testing base plate. These magnets are arranged with their poles facing each other, ensuring the desired magnetic interaction. Additionally, a load cell (PCB

208C01) is incorporated into the setup to accurately measure the dynamic excitation force. The linear spring connects the piezoelectric material with the equivalent mass. The mounting structures utilized within the energy generator test setup are fabricated by 3D printing using polylactic acid (PLA) material. Figure 6-8(c) and (d) demonstrate the nonlinear in parallel and linear experimental testing design configurations, respectively.

The parameters used for the experiment and simulation are listed in Table 6-1. Figure 6-9(a) and (c) display the comparison of output voltage versus time from experiment and simulation, and Figure 6-9(b) and (d) show the dynamic excitation force in the experiments, respectively. The resistance R used for simulating the charge dissipation of the data acquisition system is based on previous experiment result [9]. The time domain voltage variations obtained from simulations and experiments match each other, proving the accuracy and effectiveness of the approach.

(a)

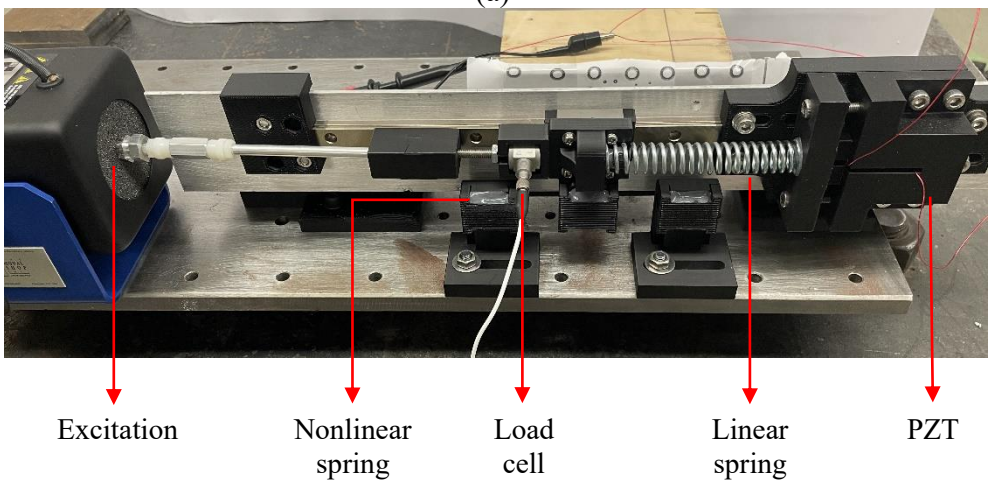

(b)

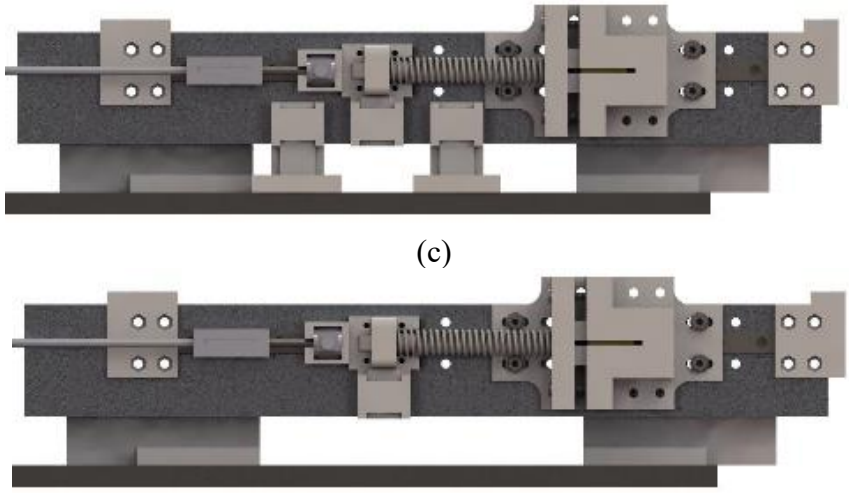

(c)

(d)

Figure 6-8 Experimental test setup. (a) Overall setup. (b) Detail design. (c) Nonlinear in parallel setup. (d) Linear setup.

Table 6-1 System parameters for experiment and simulation.

	Linear	Nonlinear in parallel
Equivalent mass m (kg)	0.158	0.158
Damping ratio ζ	5e-3	5e-3
Linear spring stiffness k_{l} (N/m)	2768	2768
Nonlinear spring stiffness k_{nl1} (N/m)	-	345.5
Nonlinear spring stiffness k_{nl3} (N/m^3)	-	3329371
Equivalent resistance R (Ohm)	1800000	1800000
Piezoelectric coefficient d_{33} ($10\mathrm{e}^{-12}$ C/N)	400	400
Force factor α (V/N)	0.2768	0.2768
PZT capacitance C_{p} (F)	2.136e-10	2.136e-10
Excitation amplitude F_0 (N)	6.25	6.25
Excitation frequency ω (rad/s)	62.832	62.832

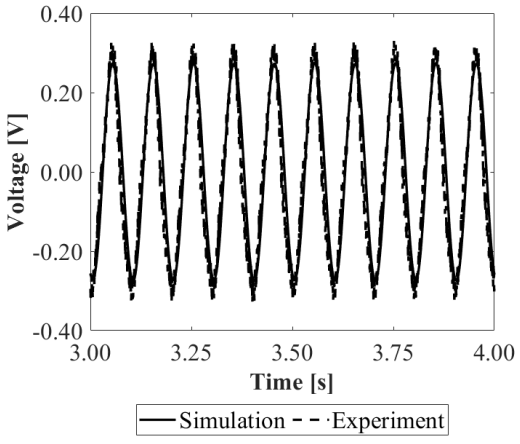

(a)

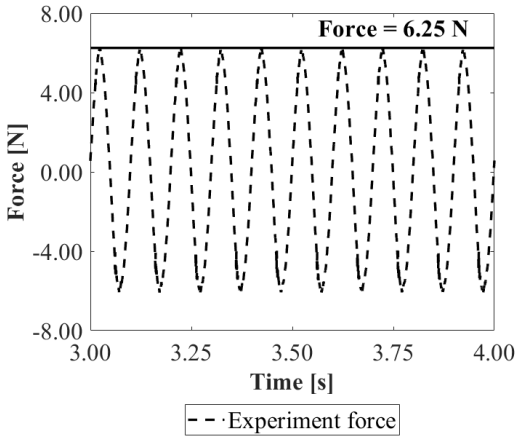

(b)

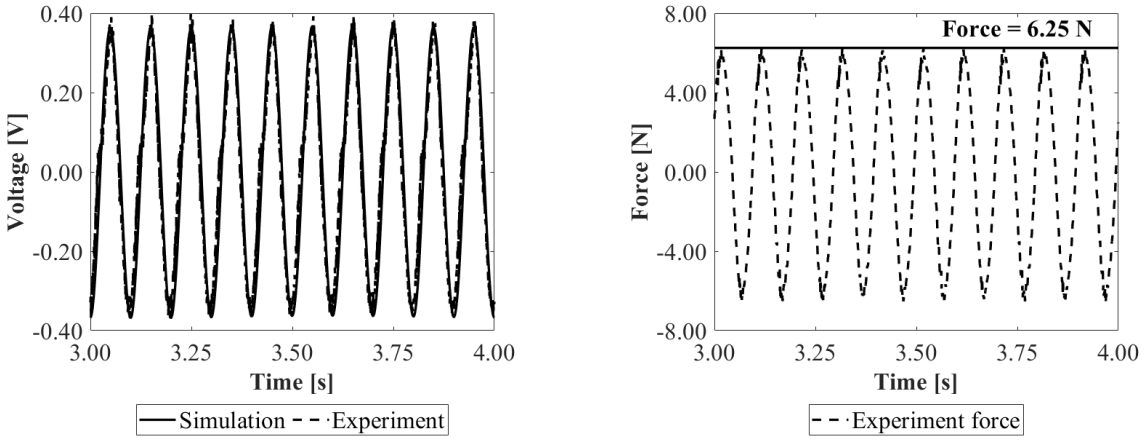

(c) (d)

Figure 6-9 Comparison of output voltage from experiment and simulation. (a) Voltage variation for nonlinear in parallel design. (b) Force variation for nonlinear in parallel. (c) Voltage variation for linear design. (d) Force variation for linear.

6.1.3 Parameter studies on energy generation

Figure 6-10(a)-(d) represents the RMS charging power distribution in the frequency domain with different linear spring ratio μ_{kl} of the linear spring in parallel system, nonlinear spring in parallel system, linear spring in series system, and nonlinear spring in series system, respectively. μ_{kl} is defined to be the ratio between the k_{l} and k_{nl1}. In order to properly compare the result, for the linear in parallel system, the equivalent spring stiffness of the whole system k is calculated to be $k = k_{\mathrm{eq}} + k_{\mathrm{nl1}}$. The stiffness of the linear spring itself in all different systems is calculated by $k_{\mathrm{l}} = \mu_{\mathrm{kl}} k_{\mathrm{nl1}}$ in this section. The RMS charging power is calculated based on Eq. (2.93). The operation bandwidth (OB) is calculated based on whether the saturated voltage on the storage capacitor meets the minimum required voltage (3 V). The sum of RMS charging power (SRCP) is obtained to be,

$$SRCP = \sum_{i=1}^{n} RMSP_i \times \Delta Freq, \tag{6.7}$$

where $RMSP_i$ is the RMS charging power in the corresponding frequencies within the operation bandwidth, and $\Delta Freq$ is the frequency interval.

And the following common parameters are used for the in parallel systems: m = 0.18563 kg, ζ = 0.005, F_0 = 0.15 N, k_{nl1} = 381.26 N/m, α = 0.23152 V/N, C_{p} = 3.0267e^{-10} F, C_{s} = 6e^{-8} F, and R = 36 MΩ. The following common parameters are used for the in series systems: m_1 =

0.02925 kg, m_2 = 0.15637 kg, ζ = 0.005, F_0 = 0.15 N, k_{nl1} = 381.26 N/m, α = 0.23152 V/N, C_{p} = 3.0267e^{-10} F, C_{s} = 6e^{-8} F, and R = 36 MΩ.

The resonance regions shift to the high frequency with higher peak RMS charging power in the frequency domain with the increase of linear spring ratio μ_{kl}. The sum of the RMS charging powers (SRCP) within the operation bandwidth increases with the increase of μ_{kl} as the equivalent deformation in the piezoelectric patch increases. The operation bandwidths (OB) increase with the increase of μ_{kl} for the linear in parallel system, linear in series system, and nonlinear in series system. The operation bandwidth (OB) decreases with the increase of μ_{kl} for the nonlinear in parallel system because of the weakened nonlinear effect.

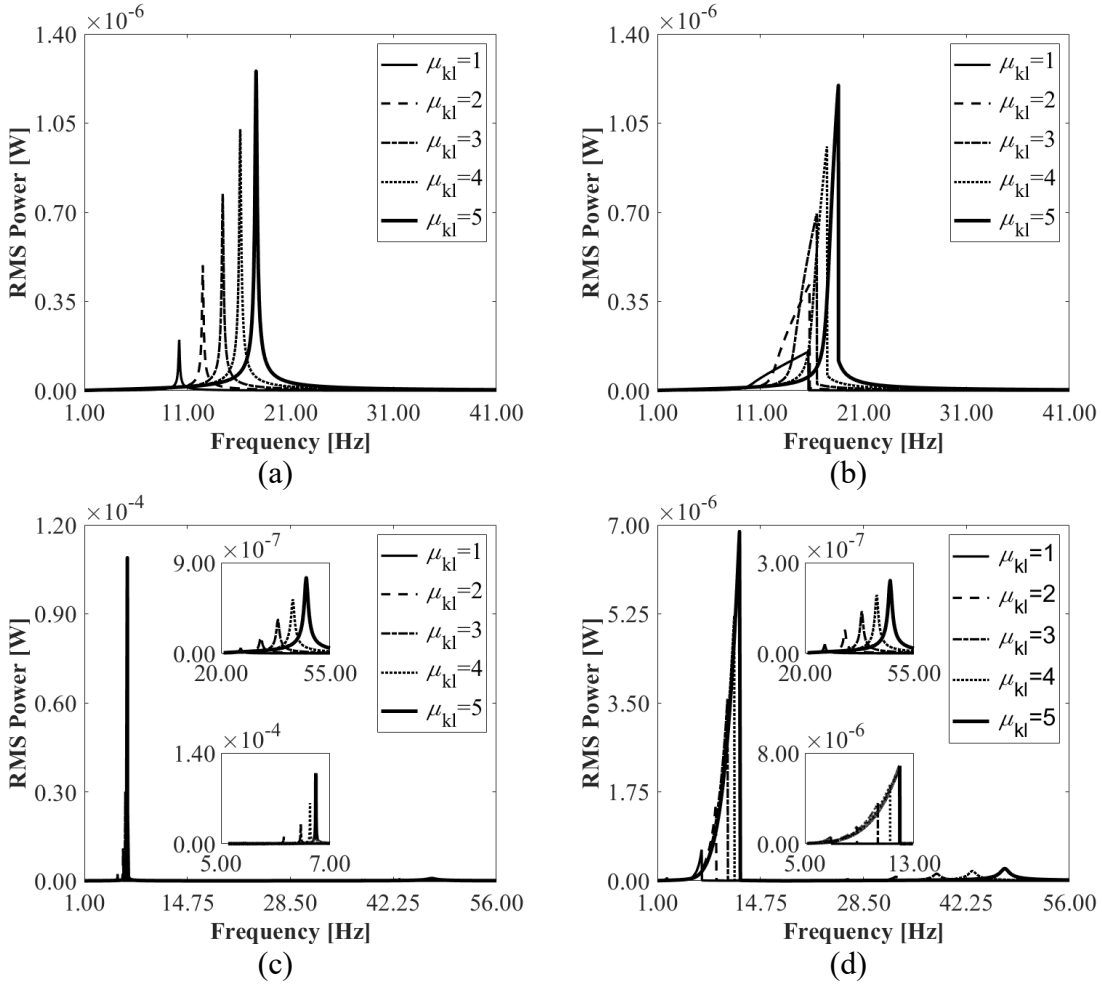

Figure 6-10 RMS charging power frequency response with different linear spring ratio μ_{kl}. (a) Linear in parallel system (k_{nl3} = 0 N/m^3). (b) Nonlinear in parallel system (k_{nl3} = 8261267.7 N/m^3). (c) Linear in series system (k_{nl3} = 0 N/m^3). (d) Nonlinear in series system (k_{nl3} = 8261267.7 N/m^3).

Comparing with the linear in parallel system with μ_{kl} = 5 (OB: 1.09 Hz; SRCP: 0.56 μW), the nonlinear in series system with μ_{kl} = 5 has an increment of 263.9% in OB and 1822.9% in SRCP. Comparing with the nonlinear in parallel system with μ_{kl} = 5 (OB: 1.43 Hz; SRCP: 0.99 μW), the nonlinear in series system with μ_{kl} = 5 has an increment of 177.0% in OB and 985.8% in SRCP. Comparing with the linear in series system with μ_{kl} = 5 (OB: 0.24 Hz; SRCP: 1.91 μW), the nonlinear in series system with μ_{kl} = 5 has an increment of 1527.0% in OB and 463.6% in SRCP. With the increase of μ_{kl} from 1 to 5, the OB of the nonlinear in series system increases from 0.91 Hz to 3.97 Hz, and the SRCP increases from 0.28 μW to 10.74 μW. However, the increase of μ_{kl} brings an opposite effect to the OB of the nonlinear in parallel system. It proves the possibility of increasing the OB and SRCP simultaneously by increasing μ_{kl} of the nonlinear in series system.

Table 6-2 The effect of the linear spring ratio μ_{kl} on operating bandwidth and sum of RMS charging power.

		μ_{kl} = 1	μ_{kl} = 2	μ_{kl} = 3	μ_{kl} = 4	μ_{kl} = 5
Config#1	OB (Hz)	0.27	0.51	0.73	0.92	1.09
	OBR (Hz)	10.07-10.34	12.24-12.75	14.06-14.79	15.67-16.59	17.12-18.21
	SRCP (μW)	0.03	0.13	0.26	0.40	0.56
Config#2	OB (Hz)	3.93	3.20	2.30	1.75	1.43
	OBR (Hz)	11.72-15.65	12.56-15.76	14.17-16.47	15.72-17.47	17.15-18.58
	SRCP (μW)	0.43	0.88	1.02	1.02	0.99
Config#3	OB (Hz)	0.18	0.21	0.23	0.24	0.24
	OBR (Hz)	5.33-5.51	6.05-6.26	6.35-6.58	6.51-6.75	6.62-6.86
		~	~	~	~	~
	SRCP (μW)	0.12	0.40	0.81	1.32	1.91
Config#4	OB (Hz)	0.91	1.83	2.85	3.45	3.97
	OBR (Hz)	6.00-6.91	6.99-8.82	7.51-10.36	7.81-11.26	7.99-11.96
		~	~	~	~	~
	SRCP (μW)	0.28	1.29	4.29	7.31	10.74

Abbreviation: OBR=operating bandwidth range.

Figure 6-11(a)-(d) shows the RMS charging power distribution in the frequency domain for the linear in series system and the nonlinear in series system with different mass ratios μ_m. The

equivalent mass of the linear and nonlinear in parallel system is 0.185625 kg for this study which consists of the weight of the magnet (0.02925 kg) and the rest of the components in the system. The mass ratio μ_{m} of the in-series system is defined to be m_1/m_2. To keep the total equivalent mass consistent with the in-parallel system, $m_2 = 0.185625/(1+\mu_{\mathrm{m}})$ and $m_1 = 0.185625 - m_2$. The operation bandwidth (OB) and SRCP of both the linear in series system and nonlinear in series system increase with the increase of μ_m.

And the following common parameters are used for the in series systems: ζ = 0.005, F_0 = 0.15 N, k_{l} = 450 N/m, k_{nl1} = 381.26 N/m, α = 0.23152 V/N, C_{p} = 3.0267e^{-10} F, C_{s} = 6e^{-8} F, and R = 36 MΩ.

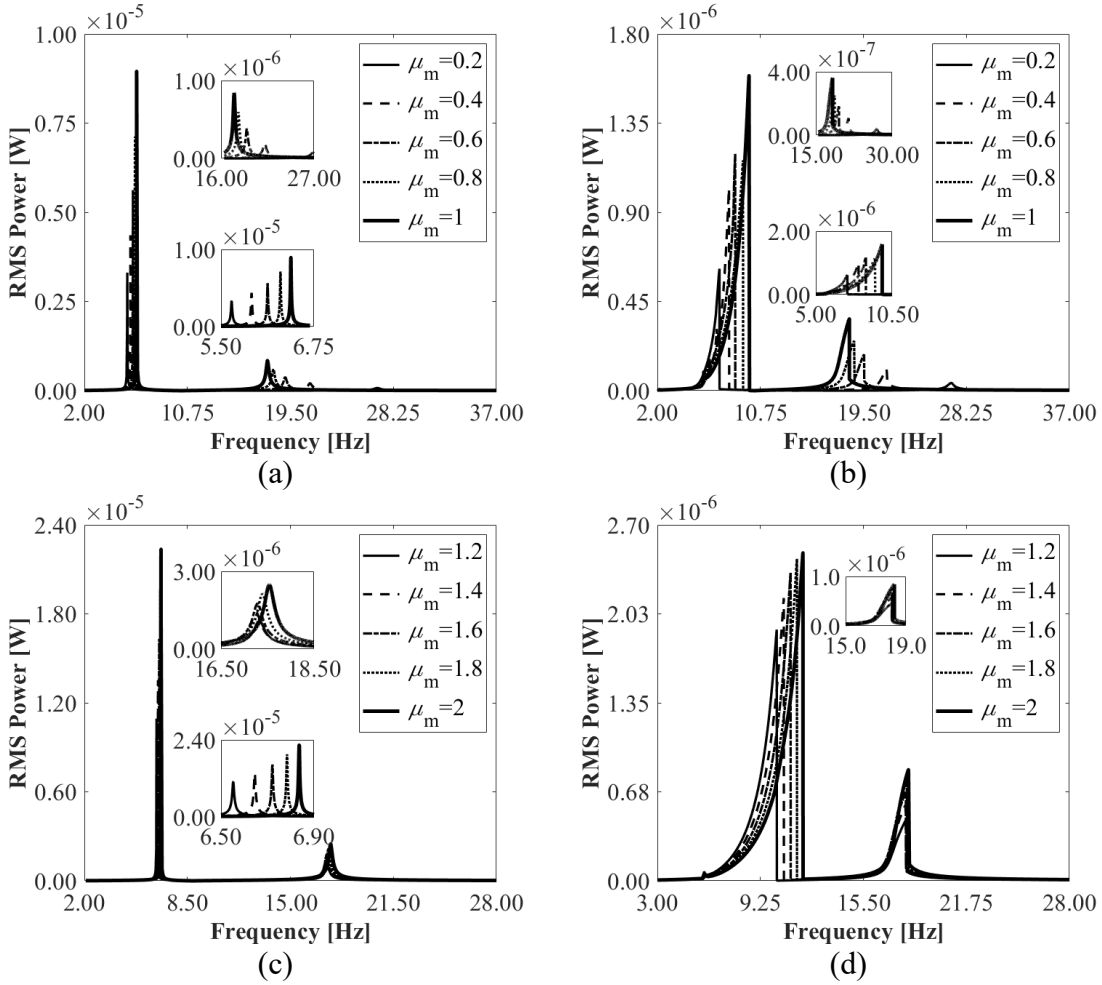

Figure 6-11 RMS charging power frequency response of nonlinear in series design with different mass ratios μ_{m}. (a) Linear in series μ_{m} = 0.2~1. (b) Nonlinear in series μ_{m} = 0.2~1. (c) Linear in series μ_{m} = 1.2~2. (d) Nonlinear in series μ_{m} = 1.2~2.

Comparing with the linear in series system with μ_m = 2 (OB: 0.80 Hz; SRCP: 1.35 μW), the nonlinear in series system with μ_m = 2 has an increment of 408.2% in OB and 162.9% in SRCP. While μ_m changes from 0.2 to 2, the OB of the nonlinear in series system increases from 1.039 Hz to 4.050 Hz, and the SRCP increases from 0.33 μW to 3.54 μW. It proves the possibility of increasing the OB and SRCP by adjusting the mass ratio of the nonlinear in series system.

Table 6-3 The effect of the mass ratios μ_m on operating bandwidth and sum of RMS charging power.

	Config#3			Config#4		
	OB (Hz)	OBR (Hz)	SRCP (μW)	OB (Hz)	OBR (Hz)	SRCP (μW)
μ_m = 0.2	0.19	5.55-5.74 ~ 5.82-6.01	0.16	1.04	6.24-7.28 ~ 6.75-8.08	0.33
μ_m = 0.4	0.19	5.82-6.01 ~ 6.03-6.21 19.01-19.11	0.20	1.33	6.75-8.08 ~ 6.85-8.61 19.53-19.57	0.61
μ_m = 0.6	0.30	6.03-6.21 19.01-19.11	0.27	1.81	6.85-8.61 19.53-19.57	0.87
μ_m = 0.8	0.44	6.21-6.39 17.93-18.18	0.39	2.60	7.08-9.28 18.31-18.72	1.25
μ_m = 1.0	0.52	6.35-6.53 17.39-17.73	0.51	2.95	7.49-9.78 17.66-18.31	1.76
μ_m = 1.2	0.58	6.47-6.64 17.11-17.53	0.65	3.24	7.80-10.24 17.32-18.12	2.20
μ_m = 1.4	0.64	6.57-6.72 17.01-17.50	0.81	3.50	8.07-10.67 17.17-18.06	2.60
μ_m = 1.6	0.70	6.65-6.79 17.02-17.56	0.98	3.72	8.31-11.08 17.13-18.07	2.99
μ_m = 1.8	0.75	6.71-6.85 17.09-17.69	1.16	3.90	8.54-11.47 17.18-18.14	3.27
μ_m = 2.0	0.80	6.77-6.90 17.21-17.87	1.34	4.05	8.74-11.83 17.28-18.24	3.54

Abbreviation: OBR=operating bandwidth range.

Figure 6-12(a)-(d) indicates the RMS charging power distribution in the frequency domain for the linear in parallel system, the nonlinear in parallel system, the linear in series system, and the nonlinear in series system with different widths of magnet w_m. While keeping the total volume of

the magnet the same, the weight of the magnet stays the same. However, Eqs. (6.1)-(6.3) indicate that changing the width, length, and thickness of the magnet result in different magnet forces, which may affect the system response. Here, the effect of changing the width of the magnet on the energy generation is studied when the length of the magnet is fixed. Keeping other parameters unchanged, the increase of w_{m} leads to the increase of both linear and nonlinear terms in the magnetic force, and the charging power variations can be seen in Figure 6-3(b). The SRCP of the four proposed systems decrease with the increase of w_{m}. For the linear in parallel system, nonlinear in parallel system and nonlinear in series system, the OB decrease with the increase of w_{m}. The OB increase with the increase of w_{m} for the linear in series system.

And the following common parameters are used for the in parallel systems: m = 0.18563 kg, ζ = 0.005, F_0 = 0.15 N, k_{l} = 450 N/m, α = 0.23152 V/N, C_{p} = 3.0267e^{-10} F, C_{s} = 6e^{-8} F, and R = 36 MΩ. The following common parameters are used for the in series systems: m_1 = 0.02925 kg, m_2 = 0.15637 kg, ζ = 0.005, F_0 = 0.15 N, k_{l} = 450 N/m, α = 0.23152 V/N, C_{p} = 3.0267e^{-10} F, C_{s} = 6e^{-8} F, and R = 36 MΩ.

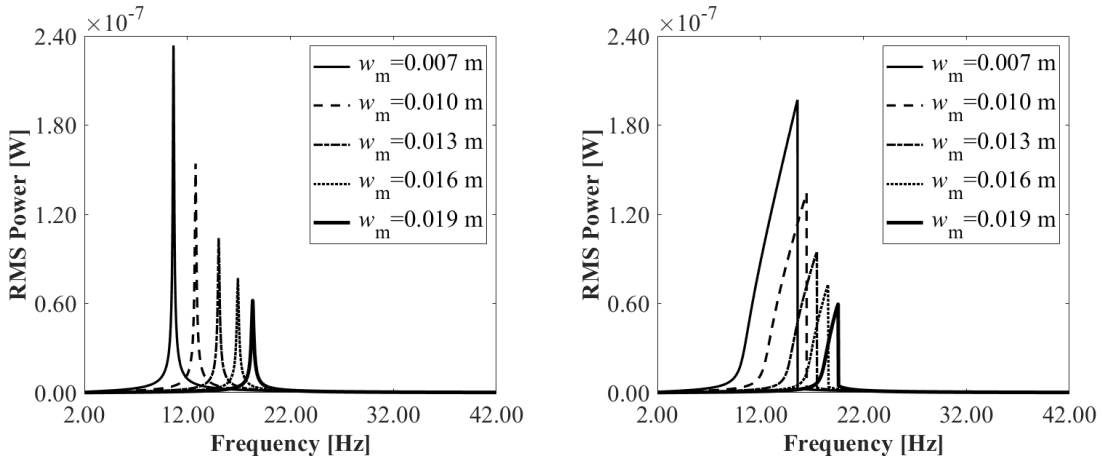

(a) (b)

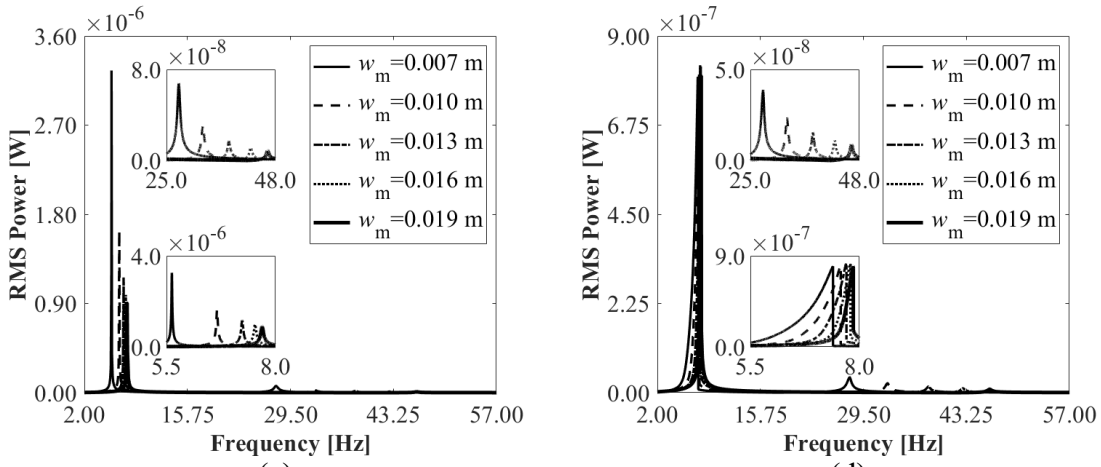

Figure 6-12 RMS charging power frequency response with different width of magnets w_m. (a) Linear in parallel system. (b) Nonlinear in parallel system. (c) Linear in series system. (d) Nonlinear in series system.

Comparing with the linear in parallel system with w_m = 0.007 m (OB: 0.31 Hz; SRCP: 0.04 μW), the nonlinear in series system with w_m = 0.007 m has an increment of 264.5% in OB and 902.5% in SRCP. Comparing with the linear in series system with w_m = 0.007 m (OB: 0.19 Hz; SRCP: 0.16 μW), the nonlinear in series system with w_m = 0.007 m has an increment of 513.4% in OB and 184.6% in SRCP. With w_m changes from 0.007 m to 0.019 m, the OB of the nonlinear in series system decreases from 1.14 Hz to 0.34 Hz, and the SRCP decreases from 0.45 μW to 0.14 μW. It shows that the increase of magnetic force has a negative effect on energy generation under the current excitation force amplitude.

Table 6-4 The effect of the width of magnet w_m on operating bandwidth and sum of RMS charging power.

		w_m = 0.007 m	w_m = 0.010 m	w_m = 0.013 m	w_m = 0.016 m	w_m = 0.019 m
Config#1	OB (Hz)	0.31	0.28	0.24	0.21	0.18
	OBR (Hz)	10.50-10.81	12.66-12.94	14.92-15.16	16.80-17.01	18.25-18.43
	SRCP (μW)	0.04	0.03	0.02	0.01	0.01
Config#2	OB (Hz)	3.94	2.75	1.65	0.98	0.60
	OBR (Hz)	11.66-15.60	13.74-16.49	15.84-17.49	17.60-18.58	18.95-19.55
	SRCP (μW)	0.55	0.28	0.12	0.06	0.03
Config#3	OB (Hz)	0.19	0.26	0.31	0.33	0.34
	OBR (Hz)	5.53-5.72	6.53-6.79	7.08-7.39	7.37-7.70	7.53-7.87
		~	~	~	~	~
	SRCP (μW)	0.16	0.14	0.13	0.13	0.13
Config#4	OB (Hz)	1.14	0.80	0.55	0.41	0.34
	OBR (Hz)	6.25-7.39	6.77-7.57	7.15-7.70	7.39-7.80	7.54-7.88
		~	~	~	~	~
	SRCP (μW)	0.45	0.32	0.24	0.18	0.14

Abbreviation: OBR=operating bandwidth range.

The above analysis proves the possibility of designing an energy generator with wide OB and high SRCP by adjusting μ_{kl}, μ_m, and w_m. A comparison of operating bandwidth and sum of RMS charging power for systems with the same linear spring stiffness is shown in Table 6-5. The difference between linear and nonlinear designs is nonlinearity induced by the magnet, the linear effect of the magnet is considered for both systems. The comparison is made under the conditions that the equivalent mass of the linear and nonlinear in parallel systems (1-DOF) and the total equivalent mass (m_1 and m_2) of the linear and nonlinear in series systems (2-DOF), the dimension of the piezoelectric shear patch, the dimension of the magnet, the harmonic excitation amplitude, and the stiffness of the linear spring are the same. These conditions make it possible to fabricate the energy generators with the same amount of material, which proves the practical application value and the possible improvement in energy generation.

Comparing with the linear in-parallel system with k_l = 450 N/m (OB: 0.31 Hz; SRCP: 0.05 μW), the nonlinear in parallel system with k_l = 450 N/m has an increment of 1160.0% in OB and 1030.9% in SRCP. Comparing with the linear in series system with k_l = 450 N/m and μ_m = 2.0

(OB: 0.80 Hz; SRCP: 1.35 μW), the nonlinear in series system with k_l = 450 N/m and μ_m = 2.0 has an increment of 408.2% in OB and 162.9% in SRCP. The result in Table 6-5 indicates that both the nonlinear in parallel and nonlinear in series systems can effectively broaden the operation bandwidth and enhance the sum of RMS charging power compared with the corresponding linear systems. The sum of RMS charging power of the in-series systems can be improved by tuning the mass ratio μ_m. Comparing with the linear in parallel system with k_l = 450 N/m (OB: 0.31 Hz; SRCP: 0.05 μW), nonlinear in parallel system with k_l = 450 N/m (OB: 3.94 Hz; SRCP: 0.55 μW), and the linear in series system with k_l = 450 N/m and μ_m = 2.0 (OB: 0.80 Hz; SRCP: 1.35 μW), the nonlinear in series system with k_l = 450 N/m and μ_m = 2.0 has increment of 1194.0% in OB and 7253.3% in SRCP, 2.7% in OB and 550.2% in SRCP, 408.2% in OB and 162.9% in SRCP, respectively. It proves the possibility of achieving both wide OB and high SRCP by properly designing the nonlinear in series system.

Table 6-5 Comparison of operating bandwidth and sum of RMS charging power for different systems with linear spring stiffness k_l = 450 N/m.

	OB (Hz)	OBR (Hz)	SRCP (μW)
Config#1 (k_l = 450 N/m)	0.31	10.50-10.81	0.05
Config#2 (k_l = 450 N/m)	3.94	11.66-15.60	0.55
Config#3 (k_l = 450 N/m and μ_m = 1.0)	0.52	6.35-6.53 17.39-17.73	0.51
Config#3 (k_l = 450 N/m and μ_m = 2.0)	0.80	6.77-6.90 17.21-17.87	1.35
Config#4 (k_l = 450 N/m and μ_m = 1.0)	2.95	7.49-9.78 17.66-18.30	1.76
Config#4 (k_l = 450 N/m and μ_m = 2.0)	4.05	8.74-11.83 17.28-18.24	3.54

Abbreviation: OBR=operating bandwidth range.

6.2 Magnet-engaged piezoelectric energy generation under friction excitation

The schematics of the proposed piezoelectric energy generators are shown in Figure 6-14 and Figure 6-14, which represent the shear mode nonlinear in-parallel system and shear mode nonlinear in-series system. The difference between the shear mode nonlinear in-parallel system and the shear mode nonlinear in-series system is the layout of the piezoelectric patch and the total system equivalent mass. The piezoelectric patch in both systems, which is shown in hatch line, is considered as connected in series with the linear shear tension spring k_l and the stiffness constant

k_{piezo} of the piezoelectric patch in shear mode is calculated from the elastic constant c_{55}^{E}. Figure 6-14(a) demonstrates the shear mode nonlinear in-parallel system, in which two magnets are attached to the mass block. The generated magnetic force acts as a nonlinear spring expressed in an empirical form ($F_{\text{m}}(y(t)) = k_{\text{nl1}}y(t) + k_{\text{nl3}}y(t)^3$), and nonlinear spring is connected in parallel with the equivalent linear spring. Figure 6-14(a) displays the shear mode nonlinear in-series system, and the nonlinear spring is connected in series with the system described in Figure 6-14(a) by adding the magnet to the bottom of the linear tension spring k_{l} to form a new nonlinear system. Corresponding linear systems for comparison are made by adding an equivalent linear shear spring with the same stiffness of the linear term of the nonlinear magnetic force to the top of m and the bottom of m_1, correspondingly, they are shown in Figure 6-14(b) and Figure 6-14(b).

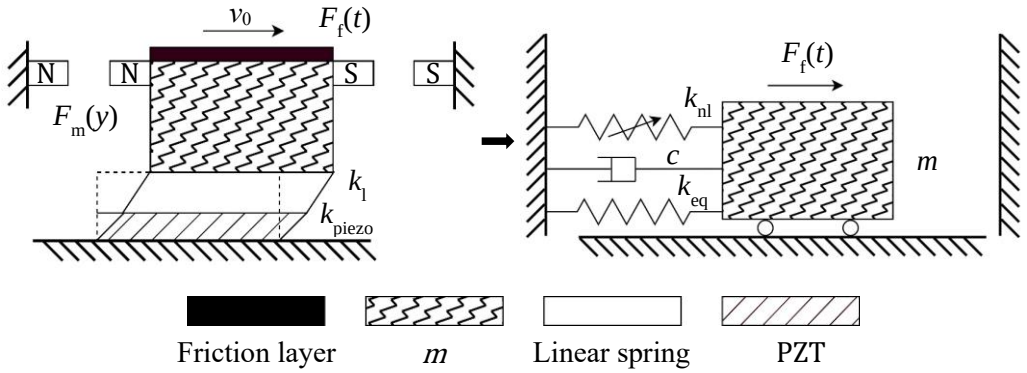

(a)

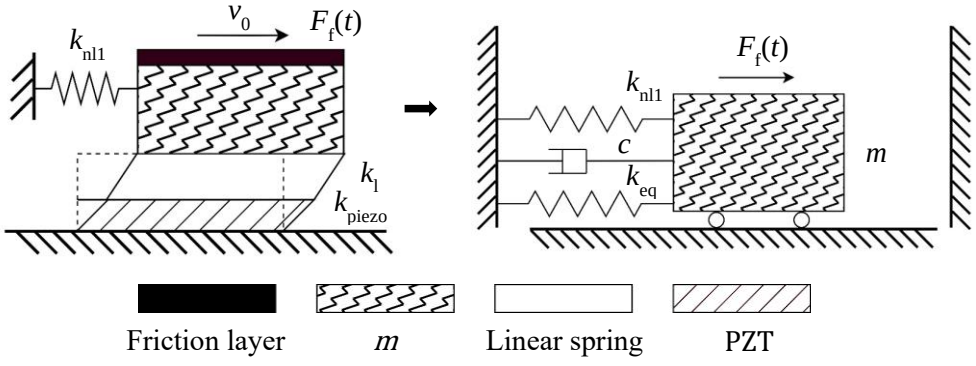

(b)

Figure 6-13 Schematic diagrams of the proposed nonlinear spring in parallel piezoelectric energy generators. (a) Shear-mode system with nonlinear spring in parallel under friction excitation. (b) Shear-mode system with linear spring in parallel under friction excitation.

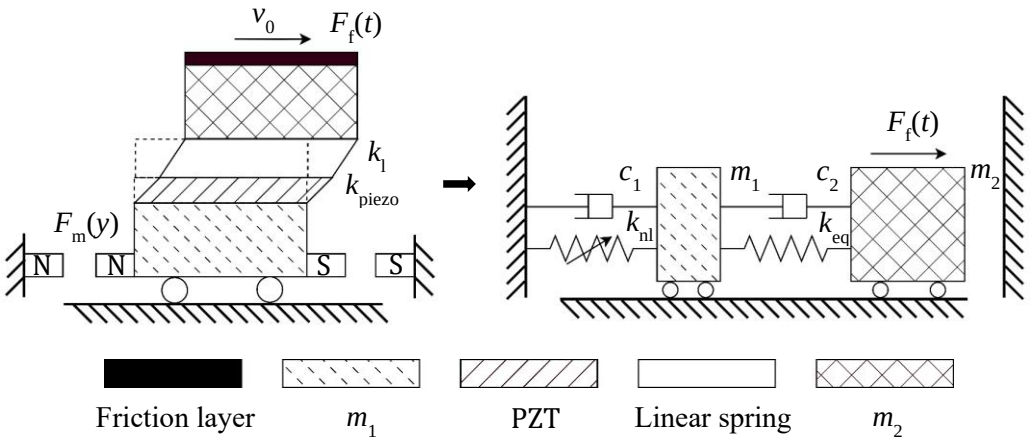

(a)

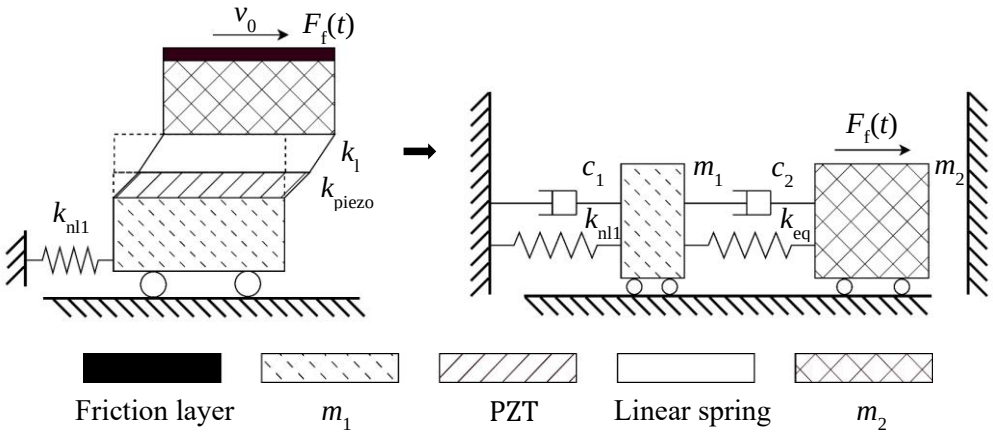

(b)

Figure 6-14 Schematic diagrams of the proposed nonlinear spring in series piezoelectric energy generators. (a) Shear-mode system with nonlinear spring in series under friction excitation. (b) Shear-mode system with linear spring in series under friction excitation.

A rigid moving plate is contacting with the friction layer of the mass block and moving at a constant velocity v_0 horizontally, and friction force will be generated between the moving plate and the friction layer of the mass block. The systems will be under FIV. The detailed derivation of the empirical form of the magnetic force will be introduced in the next section, and the details of the system parameters are then explained. The calculation of the equivalent magnetic force and its representation is described in Section 6.1.

6.2.1 Mechanical and piezoelectric coupled modeling

Considering the electromechanical effect of the system, the mechanical and piezoelectric coupling equations of the systems under friction can be written as follows.

Nonlinear spring in-parallel:

$$\begin{cases} m\ddot{y}(t) + c\dot{y}(t) + k_{\mathrm{eq}}y(t) + k_{\mathrm{nl1}}y(t) + k_{\mathrm{nl3}}y^3(t) + \alpha\frac{k_{\mathrm{l}}}{k_{\mathrm{l}}+k_{\mathrm{piezo}}}V_{\mathrm{RIP}}(t) = F_{\mathrm{f}}(t) \\ V_{\mathrm{RIP}}(t) + RC_{\mathrm{p}}\dot{V}_{\mathrm{RIP}}(t) - R\alpha\frac{k_{\mathrm{l}}}{k_{\mathrm{l}}+k_{\mathrm{piezo}}}\dot{y}(t) = 0 \end{cases}. \tag{6.8}$$

Linear spring in-parallel:

$$\begin{cases} m\ddot{y}(t) + c\dot{y}(t) + k_{\mathrm{eq}}y(t) + k_{\mathrm{nl1}}y(t) + \alpha\frac{k_{\mathrm{l}}}{k_{\mathrm{l}}+k_{\mathrm{piezo}}}V_{\mathrm{RIP}}(t) = F_{\mathrm{f}}(t) \\ V_{\mathrm{RIP}}(t) + RC_{\mathrm{p}}\dot{V}_{\mathrm{RIP}}(t) - R\alpha\frac{k_{\mathrm{l}}}{k_{\mathrm{l}}+k_{\mathrm{piezo}}}\dot{y}(t) = 0 \end{cases}. \tag{6.9}$$

Nonlinear spring in-series:

$$\begin{cases} m_1\ddot{y}_1(t) + (c_1+c_2)\dot{y}_1(t) - c_2\dot{y}_2(t) + \left(k_{\mathrm{nl1}}+k_{\mathrm{eq}}\right)y_1(t) \\ \quad +k_{\mathrm{nl3}}{y_1}^3(t) - k_{\mathrm{eq}}y_2(t) = 0 \\ m_2\ddot{y}_2(t) + c_2(\dot{y}_2(t) - \dot{y}_1(t)) + k_{\mathrm{eq}}(y_2(t) - y_1(t)) \\ \quad +\alpha\frac{k_{\mathrm{l}}}{k_{\mathrm{l}}+k_{\mathrm{piezo}}}V_{\mathrm{RIS}}(t) = F_{\mathrm{f}}(t) \\ V_{\mathrm{RIS}}(t) + RC_{\mathrm{p}}\dot{V}_{\mathrm{RIS}}(t) - R\alpha\frac{k_{\mathrm{l}}}{k_{\mathrm{l}}+k_{\mathrm{piezo}}}(\dot{y}_2(t) - \dot{y}_1(t)) = 0 \end{cases}. \tag{6.10}$$

Linear spring in-series:

$$\begin{cases} m_1\ddot{y}_1(t) + (c_1+c_2)\dot{y}_1(t) - c_2\dot{y}_2(t) + (k_{\mathrm{nl1}}+k_{\mathrm{eq}})y_1(t) - k_{\mathrm{eq}}y_2(t) = 0 \\ m_2\ddot{y}_2(t) + c_2(\dot{y}_2(t) - \dot{y}_1(t)) + k_{\mathrm{eq}}(y_2(t) - y_1(t)) + \alpha\frac{k_{\mathrm{l}}}{k_{\mathrm{l}}+k_{\mathrm{piezo}}}V_{\mathrm{RIS}}(t) = F_{\mathrm{f}}(t) \\ V_{\mathrm{RIS}}(t) + RC_{\mathrm{p}}\dot{V}_{\mathrm{RIS}}(t) - R\alpha\frac{k_{\mathrm{l}}}{k_{\mathrm{l}}+k_{\mathrm{piezo}}}(\dot{y}_2(t) - \dot{y}_1(t)) = 0 \end{cases}. \tag{6.11}$$

k_{eq} is the equivalent stiffness of the linear spring k_{l} and k_{piezo} in the series-connected state, which can be calculated as $k_{\mathrm{eq}} = k_{\mathrm{l}}k_{\mathrm{piezo}}/\left(k_{\mathrm{l}} + k_{\mathrm{piezo}}\right)$. The detailed iterative solving process is depicted in Section 2.3 for the in-parallel system, and Section 2.4 for the in-series systems.

The experiment validation of the proposed PEGs will be carried out as one of the future works to investigate the actual operating velocity range and energy generation performance.

6.2.2 System stability analysis

The stability of the systems is judged by the stability of the equilibrium points, obtained by solving the nonlinear equations in the state space form. Based on the first-order approximation theory, the stability of the systems near the equilibrium point can be obtained by linear analysis. Assuming that the relative velocity v_{r} is always positive [67], [130], $\mu_{\mathrm{slide}}(v_{\mathrm{r}})$ and F_{f} can be expressed as,

$$\mu_{\mathrm{slide}}(v_r) = \mu_{\mathrm{k}} + (\mu_{\mathrm{static}} - \mu_{\mathrm{k}})e^{-\beta v_{\mathrm{r}}}\ (v_{\mathrm{r}} \geq 0), \tag{6.12}$$

$$F_{\mathrm{f}} = [\mu_{\mathrm{k}} + (\mu_{\mathrm{static}} - \mu_{\mathrm{k}})e^{-\beta(v_0 - \dot{y})}]F_{\mathrm{N}}. \tag{6.13}$$

Based on Eq. (6.8) and defining $x_1 = y$, $x_2 = \dot{y}$, $x_3 = V_{\mathrm{RIP}}$, the state space form of the nonlinear in-parallel system can be expressed as,

$$\begin{cases} \dot{x}_1 = x_2 \\ \dot{x}_2 = -\frac{c}{m}x_2 - \frac{(k_{\mathrm{eq}}+k_{\mathrm{nl1}})}{m}x_1 - \frac{k_{\mathrm{nl3}}}{m}{x_1}^3 - \frac{\alpha}{m}\left(\frac{k_{\mathrm{l}}}{k_{\mathrm{l}}+k_{\mathrm{piezo}}}\right)x_3 \\ \qquad + \frac{[\mu_{\mathrm{k}}+(\mu_{\mathrm{static}}-\mu_{\mathrm{k}})e^{-\beta(v_0-x_2)}]F_{\mathrm{N}}}{m} \\ \dot{x}_3 = \frac{\alpha}{C_{\mathrm{p}}}\left(\frac{k_{\mathrm{l}}}{k_{\mathrm{l}}+k_{\mathrm{piezo}}}\right)x_2 - \frac{x_3}{RC_{\mathrm{p}}} \end{cases}. \tag{6.14}$$

Let the terms on the right-hand side of Eq. (6.14) be zero to obtain the equilibrium points $x_0 = [x_{10}, 0, 0]$,

$$\begin{cases} x_{20} = 0 \\ -cx_{20} - (k_{\mathrm{eq}} + k_{\mathrm{nl1}})x_{10} - k_{\mathrm{nl3}}{x_{10}}^3 - \alpha\frac{k_{\mathrm{l}}}{k_{\mathrm{l}}+k_{\mathrm{piezo}}}x_{30} \\ \qquad +[\mu_{\mathrm{k}} + (\mu_{\mathrm{static}} - \mu_{\mathrm{k}})e^{-\beta(v_0 - x_{20})}]F_{\mathrm{N}} = 0 \\ \frac{\alpha}{C_{\mathrm{p}}}\left(\frac{k_{\mathrm{l}}}{k_{\mathrm{l}}+k_{\mathrm{piezo}}}\right)x_{20} - \frac{x_{30}}{RC_{\mathrm{p}}} = 0 \end{cases}. \tag{6.15}$$

Substituting x_{20} = 0 and x_{30} = 0 into Eq. (6.15), a cubic equation of x_{10} can be obtained as,

$$-(k_{\mathrm{eq}} + k_{\mathrm{nl1}})x_{10} - k_{\mathrm{nl3}}{x_{10}}^3 + [\mu_{\mathrm{k}} + (\mu_{\mathrm{static}} - \mu_{\mathrm{k}})e^{-\beta v_0}]F_{\mathrm{N}} = 0. \tag{6.16}$$

Though there are three roots in Eq. (6.16), only one root has the physical meaning because the other two are a pair of complex conjugates. For the linear in-parallel system, equilibrium points can be obtained by substituting k_{nl3} = 0 into Eq. (6.16). Considering the emergence of limit cycle to be the boundary of the stable and unstable region of the system, the vibration of the system tends to the equilibrium position, and the system is in the stable region, whereas the system diverges to limit cycle oscillation and the system is in the unstable region. Then, we can do the iteration with a small step size using different parameters to plot the stable region. Considering the impact of the

friction characteristics on stability analysis, the effects of μ_{static}, μ_{k}, and β on the stable region is calculated.

Based on Eq. (6.10) and defining $z_1 = y_1$, $z_2 = \dot{y}_1$, $z_3 = y_2$, $z_4 = \dot{y}_2$, $z_5 = V_{\text{RIS}}$, the state space form of the nonlinear in-series system can be expressed as,

$$\begin{cases} \dot{z}_1 = z_2 \\ \dot{z}_2 = \frac{c_2}{m_1} z_4 - \frac{(c_1+c_2)}{m_1} z_2 - \frac{(k_{\text{eq}}+k_{\text{nl1}})}{m_1} z_1 - \frac{k_{\text{nl3}}}{m_1} {z_1}^3 + \frac{k_{\text{eq}}}{m_1} z_3 \\ \dot{z}_3 = z_4 \\ \dot{z}_4 = -\frac{c_2}{m_2}(z_4 - z_2) - \frac{k_{\text{eq}}}{m_2}(z_3 - z_1) - \frac{\alpha}{m}\left(\frac{k_{\text{l}}}{k_{\text{l}}+k_{\text{piezo}}}\right) z_5 \\ \qquad + \frac{[\mu_{\text{k}} + (\mu_{\text{static}} - \mu_{\text{k}}) e^{-\beta(v_0 - z_4)}] F_{\text{N}}}{m_2} \\ \dot{z}_5 = \frac{\alpha}{C_{\text{p}}}\left(\frac{k_{\text{l}}}{k_{\text{l}}+k_{\text{piezo}}}\right)(z_4 - z_2) - \frac{z_5}{RC_{\text{p}}} \end{cases} . \tag{6.17}$$

Let the terms on the right-hand side of Eq. (6.17) be zero to obtain the equilibrium points $z_0 = [z_{10}, 0, z_{30}, 0, 0]$,

$$\begin{cases} z_{20} = 0 \\ c_2 z_{40} - (c_1 + c_2) z_{20} - \left(k_{\text{eq}} + k_{\text{nl1}}\right) z_{10} - k_{\text{nl3}} {z_{10}}^3 + k_{\text{eq}} z_{30} = 0 \\ z_{40} = 0 \\ -c_2(z_{40} - z_{20}) - k_{\text{eq}}(z_{30} - z_{10}) - \alpha \frac{k_{\text{l}}}{k_{\text{l}}+k_{\text{piezo}}} z_{50} \\ \qquad + [\mu_{\text{k}} + (\mu_{\text{static}} - \mu_{\text{k}}) e^{-\beta(v_0 - z_{40})}] F_{\text{N}} = 0 \\ \frac{\alpha}{C_{\text{p}}}\left(\frac{k_{\text{l}}}{k_{\text{l}}+k_{\text{piezo}}}\right)(z_{40} - z_{20}) - \frac{z_{50}}{RC_{\text{p}}} = 0 \end{cases} . \tag{6.18}$$

Substituting $z_{20} = 0$, $z_{40} = 0$, and $z_{50} = 0$ into Eq. (6.18), z_{10} and z_{30} can be obtained as,

$$-k_{\text{eq}}(z_{30} - z_{10}) + k_{\text{nl1}} z_{10} + k_{\text{nl3}} {z_{10}}^3 = 0, \tag{6.19}$$

$$-k_{\text{eq}}(z_{30} - z_{10}) + [\mu_{\text{k}} + (\mu_{\text{static}} - \mu_{\text{k}}) e^{-\beta v_{\text{r}}}] F_{\text{N}} = 0, \tag{6.20}$$

where $v_{\text{r}} = v_0 - z_{40}$, re-arranging Eq. (6.19) and Eq. (6.20) yields,

$$k_{\text{nl1}} z_{10} + k_{\text{nl3}} {z_{10}}^3 - [\mu_{\text{k}} + (\mu_{\text{static}} - \mu_{\text{k}}) e^{-\beta v_0}] F_{\text{N}} = 0, \tag{6.21}$$

$$z_{30} = z_{10} + [\mu_{\text{k}} + (\mu_{\text{static}} - \mu_{\text{k}}) e^{-\beta v_0}] \frac{F_{\text{N}}}{k_{\text{eq}}}, \tag{6.22}$$

The real root can be solved. For the linear in-series system, equilibrium points can be obtained by substituting $k_{\text{nl3}} = 0$ into Eq. (6.21). Then, we can do the iteration with a small step size using different parameters to plot the stable region and study the effects of μ_{static}, μ_{k}, and β on the stable region.

Figure 6-15 and Figure 6-16 showed the effect of different exponential decay factor β and damping coefficient c on stable and unstable regions of the in-parallel and the in-series systems. Figure 6-15(a) and Figure 6-16(a) demonstrated the systems' stability under the nonlinear magnetic force, whereas Figure 6-15(b) and Figure 6-16(b) displayed the linear systems' stability for comparison in which the nonlinear term k_{nl3} is set to be zero. It is worth noting that this work concentrates on utilizing the self-excited FIV in the unstable region, and it is different from other research work focusing on suppressing FIV. It can be seen from Figure 6-15 and Figure 6-16 that the damping coefficient has a significant effect on the stable and unstable regions of all the systems, and a smaller damping coefficient can increase the unstable region. Figure 6-15(a) and (b) showed that, with the increase of β, the critical velocity v_0 reduces, which consequently leads to a smaller unstable region. And the critical velocities under different applied normal force F_{N} in the linear and nonlinear in-parallel systems are close to each other. Figure 6-16(a) and (b) showed similar variation trends of the unstable region with the increase of β, but critical velocities under different applied normal forces in the linear in-series system are smaller than the nonlinear in-series system, which can be caused by the introduced nonlinearity.

And the following common parameters are used for the in parallel designs: m = 0.619 kg, k_{l} = 50000 N/m, k_{nl1} = 1.903e^3 N/m, μ_{static} = 0.6, and μ_{k} = 0.2. The following standard parameters are used for the in-series designs: m_1 = 0.093 kg, m_2 = 0.526 kg, k_{l} = 50000 N/m, k_{nl1} = 1.903e^3 N/m, μ_{static} = 0.6, and μ_{k} = 0.2.

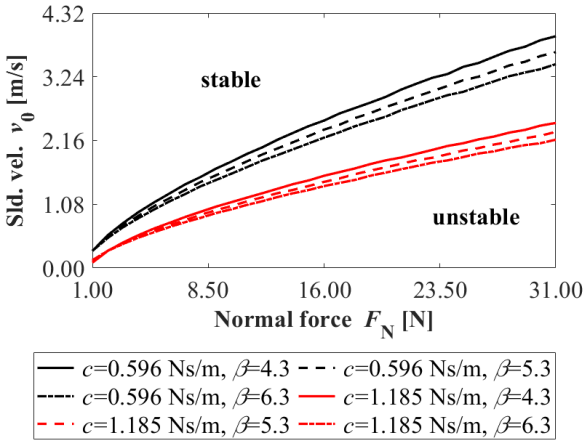

(a)

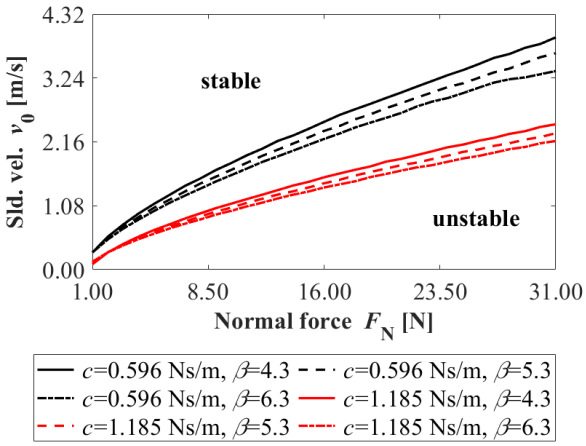

(b)

Figure 6-15 Stable region in terms of β. (a) Nonlinear in-parallel design (k_{nl3} = 1.123e^7 N/m^3). (b) Linear in-parallel design (k_{nl3} = 0 N/m^3).

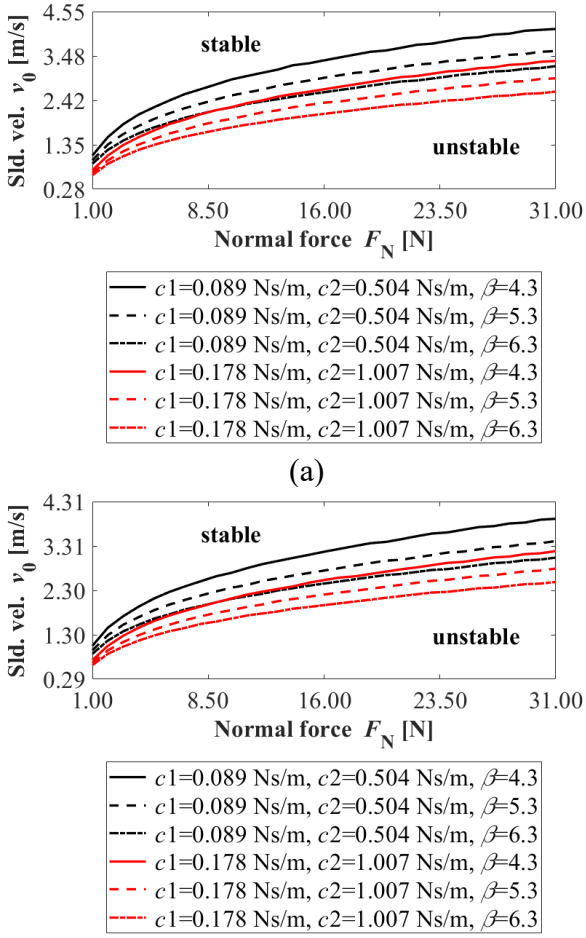

(a)

(b)

Figure 6-16 Stable regions in terms of β. (a) Nonlinear in-series design (k_{nl3} = 1.123e^7 N/m^3). (b) Linear in-series design (k_{nl3} = 0 N/m^3).

Figure 6-17 and Figure 6-18 showed the effect of different static friction coefficient μ_{static} on stable and unstable regions of the in-parallel and the in-series systems, and they revealed similar variation trends in the stable and unstable regions with different damping coefficients. Figure 6-17(a) and (b) showed that, with the increase of μ_{static}, the critical velocity v_0 increases, which consequently leads to a larger unstable region. And the critical velocities under different applied normal force F_{N} in the linear and nonlinear in-parallel systems are close to each other with small μ_{static}. With F_{N} = 31 N, μ_{static} = 0.4, and c = 0.596 Ns/m, v_0 in the nonlinear in-parallel system is 2.453 m/s and v_0 in the linear in-parallel system is 2.452 m/s. With μ_{static} = 0.8 and other parameters unchanged, v_0 in the nonlinear in-parallel system is 5.205 m/s and v_0 in the linear in-parallel system is 5.029 m/s. It implied that the increased μ_{static} may induce stronger nonlinear effect on the system which can enlarge the unstable region. Figure 6-18(a) and (b) showed similar variation trends of unstable region with the increase of μ_{static}, and the critical velocities in the linear in-series and the nonlinear in-series systems still revealed introduced nonlinear effect which can expand the unstable region.

And the following common parameters are used for the in parallel designs: m = 0.619 kg, k_{l} = 50000 N/m, k_{nl1} = 1.903e^3 N/m, β = 4.3, and μ_{k} = 0.2. The following common parameters are used for the in series designs: m_1 = 0.093 kg, m_2 = 0.526 kg, k_{l} = 50000 N/m, k_{nl1} = 1.903e^3 N/m, β = 4.3, and μ_{k} = 0.2.

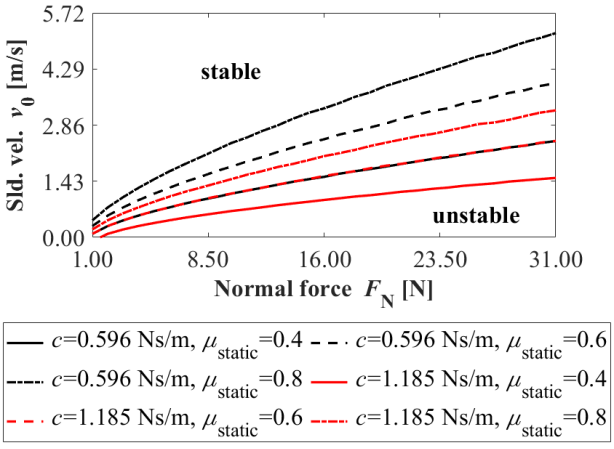

(a)

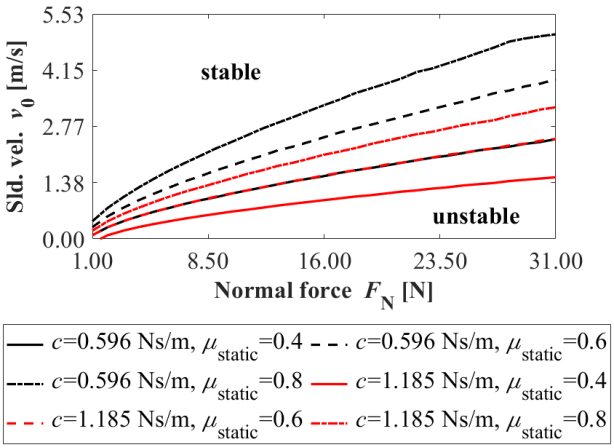

(b)

Figure 6-17 Stable regions in terms of μ_{static}. (a) Nonlinear in-parallel design (k_{nl3} = 1.123e^7 N/m^3). (b) Linear in-parallel design (k_{nl3} = 0 N/m^3).

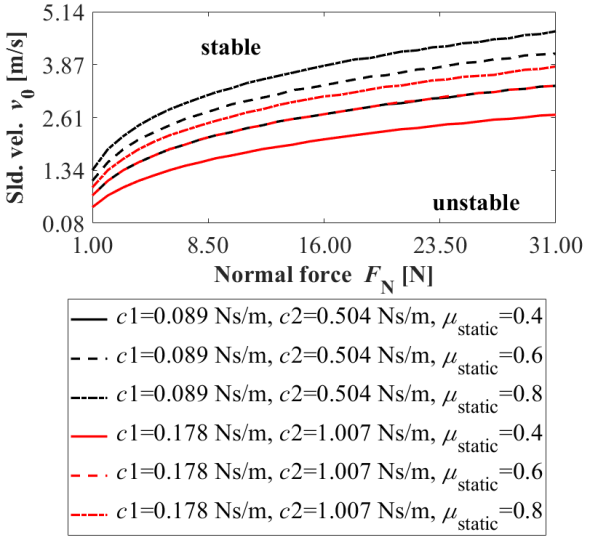

(a)

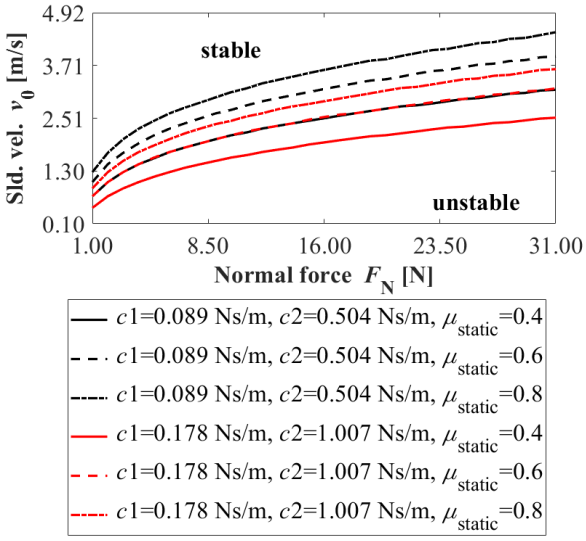

(b)

Figure 6-18 Stable region in terms of μ_{static} of in-series design. (a) Nonlinear in-series design (k_{nl3} = 1.123e^7 N/m^3). (b) Linear in-series design (k_{nl3} = 0 N/m^3).

Figure 6-19 and Figure 6-20 showed the effect of different dynamic friction coefficient μ_{k} on stable and unstable regions of the in-parallel and the in-series systems, and they displayed similar variation trends on the stable and unstable regions with different β. With other parameters unchanged, larger μ_{k} brought smaller unstable region. With the selected μ_{static} = 0.6, no obvious nonlinear effect with larger v_0 in the nonlinear in-parallel system can be observed. However, the larger v_0 in the nonlinear in-series system compared to the linear in-series can still be noticed. The effects of μ_{static}, μ_{k}, and β on the stability of linear and nonlinear systems indicates that the broad unstable region can be achieved via the introduced nonlinearity. The analysis of energy generation performance will be introduced in the energy generation section.

And the following common parameters are used for the in parallel designs: m = 0.619 kg, k_{l} = 50000 N/m, k_{nl1} = 1.903e^3 N/m, β = 4.3, and μ_{static} = 0.6. The following common parameters are used for the in-series designs: m_1 = 0.093 kg, m_2 = 0.526 kg, k_{l} = 50000 N/m, k_{nl1} = 1.903e^3 N/m, β = 4.3, and μ_{static} = 0.6.

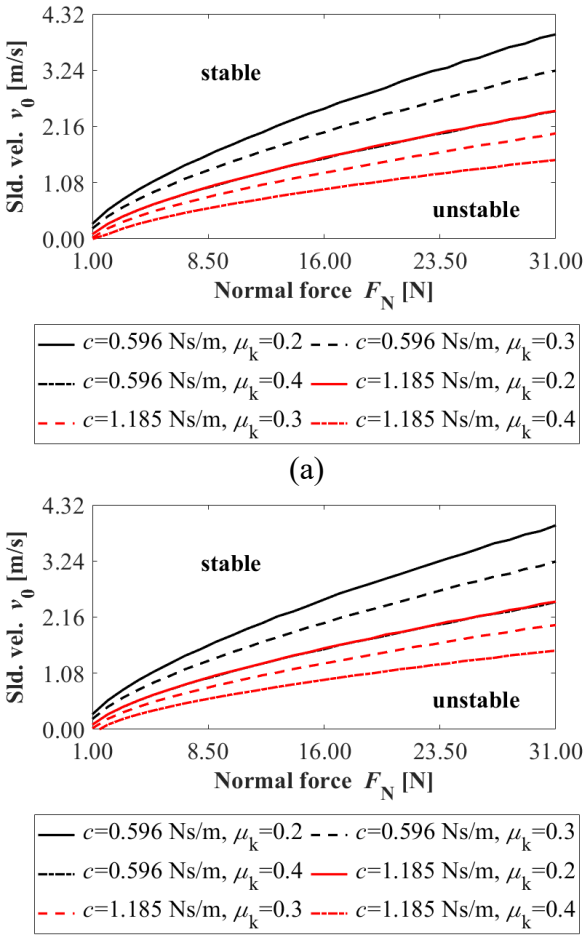

(a)

(b)

Figure 6-19 Stable regions in terms of μ_k. (a) Nonlinear in-parallel design (k_{nl3} = 1.123e^7 N/m^3). (b) Linear in-parallel design (k_{nl3} = 0 N/m^3).

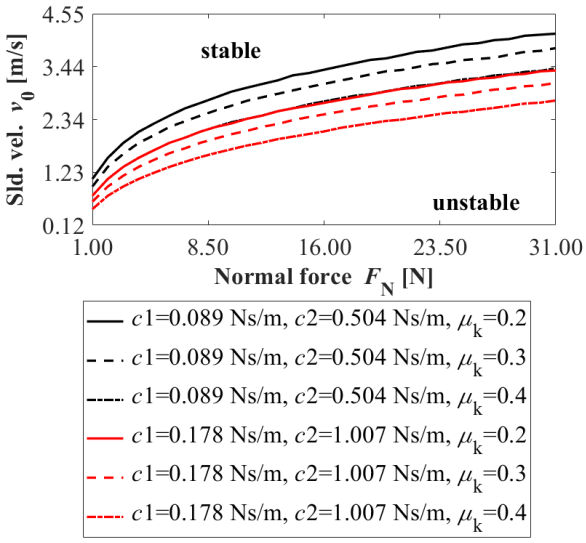

(a)

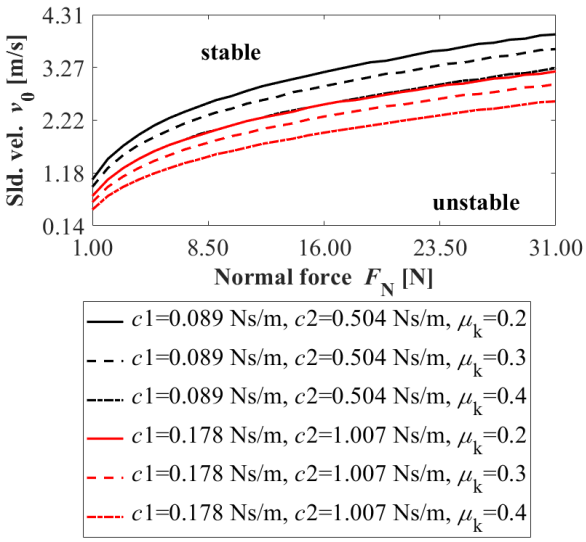

(b)

Figure 6-20 Stable region in terms of μ_k. (a) Nonlinear in-series design (k_{nl3} = 1.123e^7 N/m^3). (b) Linear in-series design (k_{nl3} = 0 N/m^3).

Overall, the introduction of magnetic nonlinearity of the vibration system will slightly increase the critical sliding velocity leading to FIV. This effect is more obvious with the in-series connection between the magnetic spring and the linear piezoelectric module, and it is not significant for the in-parallel systems.

6.2.3 Parameter studies on energy generation

The influence of μ_{static}, μ_k, and β on the energy generation performance is studied in this section, and the operating velocity range (OVR) and the sum of RMS charging power (SRCP) are used to assess the performance. The RMS charging power is calculated based on Eq. (2.93). The operating velocity range (OVR) is calculated based on whether the saturated voltage on the storage capacitor reaches the minimum required voltage (3 V). The sum of RMS charging power (SRCP) is obtained to be,

$$SRCP = \sum_{i=1}^{n} RMSP_i \times \Delta v_0, \tag{6.23}$$

where $RMSP_i$ is the RMS charging power of the corresponding velocity within the OVR, and Δv_0 is the interval of sliding velocity. $SRCP$ represents the covered area of the RMS charging power curve, which can be used to reflect the energy generation performance within the operating velocity range.

Figure 6-21 and Figure 6-22 demonstrate the effect of the exponential decay factor β on energy generation performance under two different electric resistance R conditions while charging a storage capacitor C_s = 300 nF. R represents the equivalent resistance connected in parallel to the charging circuit, and it represents the internal resistance of the piezoelectric voltage measuring device in this study. The RMS charging power, peak instant power, and saturated voltage of the nonlinear in-parallel, linear in-parallel, nonlinear in-series, and linear in-series systems increase with the increase of v_0 until the critical velocity. A sudden drop happens in all of the four systems on energy generation performance after the sliding velocity exceeds the critical values because the systems change from unstable to stable states. The critical velocities match with the result in Figure 6-15 and Figure 6-16 in the system stability analysis section. While R changed from 1.8 MΩ to 36 MΩ, the energy generation performance shows a boost. The reason is that the larger R brings the circuit close to an open-circuit condition, and there is less charge dissipation happened on R and most of the generated energy by piezoelectric patch is stored in C_s. Table 6-6 summarizes the effect of β on operating velocity range (OVR) and the sum of RMS charging power (SRCP) of the four investigated systems. Both OVR and SRCP decrease with the increase of β, and β is mainly determined by the contacting surfaces of friction material. The OVR and SRCP of the linear in-parallel system are slightly smaller than the nonlinear in-parallel system, and it could be due to the weak nonlinearity induced by the magnetic force. The OVR of the linear in-series system is slightly smaller than the nonlinear in-series system. However, the SRCP of the linear in-series system is much smaller than the nonlinear in-series system. As a result, considering both in-parallel and in-series systems, the induced nonlinearity from the magnetic force is beneficial for energy generation in OVR and SRCP compared to the linear configurations. Apart from these, the OVRs of the in-series systems are larger than the in-parallel systems, and the SRCPs of in-parallel systems are larger than the in-series systems. It indicates that the in-parallel systems have better energy generation performance within their OVR compared to the in-series systems. However, the in-series systems are more likely to excite FIV with a wider OVR.

And the following common parameters are used for the in parallel systems: m = 0.619 kg, F_N = 12 N, c = 1.185 Ns/m, k_l = 50000 N/m, k_{nl1} = 1.903e^3 N/m, μ_k = 0.2, μ_{static} = 0.6, and C_s = 3e^{-7} F. The following common parameters are used for the in series systems: m_1 = 0.093 kg, m_2 = 0.526 kg, F_N = 12 N, c_1 = 0.178 Ns/m, c_2 = 1.007 Ns/m, k_l = 50000 N/m, k_{nl1} = 1.903e^3 N/m, μ_k = 0.2, μ_{static} = 0.6, and C_s = 3e^{-7} F.

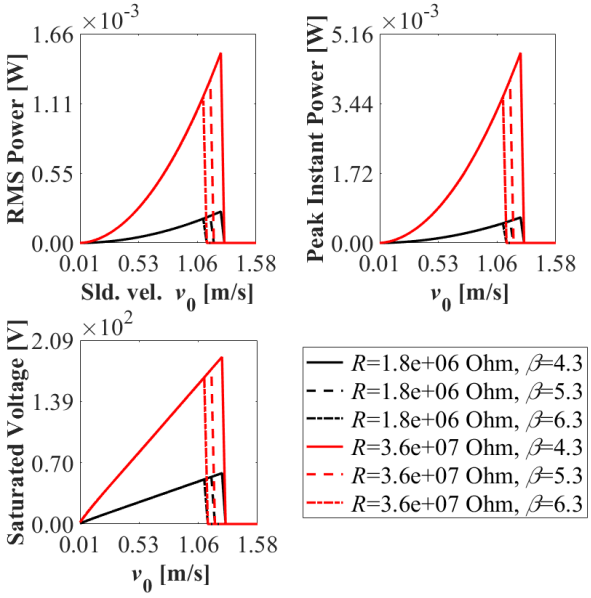

(a)

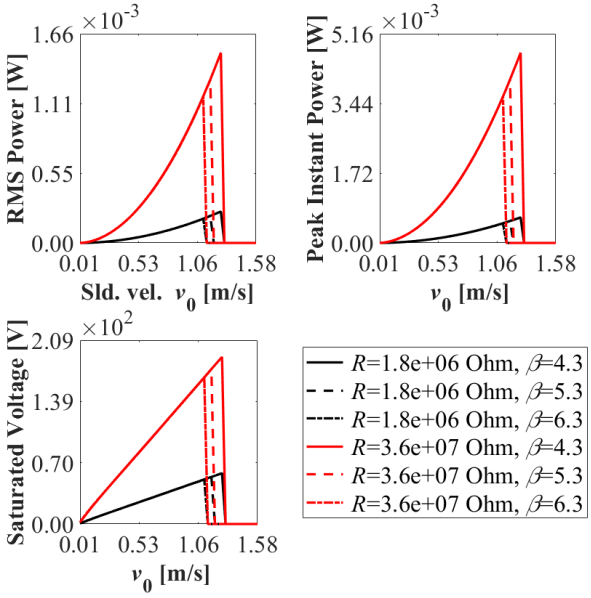

(b)

Figure 6-21 RMS charging power with different v_0 in terms of β. (a) Nonlinear in-parallel design (k_{nl3} = 1.123e^7 N/m^3). (b) Linear in-parallel design (k_{nl3} = 0 N/m^3).

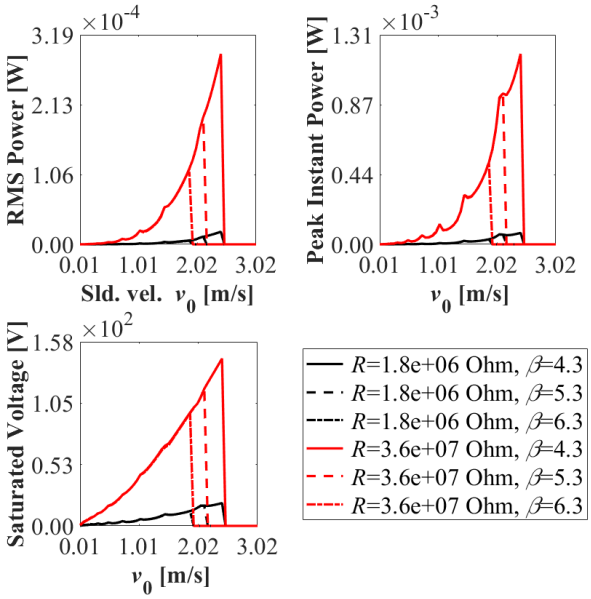

(a)

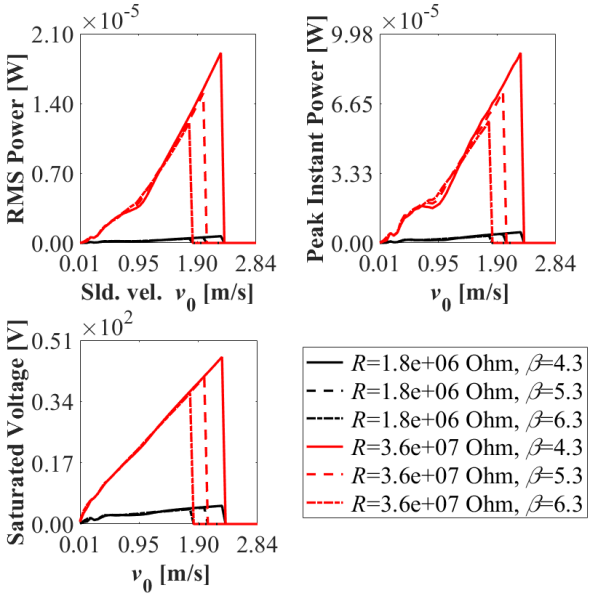

(b)

Figure 6-22 RMS charging power with different v_0 in terms of β. (a) Nonlinear in-series design (k_{nl3} = 1.123e^7 N/m^3). (b) Linear in-series design (k_{nl3} = 0 N/m^3).

Table 6-6 The effects of the exponential decay factor β on OVR and SRCP.

		β = 4.3		β = 5.3		β = 6.3	
		R = 1.8 (MΩ)	R = 36 (MΩ)	R = 1.8 (MΩ)	R = 36 (MΩ)	R = 1.8 (MΩ)	R = 36 (MΩ)
NLIP	OVR (m/s)	0.073-1.269	0.042-1.269	0.073-1.182	0.042-1.183	0.073-1.112	0.042-1.112
	SRCP (μW)	111.055	672.393	88.371	535.383	75.107	455.095
LIP	OVR (m/s)	0.073-1.269	0.042-1.269	0.073-1.175	0.042-1.175	0.073-1.112	0.042-1.112
	SRCP (μW)	111.004	672.292	88.352	534.698	75.082	455.062
NLIS	OVR (m/s)	0.673-2.419	0.063-2.419	0.673-2.118	0.063-2.118	0.673-1.877	0.063-1.877
	SRCP (μW)	9.741	167.567	4.918	92.978	2.715	54.014
LIS	OVR (m/s)	1.029-2.275	0.067-2.275	1.029-1.992	0.067-1.992	1.029-1.765	0.067-1.765
	SRCP (μW)	0.518	16.844	0.357	11.881	0.2475	8.644

Abbreviation: NLIP=nonlinear in parallel; LIP=linear in parallel; NLIS=nonlinear in series; LIS=linear in series.

Figure 6-23 and Figure 6-24 show the effect of the static friction coefficient μ_{static} on energy generation performance considering the RMS charging power, peak instant power, and saturated voltage. Table 6-7 summarizes the effect of μ_{static} on operating velocity range (OVR) and the sum of RMS charging power (SRCP) of the systems. On the contrary to the induced variation trend of β, OVR and SRCP increase with the increase of μ_{static}, which implies the growth of critical velocity and μ_{static} plays an important role in the generation of FIV. Meanwhile, the in-parallel systems keep the energy generation performance, and the in-series systems possess wide OVR.

And the following common parameters are used for the in parallel systems: m = 0.619 kg, F_{N} = 12 N, c = 1.185 Ns/m, k_{l} = 50000 N/m, k_{nl1} = 1.903e^3 N/m, μ_{k} = 0.2, β = 4.3, and C_{s} = 3e^{-7} F. The following common parameters are used for the in series systems: m_1 = 0.093 kg, m_2 = 0.526 kg, F_{N} = 12 N, c_1 = 0.178 Ns/m, c_2 = 1.007 Ns/m, k_{l} = 50000 N/m, k_{nl1} = 1.903e^3 N/m, μ_{k} = 0.2, β = 4.3, and C_{s} = 3e^{-7} F.

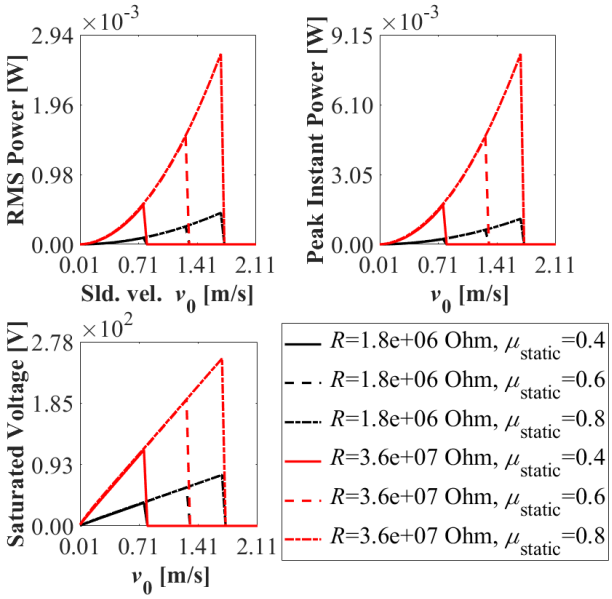

(a)

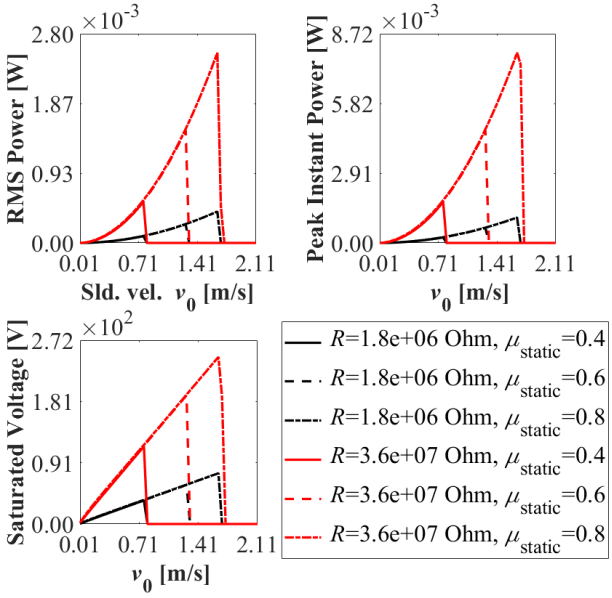

(b)

Figure 6-23 RMS charging power with different v_0 in terms of μ_{static}. (a) Nonlinear in-parallel design (k_{nl3} = 1.123e^7 N/m^3). (b) Linear in-parallel design (k_{nl3} = 0 N/m^3).

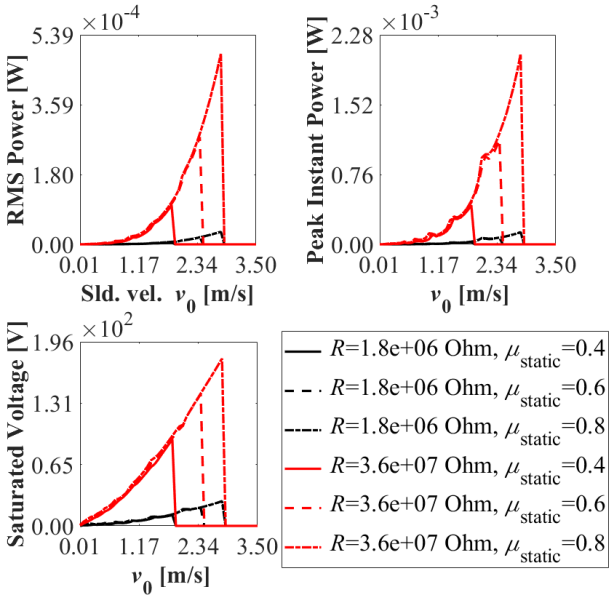

(a)

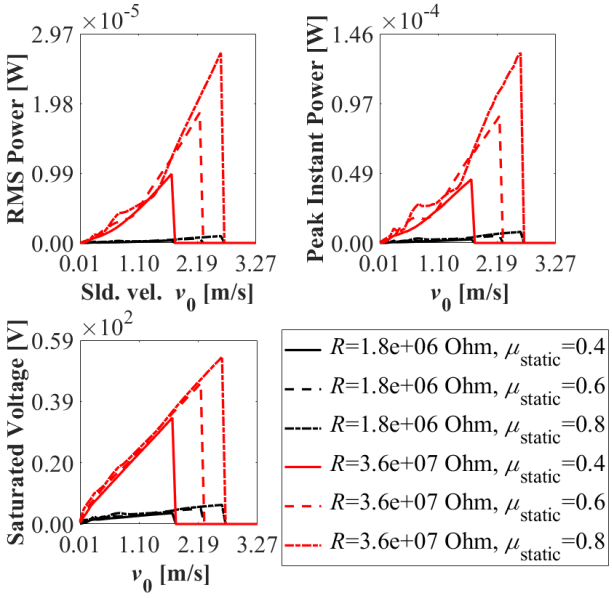

(b)

Figure 6-24 RMS charging power with different v_0 in terms of μ_{static}. (a) Nonlinear in-series design (k_{nl3} = 1.123e^7 N/m^3). (b) Linear in-series design (k_{nl3} = 0 N/m^3).

Table 6-7 The effects of the static friction coefficient μ_{static} on OVR and SRCP.

		μ_{static} = 0.4		μ_{static} = 0.6		μ_{static} = 0.8	
		R = 1.8 (MΩ)	R = 36 (MΩ)	R = 1.8 (MΩ)	R = 36 (MΩ)	R = 1.8 (MΩ)	R = 36 (MΩ)
NLIP	OVR (m/s)	0.073- 0.766	0.052-0.766	0.073-1.269	0.052-1.269	0.073-1.690	0.052-1.690
	SRCP (μW)	25.389	153.788	111.055	681.308	262.403	1588.444
LIP	OVR (m/s)	0.073-0.766	0.052-0.766	0.073-1.175	0.052-1.269	0.073-1.648	0.052-1.648
	SRCP (μW)	25.386	153.816	111.025	681.295	243.672	1497.470
NLIS	OVR (m/s)	0.778-1.825	0.140-1.825	0.708-2.384	0.074-2.384	0.708-2.802	0.074-2.802
	SRCP (μW)	2.2145	45.373	9.119	158.335	20.618	331.788
LIS	OVR (m/s)	1.381-1.708	0.141-1.708	1.185-2.230	0.075-2.230	0.898-2.622	0.075-2.622
	SRCP (μW)	0.117	6.745	0.494	16.060	1.007	26.397

Abbreviation: NLIP=nonlinear in parallel; LIP=linear in parallel; NLIS=nonlinear in series; LIS=linear in series;

Figure 6-25 and Figure 6-26 illustrate the effect of the dynamic friction coefficient μ_{k} on energy generation performance. Table 6-8 summarizes the effect of μ_{k} on operating velocity range (OVR) and the sum of RMS charging power (SRCP) of the systems. Following the same trend with the increase of β, OVR and SRCP decrease with the increase of μ_{k}, and critical velocity decreases with the increase of μ_{k}. FIV occurs due to energy conversion through friction, which is mainly from the stick and slip motion of two contacting objects. When the velocity of the sliding object is small, the velocity of the vibrating object can easily reach the velocity of the sliding object and form the stick and slip motions. Energy can be converted from the sliding object to the vibrating object. With the increased velocity of the sliding object, the difference in velocity between the vibrating object and the sliding object increases, and the two objects are always in relative motion with fading stick-slip motion, and the vibration system ultimately ends up at the equilibrium position. Based on Eq. (6.12) and keeping other parameters unchanged, $\mu_{\text{slide}}(v_{\text{r}})$ will approach μ_{k} as μ_{k} increases, resulting in a shorter transiting period of stick and slip motion and less friction energy converting into vibrational energy. As a result, both OVR, SRCP, and critical velocity decrease with the increase of μ_{k}.

And the following common parameters are used for the in parallel systems: m = 0.619 kg, F_{N} = 12 N, c = 1.185 Ns/m, k_{l} = 50000 N/m, k_{nl1} = 1.903e^3 N/m, μ_{static} = 0.6, β = 4.3, and C_{s} = 3e^{-7} F. The following common parameters are used for the in series systems: m_1 = 0.093 kg, m_2 =

0.526 kg, F_N = 12 N, c_1 = 0.178 Ns/m, c_2 = 1.007 Ns/m, k_l = 50000 N/m, k_{nl1} = 1.903e^3 N/m, μ_{static} = 0.6, β = 4.3, and C_s = 3e^{-7} F.

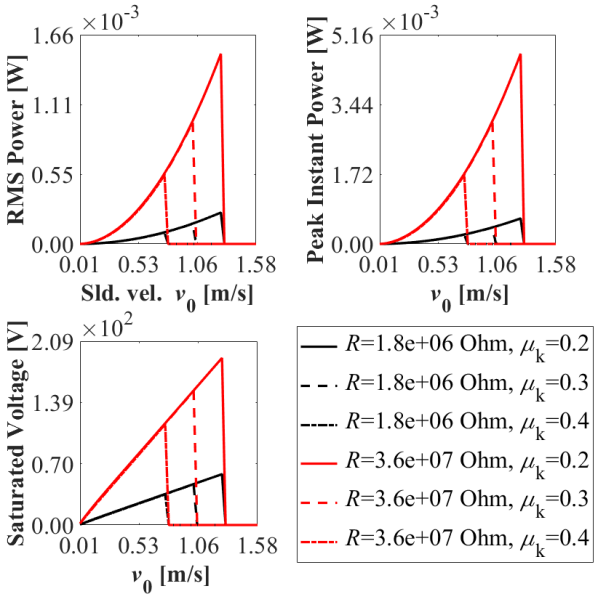

(a)

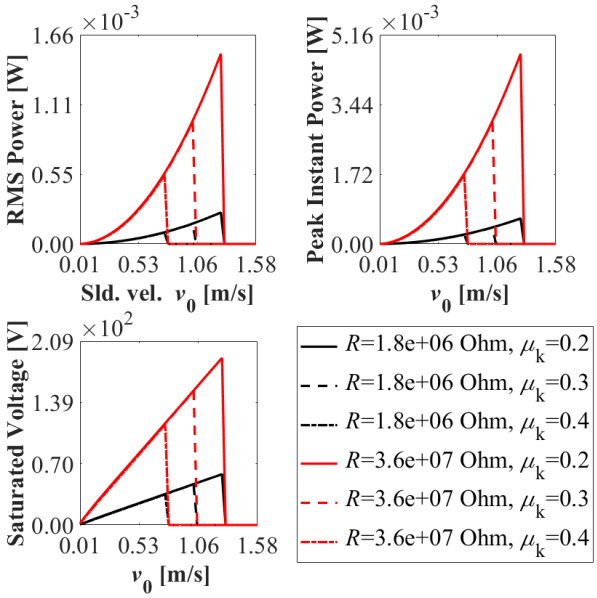

(b)

Figure 6-25 RMS charging power with different v_0 in terms of μ_k. (a) Nonlinear in-parallel design (k_{nl3} = 1.123e^7 N/m^3). (b) Linear in-parallel design (k_{nl3} = 0 N/m^3).

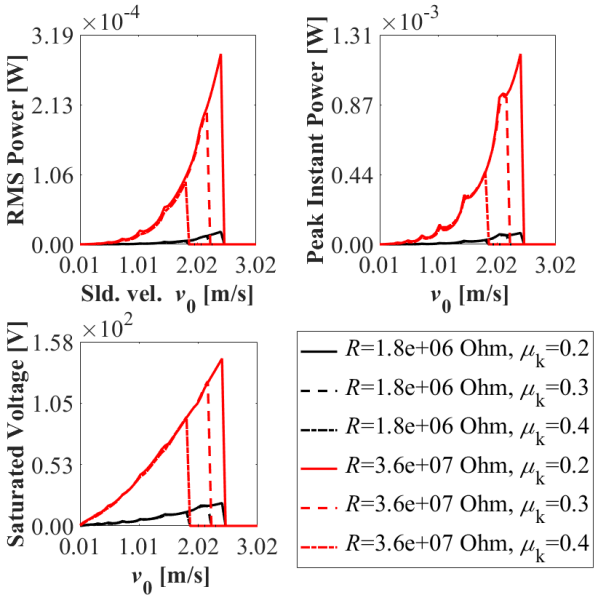

(a)

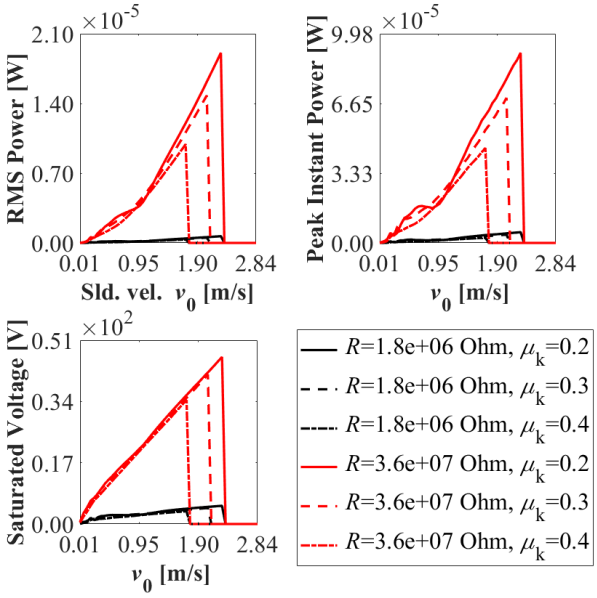

(b)

Figure 6-26 RMS charging power with different v_0 in terms of μ_k. (a) Nonlinear in-series design (k_{nl3} = 1.123e^7 N/m^3). (b) Linear in-series design (k_{nl3} = 0 N/m^3).

Table 6-8 The effects of the dynamic friction coefficient μ_k on OVR and SRCP.

		$\mu_k = 0.2$		$\mu_k = 0.3$		$\mu_k = 0.4$	
		R = 1.8 (MΩ)	R = 36 (MΩ)	R = 1.8 (MΩ)	R = 36 (MΩ)	R = 1.8 (MΩ)	R = 36 (MΩ)
NLIP	OVR (m/s)	0.073-1.269	0.042-1.269	0.073-1.017	0.042-1.017	0.073-0.766	0.042-0.766
	SRCP (μW)	111.055	672.393	57.635	348.949	24.844	150.447
LIP	OVR (m/s)	0.073-1.269	0.042-1.269	0.073-1.235	0.042-1.017	0.073-0.765	0.042-0.766
	SRCP (μW)	111.004	672.234	57.622	348.245	24.839	150.435
NLIS	OVR (m/s)	0.673-2.419	0.063-2.419	0.733-2.178	0.121-2.178	0.733-1.817	0.121-1.817
	SRCP (μW)	9.741	167.567	5.459	101.294	2.240	42.307
LIS	OVR (m/s)	1.200-2.275	0.067-2.275	1.142-2.048	0.123-2.048	1.369-1.709	0.123-1.709
	SRCP (μW)	0.518	16.844	0.356	12.078	0.118	6.775

Abbreviation: NLIP=nonlinear in parallel; LIP=linear in parallel; NLIS=nonlinear in series; LIS=linear in series;

Considering the possible working circumstances with varying F_N and v_0, the influences of the random F_N and v_0 on the systems' vibration response and energy generation performance are studied. The normal load F_N varies based on $F_N \sim N(F_N, (0.1F_N)^2)$, $F_N \sim N(F_N, (0.2F_N)^2)$ and $F_N \sim N(F_N, (0.3F_N)^2)$, while the constant normal load is F_N. The sliding velocity v_0 changes according to $v_0 \sim N(v_0, (0.03v_0)^2)$, $v_0 \sim N(v_0, (0.05v_0)^2)$ and $v_0 \sim N(v_0, (0.07v_0)^2)$, while the constant sliding velocity is v_0.

Figure 6-27 and Figure 6-28 exhibit the effect of varying F_N on energy generation performance under two different electric resistance R conditions while charging a storage capacitor. The solid black lines in Figure 6-21 and Figure 6-22. show the corresponding RMS charging power, peak instant power, and saturated voltage with constant F_N. Table 6-9 compares the effect of F_N with different standard deviation ratio to the constant F_N value on OVR and SRCP. The results show that with R = 1.8 MΩ, while standard deviation ratio changing from 0.1 to 0.3, SRCPs of the nonlinear in-parallel, linear in-parallel, nonlinear in-series, and linear in-series systems reduce from 103.389 μW to 95.246 μW, 103.345 μW to 95.205 μW, 9.563 μW to 9.097 μW, and 0.506 μW to 0.423 μW, respectively. It indicates a decrease of 7.8%, 7.8%, 4.9%, and 16.4%, respectively. Comparing the results in Table 6-9 with the ones at constant F_N value in Table 6-6, SRCPs reduce by 14.2%, 14.2%, 6.6%, and 18.3%, correspondingly. Though SRCPs reduce, OVRs are almost unchanged compared to the result of constant F_N. The energy generation systems can still satisfy the minimum required voltage for a similar operating velocity range with slightly

smaller charging power. With the least affected SRCP and almost unchanged OVR, the nonlinear in-series system shows better robustness under varying F_{N}. The same conclusion can be made for the R = 36 MΩ case as clearly seen from the data curves in Figure 6-27 and Figure 6-28.

And the following common parameters are used for the in parallel systems: m = 0.619 kg, F_{N} = 12 N, c = 1.185 Ns/m, k_{l} = 50000 N/m, k_{nl1} = 1.903e^3 N/m, μ_{k} = 0.2, μ_{static} = 0.6, β = 4.3, and C_{s} = 3e^{-7} F. The following common parameters are used for the in-series systems: m_1 = 0.093 kg, m_2 = 0.526 kg, F_{N} = 12 N, c_1 = 0.178 Ns/m, c_2 = 1.007 Ns/m, k_{l} = 50000 N/m, k_{nl1} = 1.903e^3 N/m, μ_{k} = 0.2, μ_{static} = 0.6, β = 4.3, and C_{s} = 3e^{-7} F.

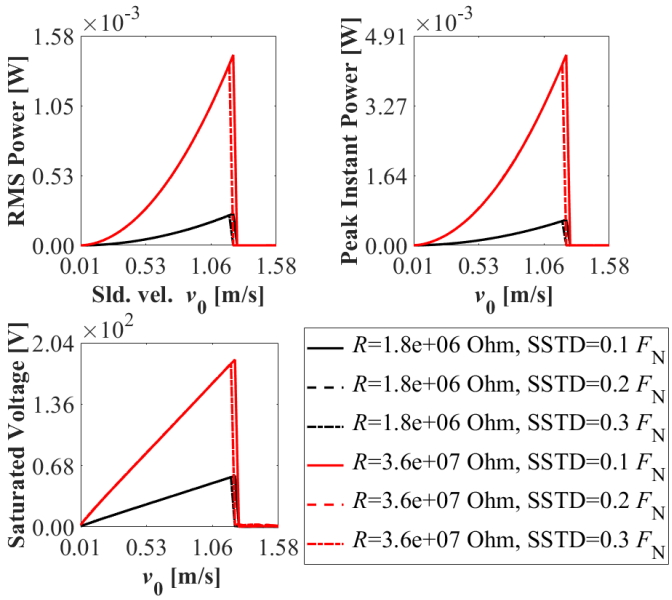

(a)

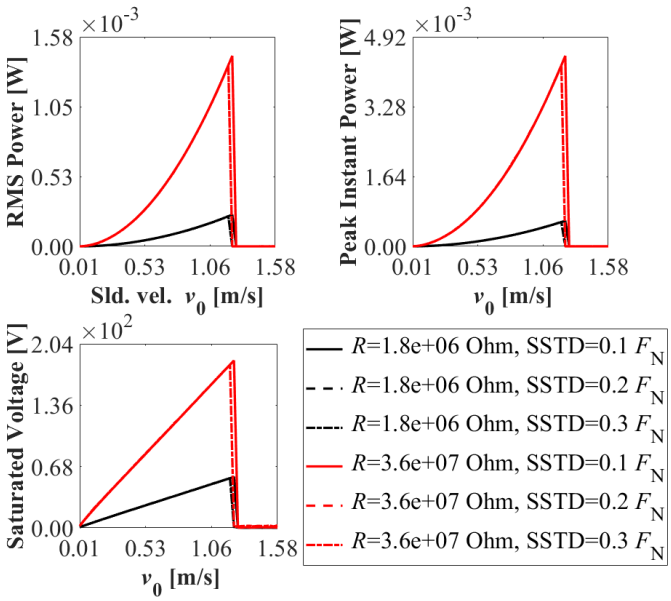

(b)

Figure 6-27 RMS charging power with varying F_{N}. (a) Nonlinear in-parallel design (k_{nl3} = 1.123e^7 N/m^3). (b) Linear in-parallel design (k_{nl3} = 0 N/m^3).

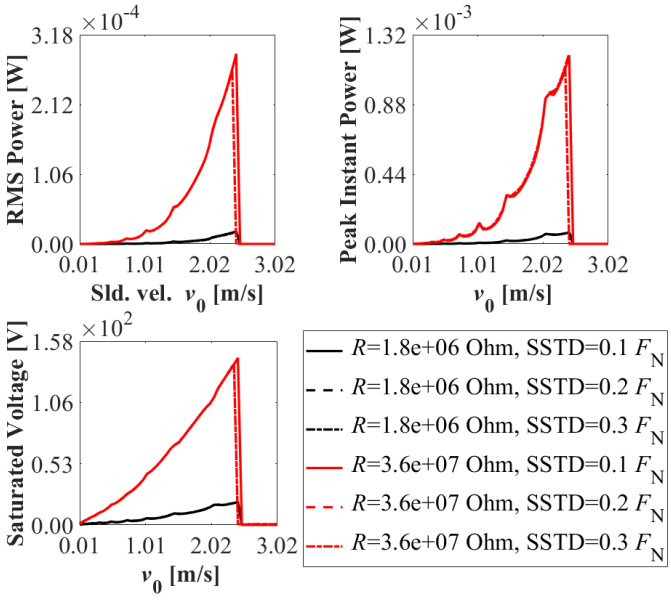

(a)

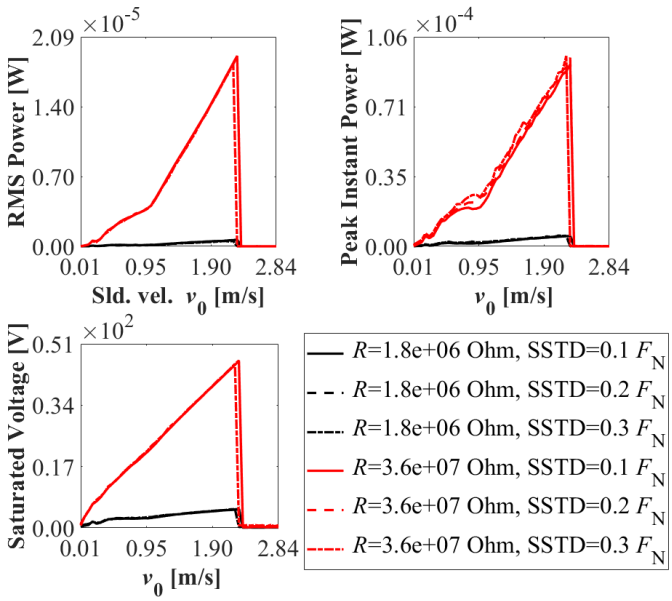

(b)

Figure 6-28 RMS charging power with varying F_N. (a) Nonlinear in-series design (k_{nl3} = 1.123e^7 N/m^3). (b) Linear in-series design (k_{nl3} = 0 N/m^3).

Table 6-9 The effects of the varying F_N on OVR and SRCP.

		SSTD = 0.1F_N		SSTD = 0.2F_N		SSTD = 0.3F_N	
		R = 1.8 (MΩ)	R = 36 (MΩ)	R = 1.8 (MΩ)	R = 36 (MΩ)	R = 1.8 (MΩ)	R = 36 (MΩ)
NLIP	OVR (m/s)	0.073-1.238	0.042-1.238	0.073-1.237	0.042-1.237	0.073-1.206	0.042-1.206
	SRCP (μW)	103.389	624.111	103.060	623.333	95.246	577.018
LIP	OVR (m/s)	0.073-1.238	0.042-1.238	0.073-1.237	0.042-1.206	0.073-1.206	0.042-1.206
	SRCP (μW)	103.345	624.402	102.980	578.256	95.205	577.471
NLIS	OVR (m/s)	0.673-2.419	0.063-2.419	0.673-2.419	0.063-2.419	0.673-2.419	0.063-2.419
	SRCP (μW)	9.563	167.187	9.326	166.515	9.097	148.671
LIS	OVR (m/s)	1.086-2.275	0.067-2.275	1.086-2.275	0.067-2.275	1.086-2.218	0.067-2.218
	SRCP (μW)	0.506	16.783	0.478	16.693	0.423	15.539

Abbreviation: NLIP=nonlinear in parallel; LIP=linear in parallel; NLIS=nonlinear in series; LIS=linear in series;

Figure 6-29 and Figure 6-30 reveal the effect of varying v_0 on energy generation performance. The solid black lines in Figure 6-21 and Figure 6-22 show the corresponding RMS charging power, peak instant power, and saturated voltage with constant v_0. Table 6-10 compares the effect of v_0 with different standard deviation ratio to the constant v_0 value on OVR and SRCP. The results show that with R = 1.8 MΩ, while standard deviation ratio changing from 0.03 to 0.07, SRCPs of

the nonlinear in-parallel, linear in-parallel, nonlinear in-series, and linear in-series systems change from 65.872 μW to 42.51 μW, 65.598 μW to 42.545 μW, 7.531 μW to 7.505 μW, and 0.212 μW to 0.201 μW, respectively. It indicates 35.4%, 35.1%, 0.4%, and 5.1% decrease, correspondingly. Comparing the result with constant v_0 value in Table 6-6 and outcome in Table 6-10 with R = 1.8 MΩ and $SSTD$ = 0.07, SRCPs reduce by 61.7%, 61.6%, 22.9%, and 61.2%, correspondingly. OVRs of the nonlinear in-parallel, linear in-parallel, and linear in-series systems shrink a bit, but the OVR of the nonlinear in-series system is almost unchanged. The nonlinear in-series system shows better robustness of the piezoelectric power output under varying F_{N} and v_0 conditions. Same conclusion can be made for the R = 36 MΩ case as seen from the data curves in Figure 6-29 and Figure 6-30.

And the following common parameters are used for the in parallel systems: m = 0.619 kg, F_{N} = 12 N, c = 1.185 Ns/m, k_{l} = 50000 N/m, k_{nl1} = 1.903e^3 N/m, μ_{k} = 0.2, μ_{static} = 0.6, β = 4.3, and C_{s} = 3e^{-7} F. The following common parameters are used for the in-series systems: m_1 = 0.093 kg, m_2 = 0.526 kg, F_{N} = 12 N, c_1 = 0.178 Ns/m, c_2 = 1.007 Ns/m, k_{l} = 50000 N/m, k_{nl1} = 1.903e^3 N/m, μ_{k} = 0.2, μ_{static} = 0.6, β = 4.3, and C_{s} = 3e^{-7} F.

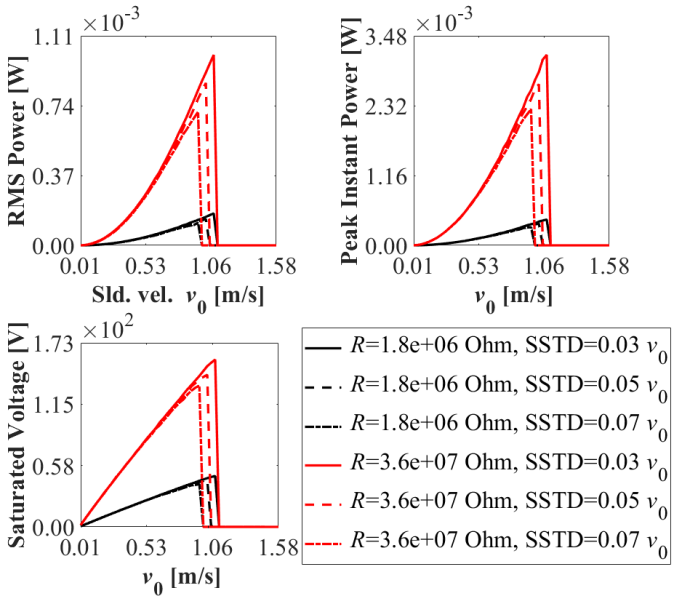

(a)

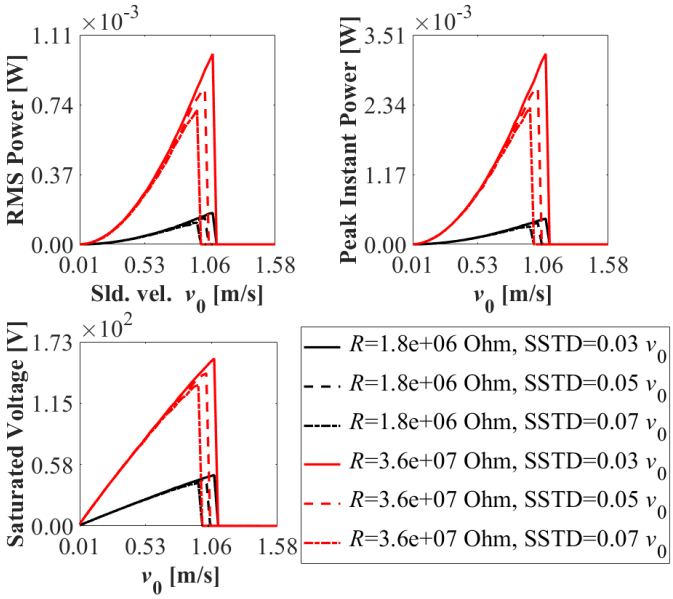

(b)

Figure 6-29 RMS charging power with varying v_0. (a) Nonlinear in-parallel design (k_{nl3} = 1.123e^7 N/m^3). (b) Linear in-parallel design (k_{nl3} = 0 N/m^3).

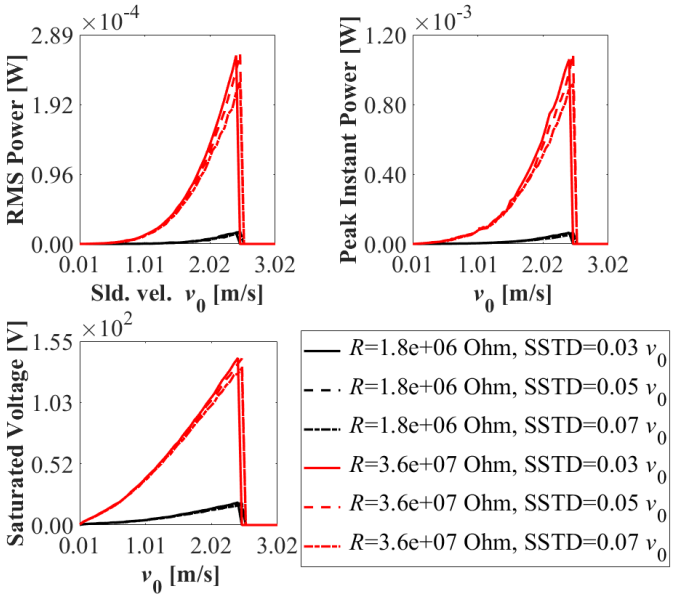

(a)

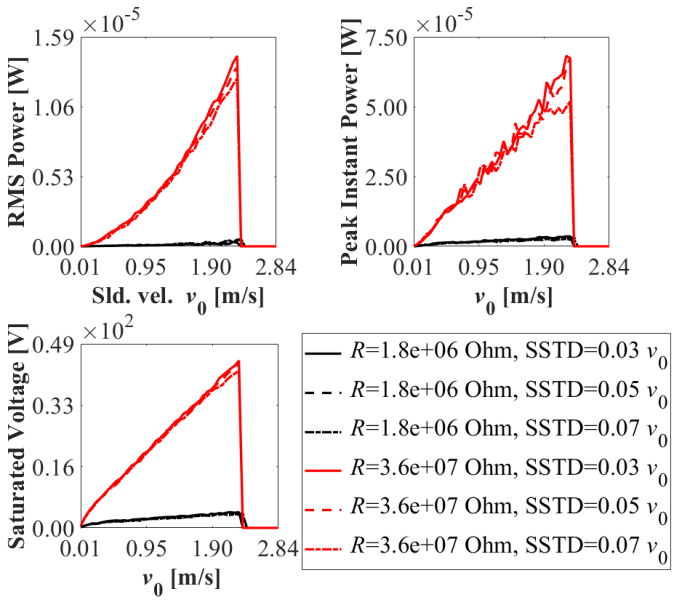

(b)

Figure 6-30 RMS charging power with varying v_0. (a) Nonlinear in-series design (k_{nl3} = 1.123e^7 N/m^3). (b) Linear in-series design (k_{nl3} = 0 N/m^3).

Table 6-10 The effects of the varying v_0 on OVR and SRCP.

		SSTD = $0.03v_0$		SSTD = $0.05v_0$		SSTD = $0.07v_0$	
		R = 1.8 (MΩ)	R = 36 (MΩ)	R = 1.8 (MΩ)	R = 36 (MΩ)	R = 1.8 (MΩ)	R = 36 (MΩ)
NLIP	OVR (m/s)	0.073-1.080	0.042-1.080	0.073-1.017	0.042-1.017	0.073-0.955	0.042-0.955
	SRCP (μW)	65.872	401.643	53.059	326.342	42.510	261.409
LIP	OVR (m/s)	0.073-1.080	0.042-1.080	0.073-1.017	0.042-1.017	0.073-0.955	0.042-0.955
	SRCP (μW)	65.598	401.642	53.042	323.862	42.545	261.371
NLIS	OVR (m/s)	0.793-2.419	0.121-2.419	0.793-2.479	0.121-2.479	0.793-2.479	0.121-2.479
	SRCP (μW)	7.531	147.604	8.378	153.641	7.505	138.186
LIS	OVR (m/s)	1.426-2.275	0.123-2.275	1.595-2.331	0.123-2.275	1.652-2.331	0.123-2.275
	SRCP (μW)	0.212	12.268	0.232	11.772	0.201	11.248

Abbreviation: NLIP=nonlinear in parallel; LIP=linear in parallel; NLIS=nonlinear in series; LIS=linear in series;

6.3 Summary and discussion

Section 6.1 investigates the performance of magnet-engaged piezoelectric energy generators under harmonic excitation. The in-parallel and in-series design configurations exhibit hardening nonlinearity, resulting in extended operation bandwidth and improved output power. The effects of damping ratio ζ, excitation amplitude F_0, and equivalent resistor R on the system's frequency

response are studied. Increasing ζ reduces voltage response peak values and restrains nonlinear phenomena. Increasing F_0 increases voltage response peak values and improves nonlinear phenomena. Increasing R increases voltage response peak values due to reduced energy dissipation. The nonlinear phenomena are almost unchanged in the two corresponding nonlinear design configurations because of the weak mechanical and piezoelectric coupling conditions. Investigation on energy generation performance in terms of OB and SRCP is carried out considering the linear spring ratio μ_{kl}, mass ratio μ_{m}, and magnet width w_{m}. Increasing the linear spring ratio μ_{kl} results in an increase in SRCP for all design configurations, and an increase in OB can be observed except for the nonlinear in-parallel design configuration due to weakened nonlinearity. Increasing the mass ratios μ_{m} has a positive effect on OB and SRCP in both linear in-series and nonlinear in-series designs. Keeping the total volume of the magnet and magnet length constants, OB decreases with increasing w_{m}, except for the linear in-series system. SRCP decreases with increasing w_{m} for all systems. Properly designed nonlinear configurations achieve significant improvements in operation bandwidth and sum of the RMS charging powers compared to linear designs.

In Section 6.2, similar piezoelectric energy generators are studied, but under friction excitation. A critical sliding velocity v_0 exists, separating stick-slip phenomenon and continuous slip motion. This critical velocity changes with friction model parameters. The system tends to the equilibrium position in the stable region, while stick-slip motion occurs in the unstable region, characterized by FIV. The occurrence of FIV is influenced by parameters such as β, μ_{k}, F_{N}, and μ_{static}. Parameters studies about energy generation performance are conducted to compare the operation sliding velocity range (OVR) and the sum of RMS power (SRCP) among the nonlinear in-parallel, linear in-parallel, nonlinear in-series, and linear in-series systems. The in-parallel systems have better energy generation performance within their OVRs compared to the in-series systems. However, the FIVs of the in-series systems have a wider OVR. Considering the possible working circumstances, the normal load F_{N} and sliding velocity v_0 may be affected by the environment, energy generation simulations with varying F_{N} and v_0 are carried out. Both varying F_{N} and v_0 have negative effect on energy generation, and varying F_{N} has less effect on systems' performance. Furthermore, the nonlinear in-series system shows better robustness with the least affected SRCP and almost unchanged OVR compared to working circumstances with constant F_{N} and v_0.

Section 6.1 and Section 6.2 investigate the performance of magnet-engaged piezoelectric energy generators under harmonic and friction as excitations, respectively. The proposed nonlinear in-parallel and nonlinear in-series design configurations demonstrate better performance compared to their linear design configurations. Possible engineering applications can be achieved under harmonic-based excitation to utilize the ambient environmental vibration and friction-based excitation to harness wasted friction energy.

Chapter 7 Piezoelectric energy generation with continuum structure

In this chapter, investigations are conducted on FIV-based PEG that utilizes continuum structure. The continuum structure is defined as a physical system that can be modeled as a continuous distribution of mass and stiffness, and it has infinite degrees of freedom. The modeling methods depicted in Sections 2.1, 2.2, 2.5, and 2.6 are utilized in this chapter.

The study involves mathematical modeling of a piezoelectric-coupled continuum beam under FIV, experimental validation of model, and analysis of material properties and friction model parameters effects on energy generation performance. It will be introduced in Section 7.1.

After exploring the dynamic behavior of a conventional piezoelectric-coupled continuum beam under FIV, the dynamic behavior of stepped design continuum beam under FIV is investigated. A Convolutional Neural Network - Long Short-Term Memory CNN-LSTM neural network is trained with simulation data. The trained model is integrated with Genetic Algorithm (GA) and utilized in the fitness function for geometric optimization of the energy generator. It will be described in Section 7.2.

7.1 Modeling of a piezoelectric-coupled beam under friction excitation

A transverse mode (d_{31}) piezoelectric coupled continuum beam under friction excitation is introduced in this research, and the continuum beam is mounted on a fixture. The test rig shown in Figure 7-1(a) mainly consists of six components: 1: oscilloscope, 2: load cell indicator, 3: variable frequency drive (VFD) module, 4: three-phase motor, 5: load cell, and 6: piezoelectric-coupled continuum beam. Figure 7-1(b) shows the detailed deformation of the beam. The three-phase motor powers the built-in shaft, with a VFD module controlling the rotating rpm. A pulley is mounted on the motor shaft, and a V-belt is attached, leading the belt to rotate along with the pulley. The belt serves as the source of friction excitation for the beam. The coupled beam is installed on a fixture mounted on an angle iron. A load cell connected to the indicator is integrated at the opposite end of the angle iron to measure the normal load. An oscilloscope is utilized to measure dynamic voltage from PZT during FIV. The electromechanical modeling of the energy generator can be referred in Section 2.5, and its experimental validation will be conducted below.

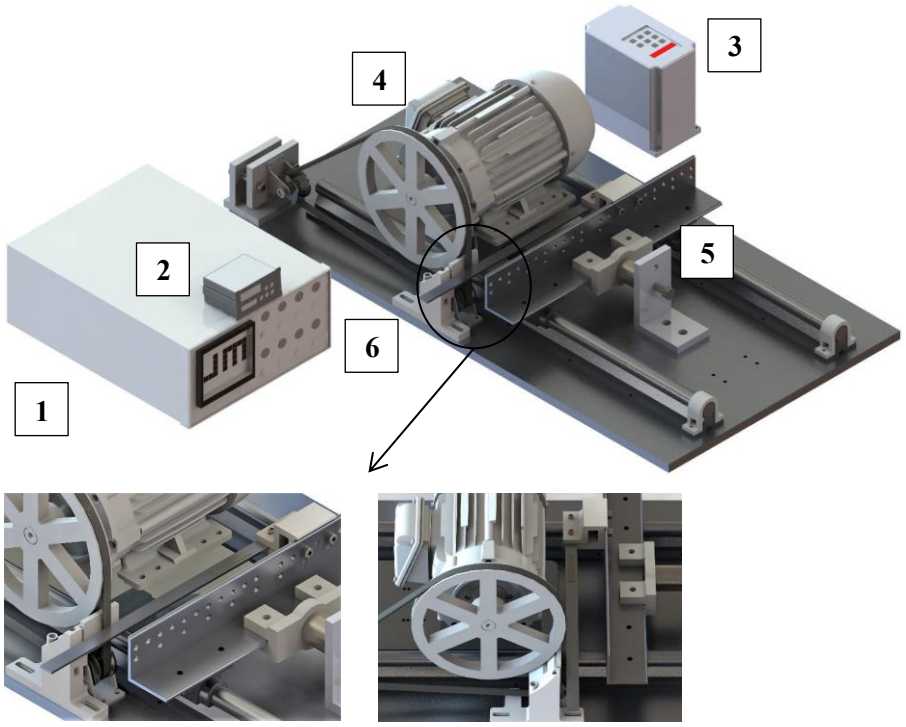

(a)

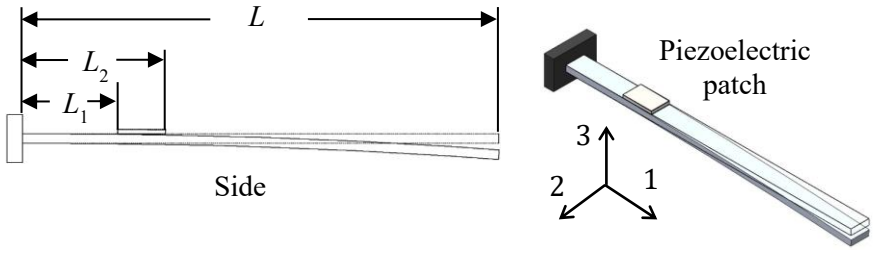

(b)

Figure 7-1 Schematic diagrams of piezoelectric-coupled continuum beam under FIV. (a) Experiment testing rig. (b) Deformation of the piezoelectric-coupled continuum beam.

7.1.1 Model validation with experiment

The parameters for the experiment are shown in Table 7-1. The PZT (APC 855) is from APC International, Ltd [131]. The host beam is purchased from a local vendor. In order to obtain the accurate material properties of the host beam, Young's modulus E and density ρ are measured experimentally. The density is calculated using the equation $\rho = m/V_s$, where m is the measured mass of the sample test beam (250×25.4×6.35 mm) and V_s corresponds to its volume derived from $V_s = L * H * b$. The Young's modulus E is calculated from the experimentally measured first resonant frequency response, and the test setup for frequency response is shown in Figure 7-2. A dynamic signal analyzer (35670A) is used for data acquisition and analysis. An accelerometer (Bruel & Kjaer 4367) is utilized to acquire the vibrational data. A force hammer is used for excitation. The spectrum result from the signal analyzer shows the first resonance peak is around 54 Hz. This value will be used to calculate E of the host beam under the clamped-free boundary condition.

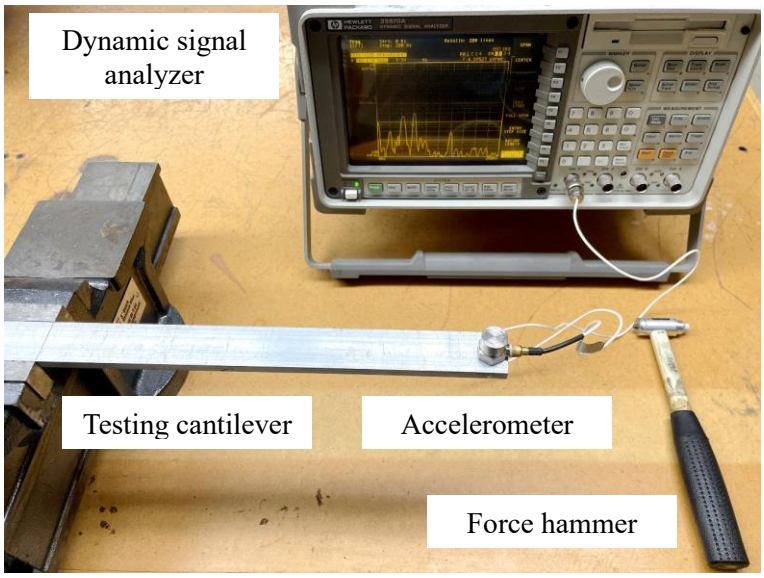

Test setup

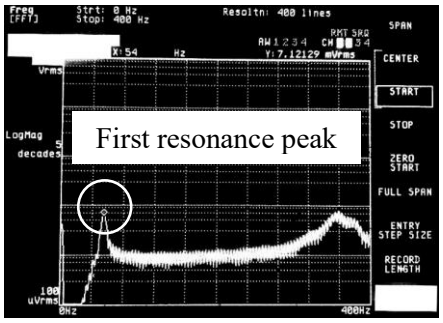

Spectrum result

Test sample

Figure 7-2 Test setup to measure E of the beam.

Table 7-1 Parameters for experimental and simulation parameter studies.

Parameter	Host beam	PZT patch	Circuit	Friction model
Length (m)	L = 0.36	L_p = 0.02	–	–
Thickness (m)	H = 0.00635	h = 0.001	–	–
Width (m)	b = 0.0254	b_p = 0.01	–	–
Young's modulus (GPa)	E = 50	E_p = 63	–	–
Density (kg/m^3)	ρ = 2705	ρ_p = 7600	–	–
Piezoelectric constant	–	d_{31} = -2.8e^{-10}	–	–
Capacitance (F)	–	C_p = 1.157e^{-8}	C_{st} = 10e^{-6}	–
Distance to fixed end from piezo-patch and friction location (m)	–	d_0 = 0.017	–	d_f = 0.281
Equivalent resistance (Ohm)	–	–	R = 1e^6	–
Normal force (N)	–	–	–	F_N = 10
Sliding velocity (m/s)	–	–	–	v_0 = 0.939
Static friction coefficient	–	–	–	μ_s = 0.8
Dynamic friction coefficient	–	–	–	μ_k = 0.5
Exponential decay factor	–	–	–	C = 20

The experimental configuration, illustrated in Figure 7-3, encompasses five key elements: an oscilloscope (DSO6014A) with an internal resistance R of 1 MΩ for data acquisition, a three-phase

motor (WEG CT002404NPW22) providing rotational power, a VFD module (CFW500B07P3B2DBN1H00) regulating rotational speed, a charging circuit dedicated to charging the storage capacitor C_s, and a load cell employed for quantifying the normal load. The detail of the piezoelectric coupled continuum beam is shown in Figure 7-3(b), which has a dimension of 360×25.4×6.35 mm. A 20×10×1 mm piezoelectric patch is bonded to the beam. The detail of the contact interface between the continuum beam and the rotating belt is shown in Figure 7-3(c). The belt functions as the sliding object with a sliding velocity v_0, and the host beam acts as the oscillating object. Assuming that the beam is under small deformation and the contacting point between the belt and beam remains unchanged. The FIV emerges as a consequence of energy conversion from the interplay of stick and slip motion between two contacting objects. When the belt starts sliding, the oscillating object can readily synchronize its motion with the belt's velocity, thus initiating the stick-slip motion. This enables energy conversion from the sliding entity to the oscillating object. It should be noted that the current study presents a fundamental investigation into the mechanism of friction-induced vibration in a piezoelectric beam and explored its energy generation performance. A motor is employed to generate and maintain a stable sliding motion. Therefore, a motor is used for representation in the structural diagram and experimental setup. The motor is not the energy source for the piezoelectric beam to harvest energy for practical applications. Additionally, in practical applications, using proper materials with enhanced properties is essential to reduce wear and ensure a longer lifespan.

Throughout the testing procedure, a fixed distance of 115 mm between the shaft and the edge of the pulley is maintained. The velocity v_0 is calculated as $v_0 = 0.1047 \times 0.115 \times N$, where N denotes the rotating speed of the shaft. The conversion factor 0.1047 is derived from $0.1047 = 2\pi/60$, enabling the conversion of rpm to rad/s. The charging experiment employs a conventional charging circuit, as depicted in the lower left portion of Figure 7-3(a). This circuit features a full bridge rectifier comprising four Schottky diodes, a toggle switch employed for initiating the charging, and a storage capacitor C_{st} for energy storage.

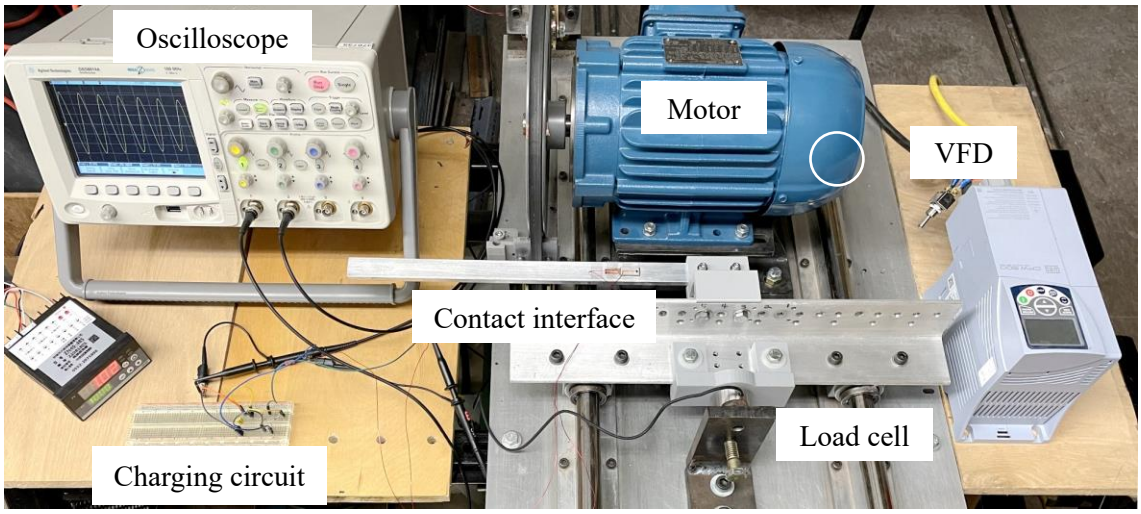

(a)

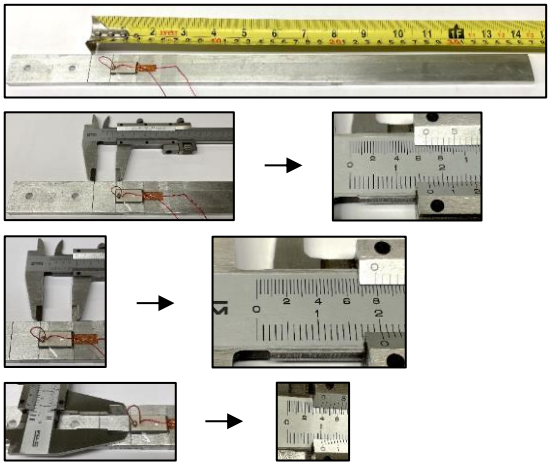

(b)

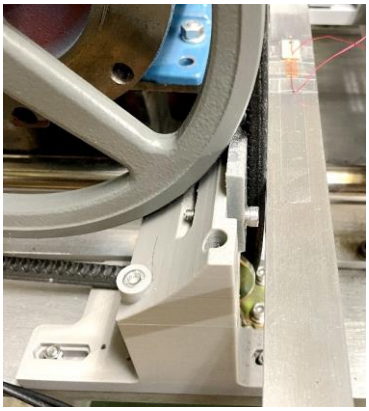

Contact interface between moving belt and beam

(c)

Figure 7-3 Test setup of piezoelectric-coupled cantilever. (a) Overall setup. (b) Dimension of material. (c) Friction contact interface.

Accurately quantifying the influence of bonding between components in theoretical modeling is very challenging. In this study, we adopt the assumption of rigid connections for the components between the load cell and the beam. This simplification allows us to focus on the dynamics and exclude structural vibration effects. The experimental parameters are listed in Table 7-1. Figure 7-4 compares the output voltage in time domain between experimental and simulated results at different rotating speeds. The changing variables are shown on the figure caption. The output voltage is calculated through Eq. (B.15), wherein the parameter R emulates the charge dissipation within the energy generation system during its connection to the oscilloscope. A resistance value of R = 1 MΩ is employed, which is based on the specifications provided in the user menu. μ_s and

μ_{k} are detemined based on the recorded value of coefficient of friction between rubber and metal [132]. C is the decay factor characterizing the transition rate during stick-slip motion, and it is determined based on the stick-slip phenomenon in the experiment. It is worth noting that C varies depending on surface conditions and material properties. It is feasible to achieve pronounced FIV featuring a robust stick-slip phenomenon by employing suitable materials or surface conditions. The temporal voltage outputs obtained through simulations match with the experimental observations. It substantiates the precision and effectiveness of the simulation result.

The experimental results demonstrate the emergence of approximately sixteen vibration peaks in 0.5 seconds. This observation signifies that the system oscillates at approximately 32 Hz, closely aligning with the continuum beam's first natural frequency of approximately 33 Hz. The results from Figure 7-4(a) and (c) indicate that a 37% augmentation in the sliding velocity v_0 coincides with an approximate 3% enhancement in the peak dynamic voltage output. After comparing Figure 7-4(a) and (b), it reveals that a 20% increment in the normal force F_{N} yields a 20% increase in the peak dynamic voltage output. These findings shows that, within the current validation parameters, the amplitude of the voltage output is mainly influenced by the variation of the normal force F_{N} compared to the changes of the sliding velocity v_0.

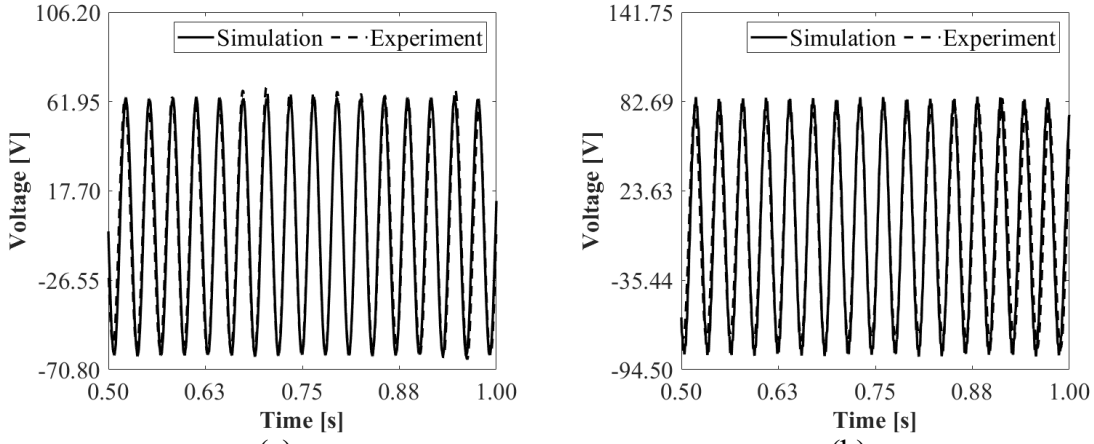

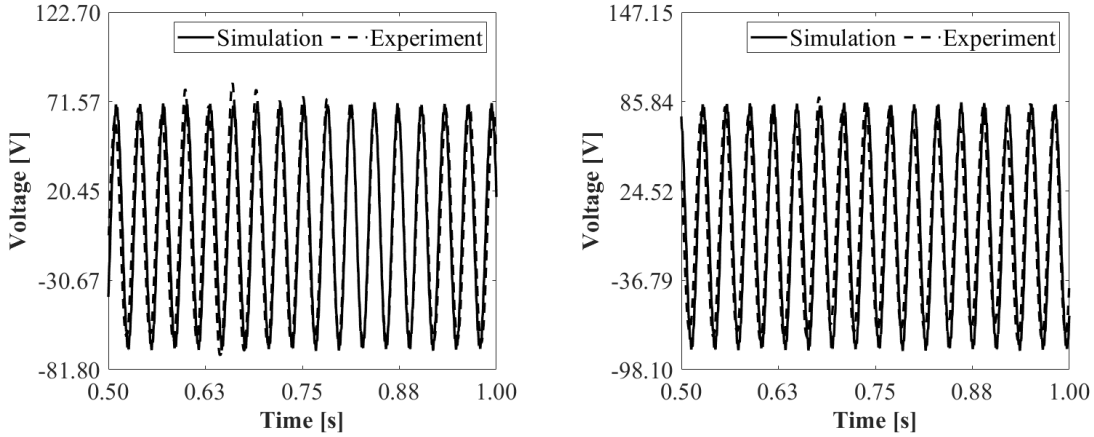

(c) (d)

Figure 7-4 Dynamic output voltage under different testing conditions. (a) F_{N} = 10 N and v_0 = 0.939 m/s. (b) F_{N} = 12 N and v_0 = 0.939 m/s. (c) F_{N} = 10 N and v_0 = 1.289 m/s. (d) F_{N} = 12 N and v_0 = 1.289 m/s.

Figure 7-5 depicts the variation of V_{s} throughout the charging process for different F_{N}. A comprehensive derivation of V_{s} and V_{p} during the charging process can be found in Section 2.6. The experimental charging curves manifest discernible fluctuations, potentially arising from loose connections within the charging circuit and the impact of structural vibrations. Overall, the simulation outcomes exhibit a congruence with the experimental results.

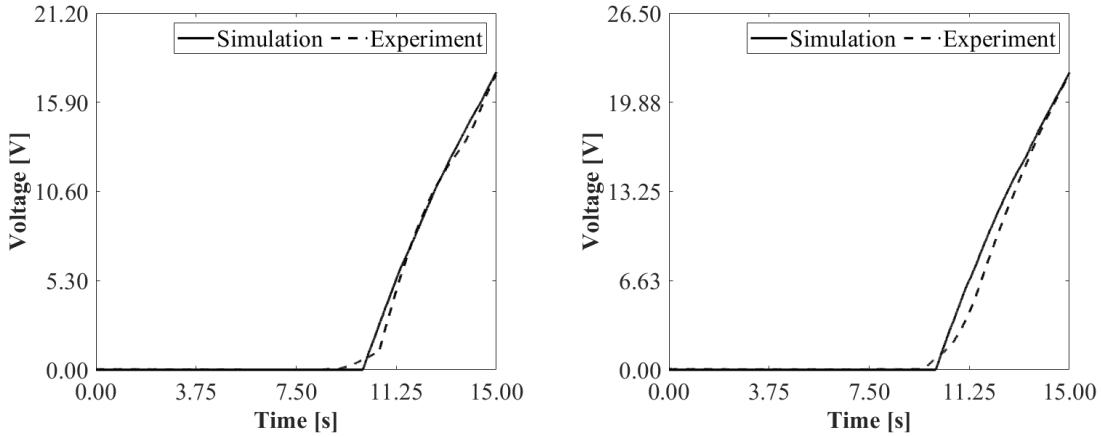

(a) (b)

Figure 7-5 Dynamic charging output under different testing conditions. (a) F_{N} = 10 N and v_0 = 0.939 m/s. (b) F_{N} = 12 N and v_0 = 0.939 m/s.

7.1.2 Parameter studies on energy generation

The experimental parameters in Table 7-1 are used as control parameters for simulation. The effects of material properties, electrode connection of piezoelectric patch, and friction model parameters on energy generation performance are investigated, aiming to provide insights into the underlying mechanisms governing the behavior of the corresponding continuum beam energy generation system. It should be noted that we split the original 20×10×1 mm piezoelectric patch into two 10×10×1 mm patches to study the effect of electrode connection, and $d_{2,0}$ is introduced to represent the distance to the fixed end from the second PZT patch.

Figure 7-6 shows the effect of the host beam's Young's modulus E and density ρ on $P_{\mathrm{e}}^{\mathrm{RMS}}$ and the peak instant charging power $P_{\mathrm{e-peak}}$ under different conditions. The material properties of the host beam are listed in Table 7-2. The dimensional parameters of the host beam remain constant. The natural frequencies are mainly determined by the ratio between E and ρ. Upon analyzing the ratio among the materials being studied, copper exhibits the smallest ratio, which indicates lowest natural frequencies. And titanium has the highest ratio. However, their energy generation performance does not follow the sequence with respective to natural frequencies. The material used in the experiment demonstrates better output among the four, with titanium, copper, and stainless steel following in descending order. It can be found that the material used in the experiment possesses the smallest E and ρ comparing to the other three material. Small E usually indicates greater flexibility, and it is easier to deform. And it is common to result in slower response to dynamic inputs for material with high ρ due to increased inertia. Proper manipulation of material properties are essential for optimizing the energy generation performance of piezoelectric cantilevers.

Table 7-2 Host beam material properties.

Parameter	Exp. Al	Stainless steel (AISI 304)	Copper	Titanium (Ti-5Al-2.5Sn)
Young's modulus E (GPa)	50	190	110	110
Density ρ (kg/m^3)	2705	8000	8900	4480

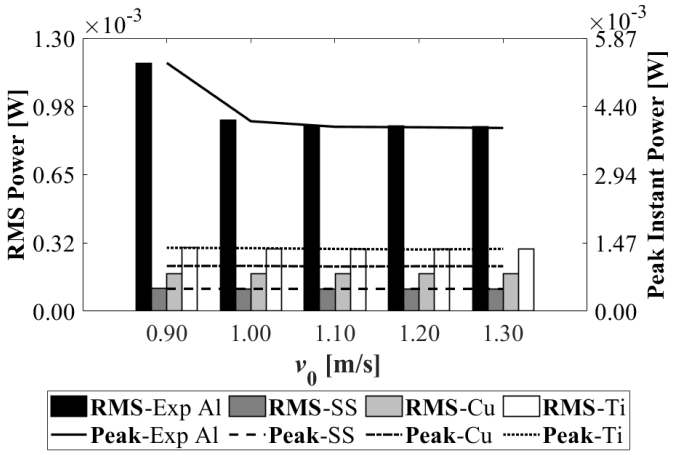

Figure 7-6 Effect of host beam material properties on energy generation.

Figure 7-7 compares the energy generation performance using different PZTs. The material properties of the PZTs are listed in Table 7-3. The piezoelectric coupled continuum beam is fabricated by bonding the PZT to the host beam. The size of the PZT is relatively small compared to the host beam. Therefore, it may not have a significant effect on the vibration dynamics. Based on the provided material properties, it can be seen that APC 855 has the highest relative dielectric constant K^{T} and piezoelectric constant d_{31}, and APC 850, APC 840, and APC 880 follows the descending sequence. The energy generation performance exhibits a similar trend because PZT with a higher K^{T} has better ability in storing and releasing energy, and PZT with low K^{T} can minimize signal interference for sensing purpose. Additionally, a higher d_{31} indicates that the material is more responsive to stress and efficient converting mechanical strain into electrical charge, consequently, generating higher energy.

Table 7-3 PZT material properties.

Parameter	APC 840	APC 850	APC 855	APC 880
Relative dielectric constant K^{T}	1275	1900	3300	1050
Electromechanical coupling factor k_{31}	0.35	0.36	0.40	0.30
Piezoelectric constant d_{31} (pC/N)	-125	-175	-276	-95
Young's modulus E_{p} (GPa)	80	63	59	90
Density ρ_{p} (kg/m^3)	7600	7600	7600	7600

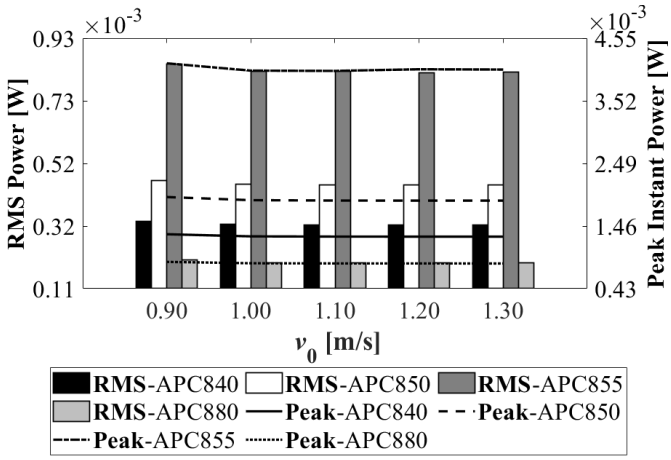

Figure 7-7 Effect of PZT patch material properties on energy generation.

Figure 7-8 demonstrates the energy generation performance of two setups of connections using the same total volume of PZT: electrically in parallel and electrically in series. Both setups are mechanically in parallel. Keeping the first patch's distance to the fixed end $d_{1,0}$ the same value as d_0, the second patch's distance to fixed end $d_{2,0}$ varies. The in parallel setup has a larger capacitance because the same electrodes of the two patches are connected. Conversely, the in series setup possesses lower capacitance because the opposite electrodes are connected, leading to a smaller effective electrode area. The variation in Figure 7-8 shows that the energy generation of both setups is enhanced with the increased normal load F_{N}. As $d_{2,0}$ increases, the energy outputs decrease for both setups. This is due to the decrease in strain in the second piezoelectric patch. $P_{\mathrm{e}}^{\mathrm{RMS}}$ of the in series connection is slightly higher than the in parallel connection under current equivalent resistance R, and this is because of the voltage and current relationships of the two connections. There is less internal power loss with the current R value for the in series connection. With further increased R, the difference in $P_{\mathrm{e}}^{\mathrm{RMS}}$ will be mitigated. Electrically in parallel configurations are usually favored for their ability to regulate the output voltage to a desirable value. Additionally, higher effective capacitance contributes to the enhancement of energy transfer efficiency.

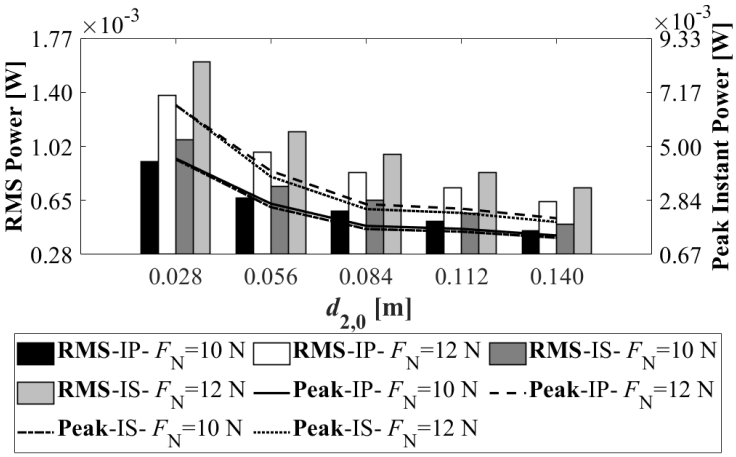

Figure 7-8 Effect of PZT patch electrode connection on energy generation. (IP: in parallel; IS: in series).

Figure 7-9 and Figure 7-10 display the effect of static friction coefficient μ_s on system dynamic response and energy generation performance. Figure 7-9 reveals the time domain and frequency domain responses with different friction locations d_f. Based on the results, a higher voltage output is achieved when d_f is closer to the free end of the structure. Conversely, when d_f is positioned closer to the fixed end, the system exhibits more higher frequency components in the spectrum. The predominant frequency component under different d_f remains proximate to the first resonant frequency of the structure. While comparing the dynamic response under different μ_s, a marginal increase in voltage amplitude is observed with larger μ_s. Derived from Eq. (2.8), a higher coefficient μ_s corresponds to a larger $\mu(v_r)$ when the relative velocity v_r approaches zero. The resulting friction force F_f is influenced by $\mu(v_r)$ and F_N. When v_r is close to zero, it approximates the static friction force. The augmented F_f consequently contributes to an increase in vibrational amplitude. The result in Figure 7-10 compares the energy generation performance with different μ_s, P_{e-peak} follows the same variation trend of voltage amplitude. The P_e^{RMS} associated with $\mu_s = 0.6$ surpasses the other three configurations in the same friction location. Upon comparing the dynamic responses within 30 - 40 s, Figure 7-9(b), (c), and (d) show an increased level of irregularity. The termination of the charging process is affected by the steady state peak voltage, and it may take longer to finish charging. The instant charging power from previous literature shows that P_e starts to decline after the peak power, indicating a reduction in P_e^{RMS} after the peak [115]. Different from P_{e-peak}, which is mainly governed by the peak voltage, P_e^{RMS} is also affected by the charging time. A longer charging period could result in a lower P_e^{RMS}.

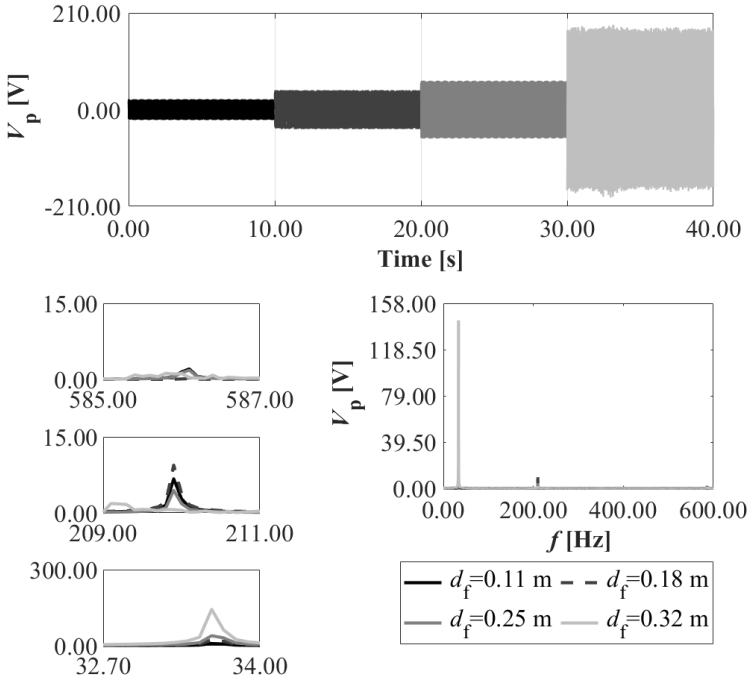
210.00
0.00
-210.00
V_p [V]
0.00
10.00
20.00
30.00
40.00
Time [s]
15.00
0.00
585.00
587.00
15.00
0.00
209.00
211.00
300.00
0.00
32.70
34.00
158.00
118.50
79.00
39.50
0.00
V_p [V]
0.00
200.00
400.00
600.00
f [Hz]
d_f=0.11 m
d_f=0.18 m
d_f=0.25 m
d_f=0.32 m

(a)

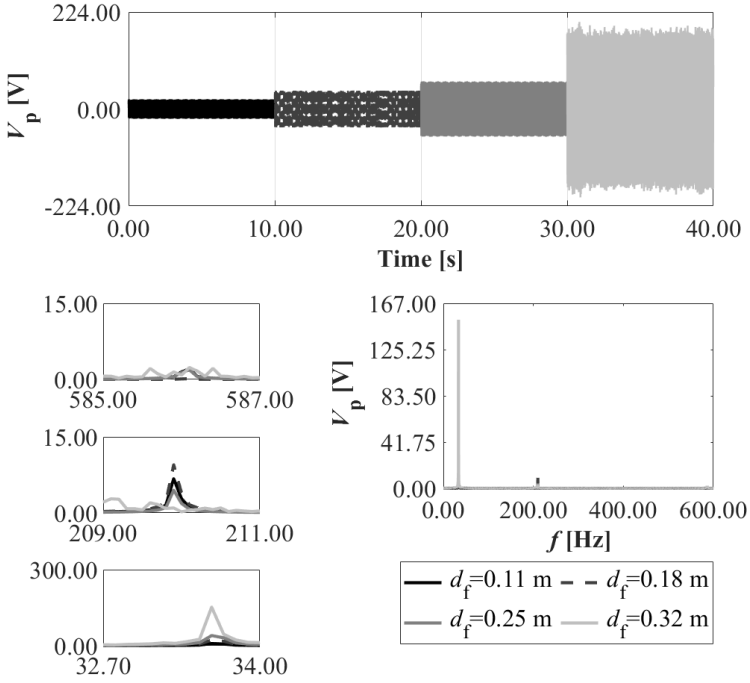
224.00
0.00
-224.00
V_p [V]
0.00
10.00
20.00
30.00
40.00
Time [s]
15.00
0.00
585.00
587.00
15.00
0.00
209.00
211.00
300.00
0.00
32.70
34.00
167.00
125.25
83.50
41.75
0.00
V_p [V]
0.00
200.00
400.00
600.00
f [Hz]
d_f=0.11 m
d_f=0.18 m
d_f=0.25 m
d_f=0.32 m

(b)

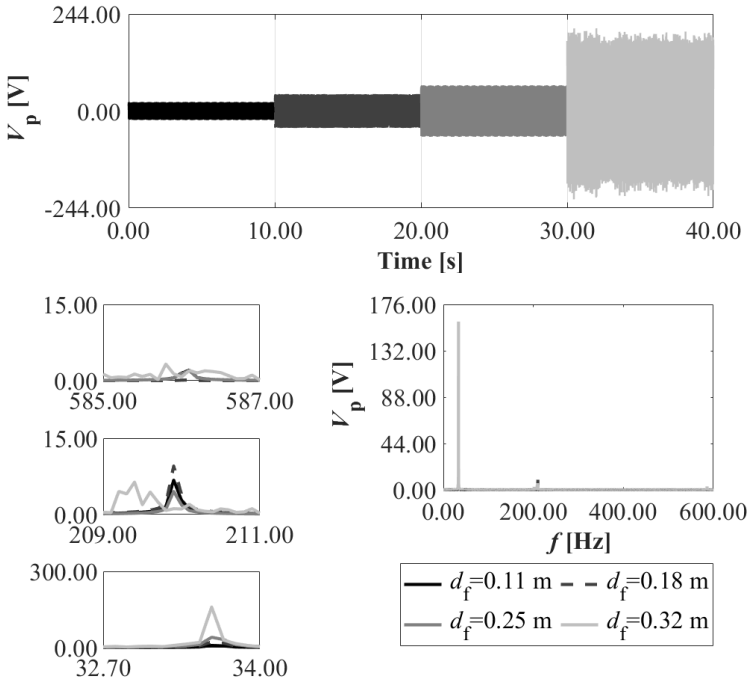

(c)

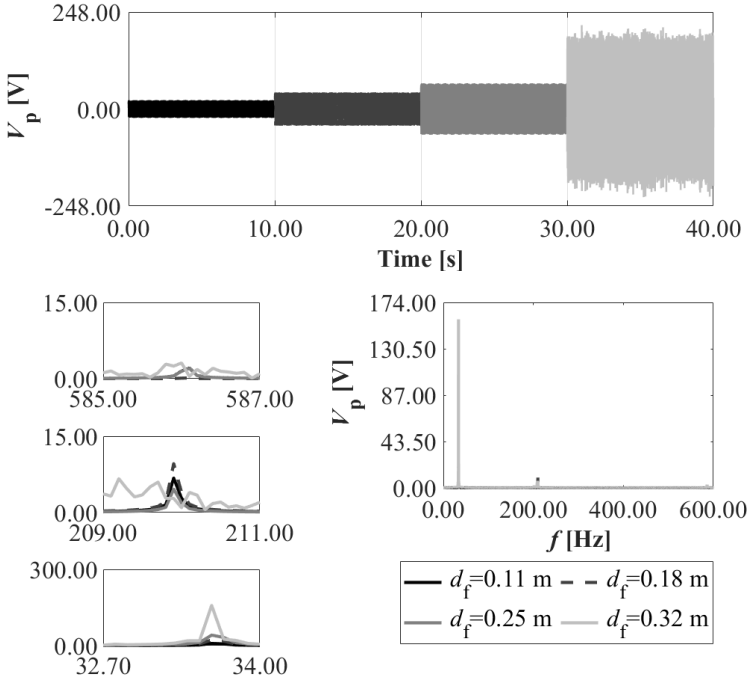

(d)

Figure 7-9 Effect of static friction coefficient μ_s on dynamic response. (a) μ_s = 0.6. (b) μ_s = 0.8. (c) μ_s = 1.0. (d) μ_s = 1.2.

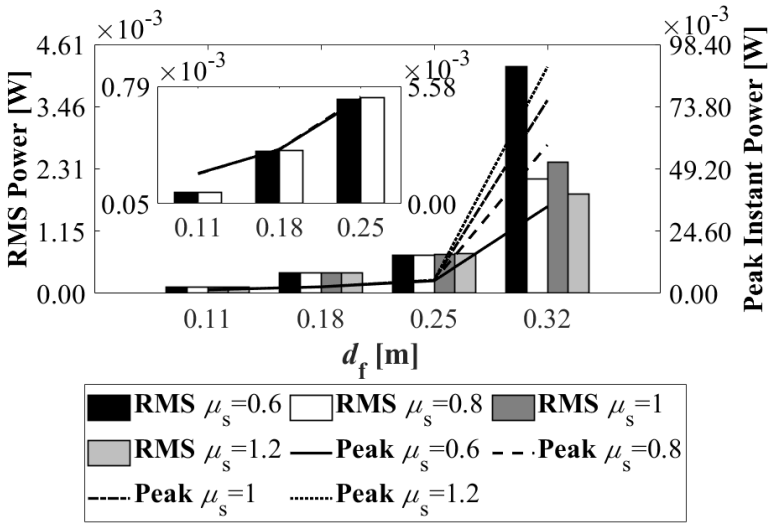

Figure 7-10 Effect of static friction coefficient μ_s on energy generation.

Figure 7-11 and Figure 7-12 analyze the influence of dynamic friction coefficient μ_k on system dynamic response and energy generation performance. Figure 7-11 shows the time domain and frequency domain responses. The variation of voltage outputs and predominant frequency components with different d_f exhibit a trend similar to that of μ_s. Larger peak voltage output is achieved with d_f closer to the free end, and the primary vibration frequency is still close to the first resonant frequency. When comparing the dynamic responses with varying μ_k, a distinct rise in voltage amplitude appears with higher μ_k. In accordance with Eq. (2.8), an increased μ_k results in a larger $\mu(v_r)$ when the relative velocity v_r is large. The system with large v_r corresponds to the slip friction state. The augmented F_f in slip state also causes an increase in vibrational amplitude. The result in Figure 7-12 compares the energy generation performance with different μ_k, both P_{e-peak} and P_e^{RMS} are enhanced with the increase of μ_k. By comparing the energy generation performance with different μ_s, there is distinct difference with different μ_k. Given that both stick state and slip state friction forces contribute to the system's dynamics, the pronounced impact of μ_k suggests that, under current parameter condition, the slip state holds a more significant role in influencing the system's dynamics.

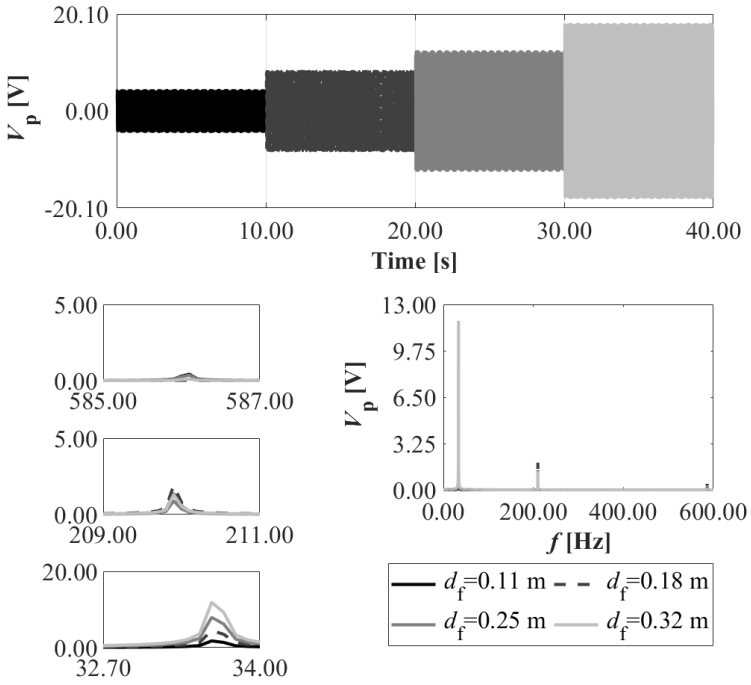
20.10
0.00
-20.10
V_p [V]
0.00
10.00
20.00
30.00
40.00
Time [s]
5.00
0.00
585.00
587.00
5.00
0.00
209.00
211.00
20.00
0.00
32.70
34.00
13.00
9.75
6.50
3.25
0.00
V_p [V]
0.00
200.00
400.00
600.00
f [Hz]
d_f=0.11 m
d_f=0.18 m
d_f=0.25 m
d_f=0.32 m

(a)

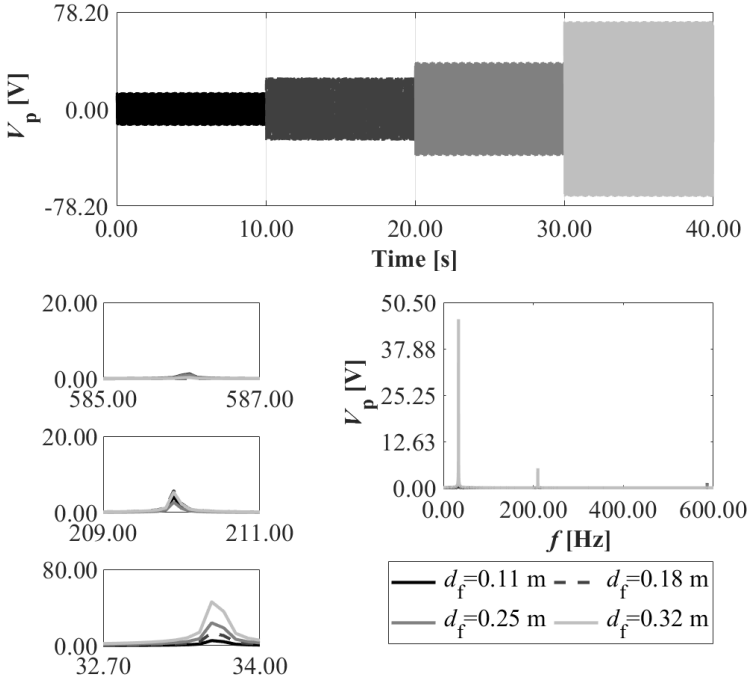
78.20
0.00
-78.20
V_p [V]
0.00
10.00
20.00
30.00
40.00
Time [s]
20.00
0.00
585.00
587.00
20.00
0.00
209.00
211.00
80.00
0.00
32.70
34.00
50.50
37.88
25.25
12.63
0.00
V_p [V]
0.00
200.00
400.00
600.00
f [Hz]
d_f=0.11 m
d_f=0.18 m
d_f=0.25 m
d_f=0.32 m

(b)

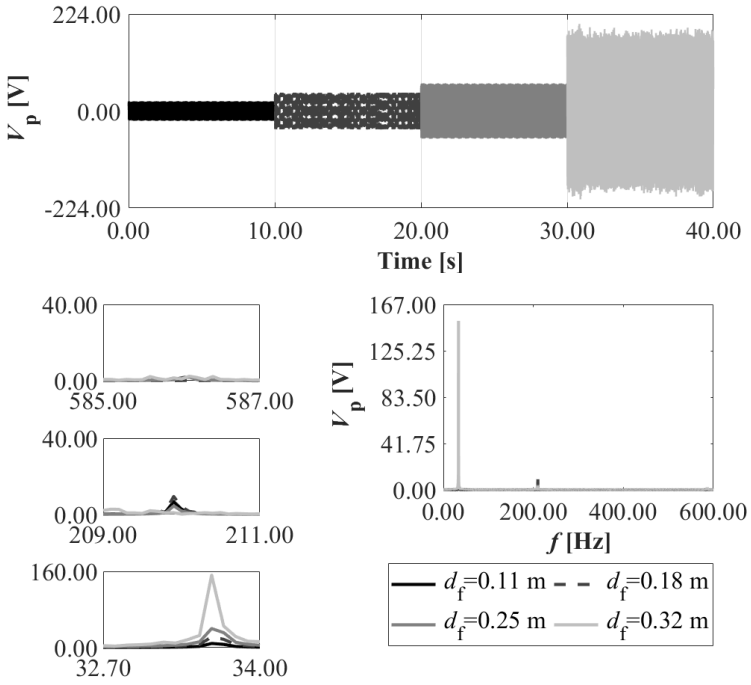

(c)

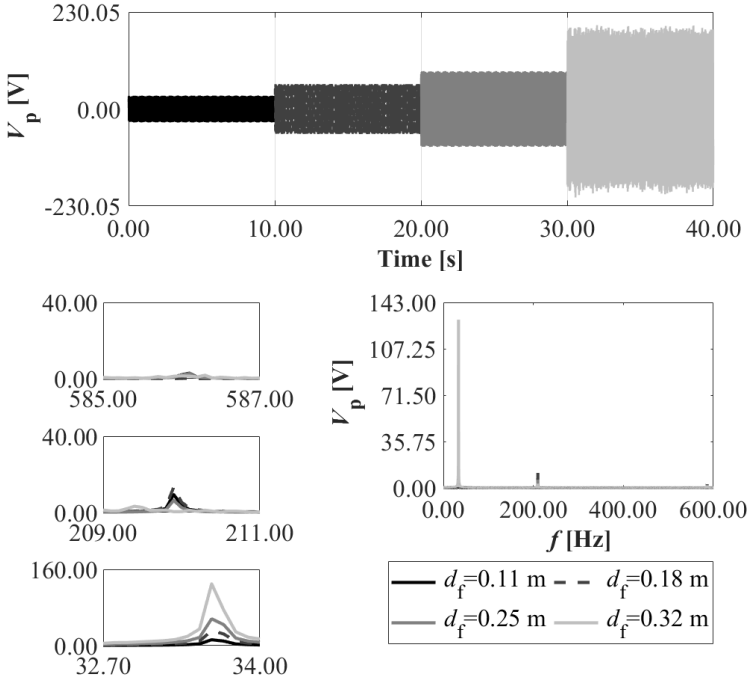

(d)

Figure 7-11 Effect of dynamic friction coefficient μ_k on dynamic response. (a) μ_k = 0.1. (b) μ_k = 0.3. (c) μ_k = 0.5. (d) μ_k = 0.7.

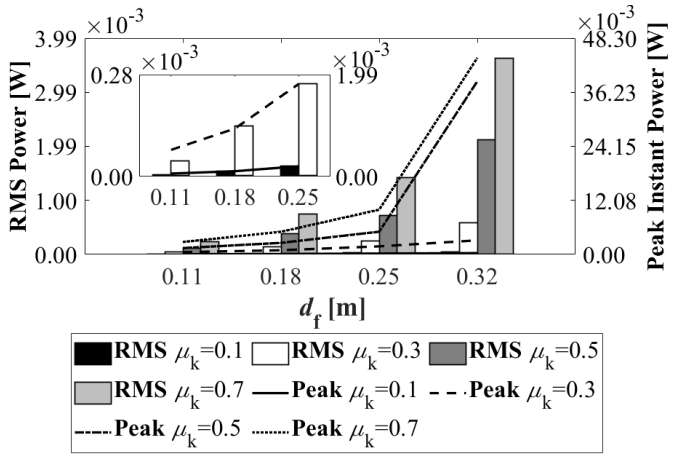

Figure 7-12 Effect of static friction coefficient μ_k on energy generation.

Figure 7-13 and Figure 7-14 demonstrate the effect of exponential decay factor C on system dynamic response and energy generation performance. Based on Eq. (2.8), $\mu(v_r)$ varies between μ_k and μ_s to characterize the dynamic variation of the effective friction coefficient. C is used to adjust the transition rate during stick-slip motion. A higher C value corresponds to a faster conversion rate. Conversely, a smaller C value yields opposite effect, with pronounced stick-slip phenomenon. Figure 7-13 depicts both time domain and frequency domain responses across different friction locations d_f. It is observed in Figure 7-13(b), (c), and (d) that the output voltages increase with the increasing d_f. For Figure 7-13(a) with C = 14, the dynamics become more intricate due to the intensified stick-slip motion. The output voltage at d_f = 0.25 m, which is closer to the fixed end, is higher compared to d_f = 0.32 m. Also, the predominant frequency component of the system shifts towards the second and third resonant frequencies. Figure 7-14 compares the energy generation performance with different C values. The energy generation performance is enhanced due to the stronger stick-slip motion associated with a smaller value of C. The exponential decay factor C plays a pivotal role in the dynamics of FIV, and it is influenced by different factors, such as the material properties and geometries of the frictional contact interfaces. The current parameter study of C on energy generation performance offers insight into the intricate dynamics of frictional interactions, and the results demonstrate the feasibility to achieve pronounced FIV with optimal energy generation performance. Future work can focus on investigating the dynamics of FIV for materials with difference surface conditions.

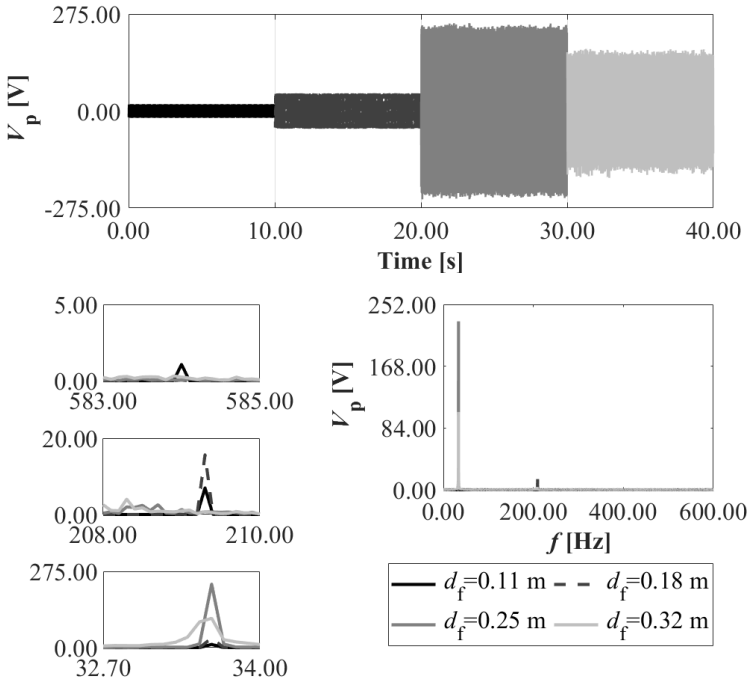
275.00
0.00
-275.00
V_p [V]
0.00
10.00
20.00
30.00
40.00
Time [s]
5.00
0.00
583.00
585.00
20.00
0.00
208.00
210.00
275.00
0.00
32.70
34.00
252.00
168.00
84.00
0.00
V_p [V]
0.00
200.00
400.00
600.00
f [Hz]
d_f=0.11 m
d_f=0.18 m
d_f=0.25 m
d_f=0.32 m

(a)

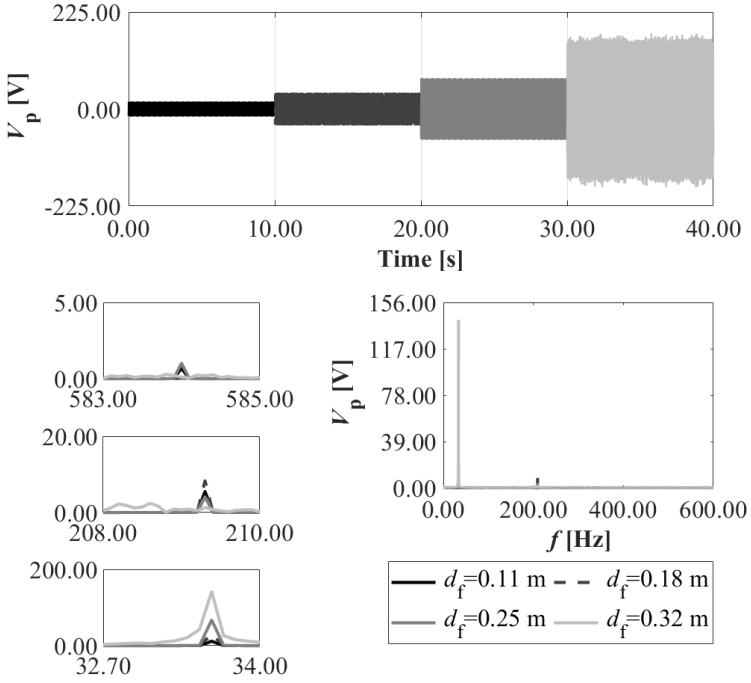
225.00
0.00
-225.00
V_p [V]
0.00
10.00
20.00
30.00
40.00
Time [s]
5.00
0.00
583.00
585.00
20.00
0.00
208.00
210.00
200.00
0.00
32.70
34.00
156.00
117.00
78.00
39.00
0.00
V_p [V]
0.00
200.00
400.00
600.00
f [Hz]
d_f=0.11 m
d_f=0.18 m
d_f=0.25 m
d_f=0.32 m

(b)

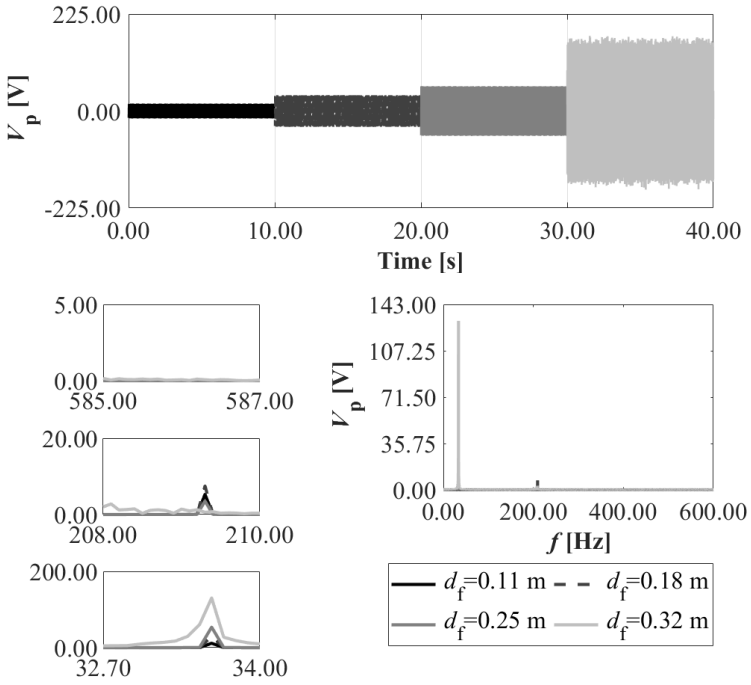

(c)

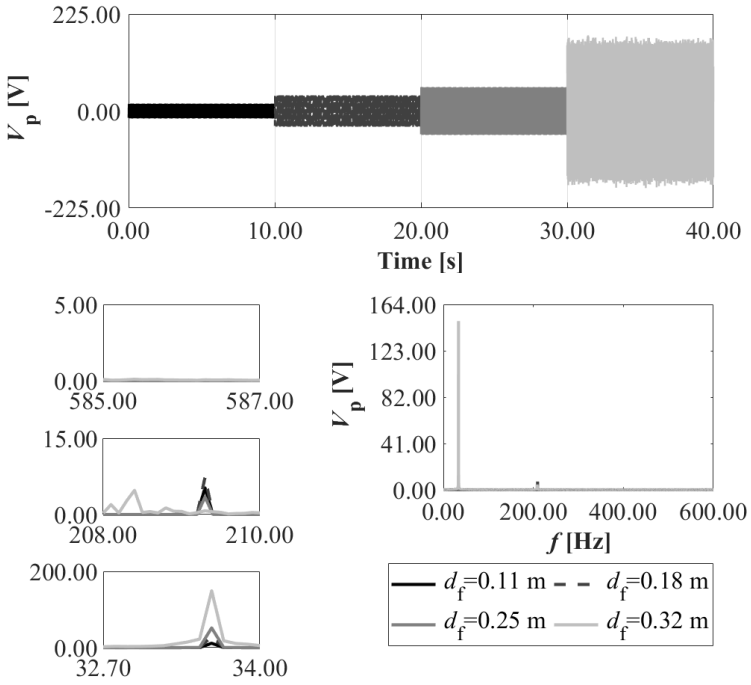

(d)

Figure 7-13 Effect of exponential decay factor C on dynamic response. (a) C = 14. (b) C = 16. (c) C = 18. (d) C = 20.

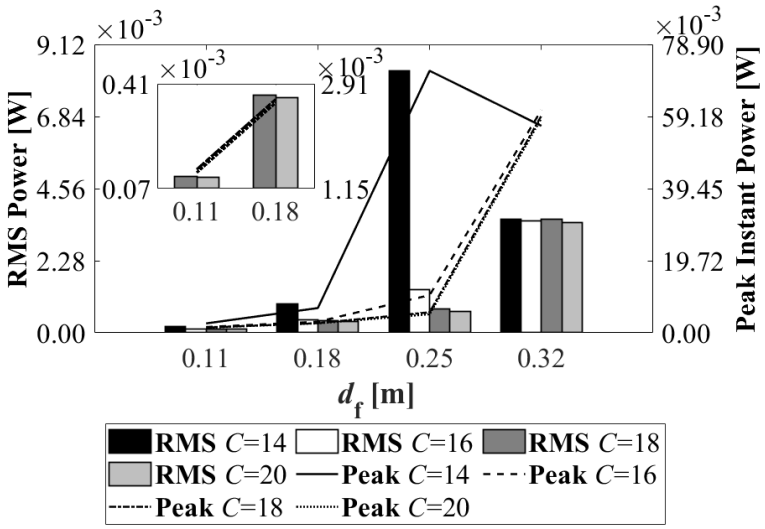

Figure 7-14 Effect of exponential decay factor C on energy generation.

7.2 Modeling and optimization of a piezoelectric stepped beam under friction excitation

The overall test setup, detailed setup, and conceptual design of the piezoelectric-coupled stepped beam are shown in Figure 7-15. An entire experimental arrangement, which includes the test apparatus and measuring devices, is displayed in the overall test setup. More specific experimental layouts of the motor, controller, oscilloscope, and frictional contact interface are illustrated in the detailed setup. The geometric parameters and the placement of piezoelectric material are depicted in the conceptual design of the prototype. The design, modeling and validation, and optimization processes are summarized in Figure 7-16. A continuum stepped beam is first introduced. The electromechanical coupled governing equation is derived based on the Euler-Bernoulli beam theory, the Stribeck friction model, and the piezoelectric constitutive equation. Experimental validation is then conducted to verify the dynamic energy output, and based on the validated model, datasets are generated to train a machine learning model. The performances of Convolutional Neural Network (CNN), Long Short-Term Memory (LSTM), and CNN-LSTM are compared to determine the most accurate model for prediction. Subsequently, the optimal model is employed for GA optimization. The GA starts with an initial population, and iterative processes are undertaken to refine these solutions. Fitness values are predicted, and individuals with high fitness are selected for reproduction through mating and mutation. Ultimately, the optimal parameters for the stepped beam design are determined.

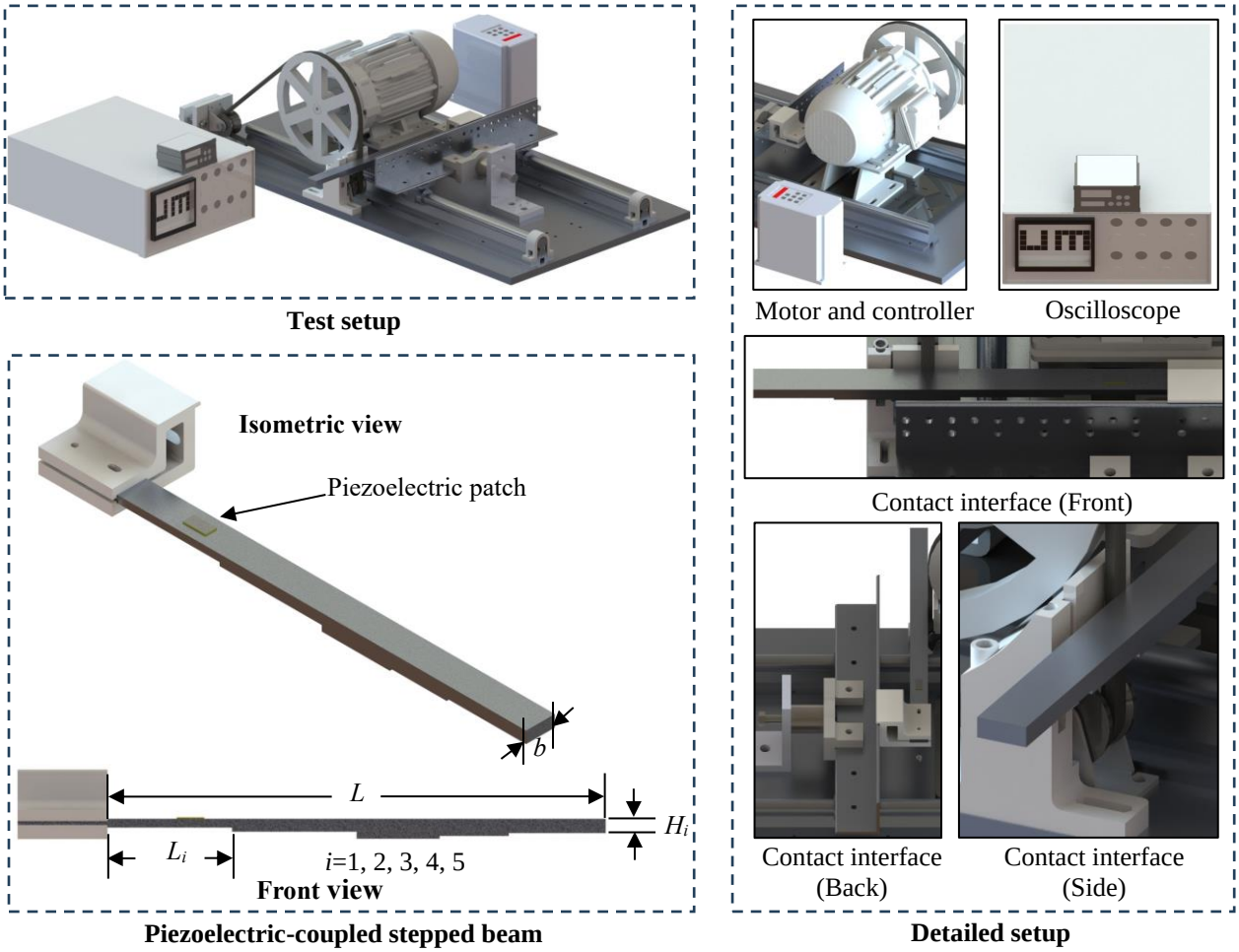

Figure 7-15 Test setup overview.

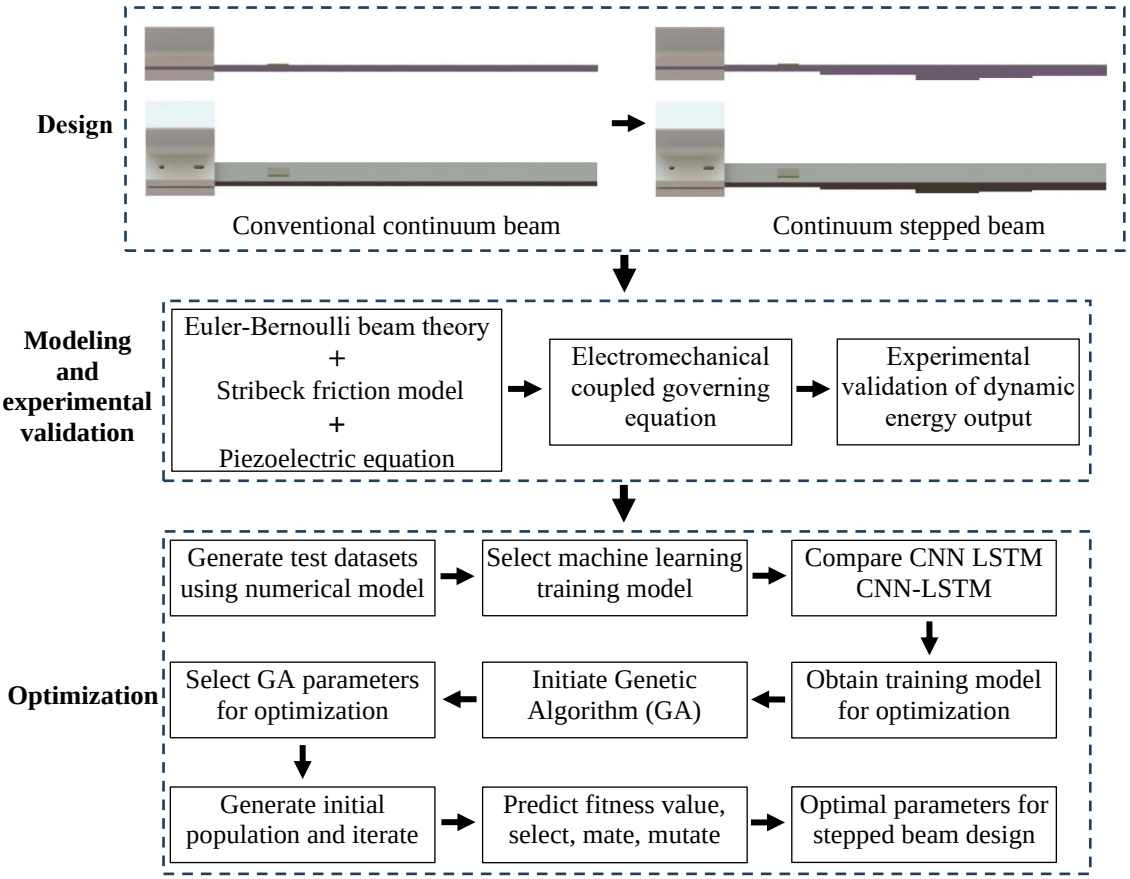

Figure 7-16 Flowchart of design, modeling and experimental validation, and optimization.

The electromechanical modeling of the energy generator can be referred in Section 2.5. To properly solve the dynamic response of the piezoelectric-coupled stepped beam, $w(s_i, t)$, the displacement function of the beam in Eq. (2.72) is divided into five sections: $0 < s_1 \leq L_1$, $L_1 < s_2 \leq L_2$, $L_2 < s_3 \leq L_3$, $L_3 < s_4 \leq L_4$, and $L_4 < s_5 \leq L_5$. Since there is a piezoelectric-coated small section in $0 < s_1 \leq L_1$, it can be divided into three small section: $0 < s_1 \leq L_{1,1}$, $L_{1,1} < s_1 \leq L_{1,2}$, and $L_{1,2} < s_1 \leq L_{1,3}$. The governing equations for free vibration can be expressed as:

$$\begin{cases} EI(s_1)\dfrac{d^4W_{1,1}^n}{ds_1{}^4} + \rho A(s_1){\omega_n}^2 W_{1,1}^n = 0, \ \ (0 < s_1 \leq L_{1,1}) \\ (EI)'\dfrac{d^4W_{1,2}^n}{ds_1{}^4} + m'{\omega_n}^2 W_{1,2}^n = 0, \ \ (L_{1,1} < s_1 \leq L_{1,2}) \\ EI(s_1)\dfrac{d^4W_{1,3}^n}{ds_1{}^4} + \rho A(s_1){\omega_n}^2 W_{1,3}^n = 0, \ \ (L_{1,2} < s_1 \leq L_{1,3}) \end{cases}, \tag{7.1}$$

$$EI(s_2)\frac{d^4W_2^n}{ds_2{}^4} + \rho A(s_2){\omega_n}^2 W_2^n = 0, \ \ \left(L_{1,3} < s_2 \leq L_2\right), \tag{7.2}$$

$$EI(s_3)\frac{d^4W_3^n}{ds_3{}^4}+\rho A(s_3){\omega_n}^2W_3^n=0,\ \ (L_2<s_3\le L_3), \tag{7.3}$$

$$EI(s_4)\frac{d^4W_4^n}{ds_4{}^4}+\rho A(s_4){\omega_n}^2W_4^n=0,\ \ (L_3<s_4\le L_4), \tag{7.4}$$

$$EI(s_5)\frac{d^4W_5^n}{ds_5{}^4}+\rho A(s_5){\omega_n}^2W_5^n=0,\ \ (L_4<s_5\le L_5), \tag{7.5}$$

where ω_n is the nth natural frequency. $W_{1,1}^n$, $W_{1,2}^n$, $W_{1,3}^n$, W_2^n, W_3^n, W_4^n, and W_5^n are the mode shape functions of the beam. The mode shape of the whole beam $W^n(s_i)$ can be expressed as $W^n(s_i)=W_{1,1}^n(s_1)+W_{1,2}^n(s_1)+W_{1,3}^n(s_1)+W_2^n(s_2)+W_3^n(s_3)+W_4^n(s_4)+W_5^n(s_5)$.

Assuming the solution of the mode shape function has the form of $W(s_i)=C_1\cos(ks_i)+C_2\sin(ks_i)+C_3\cosh(ks_i)+C_4\sinh(ks_i)$ [112], the free vibration solutions of the beam can be written as,

$$\begin{gathered}
W_{1,1}=C_1\cos(f_{1,1}s_1)+C_2\sin(f_{1,1}s_1)\\
+C_3\cosh(f_{1,1}s_1)+C_4\sinh(f_{1,1}s_1),\ \ (0<s_1\le L_{1,1})\\
W_{1,2}=C_5\cos(f_{1,2}s_1)+C_6\sin(f_{1,2}s_1)\\
+C_7\cosh(f_{1,2}s_1)+C_8\sinh(f_{1,2}s_1),\ \ (L_{1,1}<s_1\le L_{1,2})\\
W_{1,3}=C_9\cos(f_{1,3}s_1)+C_{10}\sin(f_{1,3}s_1)\\
+C_{11}\cosh(f_{1,3}s_1)+C_{12}\sinh(f_{1,3}s_1),\ \ (L_{1,2}<s_1\le L_{1,3})\\
W_2=C_{13}\cos(f_2s_2)+C_{14}\sin(f_2s_2)\\
+C_{15}\cosh(f_2s_2)+C_{16}\sinh(f_2s_2),\ \ (L_{1,3}<s_2\le L_2)\\
W_3=C_{17}\cos(f_3s_3)+C_{18}\sin(f_3s_3)\\
+C_{19}\cosh(f_3s_3)+C_{20}\sinh(f_3s_3),\ \ (L_2<s_3\le L_3)\\
W_4=C_{21}\cos(f_4s_4)+C_{22}\sin(f_4s_4)\\
+C_{23}\cosh(f_4s_4)+C_{24}\sinh(f_4s_4),\ \ (L_3<s_4\le L_4)\\
W_5=C_{25}\cos(f_5s_5)+C_{26}\sin(f_5s_5)\\
+C_{27}\cosh(f_5s_5)+C_{28}\sinh(f_5s_5),\ \ (L_4<s_5\le L_5)
\end{gathered}, \tag{7.6}$$

where $f_{1,1}$, $f_{1,2}$ and $f_{1,3}$ are calculated as ${f_{1,1}}^4={f_{1,3}}^4=(12\rho{\omega_n}^2)/(E{H_1}^2)$ and ${f_{1,2}}^4=(m'{\omega_n}^2)/(EI)'$, respectively; f_2, f_3, f_4, and f_5 can be determined as ${f_i}^4=(12\rho{\omega_n}^2)/(E{H_i}^2)$, and $i=2,3,4,5$; C_i are the unknown constants in the mode shape functions. The boundary conditions can be expressed as,

$$
\begin{aligned}
W_{1.1} &= 0, & \frac{dW_{1,1}}{ds_1} &= 0; & (s_1 = 0)\\
W_{1,1} &= W_{1,2}, & EI(s_1)\frac{d^2W_{1,1}}{{ds_1}^2} &= (EI)'\frac{d^2W_{1,2}}{{ds_1}^2}, & \\
\frac{dW_{1,1}}{ds_1} &= \frac{dW_{1,2}}{ds_1}, & EI(s_1)\frac{d^3W_{1,1}}{{ds_1}^3} &= (EI)'\frac{d^3W_{1,2}}{{ds_1}^3}; & (s_1 = L_{1,1})\\
W_{1,2} &= W_{1,3}, & EI(s_1)\frac{d^2W_{1,3}}{{ds_1}^2} &= (EI)'\frac{d^2W_{1,2}}{{ds_1}^2}, & \\
\frac{dW_{1,2}}{ds_1} &= \frac{dW_{1,3}}{ds_1}, & EI(s_1)\frac{d^3W_{1,3}}{{ds_1}^3} &= (EI)'\frac{d^3W_{1,2}}{{ds_1}^3}; & (s_1 = L_{1,2})\\
W_{1,3} &= W_2, & EI(s_2)\frac{d^2W_2}{{ds_2}^2} &= EI(s_1)\frac{d^2W_{1,3}}{{ds_1}^2}, & \\
\frac{dW_{1,3}}{ds_1} &= \frac{dW_2}{ds_2}, & EI(s_2)\frac{d^3W_2}{{ds_2}^3} &= EI(s_1)\frac{d^3W_{1,3}}{{ds_1}^3}; & (s_1 = L_{1,3})\\
W_2 &= W_3, & EI(s_3)\frac{d^2W_3}{{ds_3}^2} &= EI(s_2)\frac{d^2W_2}{{ds_2}^2}, & \\
\frac{dW_2}{ds_2} &= \frac{dW_3}{ds_3}, & EI(s_3)\frac{d^3W_3}{{ds_3}^3} &= EI(s_2)\frac{d^3W_2}{{ds_2}^3}; & (s_2 = L_2)\\
W_3 &= W_4, & EI(s_4)\frac{d^2W_4}{{ds_4}^2} &= EI(s_3)\frac{d^2W_3}{{ds_3}^2}, & \\
\frac{dW_3}{ds_3} &= \frac{dW_4}{ds_4}, & EI(s_4)\frac{d^3W_4}{{ds_4}^3} &= EI(s_3)\frac{d^3W_3}{{ds_3}^3}; & (s_3 = L_3)\\
W_4 &= W_5, & EI(s_5)\frac{d^2W_5}{{ds_5}^2} &= EI(s_4)\frac{d^2W_4}{{ds_4}^2}, & \\
\frac{dW_4}{ds_4} &= \frac{dW_5}{ds_5}, & EI(s_5)\frac{d^3W_5}{{ds_5}^3} &= EI(s_4)\frac{d^3W_4}{{ds_4}^3}; & (s_4 = L_4)\\
\frac{d^2W_5}{{ds_5}^2} &= 0, & \frac{d^3W_5}{{ds_5}^3} &= 0. & (s_5 = L_5)
\end{aligned}
\tag{7.7}
$$

The rest of the solving process is similar to the one depicted in Section 2.5.

7.2.1 Model validation with experiment

In this section, the derived model is validated by comparing simulation results with experimental data. The dimension of the PZT (APC 855) is 20×10×1 mm, which has a piezoelectric charge constant d_{31} and a piezoelectric coupling factor k_{31} of 276e^{-12} C/N and 0.40, respectively. The main components and their layouts are shown in Figure 7-17. The piezoelectric coupled beam is installed on a mounting structure, governed by fix-free boundary conditions. The

mounting structure is assumed to be rigid. A load cell is installed at the back of the mounting structure, which measures the normal load. A sliding belt, driven by a motor, is used to provide the sliding motion with a constant velocity during operation. A contact interface, depicted in Figure 7-15, is established when the belt is attached to the beam. An oscilloscope (DSO6014A) is used for data acquisition, which has an internal resistance of R = 1 MΩ. A three-phase motor (WEG CT002404NPW22) is employed to provide power, and a VFD module (CFW500B07P3B2DBN1H00) is utilized to control the rotating speed. A pully is mounted on the motor shaft, and the sliding belt is attached. The distance between the shaft and the edge of the pully $d_{\text{s-p}}$ is measured to be 115 mm. The sliding velocity v_0 is determined by $v_0 = 0.1047 N d_{\text{s-p}}$, and N is the rotating speed of the shaft. The conversion factor 0.1047 is derived from 0.1047 = 2π/60, which converts rpm to rad/s. The parameters for the experiment are shown in Table 7-4.

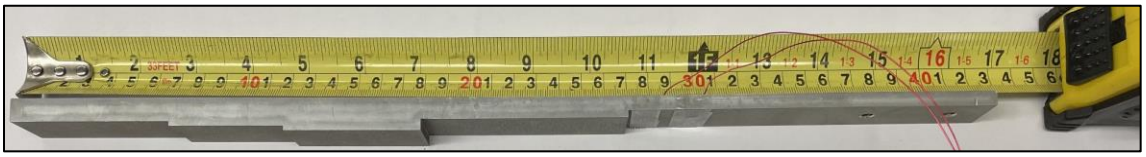

1. Stepped beam

2. VFD module

3. Load cell

4. Motor

5. Load cell display

6. Oscilloscope

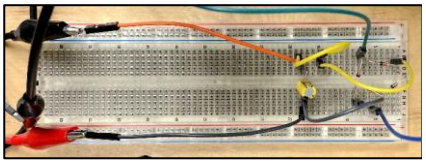

7. Charging circuit

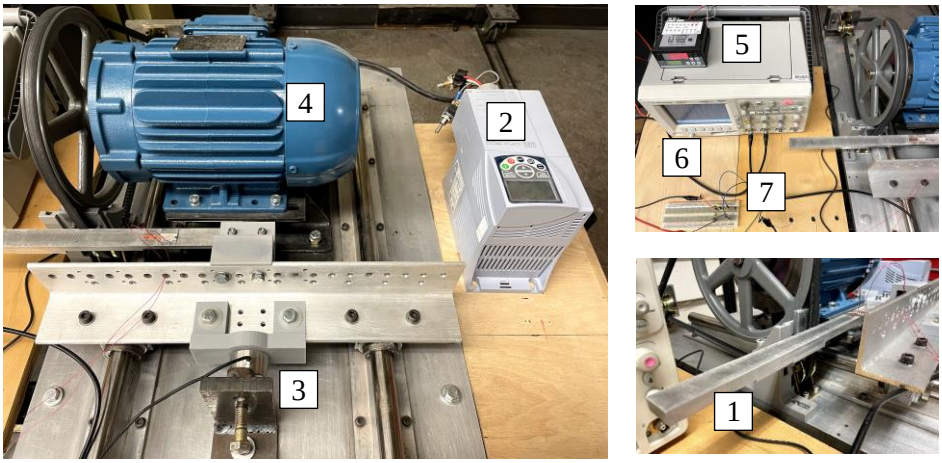

Figure 7-17 Experimental test setup.

Table 7-4 Experimental parameters.

Parameter	Stepped beam	PZT patch	Circuit	Friction model
Length (m)				
	$L_{1,1}$ = 0.05	L_{p} = 0.02	-	-
	$L_{1,2}$ = 0.07	-	-	-
	$L_{1,3}$ = 0.09	-	-	-
	L_2 = 0.18	-	-	-
	L_3 = 0.24	-	-	-
	L_4 = 0.29	-	-	-
	L_5 = 0.36	-	-	-
Thickness (m)				
	H_1 = 0.0064	h = 0.001	-	-
	H_2 = 0.0094	-	-	-
	H_3 = 0.0144	-	-	-
	H_4 = 0.0124	-	-	-
	H_5 = 0.0104	-	-	-
Width (m)	b = 0.0254	b_{p} = 0.01	-	-
Young's modulus (N/m^2)	E = 4.8e^{10}	E_{p} = 6.3e^{10}	-	-
Density (kg/m^3)	ρ = 2800	ρ_{p} = 7600	-	-
Piezoelectric constant (C/N)	-	d_{31} = -276e^{-12}	-	-
Capacitance (F)	-	C_{p} = 2.375e^{-9}	C_{s} = 10e^{-6}	-
Equivalent resistance (Ohm)	-	-	R = 1e^{6}	-
Equivalent resistance with attenuator probe (Ohm)	-	-	R' = 4e^{6}	-
Distance to fix end from friction location (m)	-	-	-	d_{f} = 0.163
Normal force (N)	-	-	-	F_{N} = 10, 15
Sliding velocity (m/s)	-	-	-	v_0 = 1.08, 1.45
Static friction coefficient	-	-	-	μ_{s} = 0.8
Dynamic friction coefficient	-	-	-	μ_{k} = 0.5
Exponential decay factor	-	-	-	C = 20

Experiments have been conducted on a stepped continuum beam with two different normal loads and sliding velocities to validate the model. In test 1, F_{N} = 10 N and v_0 = 1.08 m/s, and in test 2, F_{N} = 15 N and v_0 = 1.45 m/s. The validated model will be utilized to generate data for training a machine learning model. The other parameters in Table 7-4 remain unchanged. It should be noted that an attenuator probe is used to measure the generated voltage because the values exceed the measuring range of the oscilloscope. The equivalent resistance of the system used for simulation has been increased due to the incorporation of the attenuator probe. R' is determined based on experimental data. The dynamic output is shown in Figure 7-18. In both Figure 7-18(a) and Figure 7-18(b), thirteen to fourteen vibration peaks are observed with a period of 0.5 seconds. The first natural frequency of the continuum is 27.06 Hz. The vibration frequency of the system is close to the system's first natural frequency. The simulated dynamic outputs under different conditions are aligned with the experimental data, substantiating the occurrence of high-frequency vibrations with high voltage output through friction in a continuum beam.

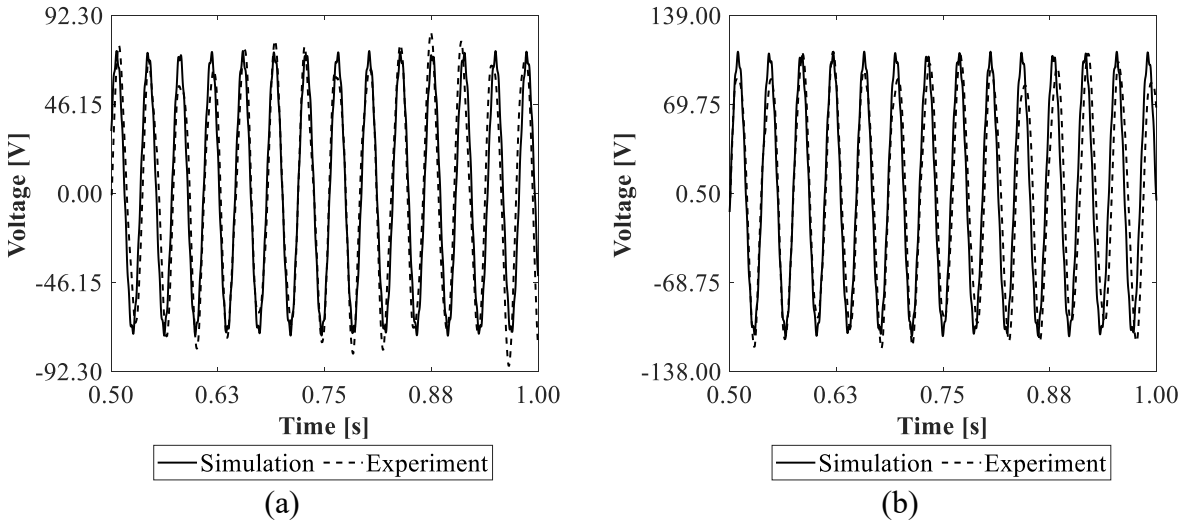

Figure 7-18 Dynamic output voltage under different testing conditions. (a) Output voltage (F_{N} = 10 N, v_0 = 1.08 m/s). (b) Output voltage (F_{N} = 15 N, v_0 = 1.45 m/s).

The energy output of the system while charging a storage capacitor is evaluated using transient charging simulation, and this method was experimentally validated in previous research [115]. The charging process under the same operating conditions depicted in Figure 7-18 is shown in Figure 7-19. The experimental charging curves exhibit some fluctuations, which can be attributed to the

loose connections within the charging circuit and the influence of structural vibrations. Overall, the simulation results align well with the experiments during the charging process.

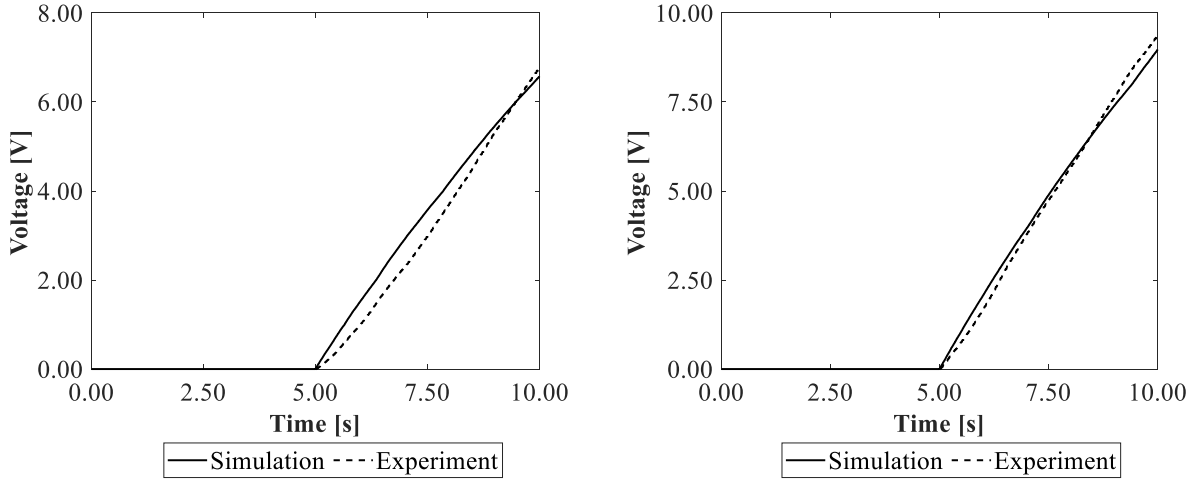

Figure 7-19 Dynamic charging output under different testing conditions. (a) Charging voltage (F_{N} = 10 N, v_0 = 1.08 m/s). (b) Charging voltage (F_{N} = 15 N, v_0 = 1.45 m/s).

7.2.2 Neural network model for prediction

Before applying GA for optimization, a neural network model is trained to represent the simulation model in optimization process. By using the neural network model to emulate the simulation model, computational cost associated with complex simulation to derive the final energy output from dynamic responses can be reduced while still achieving accurate and efficient optimization results.

Substantial progress has been conducted using deep learning techniques to deal with forecasting problems such as energy production [133], bearing health monitoring [134], and battery life prediction [135]. These models can handle complex dynamic behaviors due to their ability to learn the intricate patterns and relationships among the input data, and make prediction for unseen input data. These abilities make it a reliable and accurate tool for prediction. The CNN-LSTM network is a well-established and broadly used deep learning model aimed at solving time series forecasting problems. The conventional CNN model has feature extraction capability, but it may struggle to deal with long and intricate temporal data. Conversely, the LSTM network has demonstrated proficiency in capturing temporal dependencies from the features in the training dataset and make accurate prediction of system dynamics. Combining the feature extraction

capability of CNN and the learning advantage of LSTM, the hybrid model can potentially improve the prediction performance.

A performance evaluation of the CNN, LSTM, and CNN-LSTM models is conducted. The neural network models are trained using the simulation data from the experimentally verified model to predict the performance of the energy generator under different design parameters. The architecture of the hybrid model is shown in Figure 7-20. There are four main layers in the model: input layer, CNN layers, LSTM layer, and output layer. In the first stage, the input size is defined in the input layer, and the sequence of input is established. In the second stage, the data is passed to the first CNN layer. A set of filters is applied to the input data, and a set of feature maps is generated. Each feature map corresponds to the output of one filter and represents a specific feature in the input data. The convolutional layer then learns to detect relevant features by adjusting the weights of its filters during training. A batch normalization layer is applied after the convolutional layer to improve the stability of the network. A Rectified linear unit (ReLU), which can introduce non-linearity, is used as an activation function to the output of the batch normalization layer. It replaces negative activations with zero, effectively introducing sparsity and enabling the network to learn complex relationships in the data. To provide the model with the flexibility and capacity to learn hierarchical representations of the input data, the second CNN layer is added, and the output from the first CNN layer is used as input. In the third stage, the LSTM layer is introduced in the architecture, and the output from the second stage is passed to it. The LSTM layer is effective at capturing long-range dependencies and temporal patterns in sequential data. The output from the second stage contains high-level features extracted from the input data. The LSTM layer then processes these features and captures patterns across the sequence. LSTM network processes data sequentially and maintains a memory state. The memory state is updating based on the input sequence. The output from the LSTM layer is finally passed to a fully connected (FC) layer, which connects all the neurons from the previous layer to every neuron in its layer and forms a fully connected network. In the fourth stage, the output from the third stage is passed to a regression layer, outputting a model for prediction. By incorporating the LSTM layer after the CNN layer, the neural network architecture combines the strengths of both CNNs and LSTM, allowing it to make predictions on sequential data effectively.

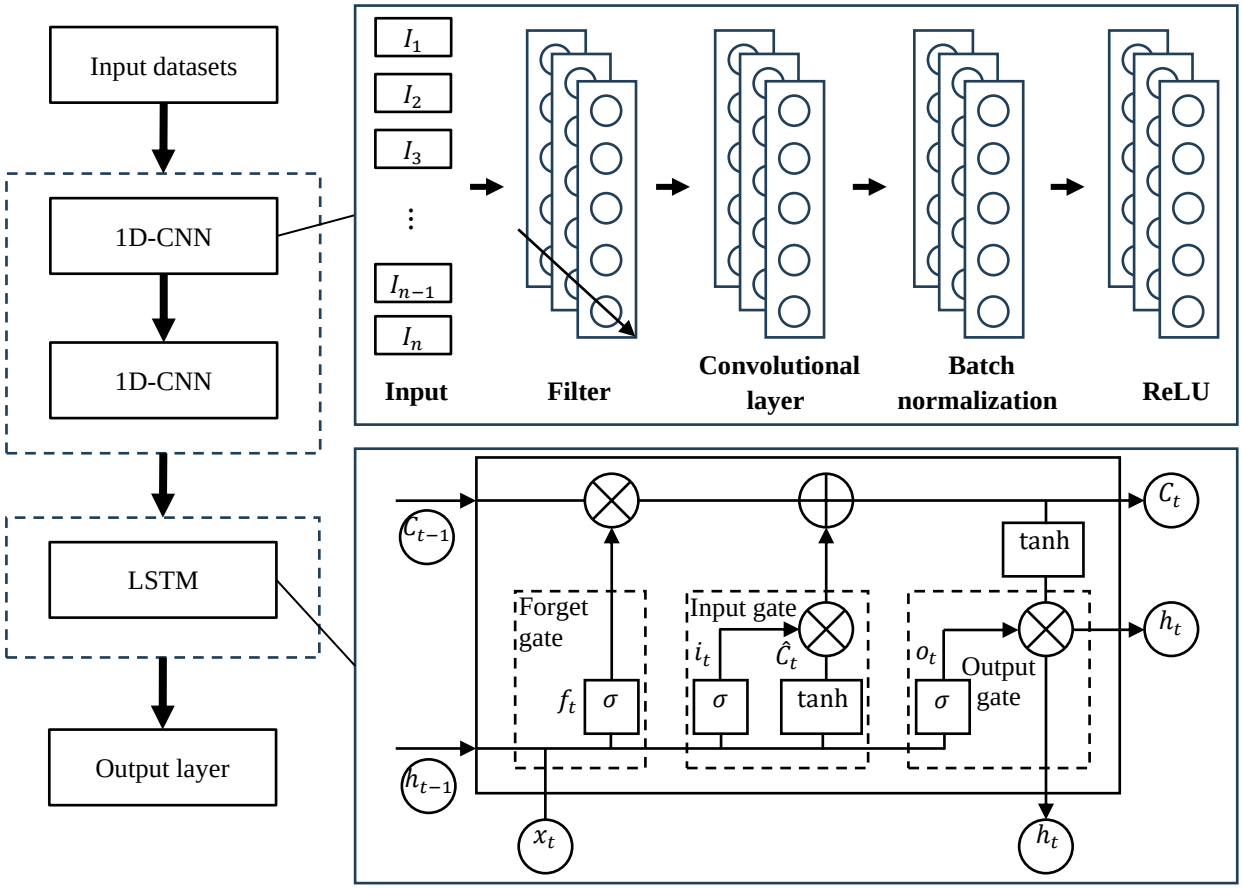

Figure 7-20 Architecture of CNN-LSTM network.

An analysis is carried out to investigate the validity of CNN-LSTM model. The architectures of different models are shown in Table 7-5. The CNN model has two one-dimensional convolutional layers and a fully connected layer. The first one-dimensional convolutional layer has 32 filters with a filter size of 3. The second one-dimensional convolutional layer has 64 filters with a filter size of 3. And the fully connected layer (dense) has 51 neurons. On the other hand, the LSTM model is designed with one LSTM layer and a fully connected layer. The LSTM layer has 200 units, and the dense layer has 51 neurons. Finally, the CNN-LSTM model is designed with two one-dimensional convolutional layers, one LSTM layer, and a fully connected layer. The number of filters and filter size in one-dimensional convolutional layers, the number of units in the LSTM layer, and the number of neurons in the dense layer are the same as the CNN and LSTM models for comparison.

The results of the CNN, LSTM, and CNN-LSTM networks are compared in detail. The training and testing datasets are created by generating random data using the simulation model. 10000

simulation results are used to train the deep learning model. 70% of the results are used to train the model, and the remaining 30% are used to evaluate the performance. The general visual comparison of the prediction results from the CNN, LSTM, and CNN-LSTM networks is shown in Figure 7-21. The black, red, and blue lines represent the output results from three sets of randomly generated input data. The solid, dashed, dash-dotted, and dotted lines illustrate the charging curves from the training models (CNN, LSTM, and CNN-LSTM) and numerical model. The detailed results of correlations between the training outputs and numerical output can be found on the right side of Figure 7-21. All the training outputs show the same variation trend compared with the numerical output, and it proves the feasibility of using a high-accuracy training model to make prediction. Among the three outputs from the training models, the visual comparison reveals that the outputs from the CNN-LSTM model have the closest alignment with the outputs from the numerical model.

Table 7-5 Architectures of the deep learning models.

CNN	LSTM	CNN-LSTM
Input	Input	Input
Conv1D (32)	LSTM (200)	Conv1D (32)
Layer normalization	Dense (51)	Layer normalization
ReLU	Regression output	ReLU
Conv1D (64)		Conv1D (64)
Layer normalization		Layer normalization
ReLU		ReLU
GlobalAveragePooling1D		LSTM (200)
Dense (51)		Dense (51)
Regression output		Regression output

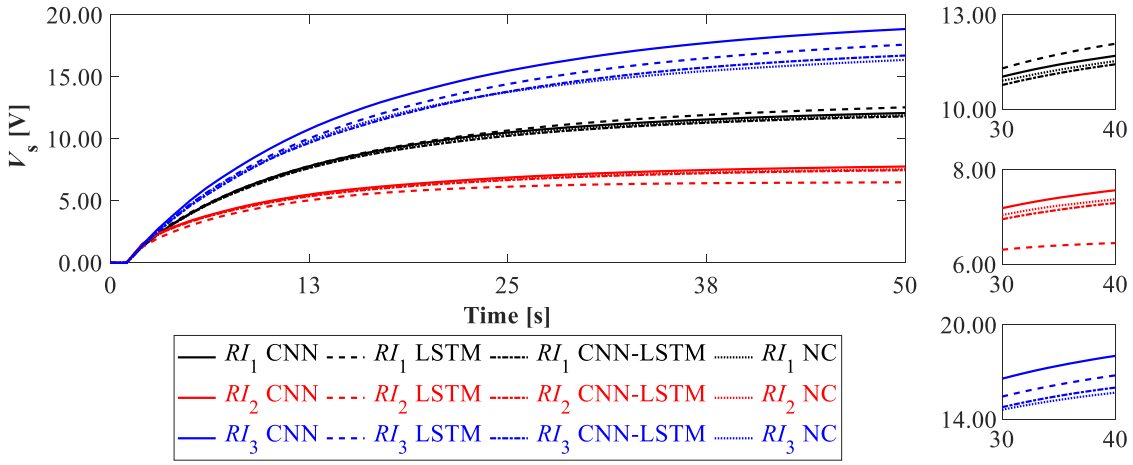

Figure 7-21 Comparison of the predicted charging curves (training model) and true charging curves (numerical model) using CNN, LSTM, and CNN-LSTM.

Different correlation coefficients and the dynamic time warping (DTW) distance are calculated to compare the prediction accuracy from the three deep learning training models. The Pearson, Kendall, and Spearman correlation coefficients, denoted by ρ_p, τ, and ρ_s, respectively, are calculated to evaluate the correlations between the outcomes generated by the training and numerical models [136]. ρ_p, τ, and ρ_s range from -1 to 1, with values closer to 1 indicating a strong positive correlation. A positive correlation means that the variation of the outputs from the training model and numerical model tends to move in the same direction. Correlation values closer to -1 indicate a strong negative correlation, which implies that the variations of the outputs move in the opposite direction. The correlation coefficients, computed using output results from 50 randomly generated instances, are depicted in Figure 7-22. The black, red, and blue symbols represent the correlation coefficients obtained from the CNN, LSTM, and CNN-LSTM models. The circle, square, and triangle symbols denote ρ_p, τ, and ρ_s. All the ρ_p, τ, and ρ_s values are close to 1, indicating a positive correlation. For the CNN model, some Spearman correlation coefficients (black square symbol) are located slightly below 1. For the LSTM model, some Pearson correlation coefficients (red circle symbol) are located slightly below 1. For the CNN-LSTM model, all the correlation coefficients (blue circle, square, and triangle symbols) are extremely close to 1. The CNN-LSTM model demonstrates the best positive correlation between the training and numerical models' outputs.

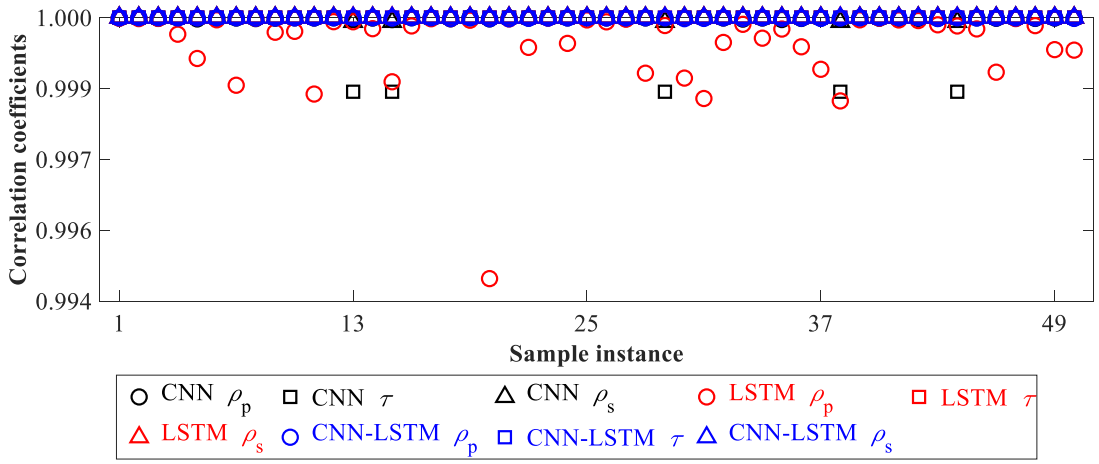

Figure 7-22 Comparison of the correlation coefficients (Pearson coefficient ρ_p, Kendall coefficient τ, and Spearman coefficient ρ_s) between the predicted charging curves (training model) and true charging curves (numerical model) using CNN, LSTM, and CNN-LSTM.

The dynamic time warping (DTW) distances of the outputs from the training models and numerical models are also calculated from the same instances used in Figure 7-22 [137]. The result is shown in Figure 7-23. Smaller DTW distance indicates a closer correlation between the curves. Some notable fluctuations are apparent in the results calculated between the training output using the LSTM model and the output using the numerical model. Additionally, subtle fluctuations can be observed in the result calculated with the CNN model. However, the DTW distances calculated with CNN-LSTM show stable and low values with almost no fluctuations. The feasibility, efficacy, and accuracy of utilizing the CNN-LSTM model for the current prediction task are substantiated.

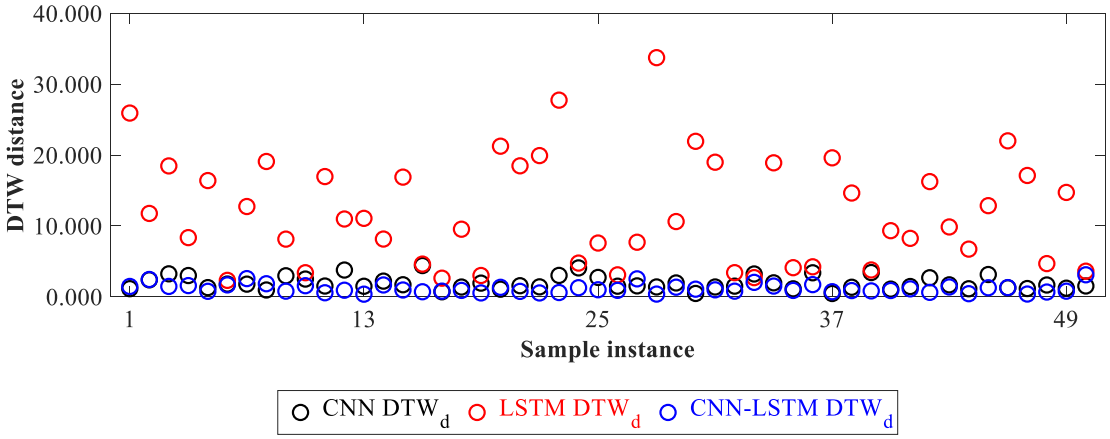

Figure 7-23 Comparison of the dynamic time warping distances between the predicted charging curves (training model) and true charging curves (numerical model) using CNN, LSTM, and CNN-LSTM.

7.2.3 Genetic algorithm for optimization

GA, developed by John Holland and his collaborators in the 1960s and 1970s, is a search-based optimization technique based on the principles of biological evolutions [138]. It is commonly used to find optimal or near-optimal solutions. The work flow of GA is depicted in Figure 7-24. It begins with a randomly generated initial population of input, and each instance in the population undergoes an evaluation based on a fitness function. In this study, the fitness function is the CNN-LSTM training model, which generates a prediction for each input instance. The prediction

includes 51 data representing the charging output from 0 to 50 seconds. The performance of the inputs is assessed based on the last data point of the output, which is then used as the fitness score for GA. Inputs with high fitness scores are selected from the current population as parents for the next generation. The selected inputs undergo genetic crossover and mutation operations to create offspring inputs. A detailed explanation of genetic operations can be found in previous literatures [139]–[141]. The offspring inputs replace some of the inputs in the previous iteration with low fitness scores. The algorithm iterates for a predefined number of generations or until a termination condition is met. These conditions may involve finding a good solution or reaching a maximum number of iterations. Eventually, the algorithm converges to the optimal or near-optimal solutions.

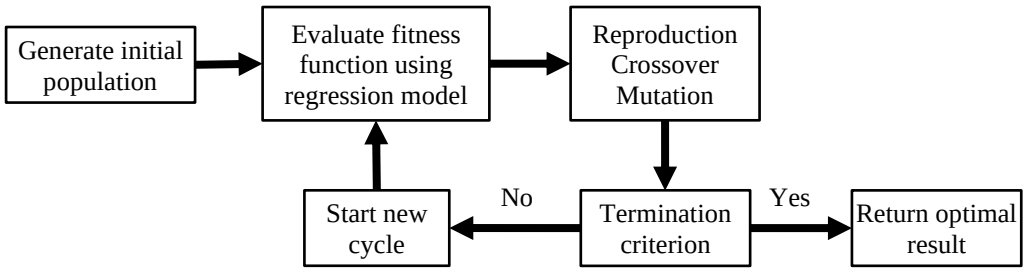

Figure 7-24 Flowchart of GA.

7.2.4 Optimization case 1 with constant total mass (CTM)

The result from optimization case 1 is presented in this section, wherein the stepped beam for optimization maintains a constant total mass of 0.157 kg. The constant geometric and friction model parameters during optimization are listed in Table 7-6. The varying geometric parameters during optimization are listed in Table 7-7. The effect of the friction model and circuit parameters on energy generation performance can be found in previous literature [142]. The present work focuses on the effect of geometric parameters on energy generation performance. The fitness values during iterative optimization are depicted in Figure 7-25. And three different friction locations are considered for optimization. The variation of the best and worst fitness values with the increase in generation is illustrated in Figure 7-26.

The length ($L_{1,1}$, $L_{1,2}$, $L_{1,3}$, L_2, L_3, L_4, L_5), the parameters of the piezoelectric-coated section ($L_{1,1}$, $L_{1,2}$, $L_{1,3}$, H_1, L_p, h, b_p), and friction model parameters (F_N, v_0, μ_s, μ_k, C) remain constant during the optimization process. The thickness of different sections of the beam (H_2, H_3, H_4, H_5) is the tuning parameters for the optimization. While the total mass of the continuum beam for

optimization case 1 remains constant, the width of the beam is adjusted in accordance with variations in thickness. The mechanical deformation of the beam is under the assumption of Euler-Bernoulli beam theory, in which the beam should be long and slender compared to its cross-sectional dimensions, allowing for the neglect of transverse shear deformations and torsional effects. The tuning parameters (H_2, H_3, H_4, H_5) have a variation ratio of $\pm 10\%$, with bounds set at H_l = 0.0057 m and H_u = 0.007 m.

Figure 7-25(a), (b), and (c) show the fitness values during the iterative optimization process at different friction locations. While the optimization process involves more than three variables, the variation of Var_3 is depicted by the circle size, and the variation of Var_4 is represented by the grey scale. From the projected view of Var_1, it can be observed that the fitness value increases with the increase of Var_1 (H_2). A similar but less obvious variation trend can be seen from the projected view of Var_2 (H_3). While analyzing the effects of variations in Var_3 and Var_4 on fitness value, it is observed that some high fitness values correspond to middle size circles with moderate gray color. These results suggest that the upper bound of H may not be the optimal values for Var_3 and Var_4. The variation ranges of fitness values in Figure 7-25(a), (b), and (c) are 8.25 to 10.25, 25.75 to 29.75, and 44.75 to 52.75, respectively. The range increases with the increase in the friction location d_f. Since the Stribeck model is used to describe the frictional behavior, and the parameters of the friction model in the optimization are the same. The reduced variation ranges of fitness values with the decreased d_f can be attributed to the imposed constraints on the motion of the beam, which results in a smaller amplitude of vibration. Figure 7-26(a), (b), and (c) illustrate the variation of the best and worst fitness values as generation increases. In the optimizations depicted in Figure 7-26(a), (b), and (c), the best fitness values keep noticeably increasing until around 150 generations, while the worst fitness values decrease until around 250 generations.

Table 7-6 Constant parameters during optimization.

Parameter	Beam	Friction model
Length (m)		
	$L_{1,1}$ = 0.04	-
	$L_{1,2}$ = 0.06	-
	$L_{1,3}$ = 0.072	-
	L_2 = 0.144	-
	L_3 = 0.216	-
	L_4 = 0.288	-
	L_5 = 0.36	-
Thickness (m)		

	$H_1 = 0.00635$	-
Width (m)	$b = 0.0254$	-
Normal force (N)	-	$F_N = 10$
Sliding velocity (m/s)	-	$v_0 = 0.9$
Static friction coefficient	-	$\mu_s = 0.8$
Dynamic friction coefficient	-	$\mu_k = 0.5$
Exponential decay factor	-	$C = 20$

Table 7-7 Varying parameters during optimization.

Parameter	Beam	Friction model
Thickness (m)		
	$0.0057 \leq H_2 \leq 0.007$	-
	$0.0057 \leq H_3 \leq 0.007$	-
	$0.0057 \leq H_4 \leq 0.007$	-
	$0.0057 \leq H_5 \leq 0.007$	-
Width (m)	$0.0230 \leq b \leq 0.0283$	-

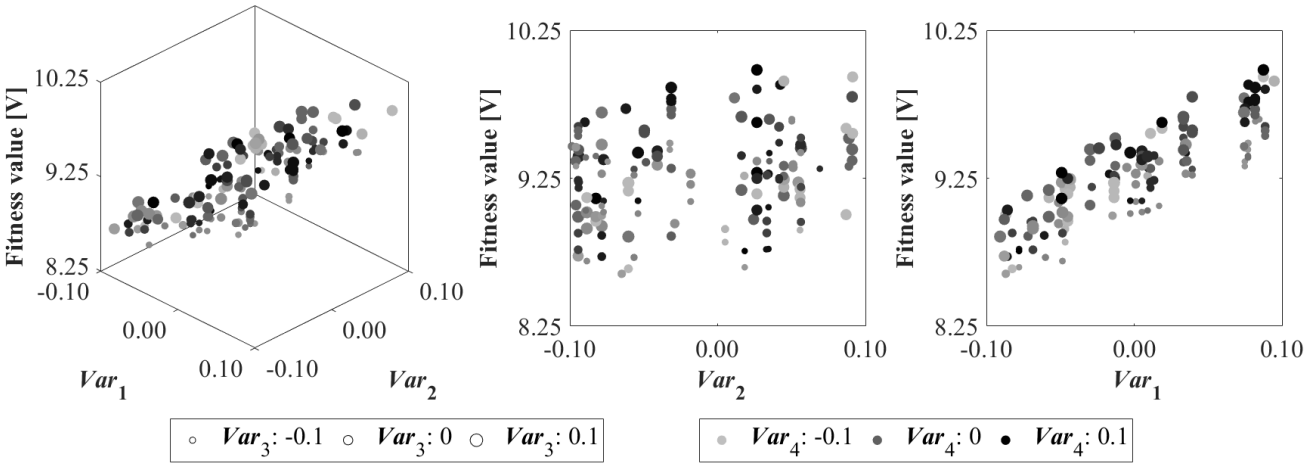

(a)

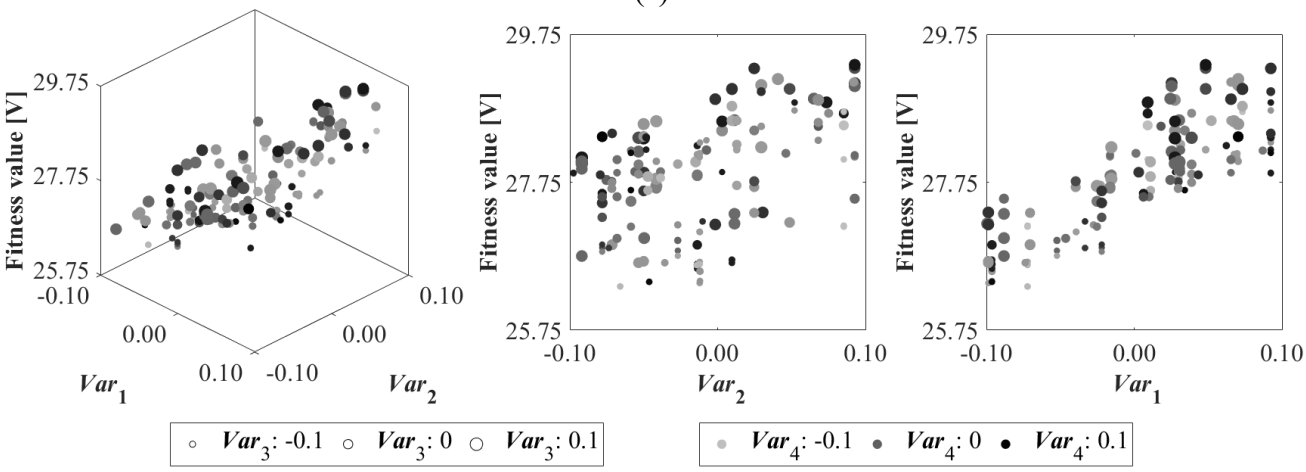

(b)

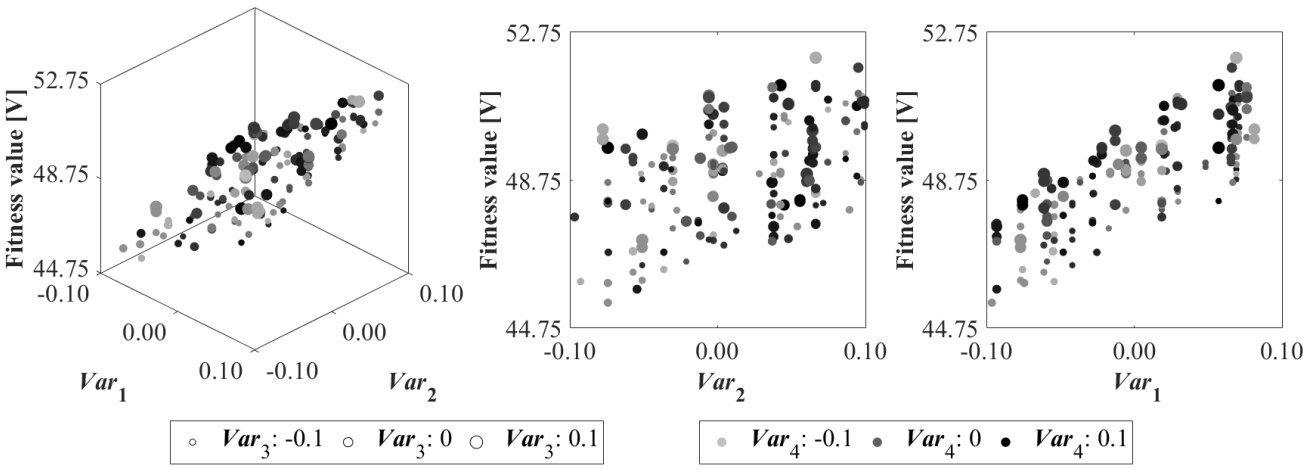

(c)

Figure 7-25 Fitness values during the iterative optimization process. (a) d_f = 0.09 m, C = 20. (b) d_f = 0.18 m, C = 20. (c) d_f = 0.27 m, C = 20. Var_1, Var_2, Var_3, and Var_4 stand for the variation ratios of H_2, H_3, H_4, and H_5, respectively.

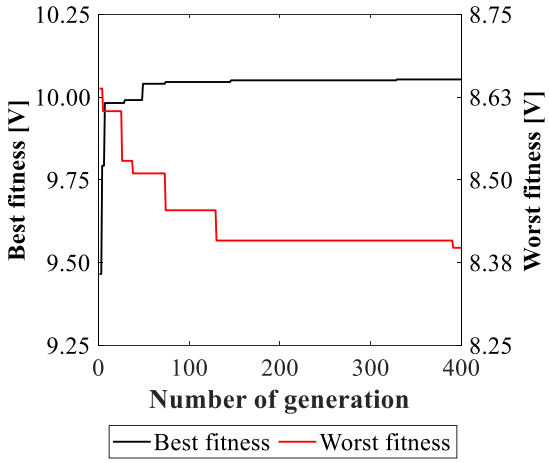

(a)

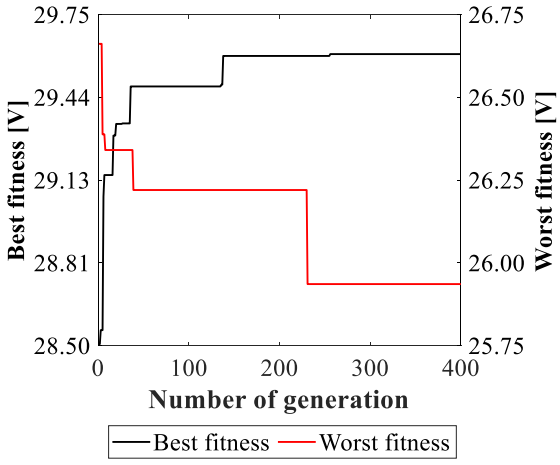

(b)

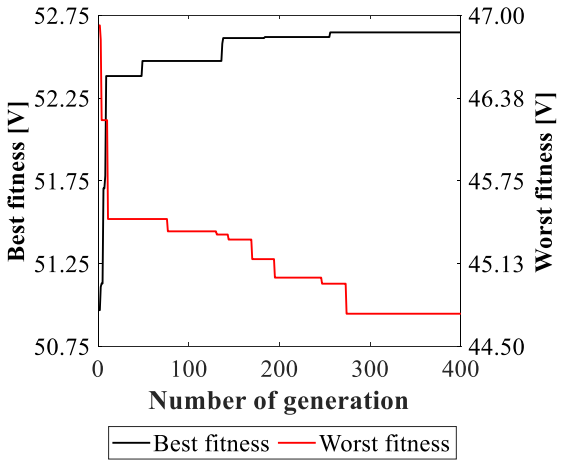

(c)

Figure 7-26 Comparison of the best and worst fitness values during the iterative optimization. (a) d_f = 0.09 m, C = 20. (b) d_f = 0.18 m, C = 20. (c) d_f = 0.27 m, C = 20. Var_1, Var_2, Var_3, and Var_4 stand for the variation ratios of H_2, H_3, H_4, and H_5, respectively.

The comparison of the optimization results in case 1 is listed in Table 7-8. For optimization case 1, the optimal values of H_2 and H_3 converge to the upper bound of H. The optimal values of H_4 in CTM#2 and CTM#3 converge to the upper bound of H. The optimal value of H_4 in CTM#1 is within the range of the midpoint and the upper bound of H, and it is smaller than the values in CTM#2 and CTM#3. Additionally, the optimal values of H_5 in CTM#1, CTM#2, and CTM#3 span from the midpoint to the upper bound of H. During the 400 generation optimization, the best fitness values in CTM#1, CTM#2, and CTM#3 are 10.05, 29.60, and 52.58 V, respectively, while the worst fitness values are 8.40, 25.94, and 44.97 V. Improvements of 19.7%, 14.1%, and 16.9% are achieved, correspondingly.

Table 7-8 Comparison of the optimization results in case 1.

Parameter	CTM#1 (d_f = 0.09 m)	CTM#2 (d_f = 0.18 m)	CTM#3 (d_f = 0.27 m)
b (m)	0.0239	0.0238	0.0239
H_1 (m)	0.00635	0.00635	0.00635
H_2 (m)	0.00692	0.00695	0.00694
H_3 (m)	0.00698	0.00689	0.00687
H_4 (m)	0.00681	0.00696	0.00694
H_5 (m)	0.00666	0.00680	0.00659
Total mass (kg)	0.157	0.157	0.157
Best V_s (V)	10.05	29.60	52.58
Worst V_s (V)	8.40	25.94	44.97
Improvement (%)	19.7	14.1	16.9

7.2.5 Optimization case 2 with varying total mass (VTM)

The result from optimization case 2 is presented in this section, wherein the stepped beam for optimization has a varying total mass. The difference between case 1 and case 2 is that in case 2, the width of the beam b remains constant of 0.0254 m. The total mass of the beam is changing based on the input of tuning parameters. All other parameters for optimization are the same between cases 1 and 2. The tuning parameters (H_2, H_3, H_4, H_5) have the same variation ratio compared to case 1. Figure 7-27(a), (b), and (c) show the fitness values during the iterative optimization process. A similar variation trend can be observed that the fitness value increases with the increase of Var_1 (H_2). Nevertheless, the effects of Var_2, Var_3, and Var_4 variations on fitness value do not exhibit a linear trend. The fitness values exhibit a randomly distributed pattern in the projected view of Var_2 (H_3), while different sizes of circles and various levels of gray color correspond to high and low fitness values. The variation ranges of fitness values in Figure 7-27(a), (b), and (c) are slightly smaller than those in Figure 7-25, but they also increase with the increase in d_f. The potential reason for this phenomena may be the same. Figure 7-28(a), (b), and (c) show the variation of the best and worst fitness values as generation increases. The variation trends of the best and worst fitness values follow a similar pattern, as shown in Figure 7-26.

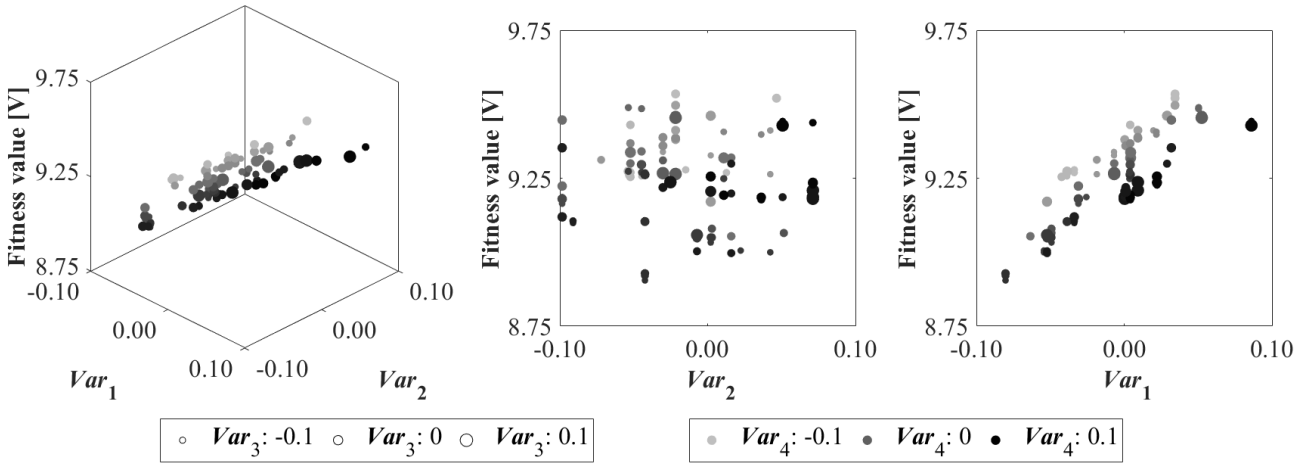

(a)

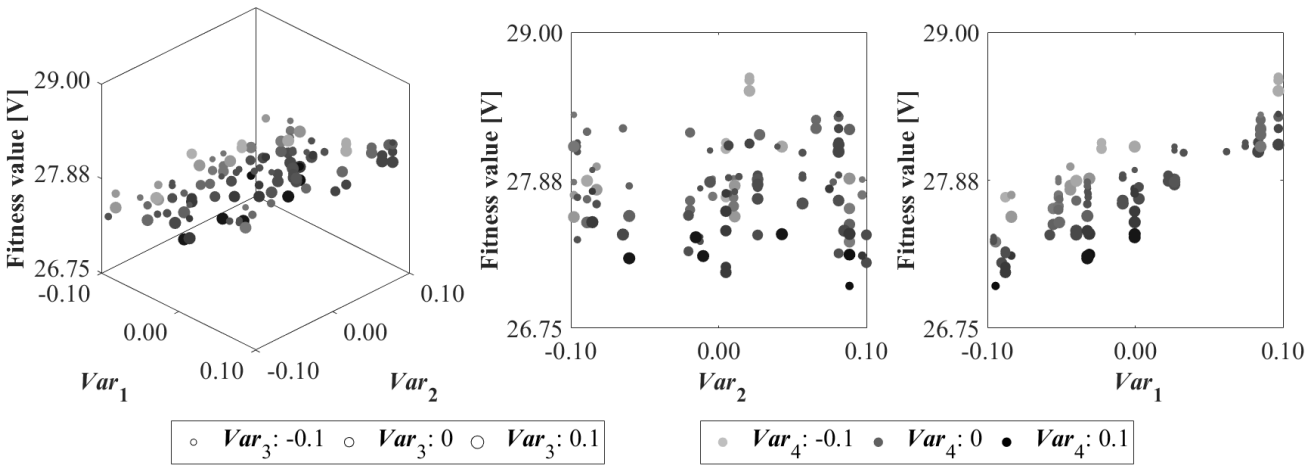

(b)

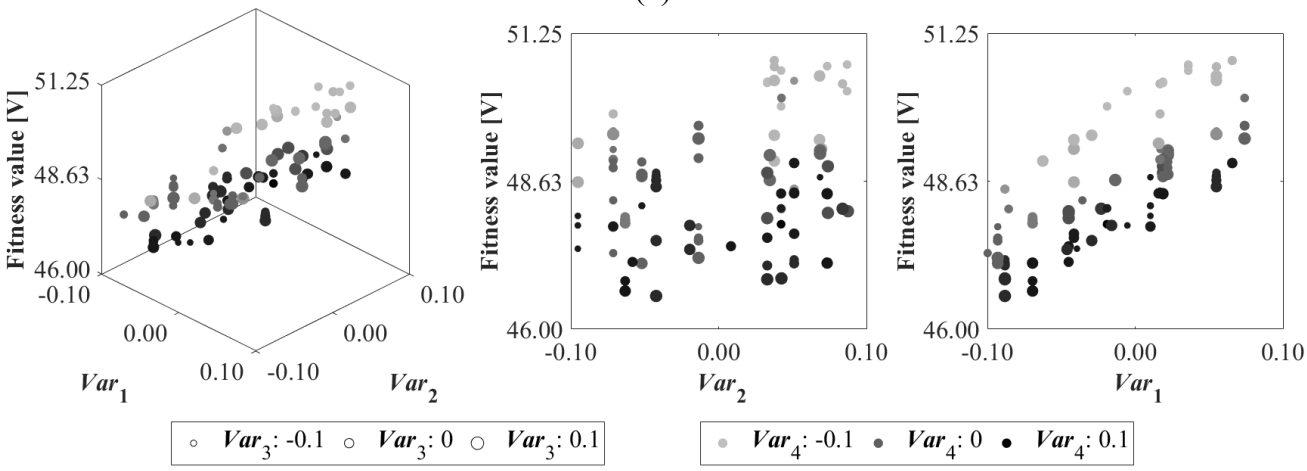

(c)

Figure 7-27 Fitness values during the iterative optimization process. (a) d_f = 0.09 m, C = 20. (b) d_f = 0.18 m, C = 20. (c) d_f = 0.27 m, C = 20. Var_1, Var_2, Var_3, and Var_4 stand for the variation ratios of H_2, H_3, H_4, and H_5, respectively.

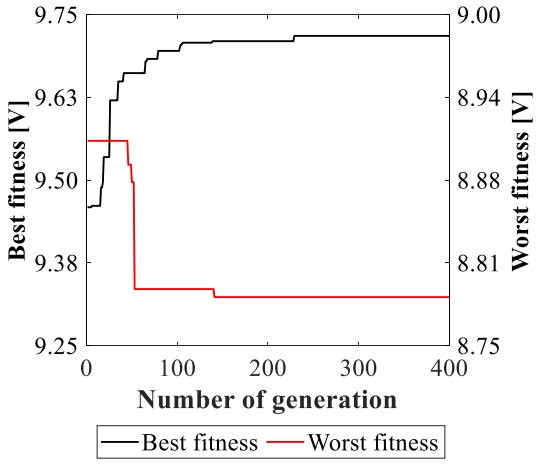

(a)

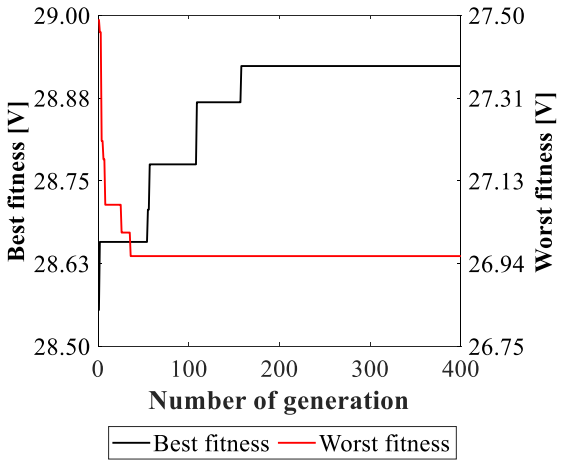

(b)

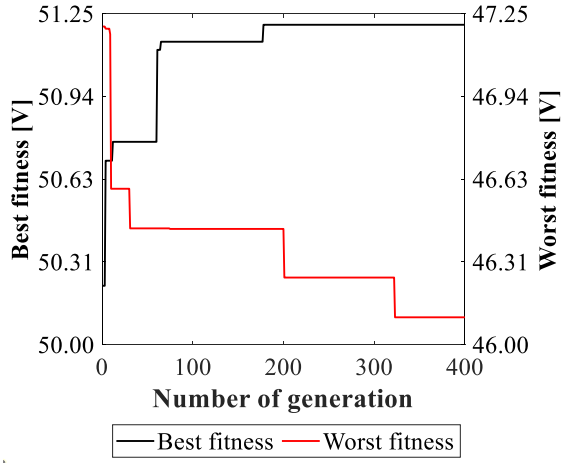

(c)

Figure 7-28 Comparison of the best and worst fitness values during the iterative optimization. (a) d_f = 0.09 m, C = 20. (b) d_f = 0.18 m, C = 20. (c) d_f = 0.27 m, C = 20. Var_1, Var_2, Var_3, and Var_4 stand for the variation ratios of H_2, H_3, H_4, and H_5, respectively.

The comparison of the optimization results in case 2 is listed in Table 7-9. For optimization case 2, the optimal values of H_2 in VTM#1, VTM#2, and VTM#3 converge to the upper bound of H. The optimal values of H_3 in VTM#2 and VTM#3 converge to the upper bound of H. The optimal value of H_3 in VTM#1 is close to the midpoint of H. The optimal value of H_4 in VTM#1 is also close to the midpoint of H, while the optimal values of H_4 in VTM#2 and VTM#3 converge to the lower bound of H. The optimal values of H_5 in VTM#1, VTM#2, and VTM#3 converge to the lower bound of H. The best fitness values in VTM#1, VTM#2, and VTM#3 are 9.72, 28.9, and 51.21 V, respectively, while the worst fitness values are 8.79, 26.95, and 46.10 V. Improvements of 10.6%, 7.3%, and 11.1% are achieved, correspondingly.

Table 7-9 Comparison of the optimization results in case 2.

Parameter	VTM#1 (d_f = 0.09 m)	VTM#2 (d_f = 0.18 m)	VTM#3 (d_f = 0.27 m)
b (m)	0.0254	0.0254	0.0254
H_1 (m)	0.00635	0.00635	0.00635
H_2 (m)	0.00695	0.00693	0.00685
H_3 (m)	0.00635	0.00698	0.00696
H_4 (m)	0.00595	0.00575	0.00572
H_5 (m)	0.00576	0.00573	0.00582
Total mass (kg)	0.155	0.157	0.157
Best V_s (V)	9.72	28.9	51.21
Worst V_s (V)	8.79	26.95	46.10
Improvement (%)	10.6	7.3	11.1

Under a variation ratio of $\pm 10\,\%$ for the selected tuning parameters, the results from optimization case 1 and optimization case 2 exhibit a noticeable level of improvement when comparing the best and worst fitness values. The energy generation performance of a piezoelectric stepped beam can be affected by variations in geometric design. Increasing the variation ratio and incorporating additional tuning parameters can potentially lead to a more significant influence on energy output. Therefore, parameter optimization should be considered to obtain the optimal or near-optimal solutions, thereby enhancing energy output.

7.3 Summary and discussion

Section 7.1 presents an investigation of a piezoelectric coupled continuum beam subjected to FIV. A piezoelectric coupled mathematical model describing the dynamic of a continuum beam under FIV is introduced and solved for the first time via an iterative method, and the accuracy of the model is validated by experiment. Dynamic voltage output is realized through high frequency FIVs occurring near the resonant frequencies of the system. The experimental results prove the feasibility of inducing higher mode vibrations through friction using a continuous structure. Parameter studies involving the host beam materials, PZT materials, and electrode connections provide insights into the design of the energy generator. For the host structure, materials with low E and ρ facilitate FIV with larger amplitude. Utilizing high performance PZT materials, placing PZT near the high strain area of the host structure, and applying proper electrode connections contribute to enhancing energy output. The friction model parameters, μ_s, μ_k, and C, have distinct effects on the dynamic characteristics of the system. μ_s and μ_k influence the friction forces

associated with stick and slip states, respectively, while C governs the transition rate between the stick and slip states. Pronounced FIV, which can contributes significantly to energy generation performance of the system by stimulating vibrations close to higher-order resonant frequencies coupled with high dynamic voltage outputs, can be realized using friction materials with a smaller C value.

In Section 7.2, a piezoelectric coupled stepped beam under FIV is developed. A testing prototype with a stepped design is fabricated, and experiments under different conditions are conducted to validate the effectiveness of the mathematical model. Additionally, a deep learning model for prediction is trained with simulation data, and GA is employed for the geometric optimization of the energy generator. The following insights are derived from the analysis. Based on Euler–Bernoulli beam theory, the validity of the modeling method for a piezoelectric coupled stepped beam under FIV, which is solved by mode superposition considering piecewise continuous eigenfunctions, is verified by experiment. The modeling method is adaptable to accommodate more complex structural designs under different boundary conditions. Energy generation performance can be enhanced through design optimization using GA, with a neural network model employed as the fitness function to make predictions based on input parameters. The ability to deal with forecasting problems using deep learning techniques is demonstrated by comparing the charging curves generated by the training model with those produced by the numerical model. Combining the feature extraction capability of CNN and the learning advantage of LSTM, the performance of a hybrid CNN-LSTM model is improved, resulting in more reliable and accurate predictions of complex dynamics. Optimization case studies under constant total mass and varying total mass are carried out separately. Under a variation ratio of ±10% for the selected parameters, the optimization results under constant total mass and varying total mass exhibit a noticeable improvement in energy generation performance when comparing the best and worst fitness values. Further improvement can be achieved by increasing the variation ratio and incorporating additional tuning parameters.

Chapter 8 Conclusion and future research plans

8.1 Conclusion

In this thesis, mathematical models of PEGs under different high frequency operations and nonlinear conditions are developed. The dynamic behaviors and energy generation characteristics of the PEGs are analyzed. A summary of each project, along with its main conclusion, is presented as follows.

8.1.1 Design and analysis of a PEG under high frequency rotation

A novel piezoelectric energy generator embedded in vehicle brake pads and excited by magnetic repulsion is developed. To illustrate the voltage generation, a mathematical model with experimental verification is established to calculate the generated electric charge and output voltage considering the charge dissipation. The energy harvesting process is evaluated by simulating the transient charging of the storage capacitor through the diode bridge, which was experimentally validated in literature. A total RMS power of 0.0710 W can be achieved with thirty-six generators embedded in both the inner and the outer brake pads within one brake caliper using APC850 (PZT4) material, and a total RMS power of 1.1226 W can be achieved using PMN-PT-B (PT = 0.3-0.33) material at 120 km/h. This novel generator will be useful for efficient and practical energy harvesting applications during vehicle braking process.

8.1.2 Design and analysis of a shear mode PEG under FIV

In this work, a shear mode piezoelectric energy generator, which utilizes FIV and high shear mode piezoelectric coefficient to improve the energy output, is proposed. A piezoelectric coupled FIV mathematical model is developed to accurately calculate the dynamic vibration response and voltage output. The dynamic voltage response is validated by experiment, and it proves the possibility of continuous friction-induced high-frequency vibration. Under ideal experiment conditions with proper parameters, a volume of 6.25×10^{-8} m^3 PZT4 piezoelectric material indicates RMS charging power density of 5.38×10^3 W/m^3 and 4.70×10^3 W/m^3 with electrically in parallel and electrically in series, respectively. While using the same amount of material and structural setup, the single crystal PMN-PT piezoelectric material shows RMS charging power density of 2.72×10^4 W/m^3 and 2.58×10^4 W/m^3 with electrically in parallel and electrically in series, correspondingly. Possible incorporation into vehicle braking systems can be considered to utilize the wasted friction energy, and it may offer an energy supply for low-power wireless devices.

8.1.3 Analysis of a PEG under linear, bi-linear, and impact conditions under FIV

In this research, a novel piezoelectric energy generator with linear, bi-linear, and impact design configurations is proposed. The dynamic response under FIV is described by a mathematical model incorporating the piezoelectric coupling effect. The reliability of the model and the stable high-frequency FIV phenomenon with linear, bi-linear, and impact design configurations are validated by experiment. High voltages can be generated under optimal operating conditions. Enhanced energy generation performance can be achieved by modifying structural design and incorporating materials with better properties.

8.1.4 Analysis of a magnet-engaged PEG under harmonic excitation

A magnet-engaged shear-mode piezoelectric energy generator with two nonlinear vibration system configurations has been proposed, and the corresponding mechanical and piezoelectric coupling models are developed. The simulation results are compared with harmonic balance method and experiment to prove the validity of the approach. Due to the magnet-induced nonlinear force with parallel and series connections to the piezoelectric element, the proposed energy

generators extend the operation bandwidth and improve the possible output power. The magnetic nonlinear spring in-parallel design configuration exhibits superiority in operation bandwidth and output power when compared to the linear spring in- parallel design. The nonlinear spring in-series design using the same amount of material reveals advantages in terms of wide operation bandwidth and high output power.

8.1.5 Analysis of a magnet-engaged PEG under FIV

This study investigated the characteristics of a magnet-engaged nonlinear piezoelectric energy generator stimulated by FIV in two distinct design configurations (in- parallel and in-series). The emergence of a stick-slip motion induced limit cycle and its vanishing delineates the unstable and stable regions of the system, respectively. A critical sliding velocity v_c splits the regions. When the sliding velocity exceeds v_c, the system remains in a stable region with exclusive slip friction behavior. The influence of decay factor β, dynamic friction coefficient μ_k, static friction coefficient μ_{static}, and normal force F_N on the energy generation was investigated relative to the operating velocity range (OVR) and sum of root mean square charging power (SRCP). The in-parallel systems exhibit a higher SRCP within the same OVR, whereas the in-series systems are more likely to excite FIV with a wider OVR. Additionally, the simulation results of fluctuating working conditions show that both fluctuating F_N and v_0 have negative effects on energy generation. The nonlinear in-series system exhibits better robustness with the least affected SRCP and almost unchanged OVR under fluctuating F_N and v_0.

8.1.6 Analysis of a PEG with continuum beam under FIV

In this research, a piezoelectric coupled continuum structure under FIV is modelled, described, and studied for the first time to characterize the system's dynamic response and energy generation performance. The model is applied to geometrically and materially uniform beam with partially bonded piezoelectric layers in the current study, and its applicability can extend to non-uniform beams with diverse piezoelectric patch layouts. The semi-analytical solution is derived to solve the dynamic responses, and the energy generation is assessed by charging simulation of a storage capacitor with experimental validation. Considering the same dimensional properties, materials with low Young's modulus E and density ρ are desired for the host structure to facilitate large

dynamic strain in piezoelectric materials. Optimal contact interface materials can induce pronounced FIV, enabling vibrations close to higher-order resonant frequencies with dynamic voltage outputs.

8.1.7 Modeling and optimization of a PEG with stepped continuum beam under FIV

In this work, a piezoelectric coupled stepped beam is developed to capture vibrational energy induced by friction. A mathematical model integrating the piezoelectric effect and Stribeck friction is proposed to describe the dynamic responses, and transient charging simulation is employed to assess the power output. A stepped beam prototype is manufactured, and its performance is tested through experiment. Subsequently, a Convolutional Neural Network - Long Short-Term Memory (CNN-LSTM) neural network is trained with simulation data. The trained model is applied as the fitness function in the Genetic Algorithm (GA) optimization process. Several GA optimizations under constant total mass (CTM) and varying total mass (VTM) conditions are conducted separately. With a variation ratio of $\pm 10\%$ for the selected parameters, the optimization results under CTM and VTM exhibit a maximum improvement of 19.7% and 11.1%, respectively. Further improvement can be achieved by increasing the variation ratio and incorporating additional tuning parameters.

8.2 Recommendations for future work

This thesis presented the mathematical modeling, experimental verification, and comprehensive parameter studies on energy generation performance of different PEGs under high-frequency excitation, encompassing rotating motion, single degree of freedom FIV, multiple degree of freedom FIV, and continuum structure FIV. Though various studies have demonstrated enhanced piezoelectric energy generation performance under high-frequency excitation, the following suggestions are proposed for future improvements.

1. Structural modifications can be considered in the PEGs, for instance, applying force amplification frame, integrating cellular lattice design, and utilizing different operation modes simultaneously. These can be achieved through the design of lever systems or compliant mechanisms that concentrate force on the piezoelectric elements. Additionally, integrating cellular lattice structures can provide better mechanical properties, such as higher strength-to-

weight ratios, and 3D printing technique can be used to create these complex lattice designs. Furthermore, utilizing multiple operation modes concurrently can involve developing control systems that dynamically switch between operating modes or combine them based on the input conditions.

2. Dynamic responses of PEGs under mixed mode excitation, which closely resemble practical working conditions, require further investigation. Proper mathematical models should be developed to describe the behaviors of these systems accurately. Coupled differential equations or finite element models, can possibly predict system behaviors under these conditions. Experimental validation can provide empirical data to refine these models.
3. Hybrid structures, for instance, L or U shape beam and beam with structural nonlinearity, can be developed to investigate their dynamic responses under different excitation sources, such as wind and water flow. Computational simulations using ANSYS or COMSOL, combined with wind tunnel or water flow testing, can be employed to study these responses. Optimizing designs based on these studies can enhance the efficiency and reliability of PEGs for specific applications.
4. The dynamic responses of hybrid structures under different boundary conditions can be further explored. The mechanisms and working conditions of phenomena such as internal resonance, frequency locking, and frequency jump are worth to be studied using both analytical approaches and experimental testing setups.
5. Materials with better properties, such as improved piezoelectricity and enhanced flexibility allowing for large deformation, can be tested in the current design to compare the energy generation performance.
6. Consideration can be given to incorporating different energy generation mechanisms, such as electrostatic and electromagnetic mechanisms, into PEGs to achieve hybrid energy generation for enhanced energy output.
7. Considering the changes in environmental conditions (such as temperature and humidity) can help predict the performance of PEGs under close to real world conditions. To simulate the effects of temperature and humidity on PEGs, varying material properties based on temperature-dependent equations and humidity effects can be considered for analytical modeling. And FEA allowing for thermal-mechanical and thermal-electric-structural coupling, can also be considered for numerical modeling.

Appendix A

The governing equations for free vibration can be expressed as:

$$EI\frac{d^4W_1}{dx^4} + \rho A{\omega_n}^2 W_1 = 0, \ \ (0 \le x < L_1), \tag{A.1}$$

$$(EI)'\frac{d^4W_2}{dx^4} + m'{\omega_n}^2 W_2 = 0, \ \ (L_1 \le x \le L_2), \tag{A.2}$$

$$EI\frac{d^4W_3}{dx^4} + \rho A{\omega_n}^2 W_3 = 0, \ \ (L_2 < x \le L), \tag{A.3}$$

where ω_n is the nth natural frequency; W_1, W_2, and W_3 are the mode shape functions corresponding to the first, second, and third modes of the beam. In this case, W can be re-defined as the combination of mode shapes of three beam sections, $W = W_1 + W_2 + W_3$. Assuming the solution of the mode shape function has the form of $W(x) = C_1\cos(\beta x) + C_2\sin(\beta x) + C_3\cosh(\beta x) + C_4\sinh(\beta x)$ [112], the free vibration solutions of the beam can be written as,

$$\begin{aligned} W_1 &= C_1\cos(f_1 x) + C_2\sin(f_1 x) + C_3\cosh(f_1 x) + C_4\sinh(f_1 x), \ \ (0 \le x < L_1) \\ W_2 &= C_5\cos(f_2 x) + C_6\sin(f_2 x) + C_7\cosh(f_2 x) + C_8\sinh(f_2 x), \ \ (L_1 \le x \le L_2), \\ W_3 &= C_9\cos(f_1 x) + C_{10}\sin(f_1 x) + C_{11}\cosh(f_1 x) + C_{12}\sinh(f_1 x), \ \ (L_2 < x \le L) \end{aligned} \tag{A.4}$$

where f_1 and f_2 are calculated as ${f_1}^4 = (12\rho{\omega_n}^2)/(EH^2)$ and ${f_2}^4 = (m'{\omega_n}^2)/(EI)'$, respectively; C_i are the unknown constants and obtained through the following boundary conditions,

$$\begin{aligned} &W_1 = 0, && \frac{dW_1}{dx} = 0; && (x = 0) \\ &W_1 = W_2, && EI\frac{d^2W_1}{dx^2} = (EI)'\frac{d^2W_2}{dx^2}, \\ &\frac{dW_1}{dx} = \frac{dW_2}{dx}, && EI\frac{d^3W_1}{dx^3} = (EI)'\frac{d^3W_2}{dx^3}; && (x = L_1) \\ &W_2 = W_3, && EI\frac{d^2W_3}{dx^2} = (EI)'\frac{d^2W_2}{dx^2}, \\ &\frac{dW_2}{dx} = \frac{dW_3}{dx}, && EI\frac{d^3W_3}{dx^3} = (EI)'\frac{d^3W_2}{dx^3}; && (x = L_2) \\ &\frac{d^2W_3}{dx^2} = 0, && \frac{d^3W_3}{dx^3} = 0. && (x = L) \end{aligned} \tag{A.5}$$

Appendix B

Through vibration modal analysis, multiplying both sides of Eq. (2.74) by $W_m(x)$ and integrating from $x = 0$ to $x = L$ in the space-domain, Eq. (2.74) results in,

$$\begin{aligned}\int_0^L \rho A(x) \sum_{n=1}^{\infty} W_n(x) \frac{\partial^2 q_n(t)}{\partial t^2} W_m(x) dx + \int_0^L EI(x) \sum_{n=1}^{\infty} q_n(t) \frac{\partial^4 W_n(x)}{\partial x^4} W_m(x) dx \\ + \int_0^L C_s I(x) \sum_{n=1}^{\infty} \frac{\partial q_n(t)}{\partial t} \frac{\partial^4 W_n(x)}{\partial x^4} W_m(x) dx \\ = \int_0^L F_{\mathrm{f}}(x,t)\, W_m(x) dx + \int_0^L \left[F_{\mathrm{p},1}(x,t) + F_{\mathrm{p},2}(x,t) + F_{\mathrm{p},3}(x,t) + F_{\mathrm{p},4}(x,t)\right] W_m(x) dx\end{aligned} \quad . \tag{B.1}$$

Assuming the beam is under structural damping, C_{s} can be expressed as $C_{\mathrm{s}} = 2E\zeta_n^{\mathrm{s}}/\omega_n$. ζ_n^{s} and ω_n are the nth mode strain rate damping ratio and natural frequency, respectively. Considering the orthogonality conditions of normal vibration modes, $q_n(t)$ in Eq. (2.72) can be written as,

$$\begin{gathered}\frac{\partial^2 q_n(t)}{\partial t^2} + 2\zeta_n^{\mathrm{s}}\omega_n \frac{\partial q_n(t)}{\partial t} + \omega_n^2 q_n(t) = \\ \frac{\int_0^L F_{\mathrm{f}}(x,t) W_n(x) dx + \int_0^L \left[F_{\mathrm{p},1}(x,t) + F_{\mathrm{p},2}(x,t) + F_{\mathrm{p},3}(x,t) + F_{\mathrm{p},4}(x,t)\right] W_n(x) dx}{\int_0^L \rho A(x) W_n^2(x) dx},\end{gathered} \tag{B.2}$$

and $q_n(t)$ can be solved via Duhamel integral as,

$$\begin{gathered}q_n(t) = \frac{1}{\omega_{d,n}} \int_0^t \left[\frac{\int_0^L F_{\mathrm{f}}(x,\tau) W_n(x) dx + \int_0^L \left[F_{\mathrm{p},1}(x,\tau) + F_{\mathrm{p},2}(x,\tau) + F_{\mathrm{p},3}(x,\tau) + F_{\mathrm{p},4}(x,\tau)\right] W_n(x) dx}{\int_0^L \rho A(x) W_n^2(x) dx}\right], \\ \times e^{-\zeta_n^{\mathrm{s}}\omega_n(t-\tau)} \sin\left(\omega_{d,n}(t-\tau)\right) d\tau\end{gathered} \tag{B.3}$$

where $\omega_{d,n}$ is the damping frequency of the nth mode, ${\omega_{d,n}}^2 = {\omega_n}^2(1 - {\zeta_n^s}^2)$. Substituting Eq. (B.3) into Eq. (2.72), the vibration response $w(x,t)$can be written as,

$$\begin{aligned}w(x,t) = \sum_{n=1}^{\infty} W_n(x) q_n(t) \\ = \sum_{n=1}^{\infty} W_n(x) \frac{1}{\omega_{d,n}} \int_0^t \left[\frac{\int_0^L \left[F_{\mathrm{p},1}(x,\tau) + F_{\mathrm{p},2}(x,\tau) + F_{\mathrm{p},3}(x,\tau) + F_{\mathrm{p},4}(x,\tau)\right] W_n(x) dx}{\int_0^L \rho A(x) W_n^2(x) dx}\right. \\ \left. + \frac{\int_0^L F_{\mathrm{f}}(x,\tau) W_n(x) dx}{\int_0^L \rho A(x) W_n^2(x) dx}\right] \times e^{-\zeta_n^{\mathrm{s}}\omega_n(t-\tau)} \sin\left(\omega_{d,n}(t-\tau)\right) d\tau\end{aligned} \quad . \tag{B.4}$$

It is noted from Eq. (2.81) that the generated voltage on the piezoelectric patch consists of two terms, the first term is related to the vibration response of the beam, and the second term includes the voltage across the resistance from the measuring device. The induced bending moment M_{e} from the piezoelectric material, which has piezoelectric coupling effect on the mechanical vibration response of the beam, is related to the generated voltage. A modified iteration method

considering the charge dissipation from the measuring device and piezoelectric coupling effect is applied in this study to accurately calculate the dynamic displacement from the cantilever beam and voltage response from the piezoelectric material [143].

Following the similar concept described in Section 2.3 and Section 2.4, the total calculation time T is divided into small discrete time segments t_i, where the subscript i indicates the iteration number and $\Delta t = t_{i+1} - t_i$ is the corresponding period of calculation. For the first iteration step ($t = 0$ s and $i = 1$), we assumed that the beam is static and no force is acting on it. The deflection at any point along the beam is 0, the velocity at any point along the beam is 0 except for the point with friction excitation, and the voltage on the piezoelectric patch is 0,

$$\begin{cases} w(x,t_1) = 0 \\ \frac{dw(x,t_1)}{dt} = \begin{cases} v_0 & (x = x_\mathrm{f}) \\ 0 & (x \neq x_\mathrm{f}) \end{cases}, \\ V_\mathrm{p}(t_1) = 0 \end{cases} \tag{B.5}$$

The responses $w(x,t)$ and $V_\mathrm{p}(t)$ in time period $t = t_1 - t_2$ is represented by,

$$\begin{gathered} w(x,t) = w_\mathrm{free}(x,t) + w_\mathrm{force}(x,t) \\ = \sum_{n=1}^{\infty} W_n(x) q_n(t) = \sum_{n=1}^{\infty} W_n(x)(q_\mathrm{free}(t) + q_\mathrm{force}(t))' \end{gathered} \tag{B.6}$$

$$\begin{gathered} w_\mathrm{free}(x,t) = \sum_{n=1}^{\infty} W_n(x) q_{\mathrm{free},n}(t) \\ = \sum_{n=1}^{\infty} W_n(x)\, e^{-\zeta_n^S \omega_n t}(A_{0,n}(t_1)\cos(\omega_{\mathrm{d},n} t) + B_{0,n}(t_1)\sin(\omega_{\mathrm{d},n} t))' \end{gathered} \tag{B.7}$$

$$\begin{gathered} w_\mathrm{force}(x,t) = \sum_{n=1}^{\infty} W_n(x) q_{\mathrm{force},n}(t) \\ = \sum_{n=1}^{\infty} W_n(x) \frac{1}{\omega_{\mathrm{d},n}} \int_0^{t-t_1} \left[\frac{\int_0^L (\sum_{l=1}^4 F_{\mathrm{p},l}(x,\tau+t_1)) W_n(x) dx}{\int_0^L \rho A(x) W_n^2(x) dx} \right. \\ \left. + \frac{\int_0^L F_\mathrm{f}(x,\tau+t_1) W_n(x) dx}{\int_0^L \rho A(x) W_n^2(x) dx} \right] \times e^{-\zeta_n^S \omega_n (t-t_1-\tau)} \sin(\omega_{\mathrm{d},n}(t-t_1-\tau)) d\tau \end{gathered} \tag{B.8}$$

$$\begin{gathered} V_\mathrm{p}(t) = V_\mathrm{p}(t_1) e^{-\frac{h}{R b_\mathrm{p} (L_2 - L_1) \varepsilon_{33}^S}(t-t_1)} \\ + \int_0^{t-t_1} \int_{L_1}^{L_2} \left[\frac{d_{31} E_\mathrm{p} h_\mathrm{pc} b_\mathrm{p} h}{\varepsilon_{33}^S b_\mathrm{p} (L_2 - L_1)} \frac{\partial^3 w(x,t)}{\partial x^2 \partial t} \right] e^{-\frac{h}{R b_\mathrm{p} (L_2 - L_1) \varepsilon_{33}^S}(t-t_1-\tau)} dx d\tau \end{gathered} \tag{B.9}$$

where $A_{0,n}$ and $B_{0,n}$ are determined by $q_{0,n}(t_1)$ and $\dot{q_{0,n}}(t_1)$, and relationship can be expressed as,

$$e^{-\zeta_n^S \omega_n t_1}\left[A_{0,n}\cos(\omega_{\mathrm{d},n} t_1) + B_{0,n}\sin(\omega_{\mathrm{d},n} t_1)\right] = q_{0,n}(t_1), \tag{B.10}$$

$$\begin{gathered} e^{-\zeta_n^S \omega_n t_1}\cos(\omega_{\mathrm{d},n} t_1)(B_{0,n}\omega_{\mathrm{d},n} - A_{0,n}\zeta_n^S \omega_n) \\ - e^{-\zeta_n^S \omega_n t_1}\sin(\omega_{\mathrm{d},n} t_1)(B_{0,n}\zeta_n^S \omega_n \omega_{\mathrm{d},n} + A_{0,n}\omega_{\mathrm{d},n}) = \dot{q_{0,n}}(t_1)' \end{gathered} \tag{B.11}$$

reorganizing Eq.(B.10) and Eq. (B.11), yields,

$$B_{0,n} = \frac{e^{\zeta_n^{\mathrm{S}}\omega_n t_1}\left[\cos(\omega_{\mathrm{d},n}t_1)(\zeta_n^{\mathrm{S}}\omega_n \mathrm{q}_{0,n}(t_1)+\dot{q_{0,n}}(t_1))+\omega_{\mathrm{d},n}\mathrm{q}_{0,n}(t_1)\sin(\omega_{\mathrm{d},n}t_1)\right]}{\omega_{\mathrm{d},n}}, \tag{B.12}$$

$$A_{0,n} = \frac{\left[\mathrm{q}_{0,n}(t_1)e^{\zeta_n^{\mathrm{S}}\omega_n t_1} - B_{0,n}\sin(\omega_{\mathrm{d},n}t_1)\right]}{\cos(\omega_{\mathrm{d},n}t_1)}. \tag{B.13}$$

Following the similar idea, when the time is in the period $t = t_j - t_{j+1}$, $w(x,t)$ and $V_{\mathrm{p}}(t)$ can be expressed as,

$$\begin{aligned} w(x,t) &= \sum_{n=1}^{\infty} W_n(x)(q_{\mathrm{free}}(t) + q_{\mathrm{force}}(t)) \\ &= \sum_{n=1}^{\infty} W_n(x)\Big[e^{-\zeta_n^s\omega_n t}(A_{0,n}(t_j)\cos\omega_{\mathrm{d},n}t + B_{0,n}(t_j)\sin\omega_{\mathrm{d},n}t) \\ &\quad + \frac{1}{\omega_{\mathrm{d},n}}\int_0^{t-t_j}\left(\frac{\int_0^L(\sum_{l=1}^4 F_{\mathrm{p},l}(x,\tau+t_j))W_n(x)dx}{\int_0^L \rho A(x)W_n^2(x)dx}\right. \\ &\quad \left. + \frac{\int_0^L F_{\mathrm{f}}(x,\tau+t_j)W_n(x)dx}{\int_0^L \rho A(x)W_n^2(x)dx}\right) \times e^{-\zeta_n^s\omega_n(t-t_j-\tau)}\sin(\omega_{\mathrm{d},n}(t-t_j-\tau))d\tau\Big] \end{aligned}, \tag{B.14}$$

$$\begin{aligned} V_{\mathrm{p}}(t) &= V_{\mathrm{p}}(t_j)e^{-\frac{h}{Rb_{\mathrm{p}}(L_2-L_1)\varepsilon_{33}^{\mathrm{S}}}(t-t_j)} \\ &\quad + \int_0^{t-t_j}\int_{L_1}^{L_2}\left[\frac{d_{31}E_{\mathrm{p}}h_{\mathrm{pc}}b_{\mathrm{p}}h}{\varepsilon_{33}^{\mathrm{S}}b_{\mathrm{p}}(L_2-L_1)}\frac{\partial^3 w(x,t)}{\partial x^2\partial t}\right]e^{-\frac{h}{Rb_{\mathrm{p}}(L_2-L_1)\varepsilon_{33}^{\mathrm{S}}}(t-t_j-\tau)}dxd\tau \end{aligned}, \tag{B.15}$$

where $A_{0,n}$ and $B_{0,n}$ can be expressed as,

$$B_{0,n} = \frac{e^{\zeta_n^{\mathrm{S}}\omega_n t_j}\left[\cos(\omega_{\mathrm{d},n}t_j)(\zeta_n^{\mathrm{S}}\omega_n \mathrm{q}_{0,n}(t_j)+\dot{q_{0,n}}(t_j))+\omega_{\mathrm{d},n}\mathrm{q}_{0,n}(t_j)\sin(\omega_{\mathrm{d},n}t_j)\right]}{\omega_{\mathrm{d},n}}, \tag{B.16}$$

$$A_{0,n} = \frac{\left[\mathrm{q}_{0,n}(t_j)e^{\zeta_n^{\mathrm{S}}\omega_n t_j} - B_{0,n}\sin(\omega_{\mathrm{d},n}t_j)\right]}{\cos(\omega_{\mathrm{d},n}t_j)}. \tag{B.17}$$

References

[1] H. Tian, X. Shan, H. Cao, and T. Xie, “Enhanced performance of airfoil-based piezoaeroelastic energy harvester: numerical simulation and experimental verification,” *Mech. Syst. Signal Process.*, vol. 162, no. March 2021, p. 108065, 2022, doi: 10.1016/j.ymssp.2021.108065.

[2] N. Wu, B. Bao, and Q. Wang, “Review on engineering structural designs for efficient piezoelectric energy harvesting to obtain high power output,” *Eng. Struct.*, vol. 235, p. 112068, 2021, doi: 10.1016/j.engstruct.2021.112068.

[3] X. D. Xie and Q. Wang, “Energy harvesting from a vehicle suspension system,” *Energy*, vol. 86, pp. 382–395, 2015, doi: 10.1016/j.energy.2015.04.009.

[4] B. Bao, Q. Wang, N. Wu, and S. Zhou, “Hand-held piezoelectric energy harvesting structure: Design, dynamic analysis, and experimental validation,” *Measurement*, vol. 174, p. 109011, 2021, doi: 10.1016/j.measurement.2021.109011.

[5] L. Zhang, X. Xu, Q. Han, Z. Qin, and F. Chu, “Energy harvesting of beam vibration based on piezoelectric stacks,” *Smart Mater. Struct.*, vol. 28, p. 125020, 2019, doi: https://doi.org/10.1088/1361-665X/ab4e09.

[6] Z. Li, X. Peng, G. Hu, and Y. Peng, “Theoretical, numerical, and experimental studies of a frequency up-conversion piezoelectric energy harvester,” *Int. J. Mech. Sci.*, vol. 223, p. 107299, 2022, doi: 10.1016/j.ijmecsci.2022.107299.

[7] Z. Min, C. Hou, G. Sui, X. Shan, and T. Xie, “Simulation and Experimental Study of a Piezoelectric Stack Energy Harvester for Railway Track Vibrations,” *Micromachines*, vol. 14, no. 4, 2023, doi: 10.3390/mi14040892.

[8] J. Wang *et al.*, “Experimental field study on a full-scale road piezoelectric energy harvester,” *Smart Mater. Struct.*, vol. 31, no. 5, 2022, doi: 10.1088/1361-665X/ac51ad.

[9] Y. Xiao, Q. Ji, S. Karnaoukh, C. Wang, and N. Wu, “Design and analysis of a d33 mode piezoelectric energy generator for vehicle braking system,” *Smart Mater. Struct.*, vol. 31, no. 6, p. 065027, 2022, doi: 10.1088/1361-665x/ac6d30.

[10] J. H. Kim *et al.*, “Development of a hybrid type smart pen piezoelectric energy harvester for an IoT platform,” *Energy*, vol. 222, p. 119845, 2021, doi: 10.1016/j.energy.2021.119845.

[11] Y. Li *et al.*, “Vibration energy harvesting with piezoelectric ceramics working in d33 mode by using a spring-mass-spring oscillator,” *J. Appl. Phys.*, vol. 127, no. 6, p. 064104, 2020, doi: 10.1063/1.5116554.

[12] W. Sheng, H. Xiang, Z. Zhang, and X. Yuan, “High-efficiency piezoelectric energy harvester for vehicle-induced bridge vibrations: Theory and experiment,” *Compos. Struct.*, vol. 299, no. August, p. 116040, 2022, doi: 10.1016/j.compstruct.2022.116040.

[13] T. Narolia, V. K. Gupta, and I. A. Parinov, “Design and experimental study of rotary-type energy harvester,” *J. Intell. Mater. Syst. Struct.*, vol. 31, no. 13, pp. 1594–1603, 2020, doi: 10.1177/1045389X20930085.

[14] N. Wu, Q. Wang, and X. D. Xie, “Ocean wave energy harvesting with a piezoelectric coupled buoy structure,” *Appl. Ocean Res.*, vol. 50, pp. 110–118, 2015, doi: 10.1016/j.apor.2015.01.004.

[15] D. Gibus, A. Morel, P. Gasnier, A. Ameye, and A. Badel, “High performance piezoelectric vibration energy harvesting by electrical resonant frequency tuning,” *Smart Mater. Struct.*, vol. 31, no. 12, p. 125012, 2022, doi: 10.1088/1361-665x/ac9d74.

[16] B. Bao, S. Zhou, and Q. Wang, “Interplay between internal resonance and nonlinear magnetic interaction for multi-directional energy harvesting,” *Energy Convers. Manag.*, vol. 244, p. 114465, 2021, doi: 10.1016/j.enconman.2021.114465.

[17] Z. Li, T. Li, Z. Yang, and H. E. Naguib, “Toward a 0.33 W piezoelectric and electromagnetic hybrid energy harvester: Design, experimental studies and self-powered applications,” *Appl. Energy*, vol. 255, p. 113805, 2019, doi: 10.1016/j.apenergy.2019.113805.

[18] S. Sadikbasha, B. Radhika, and V. Pandurangan, “Auxetic hexachiral cantilever beams for piezoelectric vibration energy harvesting,” *Smart Mater. Struct.*, vol. 31, no. 10, p. 105015, 2022, doi: 10.1088/1361-665X/ac8d3e.

[19] Q. Liu, W. Qin, Y. Yang, and Z. Zhou, “Promote performance of vibration energy harvesting by amplified inertial force and clamped piezoelectric beams,” *Mech. Syst. Signal Process.*, vol. 178, p. 109291, 2022, doi: 10.1016/j.ymssp.2022.109291.

[20] Y. Xiao, N. Wu, and Q. Wang, “Energy generation from friction-induced vibration of a

piezoelectric beam," *Int. J. Mech. Sci.*, p. 109648, 2024, doi: 10.1016/j.ijmecsci.2024.109648.

[21] G. Shi *et al.*, "A piezoelectric vibration energy harvester for multi-directional and ultra-low frequency waves with magnetic coupling driven by rotating balls," *Appl. Energy*, vol. 310, no. December 2021, p. 118511, 2022, doi: 10.1016/j.apenergy.2021.118511.

[22] K. J. I. Egbe, A. Matin Nazar, and P. Jiao, "Piezoelectric-triboelectric-electromagnetic Hybrid Rotational Energy Harvesters (H-REH)," *Int. J. Mech. Sci.*, vol. 235, p. 107722, 2022, doi: 10.1016/j.ijmecsci.2022.107722.

[23] R. K. Haldkar, A. V. Cherpakov, I. A. Parinov, and V. E. Yakovlev, "Comprehensive Numerical Analysis of a Porous Piezoelectric Ceramic for Axial Load Energy Harvesting," *Appl. Sci.*, vol. 12, p. 10047, 2022, doi: 10.3390/app121910047.

[24] X. Xie *et al.*, "A study on a novel piezoelectric bricks made of double-storey piezoelectric coupled beams," *Energy*, vol. 250, p. 123769, 2022, doi: 10.1016/j.energy.2022.123769.

[25] T. Narolia, V. K. Gupta, and I. A. Parinov, "Design and analysis of a shear mode piezoelectric energy harvester for rotational motion system," *J. Adv. Dielectr.*, vol. 10, no. 3, pp. 7–10, 2020, doi: 10.1142/S2010135X20500083.

[26] D. A. Wang and N. Z. Liu, "A shear mode piezoelectric energy harvester based on a pressurized water flow," *Sensors Actuators A Phys.*, vol. 167, no. 2, pp. 449–458, 2011, doi: 10.1016/j.sna.2011.03.003.

[27] J. Zhao, X. Zheng, L. Zhou, Y. Zhang, and J. Sun, "Investigation of a d15 mode PZT-51 piezoelectric energy harvester with a series connection structure," *Smart Mater. Struct.*, vol. 21, no. 10, p. 105006, 2012, doi: 10.1088/0964-1726/21/10/105006.

[28] Y. Xiao, W.-H. Liu, Z.-Q. Lu, and N. Wu, "Numerical investigation of nonlinear shear-mode piezoelectric energy generation under permanent magnetic conditions," *Nonlinear Dyn.*, vol. 111, pp. 18779–18817, 2023, doi: https://doi.org/10.1007/s11071-023-08805-z.

[29] P. Berik, "Piezoelectric d15 Shear-Mode Sensor in Parallel and Series Configurations," *Adv. Mater. Lett.*, vol. 11, no. 4, 2020, doi: 10.5185/amlett.2020.041497.

[30] M. A. Trindade and A. Benjeddou, "Finite element homogenization technique for the characterization of d15 shear piezoelectric macro-fibre composites," *Smart Mater. Struct.*, vol. 20, no. 7, p. 075012, 2011, doi: 10.1088/0964-1726/20/7/075012.

[31] Y. Xiao, S. Karnaoukh, and N. Wu, "Design and analysis of a d15 mode piezoelectric

energy generator using friction-induced vibration," *Smart Mater. Struct.*, vol. 32, no. 3, p. 035040, 2023, doi: 10.1088/1361-665X/acbcb1.

[32] M. Li, R. Gao, S. Liu, and L. Tong, "Modeling, analysis and validation of a novel asymmetric cruciform harvester with d15 mode," *Smart Mater. Struct.*, vol. 29, no. 2, 2020, doi: 10.1088/1361-665X/ab607a.

[33] Z. Zeng, B. Ren, L. Gai, X. Zhao, H. Luo, and D. Wang, "Shear-Mode-Based Cantilever Driving Low-Frequency Piezoelectric Energy Harvester Using 0.67Pb(Mg1/3Nb2/3)O3-0.33PbTiO3," *IEEE Trans. Ultrason. Ferroelectr. Freq. Control*, vol. 63, no. 8, pp. 1192–1197, 2016, doi: 10.1109/TUFFC.2016.2572308.

[34] X. Gao *et al.*, "High output power density of a shear-mode piezoelectric energy harvester based on Pb(In1/2Nb1/2)O3-Pb(Mg1/3Nb2/3)O3-PbTiO3 single crystals," *Appl. Energy*, vol. 271, no. May, p. 115193, 2020, doi: 10.1016/j.apenergy.2020.115193.

[35] B. Ren *et al.*, "Piezoelectric energy harvesting using shear mode 0.71Pb(Mg 1/3Nb2/3)O3-0.29PbTiO3 single crystal cantilever," *Appl. Phys. Lett.*, vol. 96, no. 8, p. 083502, 2010, doi: 10.1063/1.3327330.

[36] A. Keshmiri and N. Wu, "A Wideband Piezoelectric Energy Harvester Design by Using Multiple Non-Uniform Bimorphs," *Vibration*, vol. 1, pp. 93–104, 2018, doi: 10.3390/vibration1010008.

[37] L. Wang, P. Yu, S. Zhang, Z. Zhao, and J. Jin, "Electromechanical coupling model of variable-section piezoelectric composite beams in longitudinal vibration," *Int. J. Mech. Sci.*, vol. 241, no. August 2022, p. 107973, 2023, doi: 10.1016/j.ijmecsci.2022.107973.

[38] R. Sriramdas, S. Chiplunkar, R. M. Cuduvally, and R. Pratap, "Performance enhancement of piezoelectric energy harvesters using multilayer and multistep beam configurations," *IEEE Sens. J.*, vol. 15, no. 6, pp. 3338–3348, 2015, doi: 10.1109/JSEN.2014.2387882.

[39] J. Zhang, D. Qu, Z. Fang, and C. Shu, "Optimization of a piezoelectric wind energy harvester with a stepped beam," *J. Mech. Sci. Technol.*, vol. 34, no. 11, pp. 4357–4366, 2020, doi: 10.1007/s12206-020-1001-y.

[40] R. Usharani, G. Uma, M. Umapathy, and S. B. Choi, "A new piezoelectric-patched cantilever beam with a step section for high performance of energy harvesting," *Sensors Actuators, A Phys.*, vol. 265, pp. 47–61, 2017, doi: 10.1016/j.sna.2017.08.031.

[41] M. Rahimzadeh, H. Samadi, and N. S. Mohammadi, "Analysis of energy harvesting

enhancement in piezoelectric unimorph cantilevers," *Sensors*, vol. 21, p. 8463, 2021, doi: 10.3390/s21248463.

[42] R. Usharani, G. Uma, M. Umapathy, and S. B. Choi, "A novel piezoelectric energy harvester using a multi-stepped beam with rectangular cavities," *Appl. Sci.*, vol. 8, no. 11, 2018, doi: 10.3390/app8112091.

[43] B. Shi, J. Yang, and C. Rudd, "On vibration transmission in oscillating systems incorporating bilinear stiffness and damping elements," *Int. J. Mech. Sci.*, vol. 150, no. September 2018, pp. 458–470, 2019, doi: 10.1016/j.ijmecsci.2018.10.031.

[44] E. Hernández-Montes, M. A. Aschheim, and L. M. Gil-Martín, "Energy components in nonlinear dynamic response of SDOF systems," *Nonlinear Dyn.*, vol. 82, pp. 933–945, 2015, doi: 10.1007/s11071-015-2208-9.

[45] P. Balasubramanian, G. Franchini, G. Ferrari, B. Painter, K. Karazis, and M. Amabili, "Nonlinear vibrations of beams with bilinear hysteresis at supports: interpretation of experimental results," *J. Sound Vib.*, vol. 499, p. 115998, 2021, doi: 10.1016/j.jsv.2021.115998.

[46] G. Shan and M. Zhu, "A piezo stack energy harvester with frequency up-conversion for rail track vibration," *Mech. Syst. Signal Process.*, vol. 178, p. 109268, 2022, doi: 10.1016/j.ymssp.2022.109268.

[47] S. Fang, S. Wang, S. Zhou, Z. Yang, and W. H. Liao, "Exploiting the advantages of the centrifugal softening effect in rotational impact energy harvesting," *Appl. Phys. Lett.*, vol. 116, p. 063903, 2020, doi: 10.1063/1.5140060.

[48] M. Su, W. Wei, W. Xu, and Y. Zhang, "Stochastic response and reliability of electromagnetic energy harvester with mechanical impact and Coulomb friction," *Nonlinear Dyn.*, vol. 109, no. 4, pp. 2263–2280, 2022, doi: 10.1007/s11071-022-07596-z.

[49] W. J. Su, "Impact-driven broadband piezoelectric energy harvesting using a two-degrees-of-freedom structure," *Microsyst. Technol.*, vol. 26, pp. 1915–1924, 2020, doi: 10.1007/s00542-019-04744-1.

[50] Z. Li *et al.*, "Towards real-time self-powered sensing with ample redundant charges by a piezostack-based frequency-converted generator from human motions," *Energy Convers. Manag.*, vol. 258, no. March, p. 115466, 2022, doi: 10.1016/j.enconman.2022.115466.

[51] J. Zhang and L. Qin, "A tunable frequency up-conversion wideband piezoelectric vibration

energy harvester for low-frequency variable environment using a novel impact- and rope-driven hybrid mechanism," *Appl. Energy*, vol. 240, no. February, pp. 26–34, 2019, doi: 10.1016/j.apenergy.2019.01.261.

[52] L. He, Y. Han, R. Liu, R. Hu, G. Yu, and G. Cheng, "Design and performance study of a rotating piezoelectric wind energy harvesting device with wind turbine structure," *Energy*, vol. 256, p. 124675, 2022, doi: 10.1016/j.energy.2022.124675.

[53] P. Micek and D. Grzybek, "Experimental analysis of the arrays of macro fiber composite patches for rotational piezoelectric energy harvesting from a shaft," *Energies*, vol. 14, no. 16, 2021, doi: 10.3390/en14164815.

[54] M. Rizal, Husni, A. Z. Mubarak, M. Dirhamsyah, and Arhami, "Design and experimental study of a piezoelectric energy harvester embedded in a rotating spindle excited by magnetic force," *Sensors Actuators A Phys.*, vol. 340, no. February, p. 113521, 2022, doi: 10.1016/j.sna.2022.113521.

[55] Q. Gao *et al.*, "A rotating auxetic energy harvester for vehicle wheels," *Eng. Struct.*, vol. 288, no. May, p. 116190, 2023, doi: 10.1016/j.engstruct.2023.116190.

[56] J. Kan, Y. Wu, Y. Gu, S. Wang, F. Meng, and Z. Zhang, "A drum-like piezoelectric rotational energy harvester via magnetic beating," *Appl. Phys. Lett.*, vol. 123, no. 11, 2023, doi: 10.1063/5.0152454.

[57] L. He, Y. Han, L. Sun, H. Wang, Z. Zhang, and G. Cheng, "A rotating piezoelectric-electromagnetic hybrid harvester for water flow energy," *Energy Convers. Manag.*, vol. 290, no. June, p. 117221, 2023, doi: 10.1016/j.enconman.2023.117221.

[58] L. Qin, L. Zhang, J. Feng, F. Zhang, Q. Han, and Z. Qin, "A hybrid triboelectric-piezoelectric smart squirrel cage with self-sensing and self-powering capabilities," *Nano Energy*, vol. 124, p. 109506, 2024, doi: 10.1016/j.nanoen.2024.109506.

[59] R. R. Chand and A. Tyagi, "Design and experimental validation of an exponentially tapering width rotational piezoelectric vibration energy harvester," *J. Intell. Mater. Syst. Struct.*, vol. 34, no. 1, pp. 15–28, 2022, doi: 10.1177/1045389X221093315.

[60] M. Safaei, H. A. Sodano, and S. R. Anton, "A review of energy harvesting using piezoelectric materials: state-of-the-art a decade later (2008–2018)," *Smart Mater. Struct.*, vol. 28, no. 11, p. 113001, 2019, doi: 10.1088/1361-665x/ab36e4.

[61] E. Pennestrì, V. Rossi, P. Salvini, and P. P. Valentini, "Review and comparison of dry

friction force models," *Nonlinear Dyn.*, vol. 83, no. 4, pp. 1785–1801, 2016, doi: 10.1007/s11071-015-2485-3.

[62] F. Marques, P. Flores, J. C. Pimenta Claro, and H. M. Lankarani, "A survey and comparison of several friction force models for dynamic analysis of multibody mechanical systems," *Nonlinear Dyn.*, vol. 86, no. 3, pp. 1407–1443, 2016, doi: 10.1007/s11071-016-2999-3.

[63] C. Canudas-De-Wit, H. Olsson, K. J. Åström, and P. Lischinsky, "A New Model for Control of Systems with Friction," *IEEE Trans. Automat. Contr.*, vol. 40, no. 3, pp. 419–425, 1995, doi: 10.1109/9.376053.

[64] K. Zong, Z. Qin, and F. Chu, "Modeling of Frictional Stick-Slip of Contact Interfaces Considering Normal Fractal Contact," *J. Appl. Mech.*, vol. 89, pp. 031003–1, 2022, doi: 10.1115/1.4052882.

[65] R. I. Leine, D. H. Van Campen, A. De Kraker, and L. Van Den Steen, "Stick-Slip Vibrations Induced by Alternate Friction Models," *Nonlinear Dyn.*, vol. 16, pp. 41–54, 1998, doi: 10.1023/A.

[66] Y. F. Liu, J. Li, Z. M. Zhang, X. H. Hu, and W. J. Zhang, "Experimental comparison of five friction models on the same test-bed of the micro stick-slip motion system," *Mech. Sci.*, vol. 6, pp. 15–28, 2015, doi: 10.5194/ms-6-15-2015.

[67] D. Wei, J. Song, Y. Nan, and W. Zhu, "Analysis of the stick-slip vibration of a new brake pad with double-layer structure in automobile brake system," *Mech. Syst. Signal Process.*, vol. 118, pp. 305–316, 2019, doi: 10.1016/j.ymssp.2018.08.055.

[68] F. Al-Bender, V. Lampaert, and J. Swevers, "The generalized Maxwell-slip model: A novel model for friction simulation and compensation," *IEEE Trans. Automat. Contr.*, vol. 50, no. 11, pp. 1883–1887, 2005, doi: 10.1109/TAC.2005.858676.

[69] X. C. Wang, B. Huang, R. L. Wang, J. L. Mo, and H. Ouyang, "Friction-induced stick-slip vibration and its experimental validation," *Mech. Syst. Signal Process.*, vol. 142, p. 106705, 2020, doi: 10.1016/j.ymssp.2020.106705.

[70] W. P. Hu *et al.*, "Experimental Study on Corrugation of a Sliding Surface Caused by Frictional Self-Excited Vibration," *Tribol. Trans.*, vol. 59, no. 1, pp. 8–16, 2016, doi: 10.1080/10402004.2015.1041628.

[71] F. Körner and R. Mayer, "Analysis and characterization of the friction of vehicle body vibration dampers," *Automot. Engine Technol.*, vol. 5, pp. 79–90, 2020, doi:

https://doi.org/10.1007/s41104-020-00060-3.

[72] F. Chen, H. Ouyang, and X. Wang, “A new mechanism for friction-induced vibration and noise,” *Friction*, vol. 11, pp. 302–315, 2022, doi: doi.org/10.1007/s40544-022-0602-0.

[73] S. C. Lin, C. C. Guan, A. R. A. Bakar, M. R. Jamaluddin, W. M. M. Wan Harujan, and B. A. Ghani, “Disc brake squeal suppression through chamfered and slotted pad,” *Int. J. Veh. Struct. Syst.*, vol. 3, no. 1, pp. 28–35, 2011, doi: 10.4273/ijvss.3.1.04.

[74] M. Triches, S. N. Y. Gerges, and R. Jordan, “Reduction of squeal noise from disc brake systems using constrained layer damping,” *J. Brazilian Soc. Mech. Sci. Eng.*, vol. 26, no. 3, pp. 340–348, 2004, doi: 10.1590/s1678-58782004000300011.

[75] L. Hammerström and S. Jacobson, “Surface modification of brake discs to reduce squeal problems,” *Wear*, vol. 261, no. 1, pp. 53–57, 2006, doi: 10.1016/j.wear.2005.09.021.

[76] X. Zhao, N. Gräbner, and U. von Wagner, “Avoiding creep groan: Investigation on active suppression of stick-slip limit cycle vibrations in an automotive disk brake via piezoceramic actuators,” *J. Sound Vib.*, vol. 441, pp. 174–186, 2019, doi: 10.1016/j.jsv.2018.10.049.

[77] Y. Wang, M. Xu, S. Shao, S. Song, and Y. Shao, “A Novel Stick-Slip Type Rotary Piezoelectric Actuator,” *Adv. Mater. Sci. Eng.*, vol. 2020, p. 2659475, 2020, doi: 10.1155/2020/2659475.

[78] C. Tadokoro, A. Matsumoto, T. Nagamine, and S. Sasaki, “Piezoelectric power generation using friction-induced vibration,” *Smart Mater. Struct.*, vol. 26, no. 6, p. 065012, 2017, doi: 10.1088/1361-665X/aa7042.

[79] D. W. Wang, J. L. Mo, X. F. Wang, H. Ouyang, and Z. R. Zhou, “Experimental and numerical investigations of the piezoelectric energy harvesting via friction-induced vibration,” *Energy Convers. Manag.*, vol. 171, no. June, pp. 1134–1149, 2018, doi: 10.1016/j.enconman.2018.06.052.

[80] Z. Y. Xiang, J. L. Mo, H. H. Qian, W. Chen, D. B. Luo, and Z. R. Zhou, “Friction-induced vibration energy harvesting of a high-speed train brake system via a piezoelectric cantilever beam,” *Tribol. Int.*, vol. 162, no. June, p. 107126, 2021, doi: 10.1016/j.triboint.2021.107126.

[81] L. E. Helseth, “Excitation of energy harvesters using stick-slip motion,” *Smart Mater. Struct.*, vol. 23, p. 085024, 2014, doi: 10.1088/0964-1726/23/8/085024.

[82] H. Xue, Y. Hu, and Q. Wang, “Broadband Piezoelectric Energy Harvesting Devices Using Multiple Bimorphs with Different Operating Frequencies,” *IEEE Trans. Ultrason.*

Ferroelectr. Freq. Control, vol. 55, no. 9, pp. 2104–2108, 2008, doi: 10.1109/TUFFC.903.

[83] A. Erturk, J. M. Renno, and D. J. Inman, "Modeling of Piezoelectric Energy Harvesting from an L-shaped Beam-mass Structure with an Application to UAVs," *J. Intell. Mater. Syst. Struct.*, vol. 20, no. 5, pp. 529–544, 2009, doi: 10.1177/1045389X08098096.

[84] H. Abdelmoula, S. Zimmerman, and A. Abdelkefi, "Accurate modeling, comparative analysis, and performance enhancement of broadband piezoelectric energy harvesters with single and dual magnetic forces," *Int. J. Non. Linear. Mech.*, vol. 95, pp. 355–363, 2017, doi: 10.1016/j.ijnonlinmec.2017.07.008.

[85] G. Hu, L. Tang, R. Das, and P. Marzocca, "A two-degree-of-freedom piezoelectric energy harvester with stoppers for achieving enhanced performance," *Int. J. Mech. Sci.*, vol. 149, pp. 500–507, 2018, doi: 10.1016/j.ijmecsci.2017.07.051.

[86] D. Su, K. Nakano, R. Zheng, and M. P. Cartmell, "Investigations of a stiffness tunable nonlinear vibrational energy harvester," *Int. J. Struct. Stab. Dyn.*, vol. 14, no. 8, p. 1440023, 2014, doi: 10.1142/S0219455414400239.

[87] D. Upadrashta and Y. Yang, "Finite element modeling of nonlinear piezoelectric energy harvesters with magnetic interaction," *Smart Mater. Struct.*, vol. 24, no. 4, p. 045042, 2015, doi: 10.1088/0964-1726/24/4/045042.

[88] A. Alomari, A. Batra, A. Tan, and M. Schamschula, "Enhanced piezoelectric energy harvester performance using magnetic force and thermal energy," *Integr. Ferroelectr.*, vol. 176, pp. 291–302, 2016, doi: 10.1080/10584587.2016.1252663.

[89] A. Abdelkefi and N. Barsallo, "Nonlinear analysis and power improvement of broadband low-frequency piezomagnetoelastic energy harvesters," *Nonlinear Dyn.*, vol. 83, pp. 41–56, 2016, doi: 10.1007/s11071-015-2306-8.

[90] D. Upadrashta and Y. Yang, "Nonlinear piezomagnetoelastic harvester array for broadband energy harvesting," *J. Appl. Phys.*, vol. 120, p. 054504, 2016, doi: 10.1063/1.4960442.

[91] P. Firoozy, S. E. Khadem, and S. M. Pourkiaee, "Broadband energy harvesting using nonlinear vibrations of a magnetopiezoelastic cantilever beam," *Int. J. Eng. Sci.*, vol. 111, pp. 113–133, 2017, doi: 10.1016/j.ijengsci.2016.11.006.

[92] X. Rui, Y. Li, Y. Liu, X. Zheng, and Z. Zeng, "Experimental study and parameter optimization of a magnetic coupled piezoelectric energy harvester," *Appl. Sci.*, vol. 8, p. 2609, 2018, doi: 10.3390/app8122609.

[93] K. Fan, Q. Tan, Y. Zhang, S. Liu, M. Cai, and Y. Zhu, “A monostable piezoelectric energy harvester for broadband low-level excitations,” *Appl. Phys. Lett.*, vol. 112, p. 123901, 2018, doi: 10.1063/1.5022599.

[94] S. Dhote, Z. Yang, K. Behdinan, and J. Zu, “Enhanced broadband multi-mode compliant orthoplanar spring piezoelectric vibration energy harvester using magnetic force,” *Int. J. Mech. Sci.*, vol. 135, pp. 63–71, 2018, doi: 10.1016/j.ijmecsci.2017.11.012.

[95] Z. Yang, L. Tang, M. Xie, S. Sun, W. Li, and K. Aw1, “Soft magneto-sensitive elastomer and polyvinylidene fluoride polymer based nonlinear piezoelectric energy harvesting: design, modelling and experiment,” *Smart Mater. Struct.*, vol. 28, p. 015031, 2018, doi: 10.1088/1361-665X/aaee4e.

[96] L. R. Alcala-Jimenez, T. P. Jensen, A. Lei, and E. V Thomsen, “Increased mechanical robustness of piezoelectric magnetoelastic vibrational energy harvesters,” *Microelectron. Eng.*, vol. 207, pp. 19–26, 2019, doi: 10.1016/j.mee.2018.12.003.

[97] W. Yang and S. Towfighian, “A parametric resonator with low threshold excitation for vibration energy harvesting,” *J. Sound Vib.*, vol. 446, pp. 129–143, 2019, doi: 10.1016/j.jsv.2019.01.038.

[98] X. Zhang, M. Zuo, H. Tan, Z. Wu, and Z. Lai, “Dynamics analysis of multi-field coupled piezoelectric energy harvester under random excitation,” *Mater. Sci. Eng.*, vol. 531, p. 012038, 2019, doi: 10.1088/1757-899X/531/1/012038.

[99] Z. Q. Lu, D. Shao, Z. W. Fang, H. Ding, and L. Q. Chen, “Integrated vibration isolation and energy harvesting via a bistable piezo-composite plate,” *J. Vib. Control*, vol. 26, no. 9–10, pp. 779–789, 2020, doi: 10.1177/1077546319889815.

[100] K. Li, Z. Yang, and S. Zhou, “Performance enhancement for a magnetic-coupled bi-stable flutter-based energy harvester,” *Smart Mater. Struct.*, vol. 29, p. 085045, 2020, doi: 10.1088/1361-665X/ab9238.

[101] X. Sun, F. Wang, and J. Xu, “Nonlinear Piezoelectric Structure for Ultralow-frequency Band Vibration Energy Harvesting with Magnetic Interaction,” *Int. J. Precis. Eng. Manuf. - Green Technol.*, vol. 6, no. 4, pp. 671–679, 2019, doi: 10.1007/s40684-019-00117-1.

[102] S. Zhou, J. Cao, G. Litak, and J. Lin, “Numerical analysis and experimental verification of broadband tristable energy harvesters,” *Tech. Mess.*, vol. 85, no. 9, pp. 521–532, 2018, doi: 10.1515/teme-2017-0076.

[103] S. Zhou, J. Cao, D. J. Inman, J. Lin, S. Liu, and Z. Wang, “Broadband tristable energy harvester: Modeling and experiment verification,” *Appl. Energy*, vol. 133, pp. 33–39, 2014, doi: 10.1016/j.apenergy.2014.07.077.

[104] Y. Leng, D. Tan, J. Liu, Y. Zhang, and S. Fan, “Magnetic force analysis and performance of a tri-stable piezoelectric energy harvester under random excitation,” *J. Sound Vib.*, vol. 406, pp. 146–160, 2017, doi: 10.1016/j.jsv.2017.06.020.

[105] R. Masana and M. F. D. Ã, “Relative performance of a vibratory energy harvester in mono- and bi-stable potentials,” *J. Sound Vib.*, vol. 330, no. 24, pp. 6036–6052, 2011, doi: 10.1016/j.jsv.2011.07.031.

[106] H. Liang, G. Hao, and O. Z. Olszewski, “A review on vibration-based piezoelectric energy harvesting from the aspect of compliant mechanisms,” *Sensors Actuators, A Phys.*, vol. 331, p. 112743, 2021, doi: 10.1016/j.sna.2021.112743.

[107] T. Rödig, A. Schönecker, and G. Gerlach, “A survey on piezoelectric ceramics for generator applications,” *J. Am. Ceram. Soc.*, vol. 93, no. 4, pp. 901–912, 2010, doi: 10.1111/j.1551-2916.2010.03702.x.

[108] M. H. Malakooti and H. A. Sodano, “Piezoelectric energy harvesting through shear mode operation,” *Smart Mater. Struct.*, vol. 24, p. 55005, 2015, doi: 10.1088/0964-1726/24/5/055005.

[109] V. Kulkarni, R. Ben-Mrad, S. E. Prasad, and S. Nemana, “A shear-mode energy harvesting device based on torsional stresses,” *IEEE/ASME Trans. Mechatronics*, vol. 19, no. 3, pp. 801–807, 2014, doi: 10.1109/TMECH.2013.2259635.

[110] Anon, “Ieee Standard on Piezoelectricity.,” *Am. Natl. Stand. Institute, Stand.*, 1978.

[111] D. Karnopp, “Computer Simulation of Mechanical Dynamic Systems,” *Trans. ASME J. Dyn. Syst. Meas. Control*, vol. 107, no. 1, pp. 100–103, 1985.

[112] S. S. Rao, *Mechanical Vibrations*, 6th Global. Pearson Education / Prentice Hall, 2018.

[113] A. Erturk and D. J. Inman, “A distributed parameter electromechanical model for cantilevered piezoelectric energy harvesters,” *J. Vib. Acoust. Trans. ASME*, vol. 130, no. 4, pp. 1–15, 2008, doi: 10.1115/1.2890402.

[114] E. F. Crawley and J. De Luis, “Use of piezoelectric actuators as elements of intelligent structures,” *AIAA J.*, vol. 25, no. 10, pp. 1373–1385, 1987, doi: 10.2514/3.9792.

[115] S. Bagheri, N. Wu, and S. Filizadeh, “Modeling of capacitor charging dynamics in an

energy harvesting system considering accurate electromechanical coupling effects," *Smart Mater. Struct.*, vol. 27, no. 6, p. 065026, 2018, doi: 10.1088/1361-665X/aabe9e.

[116] S. Sherrit *et al.*, "Piezoelectric multilayer actuator life test," *IEEE Trans. Ultrason. Ferroelectr. Freq. Control*, vol. 58, no. 4, pp. 820–828, 2011, doi: 10.1109/TUFFC.2011.1874.

[117] D. Zhao, L. Chu, N. Xu, C. Sun, and Y. Xu, "Development of a cooperative braking system for front-wheel drive electric vehicles," *Energies*, vol. 11, no. 2, p. 378, 2018, doi: 10.3390/en11020378.

[118] R. Hoseinnezhad, A. Bab-Hadiashar, and T. Rocco, "Real-time clamp force measurement in electromechanical brake calipers," *IEEE Trans. Veh. Technol.*, vol. 57, no. 2, 2008, doi: 10.1109/TVT.2007.906374.

[119] S. Cheedket and C. Sirisathitkul, "Comparison of closed-form solutions to experimental magnetic force between two cylindrical magnets," *EUREKA Phys. Eng.*, vol. 4, pp. 141–146, 2021, doi: 10.21303/2461-4262.2021.001955.

[120] A. Meram and Ü. Önen, "Vibration analysis of a novel magnetic-viscous nonlinear passive isolator via finite element simulation," *Turkish J. Electr. Eng. Comput. Sci.*, vol. 27, no. 3, pp. 2309–2320, 2019, doi: 10.3906/elk-1807-195.

[121] "K&J Magnetics." https://www.kjmagnetics.com/blog.asp?p=surface-fields-101 (accessed Mar. 12, 2022).

[122] W. K. Schomburg, O. Reinertz, J. Sackmann, and K. Schmitz, "Equations for the approximate calculation of forces between cuboid magnets," *J. Magn. Magn. Mater.*, vol. 506, no. March, p. 166694, 2020, doi: 10.1016/j.jmmm.2020.166694.

[123] Siemens, "Simcenter Physical Testing," 2020. https://www.plm.automation.siemens.com/global/pt/products/simcenter/simcenter-physical-testing.html (accessed Dec. 26, 2021).

[124] "PCB Model 208C01." https://www.pcb.com/products?model=208c01 (accessed Dec. 26, 2021).

[125] "APC International." https://www.americanpiezo.com/ (accessed Dec. 26, 2021).

[126] H. C. Song, H. C. Kim, C. Y. Kang, H. J. Kim, S. J. Yoon, and D. Y. Jeong, "Multilayer piezoelectric energy scavenger for large current generation," *J. Electroceramics*, vol. 23, no. 2–4, pp. 301–304, 2009, doi: 10.1007/s10832-008-9439-9.

[127] “Compression Spring-WB Jones.” https://www.springsfast.com/products/compression-springs/part-detail-compression-spring/?part=C14-047-032 (accessed May 26, 2022).

[128] W. Al-Ashtari, M. Hunstig, T. Hemsel, and W. Sextro, “Frequency tuning of piezoelectric energy harvesters by magnetic force,” *Smart Mater. Struct.*, vol. 21, p. 035019, 2012, doi: 10.1088/0964-1726/21/3/035019.

[129] D. Su, “Enhancement of energy harvesting from nonlinearly vibrating systems under harmonic and random excitations,” Ph.D. dissertation, University of Tokyo, 2015. [Online]. Available: https://repository.dl.itc.u-tokyo.ac.jp/record/47902/files/A32126.pdf

[130] J. Zeng and R. Luo, “Non-linear analysis of disc brake-induced vibrations for railway vehicles,” *Proc. Inst. Mech. Eng. Part F J. Rail Rapid Transit*, vol. 225, no. 1, pp. 48–56, 2011, doi: 10.1243/09544097JRRT307.

[131] “Piezoelectric Charge Constants.” https://www.americanpiezo.com/knowledge-center/piezo-theory/piezoelectric-constants.html (accessed Oct. 05, 2022).

[132] “Coefficient of friction, Rolling resistance, Air resistance, Aerodynamics.” https://www.tribology-abc.com/abc/cof.htm (accessed May 28, 2023).

[133] P. P. Phyo and Yung-Cheol Byun, “Hybrid Ensemble Deep Learning-Based Approach for Time Series Energy Prediction,” *Symmetry (Basel).*, vol. 13, p. 1942, 2021.

[134] Y. Kong, F. Chu, Z. Qin, and Q. Han, “Sparse learning based classification framework for planetary bearing health diagnostics,” *Mech. Mach. Theory*, vol. 173, no. February, p. 104852, 2022, doi: 10.1016/j.mechmachtheory.2022.104852.

[135] S. S. Afshari, S. Cui, X. Xu, and X. Liang, “Remaining Useful Life Early Prediction of Batteries Based on the Differential Voltage and Differential Capacity Curves,” *IEEE Trans. Instrum. Meas.*, vol. 71, pp. 1–9, 2022, doi: 10.1109/TIM.2021.3117631.

[136] S. Arndt, C. Turvey, and N. C. Andreasen, “Correlating and predicting psychiatric symptom ratings: Spearman’s v versus Kendall’s tau correlation,” *J. Psychiatr. Res.*, vol. 33, no. 2, pp. 97–104, 1999, doi: 10.1016/S0022-3956(98)90046-2.

[137] Y. Liu *et al.*, “Research on Correlation Analysis Method of Time Series Features Based on Dynamic Time Warping Algorithm,” *IEEE Geosci. Remote Sens. Lett.*, vol. 20, pp. 1–5, 2023, doi: 10.1109/LGRS.2023.3285788.

[138] X.-S. Yang, *Nature-Inspired Optimization Algorithms*, 1st ed., vol. 118. Elsevier, 2014. doi: 10.1007/978-981-10-6689-4_8.

[139] S. Bagheri, N. Wu, and S. Filizadeh, “Application of artificial intelligence and evolutionary algorithms in simulation-based optimal design of a piezoelectric energy harvester,” *Smart Mater. Struct.*, vol. 29, p. 105004, 2020, doi: 10.1088/1361-665X/ab9149.

[140] A. Homayouni-Amlashi, A. Mohand-Ousaid, and M. Rakotondrabe, “Analytical modelling and optimization of a piezoelectric cantilever energy harvester with in-span attachment,” *Micromachines*, vol. 11, no. 6, 2020, doi: 10.3390/MI11060591.

[141] H. E. Chimeh, S. Nabavi, M. Al Janaideh, and L. Zhang, “Deep-Learning-Based Optimization for a Low-Frequency Piezoelectric MEMS Energy Harvester,” *IEEE Sens. J.*, vol. 21, no. 19, pp. 21330–21341, 2021, doi: 10.1109/JSEN.2021.3102537.

[142] J. Wang, H. Huang, and H. Zhao, “Model-based optimization for structure dimension and driving signal of a stick-slip piezoelectric actuator,” *Mech. Syst. Signal Process.*, vol. 164, no. July 2021, p. 108191, 2022, doi: 10.1016/j.ymssp.2021.108191.

[143] Y. Cheng, N. Wu, and Q. Wang, “An efficient piezoelectric energy harvester with frequency self-tuning,” *J. Sound Vib.*, vol. 396, pp. 69–82, 2017, doi: 10.1016/j.jsv.2017.02.036.